Subsystems and Systems for Direct Detect Optical Fiber Transmission

Md Samiul Alam

Department of Electrical and Computer Engineering

McGill University

Montréal, Canada

August 2023

A thesis submitted to McGill University in partial fulfillment of the requirements for the degree of Doctor of Philosophy

Abstract

In this thesis, we explore several direct detect system architectures and necessary digital signal processing (DSP) algorithm to either extend the transmission speed and reach or lower the cost and complexity. This thesis can be divided into three parts. In the first part, we focus on high throughput data transmission over 500 m to 2 km of standard single-mode fiber (SSMF) enabled by Mach Zehnder modulators (MZMs). Utilizing high order pulse amplitude modulation (PAM) format and linear and nonlinear DSP algorithm, we demonstrate a record net 300 Gbps/λ intensity modulation direct detection (IM/DD) transmission with an O-band silicon photonic (SiP) traveling wave Mach-Zehnder modulator (TW-MZM). Although SiP offer a large-scale, low-cost solution, further performance improvement is gated by the inherent bandwidth (BW) and phase shifting efficiency limitations of these modulators. To push this capacity limit, we employ a thin-film lithium niobate (TFLN) MZM that enables net 350 Gbps/λ transmission with PAM8 signaling.

Transmission in the C-band with direct detection suffers from chromatic dispersion (CD) induced power fading, which ultimately limits the transmission reach for high symbol rate signals. In the second part of the thesis, we explore optical domain solutions to tackle this CD. We demonstrate the transmission of 60 Gbaud PAM-4 signal with polarization multiplexing (net 224 Gbps) over 10 km of SSMF in the C-band using Stokes vector receiver and an integrated ring resonator based optical dispersion compensator (ODC). We use a chirp free $LiNbO_3$ MZM to test the performance of the ODC. As compared to externally modulated MZM, directly modulated lasers show strong frequency chirp but are attractive for their cost and power efficiency. We study the chirp-CD interaction of DML analytically over positive and negative dispersion regime and through extensive simulation show the benefit and choice of optical filtering to enhance the transmission performance. As a next step, we experimentally verify the advantages of optical filtering in a DSP free DML/DD system and transmit 32 Gbps PAM4 signal over a CD range of -170 ps/nm to +340 ps/nm with sub-one-volt driving signal. With the aid of a proper optical filter and optimized DSP, we further extend the symbol rate to

35 Gbaud (70 Gbps) over 20 km of SSMF (340 ps/nm of CD).

In the last part of the thesis, we try to push the transmission reach to 40 km in the C-band by adopting self-coherent single-sideband (SSB) scheme with MZM, which is theoretically immune to power fading. However, creating an ideal SSB signal is complex and costly; and efficient solution is needed. We demonstrate that a skew between the differential driving signals in a dual-drive (DD) MZM based SSB transmitter can significantly relax the optical filtering requirement, reducing the cost. This enables net 200 Gbps/λ signal transmission over 40 km with a second order super gaussian (SG) optical filter. Overall, the proposed SSB scheme provides an innovative solution to enable high speed data transmission over 40 km of SSMF with direct detection in the C-band.

Résumé

Dans cette thèse, nous explorons plusieurs architectures de systèmes à détection directe et les algorithmes de traitement des signaux numériques (DSP) nécessaires pour augmenter la vitesse et la portée de la transmission ou pour réduire leur coût et complexité. Cette thèse est divisée en trois parties. Dans la première partie, nous nous concentrons sur la transmission de données à haut débit sur 500 m à 2 km de fibre monomode standard (SSMF) grâce à des modulateurs Mach Zehnder (MZM). En utilisant un format de modulation d'amplitude d'impulsion (PAM) de haut ordre et un algorithme DSP linéaire et non linéaire, nous démontrons une transmission détection directe de modulation d'intensité (IM/DD) nette record de 300 Gbps/λ avec un modulateur Mach-Zehnder à ondes progressives (TW-MZM) en bande O en photonique silicium (SiP). Bien que le SiP offre une solution à grande échelle et à faible coût, l'amélioration des performances est limitée par la largeur de bande inhérente et l'efficacité du déphasage de ces modulateurs. Pour repousser cette limite de capacité, nous utilisons un MZM en couche mince de niobate de lithium (TFLN) qui permet une transmission nette de 350 Gbps/λ avec une signalisation PAM8.

La transmission dans la bande C avec détection directe souffre de l'évanouissement de puissance induit par la dispersion chromatique (CD), ce qui limite finalement la portée de la transmission pour les signaux à taux de symbole élevé. Dans la deuxième partie de la thèse, nous explorons les solutions du domaine optique pour résoudre ce problème de CD. Nous démontrons la transmission d'un signal PAM-4 de 60 Gbaud avec multiplexage de polarisation (224 Gbps nets) sur 10 km de SSMF dans la bande C en utilisant un récepteur à vecteur de Stokes et un compensateur de dispersion optique (ODC) basé sur un résonateur en anneau intégré. Nous utilisons un MZM $LiNbO_3$ sans chirp pour tester la performance de l'ODC. Comparé aux MZMs à modulation externe, les lasers à modulation directe présentent un fort chirp de fréquence, mais restent intéressants en raison de leur coût et de leur efficacité énergétique. Nous étudions l'interaction chirp-CD d'un DML de manière analytique dans un régime de dispersion positive et négative et, grâce à une simulation approfondie, nous montrons

les avantages et le choix du filtrage optique pour améliorer les performances de transmission. Dans un deuxième temps, nous vérifions expérimentalement les avantages du filtrage optique dans un système DML/DD sans DSP et transmettons un signal PAM4 de 32 Gbps sur une plage de CD de -170 ps/nm à +340 ps/nm avec un signal de commande inférieur à un volt. Avec l'aide d'un filtre optique approprié et d'un DSP optimisé, nous étendons le taux de symboles à 35 Gbaud (70 Gbps) sur 20 km de SSMF (340 ps/nm de CD).

Dans la dernière partie de la thèse, nous essayons d'augmenter la portée de la transmission à 40 km dans la bande C en adoptant un schéma auto-cohérent à bande latérale unique (SSB) avec MZM, qui est théoriquement immunisé contre l'évanouissement de la puissance. Cependant, la création d'un signal SSB idéal est complexe et coûteuse. Une solution efficace est donc nécessaire. Nous démontrons qu'un décalage entre les signaux de commande différentiels dans un émetteur SSB basé sur un MZM à double commande (DD) peut considérablement assouplir l'exigence de filtrage optique, réduisant ainsi le coût. Cela permet la transmission d'un signal net de 200 Gbps/λ sur 40 km avec un filtre optique super gaussien (SG) de second ordre. Dans l'ensemble, le schéma SSB proposé fournissent de solution innovante pour permettre la transmission de données à haut débit sur 40 km de SSMF avec une détection directe dans la bande C.

Acknowledgements

All praise is due to **Allah SWT (Almighty God)**, the Most Gracious, and the Most Merciful, for granting me the strength, guidance, and patience to successfully pursue my doctoral studies. I am deeply thankful for His bounties and blessings upon me, and may His peace and blessings be upon His final messenger Muhammad SAW.

I would like to thank and extend my heartfelt appreciation to my supervisor, *Prof. David V. Plant*, for his outstanding academic guidance, moral and financial support, and above all his appreciation and encouragement, which have been instrumental in my journey. It has been a great privilege to work in his world class laboratory alongside all the amazing colleagues and researchers. I am impressed and amazed by Prof. Plant's dedication in obtaining the state-of-the-art instruments and managing the lab to provide us with the best in-class facilities.

I am also grateful to my PhD supervisory committee, *Prof. Lawrence Chen* and *Prof. Benoit Champagne*, for their valuable comments and important advice at every stage of my PhD program. I also attended the courses they offered, which have been very helpful throughout my PhD work.

I am immensely grateful for the support I received from my current and previous colleagues in the Photonic Systems Group (PSG) of McGill University. I would like to begin with *Dr. Mohamed Morsy-Osman* for his guidance during the early phase of my PhD study. His expertise, knowledge, and willingness to share were invaluable in my journey. I would also like to acknowledge the support of *Dr. Eslam El-Fiky*, *Dr. Md Ghulam Saber*, *Dr. Xueyang Li*, *Dr. Maxime Jacques* for all their assistance and support in the lab, which has made my journey smoother. I would like to mention *Kh Arif Shahriar* for all the discussions we have had since I joined McGill. Over the past three years, I have had the pleasure of working extensively with *Dr. Essam Berikaa*, who literally amazed me with his progress in such a short period of time. We spent of a lot time working in the lab and office. I would like to express my gratitude to our collaborators from Fonex Data Systems Inc., particularly *Dr. Reza Maram*, for his valuable suggestions on the DML/CML research project. I learned a lot from him over the years. It has also been a pleasure to work with *Dr. Deng Mao*, *Dr. Zhenping Xing*, and *Dr. Alireza Samani*. I extend my thanks to *Jinsong Zhang*, *Weijia Li*, *Yixiang Hu*, *Santiago Bernel* for all the great discussions we have had in the past few years, and I wish them success in their research endeavors.

I would like to dedicate this thesis to my father, *Dr. Md Abul Quasem*, and my mother, *Bilkis Banu* (May Allah have mercy on both); whose dreams, belief in me, and sacrifices have brought me to where I am today. I am endlessly thankful to my elder sister, *Karisma Kishoree*, and elder brother, *Muhammad Badrul Alam*, for their constant support, selflessness, and patience. I would also like to express my gratitude to my beloved wife, *Binte Amzed Tabssum*, for her unwavering support during the final phase of my PhD journey.

My sincere gratitude,

Md Samiul Alam

Associated Publications

The original contributions of the research works presented in this thesis are based on the following 8 first-authored publications (5 journal papers and 3 conference papers, 2 are under review). The contribution of the coauthors is stated for each paper below.

In addition, I have co-authored several journal papers and conference papers, which are not directly related to this thesis, through collaborations with my colleagues at McGill University.

Journal Articles Directly Related to This Thesis

1. **M. S. Alam**, R. Maram, K. A. Shahriar, P. Ricciardi, and D. V. Plant, "Chirped Managed Laser for Multilevel Modulation Formats: A Semi-analytical Approach for Efficient Filter Design" (manuscript submitted to *IEEE Journal of Lightwave Technology*).

   I conceived the idea, conducted the simulation, performed the experiment, and wrote the paper. R. Maram helped with the design of the appropriate filter. The other co-authors contributed in the discussion of the idea and in editing the paper.

2. **M. S. Alam**, K. A. Shahriar, R. Maram, P. Ricciardi, and D. V. Plant, "PAM4 Signal Transmission using Directly Modulated Lasers: A Comprehensive Analysis of Chirp Parameters, Fiber Dispersion and Optical Filtering" (manuscript submitted to *IEEE Photonics Journal)*.

   I conceived the idea, conducted the simulation, performed the experiment, and wrote the paper. The other co-authors contributed in the discussion of the idea and in editing the paper.

3. **M. S. Alam**, E. Berikaa, and D.V. Plant, "Net 350 Gbps/λ IMDD Transmission Enabled by High Bandwidth Thin Film Lithium Niobate MZM," *IEEE Photonics Technology Letters, vol. 34, no. 19, pp. 1003-1006, 2022.*

   I performed all experiments, collected, and processed the data, derived all analysis, and wrote the manuscript. E. Berikaa helped during the experiment and in editing the *manuscript. D.V. Plant supervised the overall project. HyperLight provided the TFLN modulator.*

4. **M. S. Alam**, X. Li, M. Jacques, E. Berikaa, P.C. Koh, and D.V. Plant, "Net 300 Gbps/λ Transmission Over 2 km of SMF With a Silicon Photonic Mach-Zehnder Modulator," *IEEE Photonics Technology Letters,* vol. 33, no. 24, pp. 1391-1394, 2021.

   I performed all experiments, collected, and processed the data, derived all analysis and wrote the manuscript. X. Li helped with several DSP codes. M. Jacques worked on the design and P.C. Koh helped with the fabrication of the Silicon Photonic Mach-Zehnder Modulator. D.V. Plant supervised the overall project.

5. **M. S. Alam**, X. Li, M. Jacques, Z. Xing, A. Samani, E. El-Fiky, P.C. Koh, and D.V. Plant, "Net 220 Gbps/λ IM/DD Transmission in O-Band and C-Band with Silicon Photonic Traveling-Wave MZM," *IEEE Journal of Lightwave Technology*, vol. 39, no. 13, pp. 4270-4278, 2021.

   I performed all transmission experiments, collected, and processed the data, derived all analysis, and wrote the manuscript. X. Li helped with several DSP codes. M. Jacques worked on the design and P.C. Koh helped with the fabrication of the Silicon Photonic Mach-Zehnder Modulator. The other authors contributed in the discussion and in editing the paper.

Conference Proceedings Directly Related to This Thesis

6. **M. S. Alam**, E. Berikaa, and D.V. Plant, "High Bandwidth Thin-Film Lithium Niobate MZM for Net 300 Gbps/λ IM/DD Transmission," *2022 IEEE Photonics Conference (IPC),* Vancouver, BC, Canada, 2022, pp. 1-2, doi: 10.1109/IPC53466.2022.9975680.

   I performed all experiments, collected, and processed the data, derived all analysis, and wrote the manuscript. E. Berikaa helped during the experiment and in editing the manuscript. D.V. Plant supervised the overall project. HyperLight provided the TFLN modulator.

7. **M. S. Alam**, X. Li, Z. Xing, M.E. Mousa-Pasandi, M. O'Sullivan, and D.V. Plant, "C-band 4×200 Gbit/s transmission over 40 km of SSMF with an RF delay-assisted WDM-SSB transmitter," in 2021 *Optical Fiber Communication Conference (OFC)*, 2021, p. W6A.50.

   I performed all the experiments, collected, and processed the data, derived all analysis, and wrote the manuscript. X. Li greatly helped in the laboratory with the experimental setup. The other authors contributed in the discussion and in editing the paper.

8. **M. S. Alam** *et. al.*, "224 Gb/s Transmission over 10 km of SMF at 1550 nm Enabled by a SiN Optical Dispersion Compensator and Stokes Vector Direct Detect Receiver," in *Signal Processing in Photonic Communications*, 2020, p. SpM4I.5.

   I performed all the experiments, collected, and processed the data, derived all analysis, and wrote the manuscript. M. Morsy-Osman greatly helped in the laboratory and with the experimental work. Ericsson provided the Optical Dispersion Compensator. The other authors contributed in the discussion and in editing the paper.

Journal Articles not Directly Related to This Thesis

9. E. Berikaa*, **M. S. Alam***, and D. V. Plant, "Silicon photonic modulators for net 300 Gbps/λ IM/DD and Net 1 Tbps/λ coherent transmission using All-Electronic equalization," *Optical Fiber Technology,* vol. 74, p. 103056, 2022, doi: https://doi.org/10.1016/j.yofte.2022.103056. (***Equal Contribution**, Invited Journal)

10. E. Berikaa, **M. S. Alam**, S. Bernal, R. G. Castrejón, W. Li, Y. Hu, B. Krueger, F. Pittalà, and D. V. Plant, "Next-Generation O-band Coherent Transmission for 1.6 Tbps 10 km Intra-Datacenter Interconnects," *IEEE Journal of Lightwave Technology, 2023* (Accepted for publication).

11. E. Berikaa, **M. S. Alam**, A. Samani, E. El-Fiky, Y. Hu, S. Lessard, and D. V. Plant, "Silicon Photonic Single-Segment IQ Modulator for Net 1 Tbps/λ Transmission Using All-Electronic Equalization," *IEEE Journal of Lightwave Technology*, vol. 41, no. 4, pp. 1192-1199, 2023, doi: 10.1109/JLT.2022.3191244.

12. E. Berikaa, **M. S. Alam**, and D. V. Plant, "Net 400-Gbps/λ IMDD transmission using a single-DAC DSP-free transmitter and a thin-film lithium niobate MZM," *Optics Letters*, vol. 47, no. 23, pp. 6273-6276, 2022, doi: 10.1364/OL.476399.
13. E. Berikaa, **M. S. Alam**, and D. V. Plant, "Beyond 300 Gbps Short-Reach Links Using TFLN MZMs With 500 mV pp and Linear Equalization," *IEEE Photonics Technology Letters*, vol. 35, no. 3, pp. 140-143, 2022.
14. D. Mao, **M. S. Alam**, M. Parvizi, E. El-Fiky, A. Abdo, N. Ben-Hamida, and D. V. Plant, "Design, analysis, and characterization of a compact silicon photonic modulator with meandered phase shifters," *Optics Express*, vol. 30, no. 18, pp. 32990-33002, 2022/08/29 2022, doi: 10.1364/OE.468150.
15. E. Berikaa, **M. S. Alam**, M. Jacques, X. Li, P. C. Koh, and D. V. Plant, "2D Constellation Distortion for Subduing Equalization Noise in Bandwidth- Limited IMDD Systems," *IEEE Photonics Technology Letters*, vol. 34, no. 5, pp. 267-270, 2022, doi: 10.1109/LPT.2022.3150231.
16. E. Berikaa, **M. S. Alam**, and D. V. Plant, "Unamplified Coherent Transmission of Net 500 Gbps/Polarization/λ for Intra-Datacenter Interconnects," *IEEE Photonics Technology Letters*, vol. 34, no. 21, pp. 1135-1138, 2022, doi: 10.1109/LPT.2022.3204178.
17. M. Morsy-Osman, **M. S. Alam**, K. A. Shahriar, S. Lessard, and D. V. Plant, "Optimum Three-Dimensional Constellations for Stokes Vector Direct Detect Receivers," *IEEE Photonics Technology Letters*, vol. 31, no. 8, pp. 587-590, 2019, doi: 10.1109/LPT.2019.2901625.
18. X. Li, Z. Xing, **M. S. Alam**, M. Jacques, P.-C. Koh, and D. V. Plant, "Cost-minimizing distribution matching supporting net 800 Gbit/s PS-PAM transmission over 2 km using a 4-λ EML TOSA," *Optics Letters*, vol. 45, no. 17, pp. 4718-4721, 2020/09/01 2020, doi: 10.1364/OL.395631.
19. X. Li, Z. Xing, **M. S. Alam**, M. E. Mousa-Pasandi, M. O. Sullivan, and D. V. Plant, "Demonstration of C-Band Amplifier-Free 100 Gb/s/λ Direct-Detection Links Beyond 40-

km SMF Using a High-Power SSB Transmitter," *IEEE Journal of Lightwave Technology*, vol. 38, no. 22, pp. 6170-6177, 2020, doi: 10.1109/JLT.2020.3009142.

20. A. Abdo, X. Li, **M. S. Alam**, M. Parvizi, N. Ben-Hamida, C. D'Amours, and D. Plant, "Partial Pre-Emphasis for Pluggable 400 G Short-Reach Coherent Systems," *Future Internet*, vol. 11, no. 12, p. 256, 2019.
21. R. Gutiérrez-Castrejón, M. G. Saber, **M. S. Alam**, Z. Xing, E. El-Fiky, D. E. Ceballos-Herrera, F. Cavaliere, G. Vall-Llosera, L. Giorgi, S. Lessard, R. Brunner, and D. V. Plant, "Systematic Performance Comparison of (Duobinary)-PAM-2,4 Signaling under Light and Strong Opto-Electronic Bandwidth Conditions," *Photonics*, vol. 8, no. 3, p. 81, 2021.
22. X. Li, M. O'Sullivan, Z. Xing, **M. S. Alam**, M. E. Mousa-Pasandi, and D. V. Plant, "Asymmetric self-coherent detection," *Optics Express*, vol. 29, no. 16, pp. 25412-25427, 2021/08/02 2021, doi: 10.1364/OE.421603.
23. M. G. Saber, R. Gutiérrez-Castrejón, **M. S. Alam**, Z. Xing, E. El-Fiky, L. Xu, F. Cavaliere, G. Vall-Llosera, S. Lessard, and D. V. Plant, "100 Gb/s/λ Duo-Binary PAM-4 Transmission Using 25G Components Achieving 50 km Reach," *IEEE Photonics Technology Letters*, vol. 32, no. 3, pp. 138-141, 2020, doi: 10.1109/LPT.2019.2962326.

Conference Proceedings not Directly Related to This Thesis

24. **M. S. Alam**, A. Abdo, X. Li, S. Aouini, M. Parvizi, N. Ben-Hamida, and D.V. Plant, "Performance and Complexity Analysis of Blind Timing Phase Error Detectors in Pluggable Coherent Receivers," in *Signal Processing in Photonic Communications*, 2020, p. SpTu1I.2.
25. **M. S. Alam**, A. Abdo, D. Mao, M. Parvizi, N Ben-Hamida, D.V. Plant, "Timing Phase Recovery in Digital MultiSubcarrier Coherent Optical Communication, in *2021 Photonics North (PN)*, IEEE, 2021.
26. E. Berikaa, **M. S. Alam**, S. Bernal, W. Li, B. Krueger, F. Pittalà, and D. V. Plant, "Net 1.6 Tbps O-Band Coherent Transmission Over 10 km Using a TFLN IQM and DFB Lasers

for Carrier and LO," in *2023 Optical Fiber Communication Conference (OFC),* p.Th4B.1.

27. E. Berikaa, **M S. Alam**, Y. Hu, W. Li, and D. V. Plant, "C-Band 100 Gb/s Transmission Over 40 km SSMF Using a Silicon Photonic Vestigial Sideband Transmitter Based on Dual-Drive MZM and Passive Optical Delay Line," in *2023 Optical Fiber Communication Conference (OFC),* p.Th3E.7.
28. E. Berikaa, **M. S. Alam**, Y. Hu, S. Lessard, and D. V. Plant, "Equalization Noise Reduction Through Constellation Distortion in Coherent Systems," in *Optica Advanced Photonics Congress* 2022, p. SpM2I.4.
29. E. Berikaa, **M. S. Alam**, A. Samani, S. Lessard, and D. V. Plant, "Net 1 Tbps/λ Transmission Over 80 km of SSMF Using a Single Segment SiP IQM With All-Electronic Equalization," in *Optical Fiber Communication Conference (OFC) 2022*, San Diego, California, p.Th4A.5.
30. K. A. Shahriar, **M. S. Alam**, R. Maram, A. Bayat, J. A. Altabas, J. B. Jensen, P. Ricciardi, D. V. Plant, "On the Feasibility of using DML-based Transmitter for Quasicoherent Receiver," in *2022 IEEE Photonics Conference (IPC)*, Vancouver, Canada, pp. 1-2.
31. K. A. Shahriar, **M. S. Alam**, M. Morsy-Osman, and D. V. Plant, "Pre-compensation for Attenuation-induced Distortions in NFT-based Optical Fiber Communication with EDFA," in *OSA Advanced Photonics Congress 2020*, Washington, p. SpTh3I.4.
32. D. Mao, **M. S. Alam**, M. Parvizi, E. El-Fiky, A. Abdo, N. Ben-Hamida, and D. V. Plant, "Compact Silicon Photonics Meandered Mach-Zehnder Modulator," in *Conference on Lasers and Electro-Optics (CLEO)*, San Jose, California, p. SF4M.3.
33. D. Mao, M. Parvizi, **M. S. Alam**, A. Abdo, N. Ben-Hamida, E. El-Fiky, and D. V. Plant, "Electrode Design for Slow-light based Mach-Zehnder Modulator in Silicon Photonics," in *2021 OSA Advanced Photonics Congress*, 2021, p.IW1B.4.
34. X. Li, Z. Xing, **M. S. Alam**, M. Jacques, S. Lessard, and D. V. Plant, "NN-based PCS distribution optimization for practical channels," in *2020 European Conference on Optical Communications (ECOC)*, 6-10, 2020, pp. 1-4.

35. X. Li, Z. Xing, **M. S. Alam**, M. Jacques, and D. V. Plant, "102 Gbaud PAM-4 transmission over 2 km using a pulse shaping filter with asymmetric ISI and Thomlinson-Harashima Precoding," in *Optical Fiber Communication Conference (OFC) 2020*, San Diego, California, p. T3I.1.

36. E. El-Fiky, A. Samani, **M. S. Alam**, M. Sowailem, O. Carpentier, M. Jacques, L. Guenin, D. Patel, and D. V. Plant, "A 4-Lane 400 Gb/s Silicon Photonic Transceiver for Intra-Datacenter Optical Interconnects," in *2019 Optical Fiber Communications Conference and Exhibition (OFC)*, 2019, pp. 1-3.

List of Figures

List of Tables

List of Acronyms

AC	Alternating Current
ADC	Analog-to-Digital Converter
ASE	Amplified Spontaneous Emission
AWG	Arbitrary Waveform Generator
AWGN	Additive Gaussian White Noise
BER	Bit Error Ratio
BPD	Balanced Photodetector
BPG	Binary Pattern Generator
B2B	Back to Back
BW	Bandwidth
CAP	Carrier-less Amplitude Phase Modulation
CD	Chromatic Dispersion
CDC	Chromatic Dispersion compensation
CMOS	Complementary Metal-Oxide-Semiconductor
CSPR	Carrier-to-Signal Power Ratio
CW	Continuous Wave
CWDM	Coarse Wavelength Division Multiplexing

DAC	Digital-to-Analog Converter
DC	Direct Current
DCF	Dispersion compensating fiber
DD	Direct Detection
DD-LMS	Decision Directed Least Mean Squares
DFB	Distributed-Feedback Laser
DFE	Decision Feedback Equalization
DFT	Discrete Fourier Transform
DML	Directly Modulated Laser
DMT	Discrete Multi-tone
DP	Dual Polarization
DSB	Double Sideband
DSP	Digital Signal Processing
DWDM	Dense Wavelength Division Multiplexing
EAM	Electro-Absorption Modulator
ECL	External cavity laser
EDFA	Erbium-Doped Fiber Amplifier
EML	Electro-absorption Modulated Laser

EO	Electro Optic
ER	Extinction Ratio
FEC	Forward Error Correction
FFE	Feed-Forward Equalization
FFT	Fast Fourier Transform
FIR	Finite Impulse Response
FSR	FSR Free Spectral Range
FT	Fourier Transform
FTN	Faster-Than-Nyquist
FWHM	Full Width Half Maximum
FWM	Four Wave Mixing
GbE	Gigabit Ethernet
GVD	Group Velocity Dispersion
HD-FEC	Hard Decision Forward Error Correction
IDFT	Inverse Discrete Fourier Transform
i.i.d.	Independent identically distribution
IFT	Inverse Fourier transform
IIR	Infinite Impulse Response

IL	Insertion Loss
IM/DD	Intensity Modulation Direct Detection
IQ	Inphase Quadrature
InP	Indium Phosphide
I/O	Input/Output
IQ	In-phase/Quadrature
ISI	Inter-Symbol Interference
KK	Kramers-Kronig
LCA	Lightwave Component Analyzer
LDPC	Low density parity check
LMS	Least Mean Square
LO	Local Oscillator
LP	Linear Polarized
LPF	Low Pass Filter
LSB	Left Sideband
LUT	Look-Up Table
MIMO	Multiple input multiple output
ME-MZM	Multi-Electrode MZM

MLSE	Maximum Likelihood Sequence Estimation
MOSFET	Metal-Oxide-Semiconductor Field-Effect Transistor
MRM	Micro Ring Modulator
MSA	Multi-Source Agreement
MSE	Mean Square Error
MZI	Mach-Zehnder Interferometer
MZM	Mach-Zehnder Modulator
NEP	Noise Equivalent Power
NLSE	Nonlinear Schrodinger Equation
NRZ	Non-return to zero
ODC	Optical Dispersion Compensator
OIF	Optical Internetworking Forum
OF	Optical filter
OFDM	Orthogonal frequency division multiplexing
OOK	On-off-keying
OSA	Optical spectrum analyzer
OSNR	Optical signal-to-noise ratio
PAM	Pulse Amplitude Modulation

PAPR	Peak-to-Average Power Ratio
PBC	Polarization beam combiner
PBS	Polarization beam splitter
PD	Photodetector
PDFA	Praseodymium-Doped Fiber Amplifier
PDM	Polarization Division Multiplexing
PDL	Polarization dependent loss
PLL	Phase locked loop
PM	Phase modulation
PMD	Polarization mode dispersion
PNLE	Polynomial nonlinear equalizer
POL-MUX	Polarization multiplexing
PON	Passive optical networks
PPG	Pulse pattern generator
PRBS	Pseudo random binary sequence
PSD	Power Spectral Density
PSM	Parallel Single Mode
QAM	Quadrature Amplitude Modulation

QCSE	Quantum-Confined Stark Effect
QSFP-DD	Quad Small Formfactor Pluggable Double Density
RC	Raised-Cosine (filter)
RF	Radio Frequency
RIN	Relative Intensity Noise
RLS	RLS Recursive least square
RMS	Root-Mean-Square
ROP	Received Optical Power
RC	Raised-Cosine
RRC	Root-Raised-Cosine
RS	Reed Solomon
RSB	Right sideband
RTO	Real-Time Oscilloscope
SCM	Sub-Carrier Multiplexing
SD-FEC	Soft-Decision Forward Error Correction
SE	Spectral Efficiency
SiP	Silicon Photonics
SISO	Single input single output

SMF	Single Mode Fiber
SNR	Signal to Noise Ratio
SOA	Semiconductor Optical Amplifier
SOP	State of polarization
SOI	Silicon-on-Insulator
SP	Single Polarization
SPP	Series Push Pull
SPM	Self-Phase Modulation
sps	Sample(s) per symbol
SSB	Single Sideband
SSBI	Signal-to-Signal Beating Interference
SSMF	Standard single mode fiber
SSFT	Split-Step Fourier Transform
SV-DD	Stokes vector direct detection
SVR	Stokes Vector Receiver
TEC	Thermoelectric cooler
THP	Tomlinson Harashima Precoding
TIA	Transimpedance Amplifier

TOSA	TOSA Transmitter optical sub-assembly
VA	Viterbi algorithm
VCSEL	Vertical Cavity Surface Emitting Laser
VNLE	Volterra Non-linear Equalizer
VGC	Vertical Grating Couplers
VOA	Variable Optical Attenuator
VSB	Vestigial Sideband
WDM	Wavelength division multiplexing
XPM	Cross Phase Modulation
ZF	Zero-Forcing
1D	One-Dimensional
2D	Two-Dimensional
4D	Four-Dimensional

Contents

Chapter 1 Introduction

1.1 Motivation

The advent of mobile 5G, optical fronthauling, cloud computing, massive machine-to-machine communication (M2M) has contributed to the significant growth of short-reach optical communication, making it a prominent research area and market segment in recent times. Short-reach communications, as defined by [1], encompass optical communication links ranging from hundreds of meters to tens of kilometers, connecting servers within a datacenter (DC) or between datacenters. These high-speed short-reach communication links can be broadly categorized into two groups: intra-datacenter and inter-datacenter links. The former covers data links spanning from a few meters to a few kilometers, facilitating communication between servers and racks within a datacenter, while the latter, also known as datacenter interconnects (DCI), enables data exchange among multiple datacenters over short, medium, or long distances using high-speed packet-optical connectivity. Although coherent solution is a strong contender for high-speed solution covering reach from 80 km and beyond, intensity modulation direct-detection (IM/DD) schemes, known for their cost and power efficiency, are widely employed in intra-datacenter and inter-datacenter links.

Among the various IM/DD schemes, pulse amplitude modulation (PAM) is the suitable choice for its low complexity and four-lane 400 GbE with PAM-4 has already been standardized for this reason [2]. Efforts are underway by the 800G multi-source agreement (MSA) to further extend this capacity to 800GbE, with the recent release of the first 200G/lane PAM4 industry specification. Compared to 100G/lane, 200G/lane offers better cost optimization and is expected to serve as the foundation for future short-reach interconnect standards at 800GbE and 1.6TbE capacities.

In terms of transmission reach, standards for 100 Gigabit Ethernet (100 GbE) transceivers can be classified into different segments based on reach capabilities, including short reach (SR) supporting up to 100 m OM4 multimode fiber (MMF) links, datacenter reach (DR) supporting up to 500 m single mode fiber (SMF) links, fiber reach (FR) for up to 2 km SMF, long reach (LR) for up to 10 km SMF, and extended reach (ER) offering up to 40 km SMF [3].

For transmission reach up to 10 km, O-band (1260-1360 nm) IM/DD solution is preferred as it avoids chromatic dispersion (CD)-induced power fading, and the fiber loss is manageable. On the other hand, C-band (1530-1565 nm) transmission offers advantages such as lower fiber loss (0.18 dB/km), mature wavelength division multiplexing (WDM) optics, and optical amplifiers (EDFA). C-band transmission is also preferred for the new 5G mobile transport network over 10-20 km (access networks) due to compatibility with the channel plans defined in ITU-T Recommendations G984.1 and G.698.2 [4]. However, C-band IM/DD systems are susceptible to power fading, and therefore, dispersion compensating fiber (DCF) or an optical dispersion compensation module (ODCM) becomes necessary for high symbol rate IM/DD transmission systems [5]. DCF, due to its bulky size and lossy nature, cannot be integrated into small form-factor pluggable modules, and thus, integrated dispersion compensation module can be a viable solution for IM/DD systems in such cases. Modified modulation formats, such as Nyquist or faster than Nyquist (FTN) PAM4, partial-response (PR) signaling, Tomlinson Harashima precoding have been proposed to as potential solutions to tackle the impact of power fading [6]. Advanced digital signal processing (DSP) algorithms, including pre-emphasis, feed-forward equalization (FFE), decision feedback equalization (DFE), and combinations of FFE and DFE, are actively being investigated to overcome the inter symbol interference (ISI) induced by power fading [7]. However, the adoption of complex DSP techniques may not be preferable due to the potential increase in power consumption of application-specific integrated circuits (ASICs). As a result, alternative approaches such as moderate DSP, optical domain, or RF domain solutions need to be explored.

As the transmission reach extends to 40 km, both O-band and C-band intensity modulation with direct detection (IM/DD) transmission face challenges. C-band signals are heavily distorted due to power fading, while O-band suffers from fiber loss, resulting in low received optical power. Optical amplification technologies are costly and exhibit poor performance in O-band, leading to a deteriorated signal-to-noise ratio (SNR) at this extended reach. Additionally, the accumulated chromatic dispersion (CD) for the edge channels becomes significant. Consequently, high symbol rate data transmission with simple IM/DD becomes infeasible, even with complex DSP. Single sideband (SSB)/vestigial sideband (VSB) systems offer an alternative to the conventional double sideband homodyne coherent systems, as they are immune to power fading and enable CD compensation with only one single-ended photodetector (PD) and one analog-to-digital converter (ADC) channel per polarization [8]. While separate CD compensation or field recovery DSP is not required for 40 km, it is the immunity to fading that makes SSB/VSB self-coherent systems a promising candidate for extended reach applications. However, SSB/VSB methods require complex system architecture and additional RF or optical devices (sharp filter), which may not be cost-effective. Thus, finding a cost-effective solution is imperative.

Apart from speed and reach, cost and power consumption are also critical considerations. External modulation using electro-absorption modulated laser (EML) and Mach-Zehnder modulator (MZM) can provide high bandwidth but are more expensive. On the other hand, directly modulated lasers (DMLs) are cost-effective, compact, and capable of higher output power, allowing for long-range transmission without the need for optical amplification. However, the limited electro-optic bandwidth and nonlinear behavior of DMLs due to their inherent frequency chirp restrict their capacity at lower speeds. Active research is ongoing to improve DML bandwidth, and DMLs are gaining significance in DC and 5G applications. Therefore, DMLs with DD require further attention, and effective solutions to extend their reach and capacity are crucial. These solutions can be broadly categorized into two approaches: utilizing an optical filter for chirp management and digital signal processing (DSP).

To summarize, there is a pressing need to increase the throughput of optical transceivers in a cost-effective manner to meet the growing demand for global data traffic. This motivation prompts the exploration of innovative solutions and the development of novel subsystems and systems in the field of direct detect optical communication to increase the capacity, reach and lower the power consumption.

1.2 Thesis Objective

Based on the discussions presented in the previous section, the thesis addresses the following research question:

- How can we cost-effectively increase the bitrate-distance product in an IM/DD system?

Since we are talking about two transmission performance metrics, bitrate and distance, the above research question can be broken down to two questions:

- How can we increase the bitrate in an IM/DD system and what would be the limit at B2B or at extremely short reach?
- How can we increase the transmission distance in an IM/DD system, without compromising the bitrate and cost?

Therefore, the objectives of the thesis are to:

- Analyze different modulation schemes (i.e., modulators and modulation formats) and develop necessary digital signal processing for the highest throughput in a traditional IM/DD system;
- Develop cost-effective subsystems to extend the transmission reach;
- Verify the developed solutions via experimental demonstration.

Intensity modulation can be done in two ways: direct modulation and external modulation. And there are different modulator material platforms, such as silicon photonic (SiP), lithium niobate ($LiNbO_3$), thin-film lithium niobate (TFLN) or indium phosphide (InP) for external electro-optic modulators [9]. Among these, we focus on silicon photonic (SiP) and thin-film lithium niobate modulators. SiP is lucrative because of its complementary metal oxide semiconductor

(CMOS) compatibility, high yield, and low fabrication costs. TFLN, on the other hand, is a relatively newer technology with much better electro-optic (EO) performance, including high EO bandwidth and phase-shifting efficiency, and low insertion loss. We start our thesis by characterizing best-in-class SiP and TFLN modulators based on MZM structure (external modulation), both fabricated in commercial foundry. Our research aims at increasing the throughputs with SiP and TFLN MZM with optimized modulation format and efficient DSP over intra-data center traffic distances of 2-10 km in the O-band. Next, we focus on extending transmission reach. We aim at extending the reach beyond 10 km in C-band with MZM and directly modulated lasers (DML). To that end, we first investigate the impact of chirp-CD interaction in DML/DD system. Following that, we develop a semi-analytical approach for deterministically designing an optical filter that makes the DML/DD system more tolerant to CD. To increase the throughput, we adopt higher order PAM4 formats in this analysis. We also analyze system performance with different DSP to extend the bitrate and reach. Finally, we investigate advanced direct detect system such as SSB/VSB self-coherent system to achieve high speed transmission over ER (extended reach) distances of 40 km.

1.3 Original contributions

The original contributions of the thesis can be grouped into three broad categories and are presented in the three main chapters. In this section, we try to summarize our original contributions.

High speed IM/DD Transmission using Mach Zehnder Modulator (Chapter 3)

- 200 Gbps/λ is a key node throughput for the next generation 800G/1.6T short reach optical links, which necessitates the use of modulators with high electro-optic (EO) bandwidth. Since bandwidth limitation and impairments come from different sources, DSP is an integral part for high-speed optical communication. In this chapter, therefore, we target realizing high throughput IMDD systems below 10 km of SSMF using high bandwidth Mach Zehnder Modulator (MZM), and efficient DSP. We characterize and perform transmission experiments with MZM on two different material platforms, silicon photonic (SiP) and thin-film lithium niobate (TFLN). SiP modulators are attractive for their compatibility with the CMOS process, small footprint, and cost-effectiveness. However, SiP MZMs have limited bandwidth and low phase shifting efficiency (high V_π), limiting the optical transmission speed. Still with proper MZM design and DSP, it is possible to achieve 200 Gbps/λ with SiP modulators. To that end, we present the design and characterization of O-band and C-band SiP traveling wave MZM with over 45 GHz 3-dB E-O bandwidth with a single-segment design. In the O-band (C-band), we achieve net 220 (215) Gbps data rate over 10 km (500 m) of single-mode fiber, showing the potential of SiP MZM in DCI space. We utilize PAM6 and PAM8 format and discuss the necessary DSP to achieve the results. Next, we employ our best O-band SiP MZM in a transmission system set up with the latest generation of SiGe arbitrary waveform generator (AWG) that can operate at 256 GSa/s. With this new AWG, we transmit 134 Gbaud PAM-4 (net 250 Gbps) with HD-FEC and 115 Gbaud PAM-8 (net 288 Gbps) with SD-FEC. The results are achieved with only a linear feed-forward equalizer (FFE) and a single 3 V peak-to-peak driving signal. With probabilistic shaping (PS), we extend the speed beyond 300 Gbps. This is the first net 300G transmission with a SiP modulator in an IM/DD system, fabricated entirely in a commercial foundry.

M. Jacques worked on the design and P.C. Koh helped with the fabrication of the Silicon Photonic Mach-Zehnder Modulator. X. Li helped with several DSP blocks including probabilistic shaping and assisted in writing the JLT manuscript. I performed all the transmission experiments, collected, and processed the data, and wrote the manuscript. All co-authors reviewed the manuscripts [10, 11].

- Achieving beyond net 300 Gbps with SiP modulator in an IM/DD system is extremely difficult even with strong DSP due to the limited EO BW and higher driving swing requirement. To overcome this limitation, we propose the use of TFLN modulators. In an identical experimental setup, we demonstrate ultra-high-speed data transmission at a symbol rate of up to 144 Gbaud. With 95 GHz 6-dB EO bandwidth and 1.5 V half-wave voltage, this C-band MZM enables the transmission of net 318 (308) Gbps PAM6 at B2B (after 500 m of SMF) with HD-FEC and net 360 (350) Gbps PAM8 at B2B (500 m) with SD-FEC. We also study different modulation formats, driving swing and DSP requirement to achieve these results. Our results demonstrate the suitability of the TFLN modulator platform for single lane 250, and 300+ Gbps intra-data center applications.

The TFLN modulator was designed and fabricated by HyperLight. We worked on the specifications of the MZM based on the experimental setup. I performed all the transmission experiments, collected, and processed the data, and wrote the manuscript. All co-authors reviewed the manuscripts [12, 13].

Reach Extension for C-band IM/DD Transmission with MZM and DML by Optical Filtering (Chapter 4)

- IM/DD transmission is limited by CD induced power fading in the C-band. However, C-band transmission over 10 km-20 km is important for access networks and wavelength division multiplexing (WDM) mobile transport link for lower fiber loss, device maturity, and bidirectional duplex communication. We demonstrate successful transmission of 60 Gbaud PAM4 in the polarization multiplexed system over 10 km in C-band with an integrated optical dispersion compensation module (ODCM), based on silicon nitride (SiN) micro-rings. We characterize the ODC and employ it in a dual polarization setup with Stokes vector receiver (SVR) to transmit net 200G signal with linear MIMO DSP.

  M. Morsy-Osman greatly helped in the laboratory with the experimental and DSP work. Ericsson and their collaborators provided the Optical Dispersion Compensator. I performed all the ODC transmission experiments, collected, and processed the data, *and wrote the manuscript. All co-authors reviewed the manuscripts [14].*

- Although MZM based IM/DD systems are preferable for higher throughput, direct modulation of laser diodes is attractive for higher modulated output power, cost-effectiveness, and compact footprint. However, the nonlinear response of directly modulated lasers (DML) and the interplay between chirp and CD makes it difficult to predict the performance of a PAM4 signal in a DD system over positive and negative dispersion regime. Although in prior works DML based PAM4 transmission system is explored, it has been mostly limited to a specific DML. Therefore, we study the BER dependency of PAM4 signal under varying transient and adiabatic chirp parameters over a range of transmission distances and verify the observed trends experimentally with eye diagrams and BER measurement. We demonstrate that unlike a chirp-free transmitter, the BER of a DML/DD system does not increase monotonically with increasing fiber dispersion; rather, there is a noticeable BER improvement in particular CD ranges, which depends on DML's transient and adiabatic chirp parameters, output average power, and the considered symbol rate. Furthermore, with the aid of optical filtering, we transmit 32 Gbps PAM4 signal using DML over a dispersion range of -170 ps/nm to 340 ps/nm, without any DSP, showing the potential of DML in low-cost transceivers.
- Chirp managed lasers (CMLs) were introduced as a solution to extend the transmission reach and improve receiver sensitivity by tailoring the spectrum of the DML using an optical filter. We present a simple semi-analytical approach for designing the optical filter for CMLs. This approach can be applied to design the filter for both OOK and multilevel modulation formats (PAM4). We also show that as the modulation speed increases, optical filtering alone may not be sufficient to extend the reach, and efficient DSP should be utilized as well. With the aid of a proper optical filter and DSP, we demonstrate 35 Gbaud PAM4 transmission over 20 km of standard single mode fiber, showing the potential of a low-cost C-band DML-based transceiver solution.

I performed all the simulation, transmission experiments, collected, and processed the data, and wrote the manuscripts. R. Maram helped extensively with the initial simulation and with the design of the appropriate filter. All co-authors reviewed the manuscripts [15, 16].

Self-coherent single sideband systems for 40 km C-band Transmission (Chapter 5)

- Self-coherent (SC) single sideband (SSB) direct detect (DD) systems are theoretically immune to CD induced power fading. Hence it is a promising choice to increase the throughput-distance product in C-band. The major issue lies in generating high quality SSB signal. The most conventional ways to generate SSB signal require either two high-speed DAC channels or one DAC channel with a sharp optical filter. In the thesis, we propose the use of RF skew in conjunction with an optical filter to create vestigial single sideband (VSB) signal, which can be propagated over 40 km of SSMF in the C-band. We analyze the transmission performance of200 Gbps PAM4 signal in simulation with the proposed method. Followed by that, we conduct a single channel and four channel experiment and demonstrate 200 Gbps signal transmission over 40 km of SSMF.

  I performed all the simulation, transmission experiments, collected, and processed the data, and wrote the manuscripts. X. Li helped with DWDM experiment, and in writing the manuscript. All co-authors reviewed the manuscripts [17].

1.4 Thesis organization

The remainder of this thesis is organized as follows.

In **Chapter 2**, we present a brief background of different optical communication systems, primarily focusing on conventional IM/DD systems. We describe the fundamentals of the thesis, i.e., the concepts and techniques upon which the subsequent chapters are developed. We then discuss some common sources of impairments in IM/DD systems and the classical DSP algorithms to handle these. In addition, we define some performance metrics that are used throughout the thesis.

Chapter 3 presents our works on short reach (500 m – 10 km) high throughput IM/DD systems with SiP and TFLN MZM. In section 3.2, we focus on the characterization of different SiP designs and large signal transmission at 200 Gbps. Followed by that, in section 3.3, we present a higher data rate of 300 Gbps transmission with the best MZM design using upgraded DAC and advanced DSP. In section 3.4, we employ a high bandwidth TFLN MZM to enable net 350 Gbps transmission with simple DSP. The chapter is based on our published works [11-13, 18].

Chapter 4 deals with C-band transmission with DML and MZM over 10 km to 20 km reach. Section 4.2 shows the potential of a SiN optical dispersion compensation (ODC) in compensating CD of 10 km SSMF, which is based on our paper [14]. In section 4.3 and section 4.4, we present our work with DML. First, we look at the DML performance over different propagation distances and study the impact of chirp-CD interaction, which is based on our paper [16]. Then we propose a semi-analytical approach for deterministically designing an optical filter to extend the reach of PAM4 DML signal. We start with extensive simulation, followed by experimental verification. We also utilize the necessary nonlinear DSP to enable higher throughput. The contents of this section are based on our paper [15].

In **Chapter 5**, we focus on advanced DD systems, based on SC-SSB signaling. In this chapter, we use a dual drive MZM (DD-MZM) that can generate VSB signal with the aid of RF skew. We start with a simulation study of the impact of RF skew for 112 Gbaud PAM4 signaling over 40 km of fiber in the C-band. Since RF skew is not enough for high symbol rate signals, we employ an additional optical filter to create high quality SSB signal. Next, we demonstrate the applicability of the proposed method in a single channel (wavelength) and four channel WDM system. This chapter is an expanded and updated version of our conference paper [17].

Chapter 6 summarizes the key achievements of the works presented in the thesis. In addition, we point out some potential research directions in the future in this chapter.

Chapter 2 Fundamentals of Direct Detect Communication Systems

2.1 Overview

In this chapter, we give a brief introduction to the fundamental architecture of intensity modulation direct detection (IM/DD) system and the state-of-the-art DSP algorithm that will be utilized in most of the experiments. Since we will use some advanced direct detect methods as well, we start our chapter with some fundamentals of both intensity modulation and coherent modulation in section 2.2 and 2.3. We then present Stokes Vector Direct Detect (SVDD) and single sideband modulation that act as a bridge between IM/DD and coherent system in subsequent sections. We then discuss the main system impairments in section 2.7 and 2.8.

We use digital signal processing to tackle the transmission system impairments, and these are applied both at the transmitter (Tx) and receiver (Rx). In section 2.8, we describe the basics of the employed DSP techniques. We end the chapter with some metrics that are commonly used in optical communication.

2.2 Fundamentals of Intensity Modulation Direct Detection systems

The simplest form of optical communication system is an intensity modulation direct detection (IM/DD) system and is widely employed in short reach applications. Here, at the transmitter, data information is modulated onto the intensity of the signal and a photodiode is used at the receiver that generates photocurrent proportional to the power of the incoming optical signal. The standard architecture of an IM/DD system is shown in Fig. 2.1. We should point out that DAC, ADC, and DSP are not mandatory in an IM/DD structure in its simplest form, simple pulse pattern generator (PPG) and Error detector (ED) can be used instead of more expensive DAC and ADC.

Intensity modulation can be done in two ways: direct modulation and external modulation [19]. In direct modulation, optical output power from a laser is controlled through electric current (known as injection current) fed to lasers. Vertical Cavity Surface Emitting Lasers (VCSEL) or distributed feedback lasers (DFB) are commonly used for direct modulation. This simple form of modulation is limited to shorter reach and distance because of response speed limitation and chirp effect (described in subsequent sections). External modulation requires a continuous wave (CW) light source followed by a modulator, where the amplitude, phase, or frequency is changed according to modulating signals applied on electric input ports. Here, the refractive index or absorption coefficient of modulator material are changed by the applied electric field. High speed external modulation can be achieved by electro-absorption modulator (EAM) or electro-optic modulator (EOM). The EAM and the light source are often integrated together, and commonly terms as an electro-absorption modulated laser (EML). In EOM, electro-absorption (EO) effect changes the refractive index of the material (with some unintentional change of absorption coefficient as well), which induces a phase shift of lightwaves. An optical interferometer structure is therefore needed to convert this phase shift into intensity change. The interferometer can be realized by Michelson interferometer, Fabry-Perot interferometer, or Mach-Zehnder interferometer (MZI). The EO modulator with MZI structure is called a Mach–Zehnder modulator (MZM) and is widely used for high electro-optic (EO) bandwidth, and in this thesis. An excellent review of high-speed electro-optic modulators is given in Ref. [20]. In our thesis, we use either DFB based DML (chapter 3) or MZM (chapter 2 and 4) for intensity modulation.

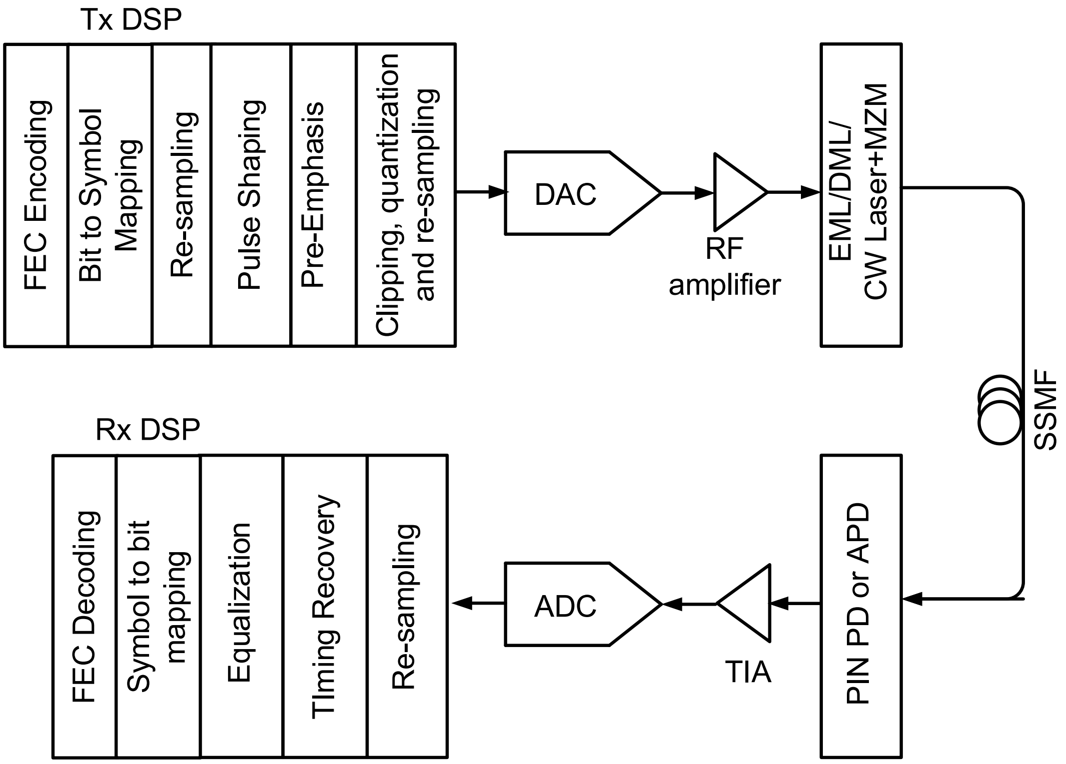

Fig. 2.1 Standard IM/DD system structure with DSP blocks.

As mentioned previously, the information signal can be generated by a pulse-pattern generator (PPG) or a digital-to-analog converter (DAC). For high-speed operation DAC and DSP are essential. Details of the Tx and Rx DSP blocks will be given in section 2.8. The output swing of PPG or DAC is usually limited to 600-700 mV and is usually too small to drive a modulator. This output is thus usually amplified by an RF amplifier (linear driver) before driving the DML or MZM.

The modulated signal is then propagated through the fiber. In this work, we mostly focus on intra-datacenter and inter datacenter links. These links are between 300 m to 40 km. Since the length scale is too long for multi-mode fiber (MMF), we only deal with standard single mode fiber (SSMF) as the transmission medium.

At the receiver, one single-ended photodiode (PD) is required to detect the signal. This can be either avalanche photodiodes (APD) [21] or traditional *p*-type/intrinsic/*n*-type (PIN) PD [22]. The photocurrent produced by the PD needs to be amplified before detection and a transimpedance amplifier (TIA) is used after photodetection. For Rx DSP, the electrical voltage after PD or PD+TIA is sampled by an analog-to-digital converter (ADC) channel. We use a real time scope (RTO) as ADC, which usually runs at 80 GSa/s – 256 GSa/s.

In our thesis, we keep ourselves limited to only pulse amplitude modulation (PAM). Apart from PAM, Discrete Multi-Tone (DMT) and carrier-less amplitude and phase modulation (CAP) have also been investigated in short reach. DMT, also known as direct detected (DD) OFDM has been shown to be useful when there is severe ISI due to bandwidth limitation or power fading. Like OFDM, DMT enables bit loading or power loading that allow a flexible set of modulation formats for each subcarrier that are optimized with respect to the channel transfer function to maximize bit rate or maximize power margin. As a result, DMT shows improved performance when power fading distorts the transmitted signal [23]. But this comes at the price of high transmitter and receiver DSP complexity, and it also puts higher load on the DAC and ADC. A nice comparison among PAM, DMT and CAP can be found in Ref [23] for the interested readers.

2.3 Fundamentals of Coherent Systems

A dual polarization (or polarization-multiplexed) coherent system with common DSP configuration is shown in Fig 2.2. This system can modulate and recover all 4 dimensions or degrees of freedom (DOF) of a single wavelength (λ) [24-26]. These are the 2 quadrature (I and Q) and 2 orthogonal polarizations (x or y). The transmitter of the full dual-pole coherent system consists of 4 to DAC channels for the generation of baseband electrical signal and a dual-pol IQ modulator modulates the information onto the optical carrier. A standard polarization and phase diversity coherent receiver consists of a local oscillator (LO) laser, two 90^0 optical hybrids and 4 balanced photodetectors (BPD). After coherent detection, the baseband electrical signals are sampled by 4 ADC channels.

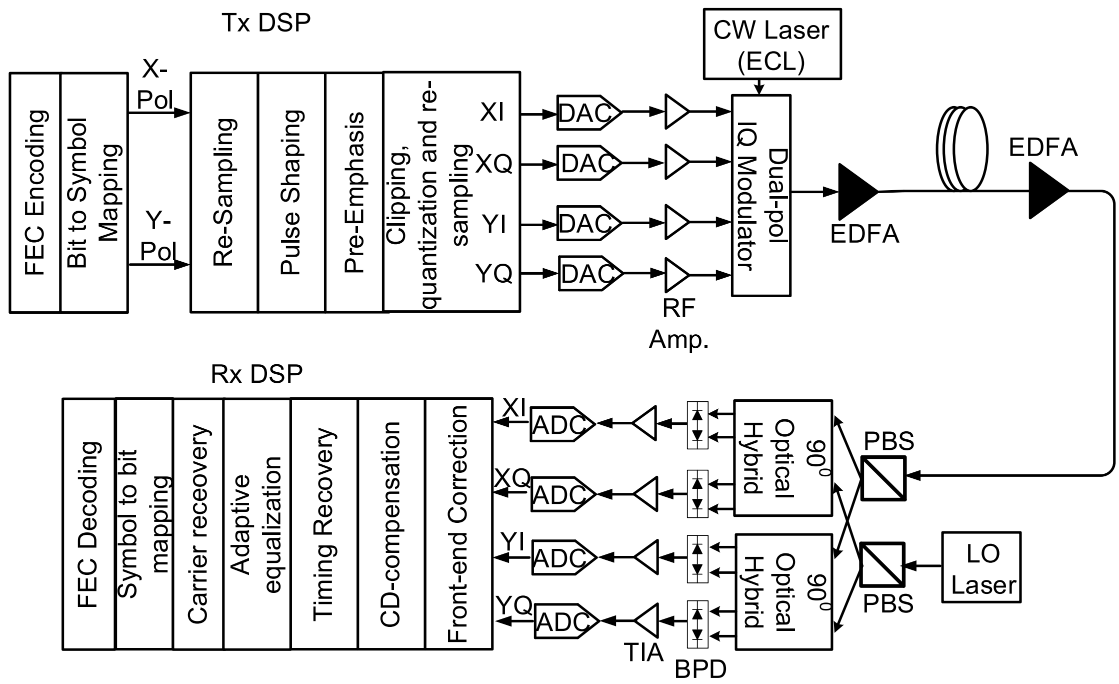

Fig. 2.2 Standard digital coherent transceiver system with DSP blocks (reproduced from [1])

The transmitted signal in the x (or y) polarization can be written as:

$$E_{t,x(y)}(t) = \sum_{k} b_{k,x(y)} p(t - kT_s)$$

where, $b_{k,x(y)}$are the k^{th} information symbols in the x(y) polarization, *p(t)* is the pulse shape and T_s is the symbol period respectively. In Jones space, it can be represented as:

$$\boldsymbol{E} = \begin{bmatrix} E_x \\ E_y \end{bmatrix} = \begin{bmatrix} |E_x| e^{j\arg\{E_x\}} \\ |E_y| e^{j\arg\{E_y\}} \end{bmatrix}$$

In a short reach fiber-optic channel, major transmission impairments include:

a) Chromatic dispersion (CD) characterized by the transfer function $H_{CD}(\omega) = e^{-j\omega^2\beta_2 L/2}$ (details will follow);

b) Polarization-mode dispersion (PMD) characterized by the 2×2 PMD matrix $H_{PMD}(\omega)$

The major challenges to deal with in a full coherent transmission system in short reach scenario lies in its system and DSP complexity, which makes it harder to integrate it in a small form factor pluggable module [27]. Therefore, current research mostly involves developing low-cost solutions with both device and DSP design. However, since coherent system utilizes all four DOF, it can achieve a much higher throughput on a single wavelength, and coherent for short reach is being actively investigated in DCI application [28].

2.4 Fundamentals of Stokes Vector Direct Detect (SVDD) System

IM/DD system allows encoding information in only one degree of freedom and as such to get higher throughput for a single wavelength or single fiber, there are only two options: either to increase the symbol rate or to go for higher order modulation format. But higher symbol rate requires all the system components to have a higher bandwidth, which is not the best choice after a certain value. On the other hand, higher order modulation format, like PAM8 or PAM16 requires very high SNR and puts a very high strain on DAC and ADC. Stokes Vector Direct Detect system allows polarization multiplexing using direct detect receivers without the aid of a local oscillator. In Stokes space, an optical field **E** is represented in the Stokes space by a 3D real vector $\mathbf{S} = [S_1 \quad S_2 \quad S_3]^{\mathbf{T}}$ where $S_1 = |E_{\hat{x}}|^2 - \left|E_{\hat{y}}\right|^2$, $S_2 = 2Re\left\{E_{\hat{x}}E_{\hat{y}}{}^*\right\}$ and $S_3 = -2Im\left\{E_{\hat{x}}E_{\hat{y}}{}^*\right\}$ where $E_{\hat{x}}$ and $E_{\hat{y}}$ are the complex fields resulting from projecting the dual-polarization field **E** onto two orthogonal polarization states. So, we can write the transmitted Stokes vector as $S_{t,1} = \left|E_{t,x}\right|^2 - \left|E_{t,y}\right|^2$, $S_{t,2} = 2\,Re\left\{E_{t,x}E_{t,y}^*\right\}$ and $S_{t,3} = 2\,Im\left\{E_{t,x}E_{t,y}^*\right\}$ with $S_{t,0} = \sqrt{S_{t,1}^2 + S_{t,2}^2 + S_{t,3}^2} = \left|E_{t,x}\right|^2 + \left|E_{t,y}\right|^2$ representing the total transmitted power, which is not impacted by polarization rotation [29].

After propagation, the fiber channel results in a unitary transformation and the received Stokes vector are given by [30]:

$$\begin{bmatrix} S_{r,0} \\ S_{r,1} \\ S_{r,2} \\ S_{r,3} \end{bmatrix} = \begin{bmatrix} \left|E_{r,x}\right|^2 + \left|E_{r,y}\right|^2 \\ \left|E_{r,x}\right|^2 - \left|E_{r,y}\right|^2 \\ 2\,Re\left\{E_{r,x}E_{r,y}^*\right\} \\ 2\,Im\left\{E_{r,x}E_{r,y}^*\right\} \end{bmatrix} = \begin{bmatrix} 1 & 0 & 0 & 0 \\ 0 & \cos\theta & -\sin\theta\cos\varepsilon & \sin\theta\sin\varepsilon \\ 0 & \sin\theta & \cos\theta\cos\varepsilon & -\cos\theta\sin\varepsilon \\ 0 & 0 & \sin\varepsilon & \cos\varepsilon \end{bmatrix} \cdot \begin{bmatrix} S_{t,0} \\ S_{t,1} \\ S_{t,2} \\ S_{t,3} \end{bmatrix} = \boldsymbol{R} \cdot \begin{bmatrix} S_{t,0} \\ S_{t,1} \\ S_{t,2} \\ S_{t,3} \end{bmatrix}$$

where, **R** is the unitary matrix that represents polarization rotation and θ and ε are the polar and azimuthal angle respectively. The Stokes vector includes four components, i.e., $|E_{t,x}|^2$, $|E_{t,y}|^2$,$Re\{E_{t,x}E_{t,y}^*\}$and $Im\{E_{t,x}E_{t,y}^*\}$, and contains 3 degrees of freedom i.e. signal power in orthogonal polarizations and the inter-polarization phase difference. Therefore, one can construct a Stokes vector receiver to support 3-dimensional modulation formats and increase the overall transmission capacity.

Fig 2.3 shows a typical 2-dimensional (2D) PDM-DD system, where two independent information streams on two orthogonal states of polarization (SOPs) from a single laser are modulated by two intensity modulators. The SVR comprises a polarization beam splitter (PBS), two 70/30 power splitters and a 90° optical hybrid followed by two balanced and two single ended photodetectors [30]. One balanced PD can be used as well to replace the two single ended ones. The DSP block consists of one 1×1 SISO and one 3×1 MISO filter. The SISO filter with real valued filter taps is used to mitigate the residual inter-symbol interference (ISI) and obtain the estimate $\hat{S}_{t,0} = \boldsymbol{h}_{00} \otimes S_0$. To recover $S_{t,1}$, a 3×1 MISO finite impulse response (FIR) filter with $\mathbf{h}_{11}$,$\mathbf{h}_{21}$ and $\mathbf{h}_{31}$ is used. $\hat{S}_{t,1}$ is given by $\hat{S}_{t,1} = \boldsymbol{h}_{\mathbf{11}} \otimes S_1 + \boldsymbol{h}_{\mathbf{21}} \otimes S_2 + \boldsymbol{h}_{\mathbf{31}} \otimes S_3$. The filter taps of SISO and MISO filters are initialized using training symbols and least-mean-squares (LMS) and switch to decision-directed (DD) mode upon convergence. $e_{x(y)} = |E_{t,x(y)}|^2 - |\hat{E}_{t,x(y)}|^2$ denotes the error signals of the x (y) polarization signal.

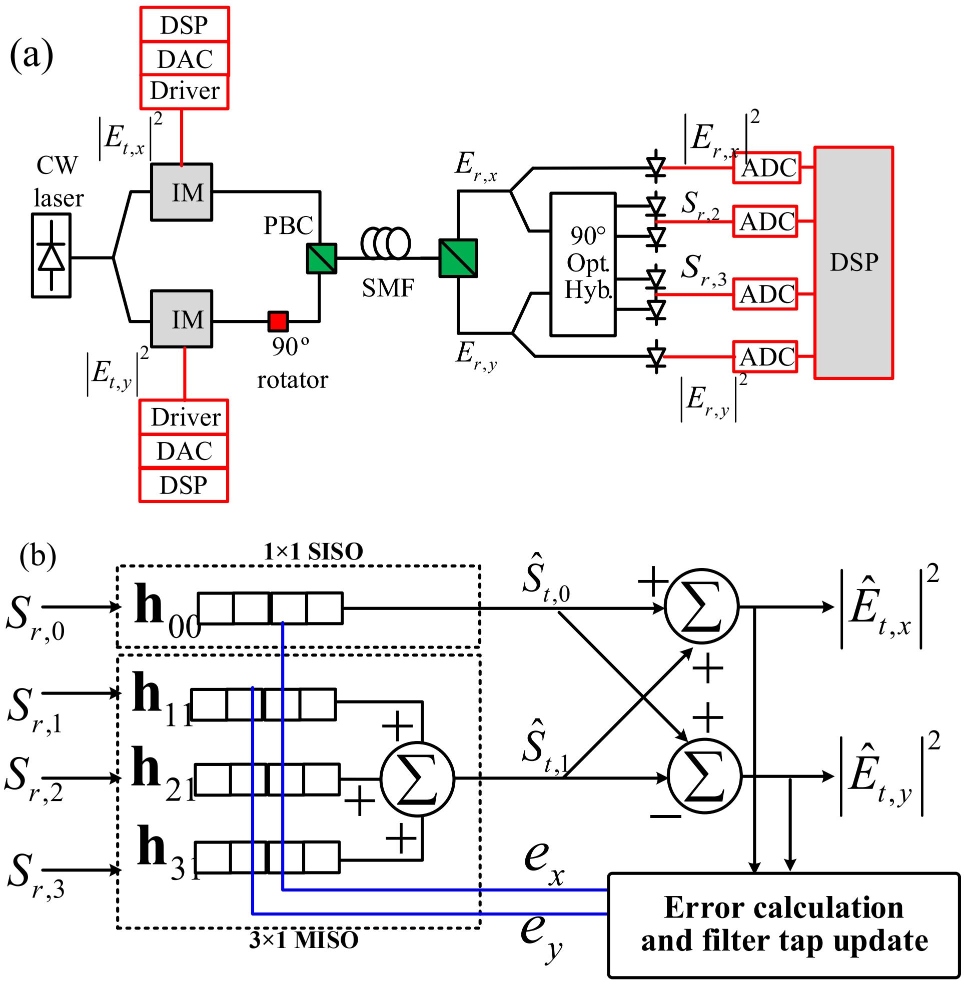

Fig. 2.3 (a) Block diagram of the DP IM/DD system and (b) MIMO DSP for polarization demultiplexing.

It is also possible to transmit a complex signal using IQ modulator on one polarization and a constant carrier on the other polarization and use the same SVR at the receiver [31]. This self-coherent scheme also allows for CD compensation as we have access to the complex field. By using a phase modulator (PM) along with an intensity modulator (IM) in one polarization and IM in other polarization, 3D PDM-DD can also be realized [32]. The receiver structure can be the same as shown in Fig. 2.3, just the receiver DSP needs to be updated using 4×4 MIMO filter.

2.5 Fundamentals of Single Sideband Self-coherent Systems

Single side band (SSB) signaling is a promising way to overcome the CD induced power fading. There are several ways to generate an SSB signal. The most straight forward way is to use two separate digital-to-analog converter (DAC) channels, where the channels carry the Hilbert transform pairs of the DSB signal and an IQM is used to modulate this complex waveform [33]. Alternatively, SSB signals can be generated by rejecting one sideband of a real-valued double sideband (DSB) signal [34], thus using a single DAC channel. This scheme creates a vestigial sideband signal (VSB) due to the limited edge sharpness of the optical filter. Dual-drive MZM (DDMZM), biased at intensity quadrature can also generate SSB signals by applying a Hilbert transform pair of signals to each of the modulator arms [35]. Instead of using two separate DAC channels, one DAC channel followed by a wideband quadrature hybrid (WQH) can be used to get a Hilbert transform pair of signals to generate the SSB signal. Different transmitter configurations for self-coherent SSB scheme are described in detail in [36]. At the receiver the transmitted signal can be recovered by the Kramers-Kronig (KK) receiver for post-CD compensation [37]. Iterative SSBI cancellation algorithm can also be used to reconstruct the single sideband signal. DD only enables the transmission up to tens of kilometers. But SSBI cancelation or Kramers-Kronig (KK), though more complicated, enables transmission up to hundreds of kilometers in C-band.

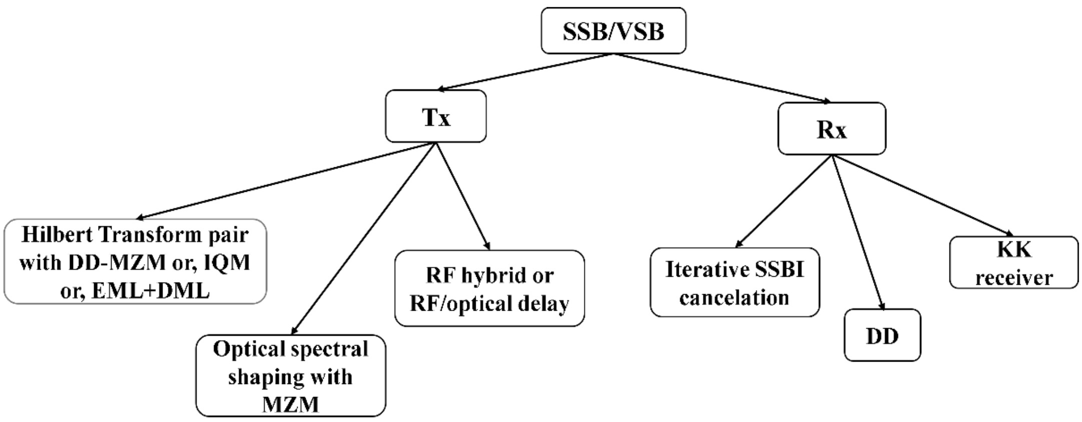

Fig. 2.4 SSB/VSB system architecture

In thesis, we limited our system analysis to 40 km or below. Therefore, CD compensation is not mandatory. In chapter 5, we employ the KK algorithm, which is described in detail in Ref [38] and in several prior works [37, 39].

2.6 Transmission System Impairments in an IM/DD system

The impairments in an IM/DD system come from both the device and the fiber (transmission medium). The major impairments for short reach IM/DD are briefly introduced in this section.

2.6.1 Bandwidth limitation

The major impairment in a practical IM/DD system comes from the bandwidth limitation of different RF components and E/O and O/E devices. These include DAC, RF amplifier, RF cables, DML, EML or MZM, PD, TIA and ADC. In Fig. 2.5, we show the bandwidth response of two devices: (a) DAC employed in section 3.3 and 3.4, (b) DML employed in section 4.3 and 4.4. This BW limits the maximum symbol rate signal one can transmit. These low-pass responses broaden the transmitted pulse and cause inter-symbol interference (ISI). Usually most of the BW limitation comes from the transmitter side, i.e., DAC and modulator. Therefore, there is a significant need to improve the BW of these devices. High bandwidth ADC and PD are already commercially available. We discuss the BW response of SiP and TFLN MZM in more detail in chapter 3. The RF drivers and TIA are sometimes designed with intentional peaking at higher frequencies to partially compensate for these low pass filtering effect. The RF packaging also distorts the signal bandwidth and is crucial for high-speed operation.

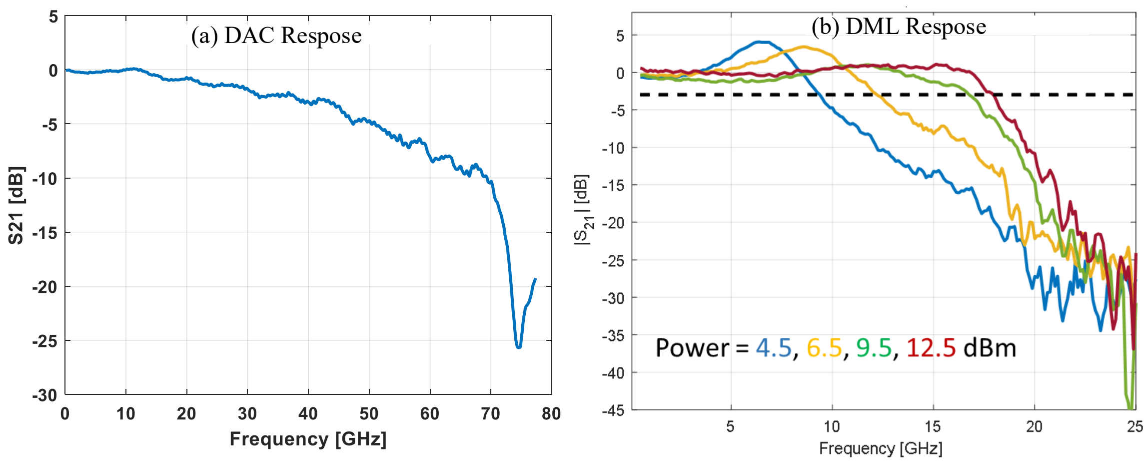

Fig. 2.5 (a) Response of Keysight DAC with RF cable, (b) DML EO response at different bias currents (P_{avg})

2.6.2 Chromatic Dispersion (CD)

CD is the main limiting factor for higher transmission reach and higher capacity. This linear effect occurs when different frequencies of light propagate with different group velocities. Fiber chromatic dispersion broadens the optical pulse and eventually leads to spectral fading when direct detection is used. The transfer function of CD in the frequency domain for a propagation over a distance L is given as:

$$H_{CD}(\omega) = e^{-j\omega^2\beta_2 L/2};$$

where, β_2 is the CD coefficient at the laser's operating frequency, which represents the group velocity dispersion and ω is the angular frequency deviation from that of the laser. The most commonly deployed fiber in networks (ITU G.652) is known as dispersion-unshifted single mode fiber, which we refer as standard single mode fiber (SSMF) and it has almost zero chromatic dispersion in the optical window around 1310 nm (O-band) but exhibits a higher CD in the 1550 nm region (C-band). At 1550 nm, for SSMF β_2 is approximately −21.66 ps^2/km. β_2 is related to the fiber dispersion coefficient, D, via the familiar formula [40]:

$$D(\lambda) = -\frac{2\pi c}{\lambda^2}\beta_2$$

where c is the speed of light in a vacuum.

We use both β_2 and D as a measure of dispersion throughout our thesis. For SSMF, at 1550 nm, D is approximately 17 ps/nm-km. This means for every km of fiber propagation, a pulse with a 1 nm spread of wavelengths will disperse by 17 ps. Therefore, in absence of laser chirp, the pulses will be broadened in the time domain, and each pulse will interfere with the neighboring leading to ISI.

Now, let us look at the fiber response for IM/DD transmission system in more detail. The channel response for CD can be written as [41]:

$$H_{IM\leftrightarrow DD}(f, L) = |\cos(\theta(f, L)) - \sin(\theta(f, L)).H_{IM\leftrightarrow PM}(f, L)| \quad (2.1)$$

Here, $H_{IM\leftrightarrow DD}(f,L)$ is the complex small-signal transfer function between intensity and phase modulation, which is essentially the frequency chirp; $\theta(f,L)$ is the phase variation induced by CD and can be expressed as $\theta(f,L) = -2\pi^2\beta_2 f^2 L$.

For an MZM in a pull-push operation, i.e., the driving RF signals are $V_1(t)$ and $V_2(t) = -V_1(t)$, make the optical signal to be purely intensity modulated with no phase modulation ($H_{IM\leftrightarrow PM} = 0$). Fig. 2.6 (a) shows the frequency response for a C band SMF transmission with zero chirp over different transmission distances.

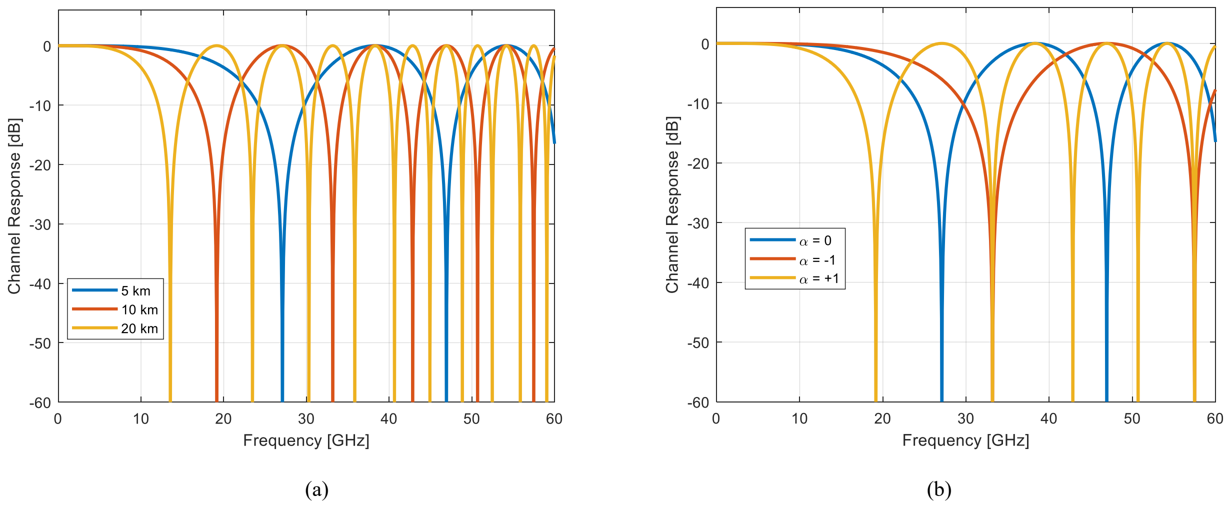

Fig. 2.6 Frequency response of fiber channel (SMF) in C band: (a) For different distances (α = 0), (b) For 5 km transmission with different chirp (α)

But, when a dual arm MZM is driven by two different RF signals that are not purely differential, a chirp factor (α) arises, which interacts with dispersion and shifts the frequency nulls. Chirp also arises in directly modulated laser (DML) and electro-absorption modulated laser (EML). A nice comparison among DML, EML and MZM can be found in Ref [42]. Both BW limitation, and CD induced power fading cause ISI. Usually, receiver equalization can tackle the ISI from BW limitation. However, the notches in the power spectrum are hard to compensate and puts an upper limit to the reach and symbol rate. From Fig. 2.6, we can see that for 10 km transmission in the C-band, the first notch in the spectrum is at 18 GHz. This means, any signal with a BW of more than 18 GHz would not be easily recoverable by simple DSP. Therefore, for IM/DD transmission, O-band transmission around 1310 nm is favorable. However, even for O-band, the channels that are farther away from the zero-dispersion wavelength will experience power fading, which limits the maximum symbol rate-distance product.

2.6.3 Frequency Chirp

In DML, due to the dependence of refractive index on the applied electrical current $n(I)$, the change in the optical intensity is accompanied by the phase modulation (PM), which causes transient frequency chirp. Additionally, the gain compression of the active medium causes frequency modulation (FM) by the adiabatic chirp. The chirp $\delta f(t)$ of DML is related to the laser output optical power $P(t)$ through the expression:

$$\delta f(t) = \frac{\alpha}{4\pi}\left(\frac{1}{P_{DML}(t)}\frac{dP_{DML}(t)}{dt} + \kappa P_{DML}(t)\right) \qquad (2.1)$$

where α is the linewidth enhancement factor (also known as Henry parameter) and κ the adiabatic chirp coefficient [43]. In 2.1, the first and second term represents a structure-independent transient and adiabatic chirp, respectively. From the laser rate equation, κ is defined as $\kappa = \frac{2\gamma\varepsilon}{\eta h\nu V}$ $[Hz/W]$. Here, γ = Confinement factor, ε = Gain Compression Factor, η = Quantum Efficiency, $h\nu$ = Photon Energy, V = Volume of the active layer.

In an EML, adiabatic chirp coefficient κ is close to zero, and EML/DD system suffers only from the transient chirp. In the following chapters of this thesis, we only focus on DML and MZM based systems, and equation 2.1 will be explained in greater detail. EMLs usually have slightly negative transient chirp ($\alpha < 0$), which can help extend the transmission reach as shown in Fig. 2.6 (b).

2.6.4 Noise

Noise limits the achievable signal-to-noise (SNR) in an IM/DD system. It can come from both optical sources and electrical devices. DAC, ADC, RF drivers and TIA all add thermal noise. This is approximated as additive Gaussian white noise (AWGN). There is laser phase noise, which follows a Wiener process and relative intensity noise (RIN) [44]. RIN is important in an IM/DD system since it sets the maximum achievable electrical SNR at the receiver for a signal at a given symbol rate [45]. Although fiber amplifiers (EDFA or PDFA) are not practical in short-reach communication, they are employed in experimental verifications in several works. Amplified spontaneous emission (ASE) noise from fiber amplifiers is a major noise source when employed in a DD system. DAC and ADC also add significant amount of noise. The first one is the quantization noise due to the nominal bit resolution of DAC and ADC. There are also harmonic distortions, clock leakage, and the flicker noise limiting the SNR [46]. In our simulation results presented in chapter 4, we mostly focused on noise coming from the PD and TIA. PD adds both thermal noise and shot noise. In DD systems without EDFA/PDFA, TIA is the main source of noise and dwarfs other noises.

2.6.5 Loss

Loss is an inherent part in any communication system. Losses in fiber transmission systems primarily come from the fiber itself. The SSMF has a loss (or, attenuation) coefficient of ~0.2 dB/km in the C-band and ~0.32 dB/km in the O-band. In the long haul, this fiber loss is compensated periodically by amplifying the optical signal by means of optical amplifiers. But for short-reach, optical amplifiers are not preferred. Due to higher loss coefficient, O-band transmission is limited to 10-20 km. There is also excess loss from different optical components (like optical filter, modulator etc.) and loss due to light coupling (grating coupling or edge coupling).

2.6.6 Device and fiber nonlinearity

In short-reach, device nonlinearity can be a major issue, specifically with higher order modulation format. The RF amplifiers and TIA are the main source of this nonlinearity. MZMs are inherently nonlinear (sinusoidal), as the power transfer function of an MZM is given by:

$$\frac{P_{out}}{P_{in}} = \frac{1}{2} + \frac{1}{2}\cos\big(\Delta\phi(t)\big)$$

where $\Delta\phi(t)$ is the phase difference between the two arms of the MZM. The MZM is biased at the quadrature point and driven with a signal to be within the linear region of the power transfer function. The modulation mechanism (material linearity) also adds nonlinearity. [47] gives a nice overview of the modulator material impact in optical communication.

Another source of nonlinear impairment is the optical fiber itself. The propagation in a SMF is governed by the nonlinear Schrodinger (NLS) equation [40], which indicates the leads to the third order nonlinearly. This third order nonlinearly, known as Kerr nonlinearly gives rise to self-phase modulation (SPM), cross phase modulation (XPM) and four wave mixing (FWM) at high launched optical power. FWM generates undesired alien signals of growing power with distance at frequencies that match those of existing signals when multiplexing is done on a frequency grid. In the O-band, due to propagation close to zero dispersion wavelength, the phase-matching condition can be satisfied easily, causing FWM for CWDM transmission. But in the C-band, due to the accumulated CD, FWM can be neglected.

Finally, due to adiabatic chirp, DML shows frequency modulation (FM) along with amplitude modulation (AM). This causes timing skew that comes due to the velocity difference of the different levels of PAM4 signal. In the anomalous dispersion ($D > 0$) region, the upper intensity levels (higher frequency components) travel faster than the lower ones and causes a skew (and vice versa for the normal dispersion), which can be predicted assuming an ideal transmitter/receiver. The peak-to-peak chirp can be approximated based on equation 2.1 (neglecting transient chirp effect) as:

$$\delta f_{pp} = \delta f_{ad,high} - \delta f_{ad,low} = \frac{\alpha}{4\pi}\kappa\left(P_{high} - P_{low}\right)$$

If $\alpha = 3$ and κ = 5 GHz/mW (typical values), for an $OMA = P_{high} - P_{low} =$ 5.2 mW, the peak-to-peak chirp, δf_{pp} = 6.2 GHz. This will cause the top level to arrive 25.3 ps earlier than the lowest level after 30 km (total $CD = +510$ ps/nm) for 1550 nm transmission. This $\Delta T_{skew} = 25.3$ ps will cause significant BER degradation as this amounts to 31% of UI (unit interval). Therefore, even with a decent eye-diagram, the BER can be quite degraded. For O-band operation the skew will be lower (18.1082 ps) for the same amount of CD. This skew sets a limit to the maximum transmission distance, which directly depends on the OMA and DML parameters. In Fig. 2.7, we show the impact of nonlinear skew, when transient chirp is absent.

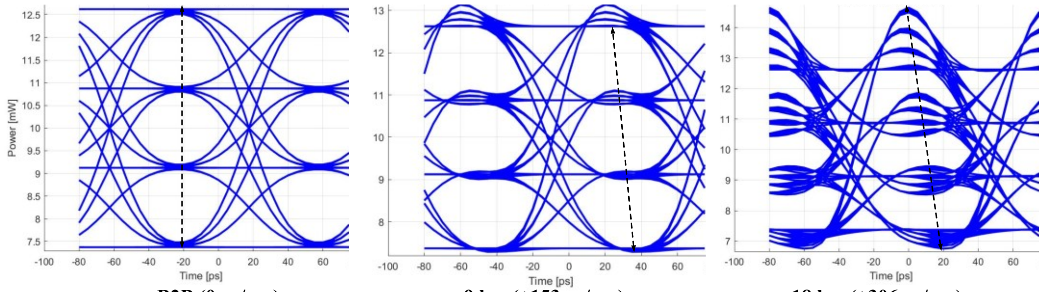

Fig. 2.7 Optical eye diagram after different amount of CD for P_{avg}=10 mW, OMA = 5.2 mW, with α = 3 and κ = 5 GHz/mW (1550 nm transmission) in absence of transient chirp at 12.5 Gbaud.

The interaction of DML chirp and CD can also be regarded as nonlinearity. To demonstrate this, we show the eye diagrams for a DML after different amount of accumulated CD in Fig. 2.8.

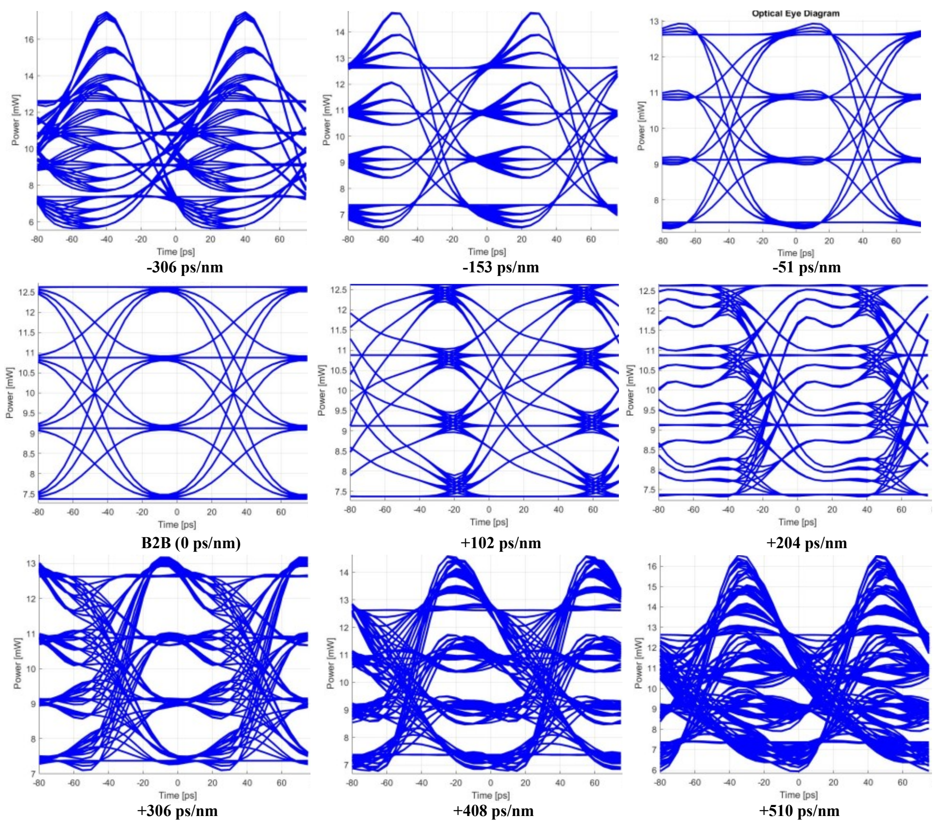

Fig. 2.8 Optical eye diagram after different amount of CD for $P_{avg} = 10\ mW$, $OMA = 5.2\ mW$, with α = 3 and κ = 5 GHz/mW (1550 nm transmission).

2.7 DSP Blocks

2.7.1 Overview

DSP has become an essential part for high-speed IM/DD transmission to tackle bandwidth limitation and nonlinearity. We give a brief overview of some standard DSP algorithms that we will mention frequently throughout the thesis.

2.7.2 Forward Error Correction (FEC)

Forward error correction (FEC) is an integral part of most digital communication scheme for reliable communication (BER < 10^{-15}). Although usually adopted for coherent communication, FEC has now become common for IM/DD systems. The FEC adds redundancy through parity check constraints to increase distance properties of transmitted codeword sequences [48]. In our works, we do not implement the FEC, rather only report the pre-FEC BER or normalized generalized mutual information (NGMI). Net coding gain (NCG) is a metric to evaluate the performance of FEC schemes, which is defined as the difference between E_b/N_0 of the uncoded and coded systems at a given bit error rate (BER) threshold. For error free communication, the widely accepted BER threshold is 10^{-15}. Throughout our thesis, we focus on two main types of FECs, soft-decision (SD) and hard-decision (HD). SD-FEC offers a higher NCG, and therefore we mostly use it when we employ higher order PAM8 or PS-PAM8 format. The overhead (OH) is another important parameter that we need to keep in mind when choosing one FEC over the other. A higher OH FEC usually gives a higher NGC and can work with a higher pre-FEC BER. However, it requires higher encoding/decoding latency, and implementation complexity. For PAM4, we frequently use KP4 FEC, which is based on Reed-Solomon RS (544, 514) code, with an OH of 5.8% and BER threshold of 2.26×10^{-4}. We also use 6.7% OH, Proprietary "P-FEC" with a BER threshold of 3.84×10^{-3}. Interested readers are encouraged to check [49] for a list of HD-FEC BER thresholds of certain codes recommended for optical communications. However, as pointed out in [49, 50], pre-FEC BER is not reliable for post-FEC BER prediction in SD decoding systems. Generalized mutual information (GMI) is a more precise metric with SD decoding. Therefore, we adopt a practical SD-FEC coding scheme where spatially coupled low-density parity-check code (code rate of 0.8469) is concatenated with an outer hard-decision, BCH code (8191,8126,5) [51] and compute the NGMI to evaluate the transmission performance [50]. The combined FEC code rate is 0.8402, and the NGMI threshold is 0.8798. The OH is therefore $^1/_{0.8402} - 1$ or, 19.02% for this SD-FEC.

One more point to note here is that we use the terms 'net rate' and 'throughput' interchangeably. Similarly, 'raw data rate' and 'gross data rate' are used synonymously. These two terms are related as: $Net\ rate\ = raw\ data\ rate/(1 + OH)$. So, for net 200G, we need to operate at 106.7 Gbaud for PAM4 signaling assuming 6.7% HD-FEC BER threshold of 3.8×10^{-3}. With SD-FEC, we need to achieve an NGMI above the adopted NGMI threshold. A set of NGMI thresholds for concatenated coding scheme can be found in Ref. [52].

2.7.3 Symbol Generation

In our thesis, we work with pulse amplitude-modulation (PAM) formats of different orders. The simplest form is PAM2, with just two levels, which is also known as non-return-to-zero (NRZ) or on–off keying (OOK). In our thesis, we mostly focus on PAM4 format, with four amplitude levels with equal Euclidean distances. Similarly, PAM8 or PAM16 will have 8 and 16 levels, with equal occurrence probability and equal Euclidean distances. PAM4, PAM8, PAM16 carry 2, 3, and 4 bits of information, respectively.

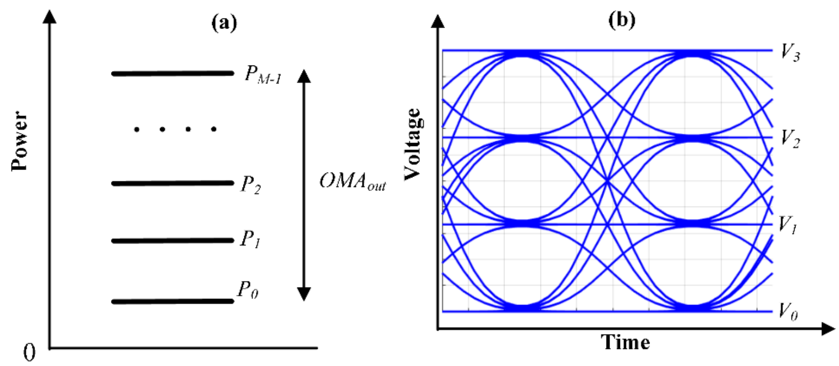

Fig. 2.9 (a) Power levels of a PAM-*M* transmission, (b) Voltage levels of a PAM4 signal.

For the same bit rate, PAM-M ($M = 2^b$) requires operation at $1/b$ times the symbol rate of PAM2 signaling. However, because of the M levels in the same time period, eye opening decreases, and it requires a higher SNR. For example, a PAM4 eye diagram has three inner and smaller eyes, and thus the decision threshold is 1/3 of an OOK signal of the same bitrate and same outer eye height. Combining the effect of the reduced noise and reduced eye opening, PAM-M has an SNR change relative to OOK of:

$$\Delta SNR = \frac{\sqrt{log_2 M}}{M-1}, \text{ or, } \Delta SNR_{dB} = 10\ log_{10}\sqrt{b} - 10\ log_{10}(M-1)$$

Going to PAM8 from PAM4 or OOK, requires much higher SNR, and is therefore hard to achieve. In our thesis, we limit ourselves to a maximum of 8 levels.

Fig. 2.9 shows that power levels of PAM-M format. When the occurrence probability is equal, the average transmit optical power P can be calculated as $P = \frac{1}{M}\sum_{i=0}^{M-1} P_i$. Two other terms that will be frequently used are outer Optical Modulation Amplitude (OMA) and extinction ratio (ER). OMA is defined as $OMA = P_{high} - P_{low}$ and $ER = P_{high}/P_{low}$; which depends directly on the P_{avg} and OMA. When BW limitation is severe, one can use partial response signaling [53, 54]. We use duo-binary (DB) PAM4 later in chapter 3. Although DB signaling lowers BW requirement [55], it increases SNR requirement due to increases number of levels. Because of the higher SNR requirement, PAM8 signaling is hard to transmit and requires SD-FEC. To transmit signals between 2 to 3 bits/symbol, we adopt PAM6 and probabilistic shaping. Here, PAM6 symbols are generated from a 32-QAM (6×6 grid with corner points removed) 2D constellation which maps five bits into two symbols with a spectral efficiency of 2.5 bits/symbol [56] as shown in Fig. 2.10. Since, the corner points from the 6×6 grid are removed, the outer symbols (± 5) are sent with less probability as is depicted in the figure as well. The probability of each amplitude level is: $^{1}/_{16} \cdot$ [2 3 3 3 3 2]. Similarly, it is possible to create PAM3 from 8-QAM or PAM12 from 128-QAM constellation.

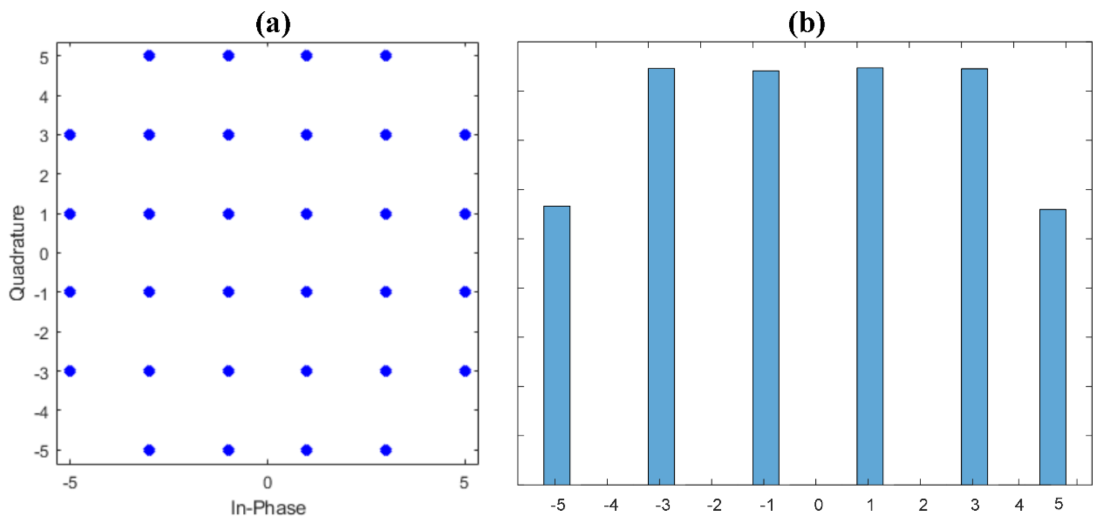

Fig. 2.10 (a) PAM6 constellation diagram reconstructed from two consecutive symbols (2D), (b) Histogram of the transmitted symbols.

Another way to achieve tune entropy or spectral efficiency with a finer granularity is probabilistic shaping (PS). PS has been used commonly in coherent optical communication to achieve channel capacity [57]. PS signals usually follow the Maxwell-Boltzmann (MB) distribution, which has the highest entropy at a given signal power for a memoryless AWGN channel. Although PS adds complexity, it is now being investigated for IM/DD systems as well to achieve higher throughput. In our thesis, we use both constant composition distribution matching (CCDM) [58] and cost-minimizing distribution matching (CMDM) [59]. CMDM is preferable since it requires a much smaller symbol block length with similar performance (entropy loss) [60]. A term that we use with PS-PAM is the information bits per symbol (IBPS), which we define as:

$IBPS = H/(1 + OH)$, where H is the entropy of the transmitted signal in bits/symbol and OH is the overhead of the adopted FEC coding. Uniform PAM8 thus has an IBPS of 2.52 (=3/1.1902), when we use 19.02% OH SD-FEC.

2.7.4 Nonlinear compensation

As we mentioned previously, nonlinearity is an issue when dealing with higher PAM formats. This nonlinearity (NL) can be compensated at the receiver with nonlinear equalization.

However, most NL equalizers are quite complex. Therefore, it is desirable to partially compensate for this at the transmitter as well. This can be simple memoryless level dependent NL compensation, or memory-based compensation. In our thesis, we limited ourselves to lookup table (LUT)-based nonlinear predistortion (NLPD) [61]. We will give an example of this NLPD in section 2.9.5 and its performance in more detail in chapter 3 and 4.

2.7.5 Pulse shaping

Pulse shaping is an important part of transmitter signal processing to tackle the BW limitation. We mostly use Nyquist pulse shaping filters, which follows the Nyquist principle of zero ISI. Assuming a channel impulse response of $h(t)$, the condition for zero ISI is given as [62]:

$$h(nT) = \begin{cases} 1; n = 0 \\ 0; n \neq 0 \end{cases}$$

for all integers n, where, T is the symbol period. The most common pulse shaping filter is the raised-cosine (RC) filter, which we will use throughout the thesis. The frequency and time domain form of the filter for a roll-off factor α is given as:

$$H(f) = \begin{cases} 1, & |f| \leq \frac{1-\alpha}{2T} \\ \frac{1}{2}\left[1 + \cos\left(\frac{\pi T}{\alpha}\left[|f| - \frac{1-\alpha}{2T}\right]\right)\right], & \frac{1-\alpha}{2T} < |f| < \frac{1+\alpha}{2T} \\ 0, & |f| \geq \frac{1+\alpha}{2T} \end{cases}$$

$$h(t) = \begin{cases} \frac{\pi}{4T} sinc\left(\frac{1}{2\alpha}\right), & t = \pm\frac{T}{2\alpha} \\ \frac{1}{T}\mathrm{sinc}\left(\frac{t}{T}\right)\frac{\cos\left(\frac{\pi\alpha t}{T}\right)}{1-\left(\frac{2\alpha t}{T}\right)^2}, & \text{otherwise.} \end{cases}$$

where, $sinc(x) = {\sin(\pi x)}/{\pi x}$.

The roll-off factor (ROF), α $(0 \leq \alpha \leq 1)$ defines the excess BW of the filter, i.e., the bandwidth occupied beyond the Nyquist bandwidth of ${1}/{2T}$. In coherent communication, it is more common to split the RC filtering equally between the transmitter and receiver to maximize the SNR in presence of white noise. In that case, one would apply a root-raised-cosine (RRC) filter at the transmitter and do matched filtering at the receiver. The RRC filter is thus given as:

$$|H_{RRC}(f)| = \sqrt{H(f)}.$$

Although RC filtering is helpful in bandwidth limited scenario, it increases peak-to-average power ratio (PAPR) of the signal and reduces eye opening and makes it difficult for the clock recovery. Fig. 2.11 shows the eyes after pulse shaping to demonstrate the closing of eye opening with lower α.

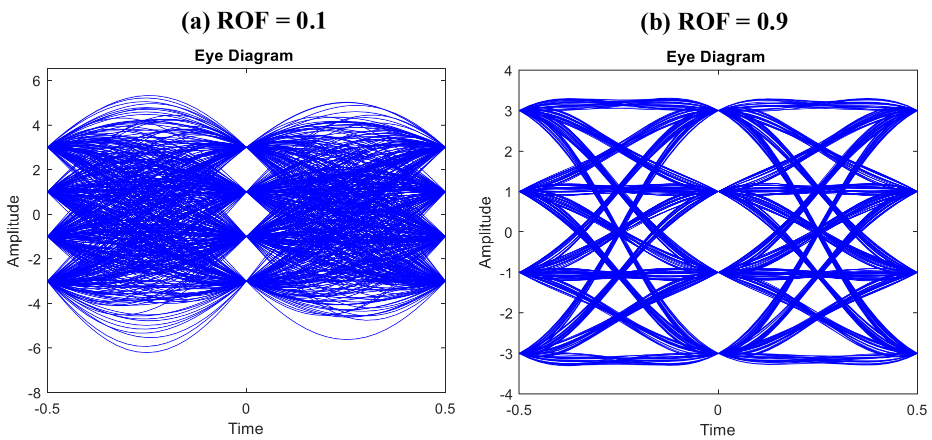

Fig. 2.11 Eye diagram of PAM4 signal for two different ROF (α).

2.7.6 Pre-emphasis

High symbol rate signal transmission is gated by the low pass filtering effect of RF and EO devices as described in 2.6.1. Linear equalizers at the receiver can compensate for the frequency response of the channel including the severely band limited transmitter, but also incur undesired noise enhancement. This can be resolved by pre-compensating the transmitter frequency response using a FIR pre-emphasis filter. Several works have been conducted on transmitter pre-emphasis targeting high speed coherent systems [63-65]. Since in most cases the transmitter (DAC, driver, and modulator) is the main BW limiting factor, pre-emphasis filter for the transmitter frequency response is most important. Pre-compensating the entire channel frequency response is also possible but usually not preferred since that would increase the signal peak-to-average ratio (PAPR) and reduce the signal power from the DAC, thus degrading the transmitter SNR. The pre-emphasis needs to be optimized based on the transmitter SNR and ISI of the channel. In Fig. 2.12, we plot the frequency response of the pre-emphasis filter for DAC and RF amplifier used in chapter 3, which shows that the depth of pre-emphasis can be close to 20 dB. Going beyond that usually degrades the SNR and lowers output signal swing considerably. In most of our experiments, we compensated for the RF transmitter response by the pre-emphasis filter and receiver equalization dealt with the ISI due to modulator, PD and TIA.

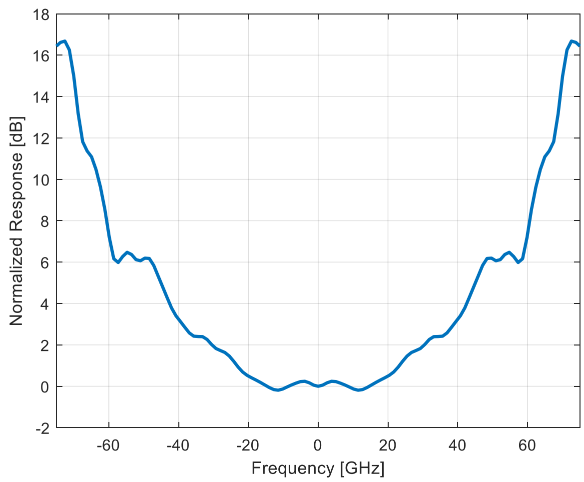

Fig. 2.12 Frequency response of the pre-emphasis filter for DAC and RF amplifier.

2.7.7 Receiver Equalization

Receiver equalization becomes necessary at higher speeds due to ISI coming from BW limitation and power fading. It is even more important for higher order modulation formats where the distortions become more severe. The ideal solution to combat ISI is maximum likelihood sequence estimation (MLSE) [62]. However, MLSE uses Viterbi algorithm for decoding, which is complex, and this complexity depends on the alphabet size, M and the number of post-cursor ISI symbols, L as M^{L+1}. Therefore, for higher order PAM formats, MLSE is usually not used unless, L is small. We use MLSE only in section 3.2 with PAM4 signaling after the post-filter, which is used to whiten the enhanced noise after feed forward equalizer (FFE). We give a brief overview of linear and nonlinear FFE used in optical communication, and more detailed analysis can be found in [1].

2.7.7.1 Linear feed forward equalizer (FFE)

The most common ISI compensation method in practical systems is the linear feed forward equalizer (FFE), which is used in almost all experiments. In Fig. 2.13, we show the standard block diagram of a linear FFE filter:

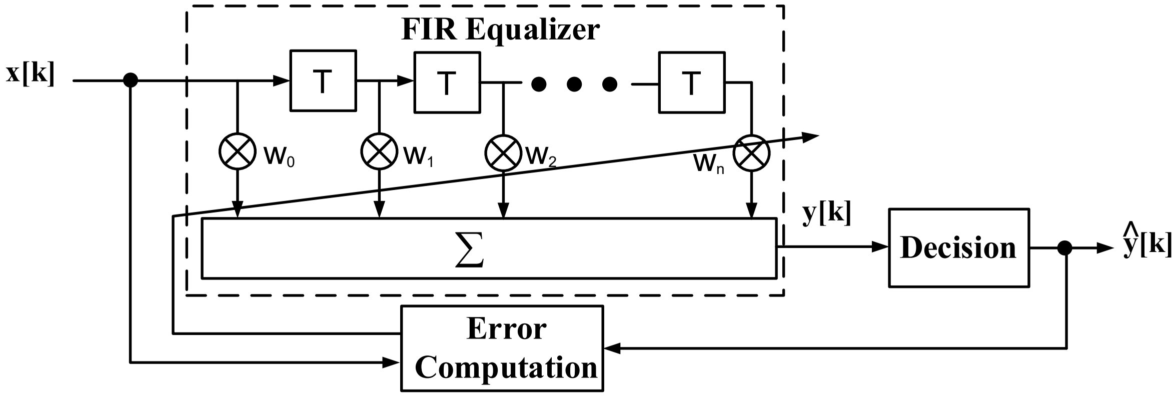

Fig. 2.13 Block diagram of FFE (reproduced from [1])

For sampled input signal $x[k]$ to the FFE filter, the output is expressed as

$$y[k] = \sum_{i=0}^{N-1} w_i^{(k)} x[(k-i)T]$$

where $y[k]$ is the output of the equalizer samples, $w_i^{(k)}$ is the tap weight, N is the number of taps, and T is the delay interval. FFE can operate at 1 sps, where $T = T_s$ (symbol duration) or at a higher sampling rate. Usually, it is limited to 2 sps, which means $T = T_s/2$, and it is also called T/2 spaced equalizer. In this thesis, we mostly use T/2 spaced FFE, unless mentioned otherwise. The tap coefficients (or, weights) are usually updated by decision directed least mean square algorithm (DD-LMS) [62]. It is a stochastic gradient descent algorithm where the taps are updated to minimize the mean square error (MSE) based on the decided symbols $\hat{y}[k]$.

Unlike zero forcing (ZF) equalizer, it will not eliminate the ISI completely, rather minimizes the total noise power and the ISI. But it will still boost the in-band noise power, sometimes resulting in poor equalization performance.

2.7.7.2 Decision feedback equalizer (DFE)

An alternative channel equalization scheme is decision feedback equalizer (DFE), where the output $y[k]$ is expressed as $y[k] = x[k] - \sum_{i=0}^{N-1} w_i \hat{y}[k-i]$ and depicted in Fig. 2. For DFE, the inputs are the symbols after decision, $\hat{y}[k]$ and it usually operates at 1sps. DFE is helpful when there are spectral null due to CD. However, DFE suffers from feedback delays, decision error propagation, and instability. Therefore, DFE and FFE can be used together to get the best performance.

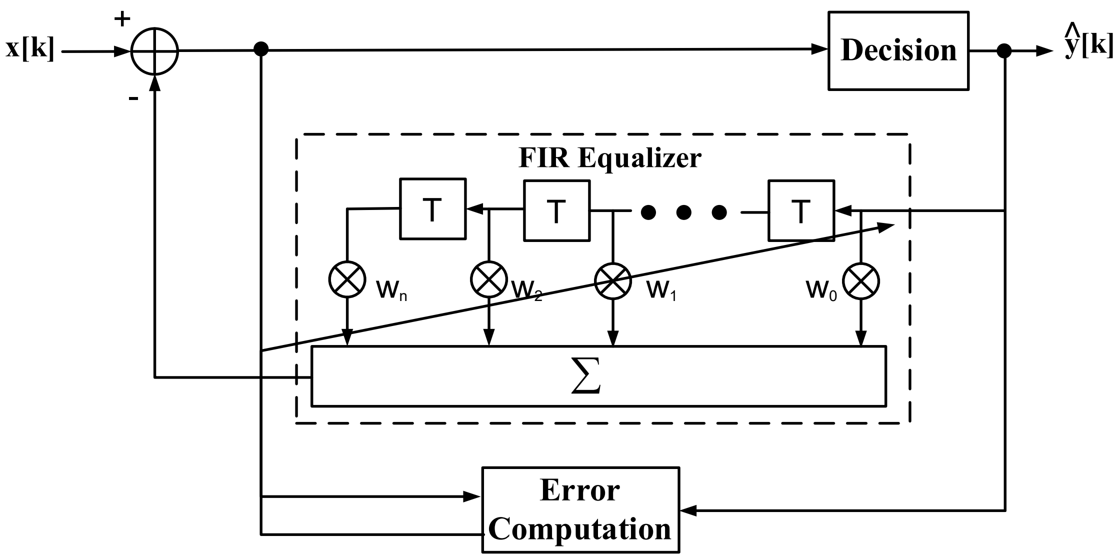

Fig. 2.14 Block diagram of DFE (reproduced from [1])

2.7.7.3 Volterra nonlinear equalizer (VNLE)

Although linear distortions can be equalized by a linear FFE, it cannot compensate for the nonlinearities that might be present in the system. These nonlinear effects can be tackled by Volterra series based- nonlinear equalizer (VNLE) [66]. Although VNLE can be implemented based on FFE or DFE, throughout the thesis we only consider FFE based VNLE. In this thesis, by FFE, we mean linear FFE. The nonlinearities present in optical systems are mostly limited to third order. A third order VNLE is given as [67]:

$$y[k] = \sum_{i_1=0}^{M_1-1} w_1(i_1)x[(k-i_1)T] + \sum_{i_2=0}^{M_2-1}\sum_{i_2=i_1}^{M_2-1} w_2(i_1,i_2)x[(k-i_1)T]x[(k-i_2)T]$$
$$+ \sum_{i_1=0}^{M_3-1}\sum_{i_2=i_1}^{M_3-1}\sum_{i_3=i_2}^{M_3-1} w_3(i_1,i_2,i_3)x[(k-i_1)T]x[(k-i_2)T]\,x[(k-i_2)T]$$

Here, M_1, M_2, M_3 represents the memory lengths of first (linear), second and third order terms, respectively. The main issue of VNLE is that it is much more complex than linear FFE and the computation complexity is very high for a third order one. The relationship between the memory lengths and the number of equalizer kernels is given in Table 2.1 [67]. The taps can be optimized by using training symbol based LMS for coarse convergence (TS-LMS) and DD-LMS for fine adaptation.

Table 2.1 Memory Length, Kernel Number, and multiplications/kernel (adapted from [67])

VNLE order	Memory Length	Number of Kernels	Multiplications/Kernel
1st	M_1	$N_1 = M_1$	1
2nd	M_2	$N_2 = M_2(M_2+1)/2$	2
3rd	M_3	$N_3 = M_3(M_3+1)(M_3+2)/6$	3

2.7.7.4 Polynomial VNLE (PNLE)

The simplest form of Volterra nonlinear equalizer (VNLE) is Polynomial VNLE or PNLE. Here, we use only the self-beating terms, which reduces the complexity significantly compared to a full VNLE. It is also possible to reduce the complexity of VNLE by L_1-regularization or pruning [68] to reduce the number of kernels after the adaptation of the full VNLE.

2.9 Performance Metric

To measure the system performance, we use several metrics throughout the thesis. Here is a brief overview of the metrics:

2.9.1 Bit Error Rate (BER)

Bit Error Ratio or Bit Error Rate (BER) after FEC implementation is the ultimate metric to characterize the system performance. However, as mentioned earlier, in our works, we only calculate pre-FEC BER. In experiments, this BER is measured by calculating the number of error bits and the number of total bits sent, i.e., $BER = Errors/Total\ number\ of\ Bits$. For OOK, PAM4, or PAM8, the symbols are sent with equal probability and are gray coded. Therefore, BER is just symbol error rate (SER) divided by bits/symbol. However, for PAM6, there is a gray mapping penalty (GMP) since 32-QAM cannot be gray coded.

In simulation, to get to the BER confidence level at low error rates (10^{-6}), we need to transmit very long symbol sequence, making the simulation extremely large. In this case, we use the variances of detected levels to predict the BER, which gives very good approximation with the true calculated BER [69]. This method is used in the simulation results presented in section 4.2 and 4.3. One thing to point out is that when the symbols are sent with unequal probability, like PAM6 or PS-PAM8, the thresholds need to be calculated using the probability of each individual levels, which should not be neglected.

2.9.2 GMI and NGMI

GMI is calculated from Log-likelihood ratios (LLRs) and quantifies the maximum number of information bits per transmit symbol that can be transmitted with a vanishingly small error rate under bit metric decoding (BMD) [50]. As mentioned, GMI is a more precise metric with soft decoding across different channel conditions and modulation formats. Here, we calculate the NGMI as:

$$NGMI(X;Y) = 1 - (H(X) - GMI(X;Y))/m$$

$$H(X) = -\sum_{x \in \chi} P_X(x) log_2 P_X(x) \text{ bits/symbol}$$

where Y and X are the received and transmitted symbols, respectively, $H(X)$ is the entropy of the transmitted symbols (source entropy), with χ being the PAM-M symbol set and $P_X(x)$ being the probability of a constellation point x. m is the number of bits used for each symbol based on the binary-reflected gray code and is defined as $m = log_2 M$ for an M-ary PAM (PAM-M). For uniform PAM-8, $H(X) = m = 3$ and for PS-PAM-8, $H(X)$ is calculated from the probability mass function of the symbol X.

2.9.3 Signal to Noise Ratio (SNR) and *Q*-factor

Signal to Noise Ratio (SNR) and Q-factor is a common metric, that is used frequently in digital communication. SNR represents the ratio of the detected signal powers (not amplitudes) to noise power. In the presence of AWGN noise, there is a direct relationship between SNR, Q-factor, and BER [69] and can also be used to predict BER. In coherent optical communication, optical SNR (OSNR) and Q^2-factor are also used frequently as a performance metric. OSNR is mostly normalized to 0.1 nm BW (12.5 GHz BW, assuming C-band). In IM/DD, due to the presence of optical carrier, and absence of EDFA, OSNR is not used commonly.

2.9.4 Error Vector Magnitude (EVM)

Error vector magnitude (EVM) is another figure of merit for assessing the quality of digitally modulated signals. When BER is small, EVM can be a good indicator of system performance. Here, by EVM, we mean RMS EVM, defined as:

$EVM_{RMS} = \sqrt{\frac{\sum_{k=1}^{N} |I_k - \widetilde{I_k}|^2}{\sum_{k=1}^{N} I_k}}$, where I_k and $\widetilde{I_k}$ represent ideal and received symbols.

2.9.5 RLM

Ratio Level Mismatch (also known as Level separation mismatch), is a figure of merit to measure vertical linearity of PAM4 signal. According to IEEE 802.3 Annex 120D Measurement, RLM is calculated as [70]:

$$RLM = \frac{smallest\ separation\ between\ adjacent\ levels}{ideal\ separation}$$

$$= \frac{\min\left(V_3 - V_2, V_2 - V_1, V_1 - V_0\right)}{\frac{V_3 - V_0}{3}}$$

where, V_0, V_1, V_2, V_3 are the voltage levels of the four level signals. A linear transmitter as shown in Fig. 2.15 yields $RLM = 1$. In Fig. 2.16, we show RLM values with eye diagrams for a DML/DD system, which shows transmitter NLPD can improve the RLM and BER significantly.

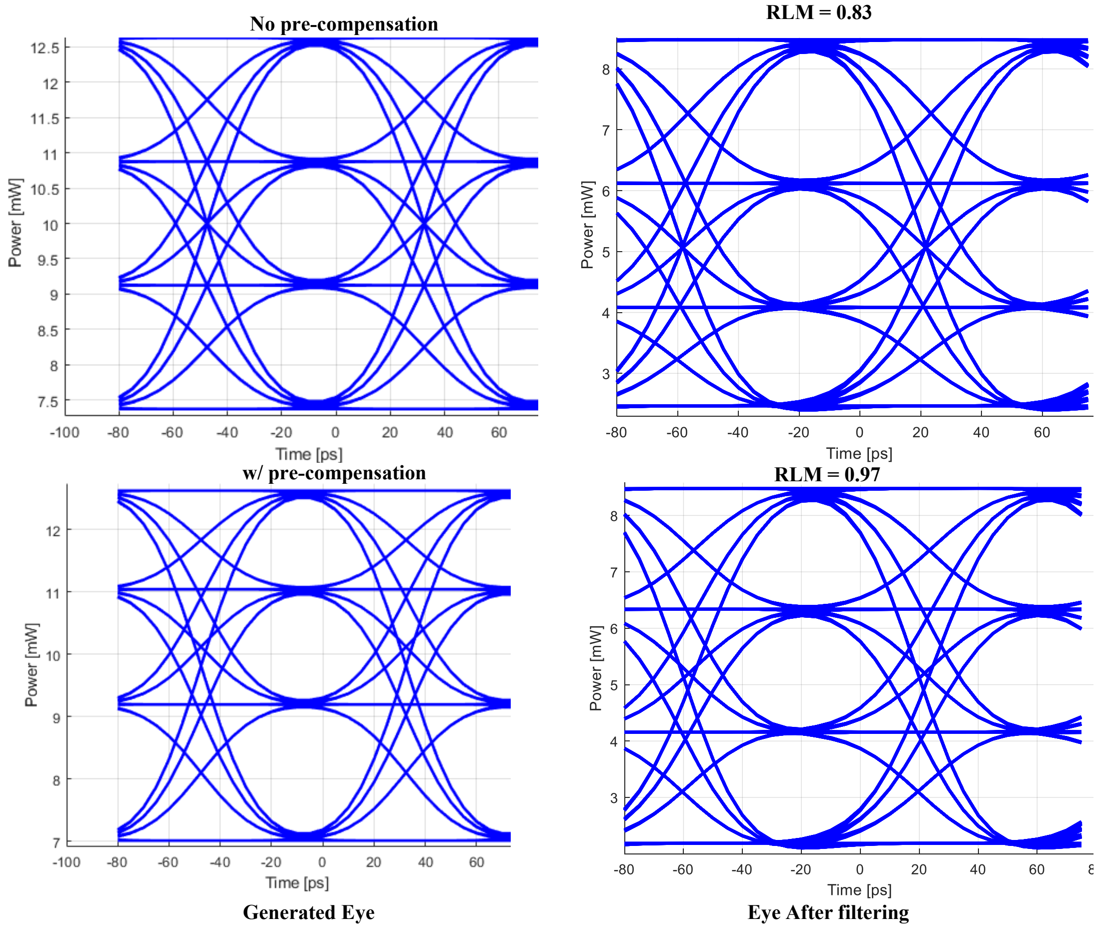

Fig. 2.16 Eyes after DML and optical filtering. The top two eyes are when no pre-compensation is applied, while the bottom pair are with pre-compensation.

Chapter 3 IM/DD Transmission using Mach Zehnder Modulator

3.1 Overview

The exponential demand for high bandwidth applications is causing a rapid increase in data-center (DC) traffic, which is why cost-effective optical transceiver solutions are essential [71]. Since most of this traffic involves intra-datacenter and inter-datacenter links, intensity modulation/direct detection (IM/DD) schemes are utilized because of the cost-effectiveness and power efficiency. To keep pace with this growing demand, optical transceivers operating at high symbol rates and higher order modulation formats are being investigated. PAM4 has been adopted in IEEE 802.3bs standard for 400 GbE and a QSFP-DD800 MSA has started working to extend the capacity of QSFP-DD pluggable module form factor from 400Gbps to 800Gbps. Though coherent is a strong contender for high-speed solution covering reach from 80 km and beyond, IM/DD solution will continue to dominate DR (datacenter reach for up to 500 m SMF), FR (fiber reach for up to 2 km SMF) and LR (long reach for up to 10 km SMF) transmission in the foreseeable future [3]. For the next generation Ethernet targeting 800 GbE and 1.6 TbE over short reach distances, 200 Gbps/λ is thus an important milestone [72].

In this chapter, we therefore focus on achieving 200 Gbps/λ transmission on two different material platforms and discuss the choice of modulation formats and necessary DSP to enable this per channel capacity. We start our chapter with the design, device characteristics of SiP travelling wave MZM that shows a 3-dB BW of over 45 GHz, with a V_π of 5.4 V. In section 3.2, we present results with both O-band and C-band designs. However, the transmission performance here is found to be mostly limited by the 120 GSa/s AWG, which barely allows us to reach 100 Gbaud. Therefore, we rely upon PAM6, PAM8 and PS-PAM8 formats, and transmit net 200G over 2 km with our best O-band design. To demonstrate the feasibility of achieving 200G in SiP platform with PAM4 format, we use next generation SiGe BiCMOS

DAC as AWG (Keysight M8199A) in section 3.3. We transmit 134 Gbaud PAM-4 (net 250 Gbps) and 115 Gbaud PAM-8 (net 288 Gbps) using HD-FEC and SD-FEC, respectively. We discuss in detail the performance with different modulation format and linear and non-linear signal processing.

The next question is can we go beyond 300G with intensity modulation. There are two ways to increase the throughput for IM/DD. One is to target higher symbol rate and the other is to for a higher modulation order. But as shown in the previous section, higher order PAM8 or PS-PAM8 requires high SNR which necessitates the adoption of more complicated SD-FEC. The alternate option is to go higher in terms of symbol rates, which requires higher BW of each transceiver component. Although SiP modulators offer low-cost solutions, there are two main limitations of SiP modulators, namely low BW (30-45 GHz) and phase shifting efficiency (5-6 V V_π). Newer material platforms are therefore being investigated to this end. Thin film lithium niobate (TFLN) has shown great promise in terms of both EO BW and phase shifting efficiency. In section 3, we study the performance of a TFLN MZM, which has a much better EO response (100 GHz usable BW) and lower V_π (1.5 V). This enables us to transmit net 350 Gbps with 1.4 V_{pp} drive signal. The lower driving signal reduces the power consumption, another important feature for DCI. This result is still limited by the current DAC technology and shows a potential for going even beyond 400 Gbps.

3.2 Net 220 Gbps/λ IM/DD Transmission in O-band and C-band with silicon photonic TW MZM

3.2.1 Motivation

In recent years, several high-speed experimental works have been reported with Mach–Zehnder modulators (MZMs) and electro-absorption modulators with distributed feedback lasers (EA-DFB) [73-79]. Lithium niobite ($LiNbO_3$) and indium phosphide (InP) based modulators have mostly been used to demonstrate these results due to their superior electro-optic properties.

However, bulk $LiNbO_3$ MZMs cannot be utilized in pluggable optical transceivers due to their larger footprint and neither InP nor $LiNbO_3$ based modulators are compatible with complementary metal-oxide-semiconductor (CMOS) foundries which hinder large-scale, low-cost production. Alternatively, hybrid integration of materials like polymers, thin-film lithium niobite, III-V semiconductors on silicon (Si) has been reported to combine the high electro-optic performance of other material platforms with the scalability of the already established CMOS process. But these designs require additional process, and thus cannot be entirely realized in a commercial silicon-on-insulator (SOI) process [74, 77]. Due to compatibility with the CMOS process, small footprint and cost-effectiveness, silicon photonics (SiP) has emerged as the most promising technology for massive deployment, and SiP modulators are now being extensively investigated both in IM/DD and coherent communication [79-85].

Most SiP modulators are based on carrier depletion traveling wave (TW) Mach-Zehnder or micro-ring resonator (MRM) structures [85]. Recent years have witnessed reports on high-speed IM/DD systems with SiP modulators targeting 200 Gbps. In [86], 200 Gbps PAM4 transmission using a silicon MRM was demonstrated at B2B in the O-band at a BER of 1.08×10^{-3}, which is the highest reported rate for a Si MRM. In [82], 200 Gbps PAM6 (net 167 Gbps) signal transmission over 1 km of SMF was achieved at a BER below the 20% HD-FEC threshold of 1.5×10^{-2} using a SiP TW-MZM with a 3-dB EO bandwidth of ~22.5 GHz and complex receiver DSP, which included post-filter and maximum likelihood sequence detector (MLSD). We have previously reported transmission of net 200 Gbps over 2 km of SMF in the O-band using a segmented-electrode MZM (SE-MZM) with 45 GHz 3-dB E-O bandwidth and simple linear feed forward equalization [87]. But this result required two drive signals with precise phase alignment making it challenging to control with practical RF delay lines. Most recently, we designed a high bandwidth single segment MZM with an on-chip termination (OCT) intentionally lower than the TW electrode characteristic impedance and demonstrated net 212.5 Gbps/λ transmission in the O-band [88].

3.2.2 Modulator Design and Characterization

In this section, we describe the design and characterization of the TW-MZMs. The C-band and O-band modulator designs both adopt the series push-pull (SPP) configuration with a layout shown in Fig. 3.1, where the two PN junctions of each arm are connected back-to-back and a DC bias is applied to the common N++ region. This doubles the junction resistance and halves the junction capacitance [89]. The fabrication process admits a RF electrode design with two metal layers that reduces microwave attenuation. For each of the two optical bands, we have designed the MZM with two different phase-shifter lengths, 1.5 mm (S) and 2.5 mm (L). Both the O-band and C-band modulator designs use the same doping densities. The only difference lies on the optical waveguide width. The waveguide widths of the MZMs have been chosen to ensure single-mode operation and maximize optical field/carrier overlap. A reduced waveguide width is used for the O-band design for this reason. As these modulators are designed for high data rate links required by the intra-data center interconnects, we peak the device frequency response to obtain a higher E-O bandwidth by implementing a 35 Ω on-chip termination (OCT), intentionally mismatched to the traveling-wave electrode characteristic impedance [90]. Vertical grating couplers (GC) are used for the optical input and output and the MZM operating point is set using thermal phase shifters.

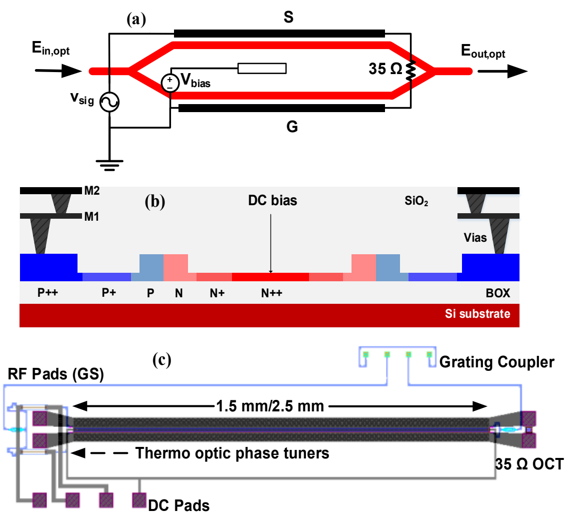

Fig. 3.1 (a) TW-MZM top-view schematic, (b) SPP-MZM cross-section. BOX: buried oxide, M1/M2: metal layers and (c) SPP-MZM layout.

Fig. 3.2 shows the E-O S_{21} and E-E S_{11} magnitude responses of the 2.5 mm C-band and O-band modulator. A 50 GHz Keysight lightwave component analyzer (LCA) and 50 GHz RF probes are used to perform the small-signal characterization. From Fig. 3.2, it can be observed that the RF return loss (S_{11}) is below 10 dB within the entire measurement spectrum. Also, the E-O S_{21} magnitude responses show that the 3-dB bandwidths of both C-band and O-band modulators are approximately 47 GHz at a 3V reverse bias (normalized to 1.5 GHz). This 3-dB bandwidth allows 100 Gbaud signaling for single-carrier 200 Gb/s links with simple linear FFE as will be shown in the following sections. The S_{21} magnitude responses of the MZMs with a shorter phase shifter length are not shown here but they have better bandwidth, at the expense of a higher V_π [91] as shown in Table 3.1. From the E-O S_{21} frequency response curves, we can also see that there is a clear peaking at lower frequency (at around 12 GHz). As mentioned earlier, the gain peaking at this frequency comes due to the impedance mismatch between the traveling-wave electrode characteristic impedance of 50 Ω and on-chip termination (OCT) of 35 Ω. It acts like a pre-emphasis and extends the bandwidth of the modulators.

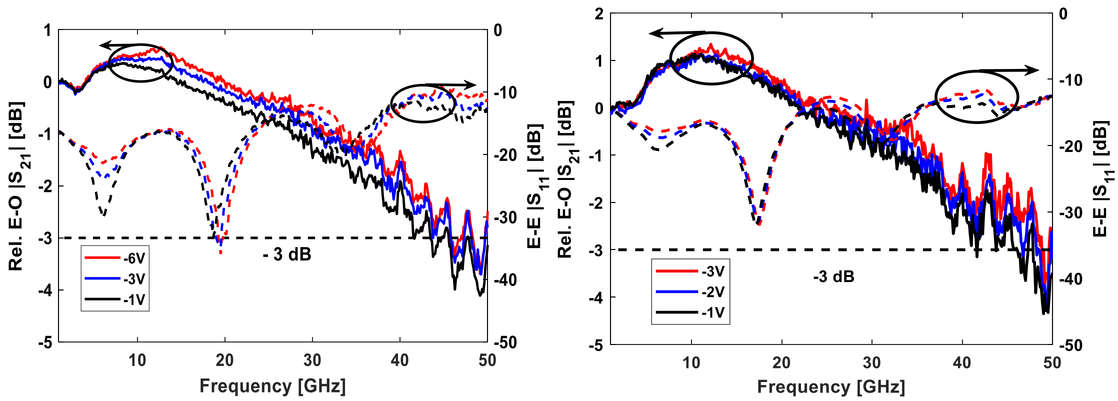

Fig. 3.2 Measured small-signal response of the MZMs (E-O $|S_{21}|$ is normalized to 1.5 GHz): C-band (L) MZM (top), and O-band (L) MZM (bottom).

From Table 3.1, we can see that the V_π of the O-band MZM is lower (5.4V) as compared to the C-band modulator (V_π of 7.6 V). The different phase shifting efficiency in O and C bands come from i) the different effective refractive index change, $\Delta n_{eff}(E)$ as a function of the applied voltage, which depends on the plasma dispersion effect and the overlap fraction between the optical mode and the free-carriers being modulated around the PN junction, and ii) the wavelength, λ at the denominator of the phase shifter equation, $\Delta\varphi = 2\pi\Delta n_{eff}(E)L/\lambda,$ where L is the phase shifter length. For the same phase shifter length, these factors cause the V_π to be higher for the C-band modulator compared to the O-band one. The V_π of the C-band MZM becomes even higher at a shorter length of 1.5 mm, which requires high driving voltages that are challenging for practical transmitter RF chains and poses a high modulation power consumption, making it unsuitable in DCI scenario. Therefore, we will mainly discuss the transmission performance of three modulator designs with their key parameters summarized in Table 3.1. The high optical propagation loss is due to a layout error (exaggerated proximity of P+ and N+ doped regions with the optical waveguide) and is worse in the C-band designs.

Table 3.1 O-band and C-band Modulators at -2 V Bias

Metric	O-band MZM (S)	O-band MZM (L)	C-band MZM (L)
Phase shifter length (mm)	1.5	2.5	2.5
DC V_π (V)	6.6	5.4	7.6
- 3dB E-O BW (GHz)	> 50	47	46
BW/V_π (GHz/V)	> 7.5	8.7	5.9
Total opt. Propagation loss (dB)	4	5.4	8.4

3.2.3 Experimental setup and Digital Signal Processing

The experimental setup and DSP used to test the transmission performance of the designed modulators is shown in Fig. 3.3. The set of instruments used to test O-band and C-band modulators are the same except for the laser and optical amplifier. In the O-band experiment, 13 dBm of power is launched at 1302.8 nm which is then coupled to the chip using the grating coupler, whereas, in C-band, 15.25 dBm of power at 1550 nm is used as the CW light source. The measured back-to-back grating coupling loss is found to be 7.5 dB and 9.5 dB for the O-band and C-band grating couplers, respectively. This difference comes from a better GC design in the O-band case. DC probes are used to reverse bias the PN junction of the modulator and tune the thermal shifters. At the transmitter, a PRBS sequence is generated and then mapped to PAM symbols. After resampling the symbols to 2 sps, pulse shaping is done via a raised cosine (RC) filter. Then we resample the samples to the DAC sampling rate. Next, a pre-emphasis filter pre-compensates for the low pass filtering of the DAC and RF amplifier. Note that we do not use any nonlinearity pre-compensation for MZM. The digital signal is then clipped, quantized, and loaded to a 120 GSa/s 8-bit digital-to-analog converter (DAC). The DAC output is amplified by an RF amplifier with 45 GHz 3-dB bandwidth and 26-dB gain and then applied to the modulator using 50 GHz RF probes. As the pre-emphasis filter flattens the entire transmitter RF chain including the RF amplifier, the lower bandwidth of the amplifier compared to the devices under test does not limit the system performance in terms of bandwidth. To test the transmission performance, we adopt different PAM formats from 65 Gbaud to 110 Gbaud and the roll-off factor is empirically optimized at these different symbol rates.

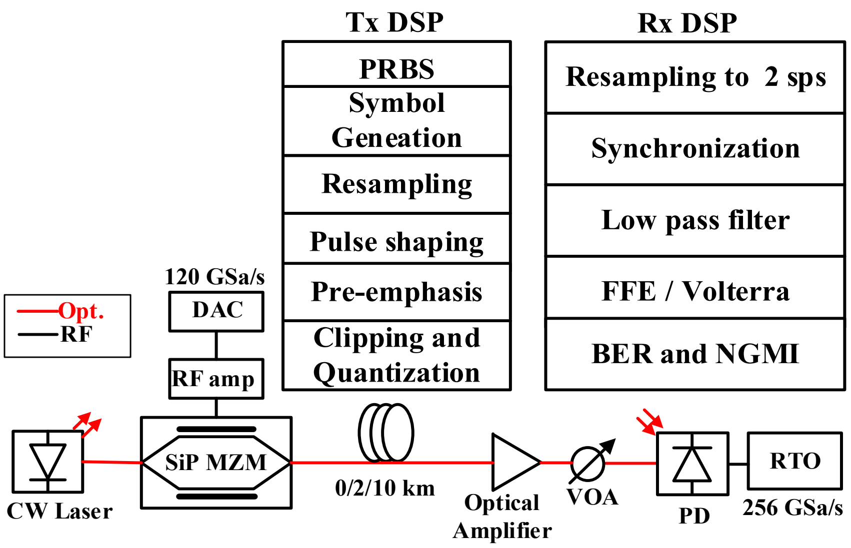

Fig. 3.3 Experimental set up and DSP deck.

After the modulator, the optical signal is transmitted over various distances of standard single-mode fiber (SSMF). To compensate for the grating coupler loss and modulator optical loss, a praseodymium-doped fiber amplifier (PDFA) or an Erbium-doped fiber amplifier (EDFA) is used to provide sufficient received optical power (ROP) to the 50 GHz PIN photodetector (PD). The noise figure of the PDFA and EDFA used is 6.5 dB and 5 dB, respectively. A variable optical attenuator (VOA) is added before the PD to control the ROP. The signal out of the PD is then digitized by a real time oscilloscope (RTO) with a bandwidth of 110 GHz operating at 256 GS/s. As the transmitter signal bandwidth is kept within 60 GHz, the RTO bandwidth is set to 63 GHz so that the out of band noise is filtered automatically. Finally, the signal is processed offline by the receiver DSP, which includes re-sampling to 2 sps, synchronization, linear feed-forward equalization (FFE) or Volterra non-linear equalization (VNLE), symbol de-mapping and bit-error ratio (BER) counting and NGMI computing.

3.2.4 O-Band Transmission Experiment Results

3.2.4.1 PAM transmission results with linear equalization

In this section, we investigate the transmission performance of the O-band 2.5 mm MZM, which has the maximum phase-shifting efficiency among the designs. A reverse bias voltage of 2 V is used, which gives the best performance for this longer modulator. This also ensures >45 GHz 3-dB bandwidth which is useful when operating at high symbol rates. At the MZM quad point, the power out of the chip is around -4 dBm, which is then launched into the SMF. The peak-to-peak driving voltage after the RF amplifier depends on the symbol rate, roll-off factor, and clipping ratio. The maximum peak-to-peak voltage, V_{pp} that we drive the modulator with is 2.6 V_{pp} and 2.3 V_{pp} at 85 Gbaud and 90 Gbaud, respectively.

Fig. 3.4 shows the BER versus interface rate at B2B and after 2 km of SMF for different PAM formats. The received optical power is set to 8.5 dBm and only linear FFE is used in the receiver signal processing. The red curves represent PAM4 BER as the symbol rate varies from 70 Gbaud to 110 Gbaud. The figure shows that we can achieve 170 Gbps and 200 Gbps interface rate PAM4 transmission over 2 km of SMF at a BER below the KP4-FEC threshold and 6.7% HD-FEC threshold, respectively. However, net 200 Gbps (214 Gbps interface rate assuming HD-FEC) with PAM4 format is not achievable due to the limited bandwidth of the system. The blue curves in Fig. 3.4 show the BER of the PAM6 format. Here, PAM6 symbols are generated from a 32-QAM 2D constellation which maps five bits into two symbols with a spectral efficiency of 2.5 bits/symbol [56]. We sweep the symbol rate for PAM6 format from 70 Gbaud (= 70×2.5 Gbps = 175 Gbps interface rate) to 105 Gbaud (262.5 Gbps interface rate). 218 Gbps PAM6, which corresponds to a throughput of 203 Gbps, is achieved with this modulator design below the HD-FEC threshold after 2 km propagation.

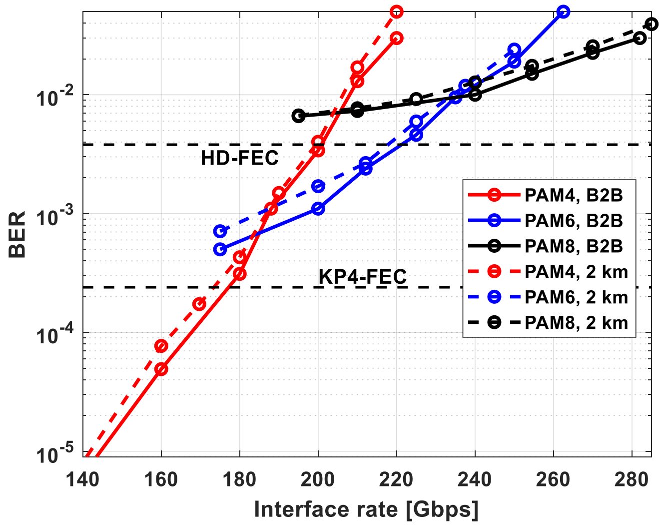

Fig. 3.4 BER vs. interface rate for PAM4, PAM6 and PAM8 at B2B and 2 km with FFE.

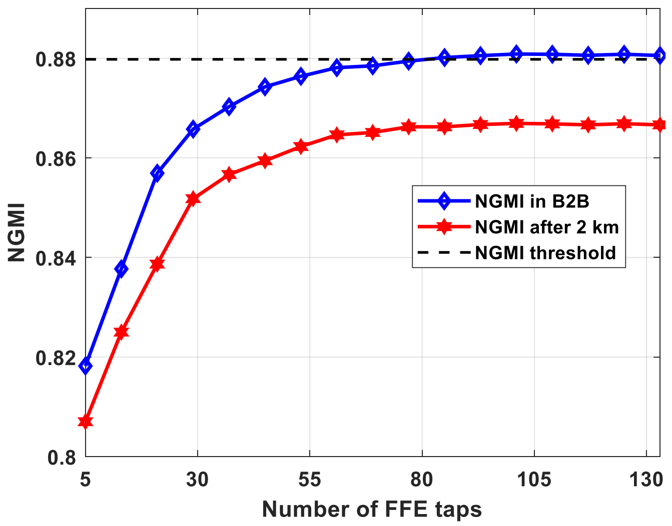

Fig. 3.5 NGMI vs. number of FFE taps for a 90 Gbaud PAM8 signal.

The PAM8 format has a higher SNR requirement and cannot achieve a throughput of interest (>200 Gbps) at the HD-FEC. Therefore, to evaluate the system performance, we adopt a practical SD-FEC [51] and compute the NGMI as a more precise metric to evaluate the transmission performance [50]. The combined FEC code rate is 0.8402, and the NGMI threshold is 0.8798. In Fig. 3.5, we show the calculated NGMI of a 90 Gbaud PAM8 signal (225 Gbps net data rate) as we sweep the number of FFE taps. We find that a minimum of 81 taps are required for an NGMI above the threshold of 0.8798 at B2B. However, this is not achievable for the case of 2 km regardless of the number of taps used. We show in the following section that by mitigating the nonlinearity using the Volterra nonlinear equalization we can achieve 225 Gbps net data rate PAM8 transmission over 2 km.

3.2.4.2 PAM transmission results with nonlinear equalization

At a transmission reach of 2 km, the non-linearity of the system primarily comes from the system components, rather than the optical fiber. One source of these impairments is the non-linear phase shifter of the SiP modulator. Also, to keep a reasonably high driving voltage swing into the modulator at high symbol rates, we clip the signal before loading it into the DAC, which also introduces non-linearity into the signal. Nonlinear equalization has been shown to be effective in improving system performance even in optical short reach scenarios [66, 92].

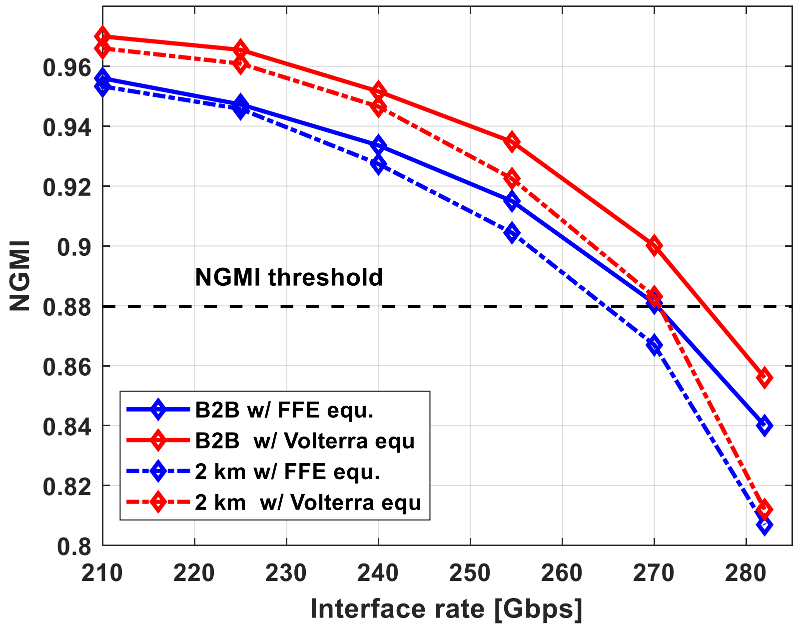

Fig. 3.6 NGMI vs. interface rate for PAM8 signals with linear and non-linear equalization.

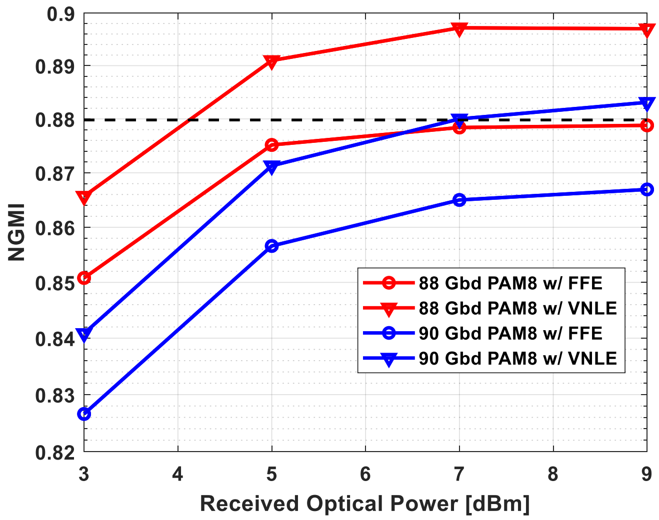

Fig. 3.7 NGMI vs. ROP after 2 km transmission with FFE and VNLE.

Fig. 3.6 plots the NGMI vs. interface rate using the PAM8 modulation format. We find that second order VNLE enables the transmission of a 90 Gbaud (270 Gbps) PAM8 signal with an NGMI above the threshold, which corresponds to net 225 Gbps, over 2 km of SMF. For these results a T/2 spaced, second order full Volterra equalizer is adopted. The memory lengths for the linear terms and the nonlinear terms of second order Volterra equalizer is chosen to be 61 and 7 respectively. The performance improvement is not significant for higher memory lengths. Thus, we use these memory lengths for the rest of the results with the VNLE. In Fig. 3.7, we show the NGMI as we sweep the received optical power for 88 and 90 Gbaud PAM8 signals. These figures show that second order VNLE allows the throughput of PAM8 format to extend by 5 Gbps only. Due to the low driving voltage swing into the modulator, we operate mostly in the linear region of modulator, leading to little non-linear effect from the modulator side. Third order Volterra equalizer do not show significant improvement as well and considering its complexity we do not employ it in our results. Fig. 3.7 also shows that the minimum required ROP for a net of 220 Gbps and 225 Gbps after 2 km transmission is 4.1 dBm and 7 dBm, respectively. Here we use PDFA followed by a VOA to sweep the ROP while the launch power is kept at -4 dBm. We also test the impact of the VNLE for PAM4 and PAM6 modulation formats. Unlike PAM8, the performance improvement is not that pronounced. This is primarily because of the smaller number of inner levels for these formats.

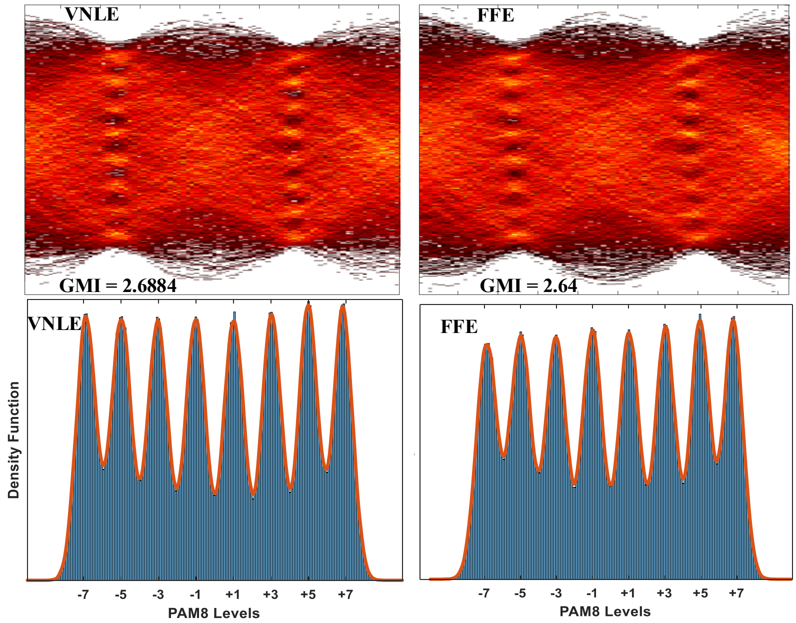

Fig. 3.8 Eye diagram and histogram of 90 Gbaud PAM8 signal with receiver VNLE and FFE at B2B

In Fig. 3.8, we draw the eye-diagram of the net 225 Gbps B2B signal with and without nonlinear equalization. We find that in both cases the outermost eyes are more closed than the inner eyes. The histogram of the received symbols shows that the outermost levels are less separated from each other than the inner levels and cause more errors. We can also see that the levels are more distinguishable at the decision thresholds using nonlinear equalization (VNLE) than linear FFE. Probabilistic shaping can improve the system performance as the outer levels are transmitted with lower probability thus improving the BER performance. However, PS-PAM8 will require higher symbol rate transmission for the same throughput and an optimum choice is to be made.

3.2.4.3 PAS PAM transmission results

The use of standard PAM formats results in a coarse grid of spectral efficiency (SE) as well as the corresponding symbol rates required at each SE to a achieve net 200 Gbps data rate. For example, PAM4 signaling requires the system to operate at 107 Gbaud assuming a 6.7% HD-FEC, which poses a stringent requirement on the system bandwidth. On the other hand, PAM8 signaling is demanding on the system SNR due to limited effective number of bits (ENoB) of the DAC and ADC. Thus, to improve the system throughput, it is desirable to transmit probabilistic shaped signals with a finer SE granularity so that we can best exploit the trade-off between inter-symbol interference (ISI) and system SNR. In this section, we use cost-minimizing distribution matching (CMDM) within the probabilistic amplitude shaping (PAS) scheme to generate PS-PAM8 signals with varied SEs. CMDM is implemented by means of a lookup-table (LUT) [60], where a varied number of bits from 13 to 19 are mapped to a block of 10 symbols and provides a tunable information bit per symbol (IBPS) from 1.8 to 2.4 bits/symbol assuming 20% FEC overhead. Since the weight of the symbol sequences are set as the sequence power, the PS-PAM8 symbols approach the Maxwell-Boltzmann distribution.

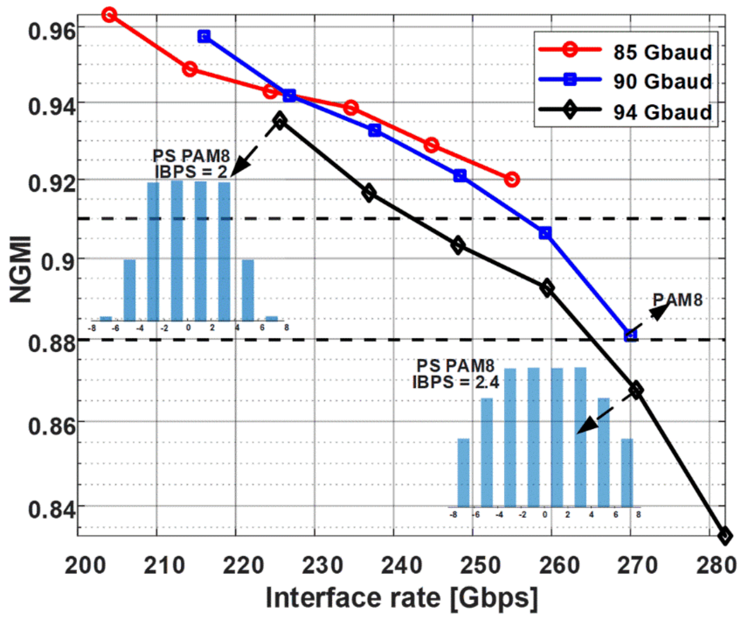

Fig. 3.9 NGMI vs. interface rate for PS-PAM8 signals with varied IBPS at three symbol rates at B2B.

In Fig. 3.9, we show the NGMI of PS-PAM8 signals with varied IBPS at three different symbol rates at B2B. Note that only linear equalization is used at the receiver. We sweep the IBPS from 2 to 2.5 bits/symbol, which means for 90 Gbaud PS-PAM8 signals, we can tune the net throughput from 180 Gbps to 225 Gbps with a step of 9 Gbps. The histogram of the transmitted symbols for two different IBPS values is also shown in the inset. As the IBPS increases, the transmitted signal becomes more and more identical to a uniform PAM8 signal, which corresponds to an IBPS of 2.5 (=3/1.2) bits/symbol. We can also see that the 94 Gbaud PS-PAM8 signal shows notably worse performance than the 90 Gbaud and 85 Gbaud signals at the same interface rate. As the symbol rate increases, the transmitted signal bandwidth increases, and the pre-emphasis filter must compensate more. As a result, the signal PAPR increases and the driving signal swing decreases. The transmitter shows a bandwidth response that drops sharply after 45 GHz and as a result the transmitted signal quality degrades faster beyond 90 Gbaud. It comes both from the RF transmitter chain that includes the DAC and RF amplifier and the modulator itself that has a 45 GHz 3-dB BW. This causes the 94 Gbaud PS-PAM8 signals to perform worse than the 90 Gbaud and 85 Gbaud signals at the same interface rate. As the roll-off of the system response degrades much slowly before 45 GHz, the NGMI difference between 85 Gbaud and 90 Gbaud signals at the same interface rate are close. At the same interface rates beyond 225 Gbps, 85 Gbaud signal at a higher IBPS shows better performance than 90 Gbaud signal at a lower IBPS. The optimum choice of symbol rate and IBPS depends on system ISI and SNR, so long as the signal swing is not too much affected due to pre-emphasis and the entropy loss is small. So, the performance (NGMI) at these symbol rates is close for most of the interface rates. For the best throughput, at each desired throughput, the symbol rate and IBPS need to be appropriately determined.

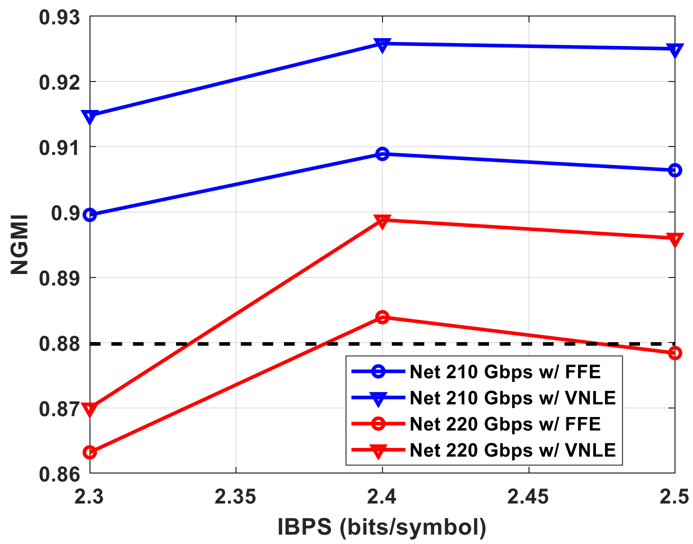

Fig. 3.10 NGMI versus IBPS for net 210 Gbps and 220 Gbps after 2 km

Next, we try to find the IBPS that achieves the highest NGMI at a target net data rate for our system after 2 km propagation with linear and non-linear equalization. The blue and red curves in Fig. 3.10 show the NGMI values at different symbol rates and corresponding SEs for net 210 Gbps and net 220 Gbps, respectively. We can see that PS-PAM8 with an IBPS of 2.4 bits/symbol delivers the highest NGMI for these net rates for both linear and non-linear equalization. Lower IBPS (2.3) at a high symbol rate is not a good choice because of stronger ISI and lower driving voltage swing. For net 220 Gbps with linear FFE, only 2.4 bits/symbol PS-PAM8 at 91.6 Gbaud is found above the NGMI threshold and outperforms uniform PAM8 signaling.

3.2.4.4 10 km PAM transmission results

10 km transmission is important for LR (long reach) datacenter interconnects and Fig. 3.11 shows the BER performance over 10 km of SMF with different modulation formats and receiver VNLE. We can see that using PAM6 format, we can transmit net 200 Gbps (interface rate of 214 Gbps) below the HD-FEC threshold. In Fig. 3.12, we show the achievable NGMI for PAM8 format with linear and nonlinear equalization schemes. The 2 km curve with linear equalization is also added here for comparison. The maximum achievable throughput after 10 km of SMF is 216 Gbps, achieved with 86 Gbaud PAM8 format and VNLE. Like 2 km results, the NGMI gain with VNLE is not significant, meaning the nonlinear degradation is not that severe for 10 km transmission as well.

Fig. 3.12 also shows that compared to 2 km transmission; the results are slightly worse for the 10 km case. The effect of dispersion is negligible over 10 km of SMF at our wavelength of operation (1302.8 nm). Therefore, the degradation comes mostly from the reduced OSNR of the received signal. As mentioned earlier, the launch power into the fiber is -4 dBm and after 10 km transmission this becomes -7.5 dBm, which is then amplified via the PDFA. But the lower input power into the PDFA increases the noise figure (NF) and worsens the signal OSNR. Considering short reach application scenario, PDFA is not a viable solution and better light coupling in this case would increase the launch power into the fiber, thereby improving the transmission performance. We show the optical spectra to show the impact of PDFA noise in Fig. 3.13.

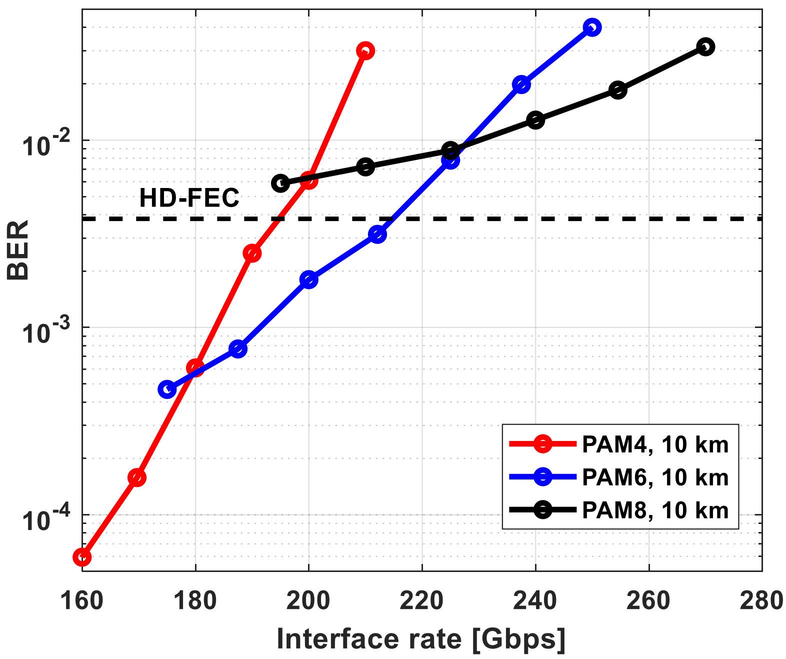

Fig. 3.11 BER vs. interface rate after 10 km transmission

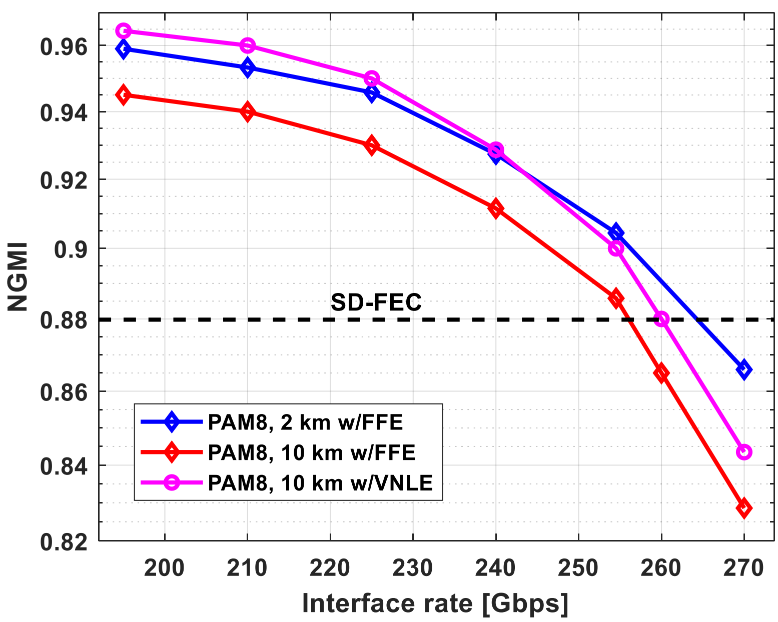

Fig. 3.12 NGMI vs. interface rate with PAM8 format

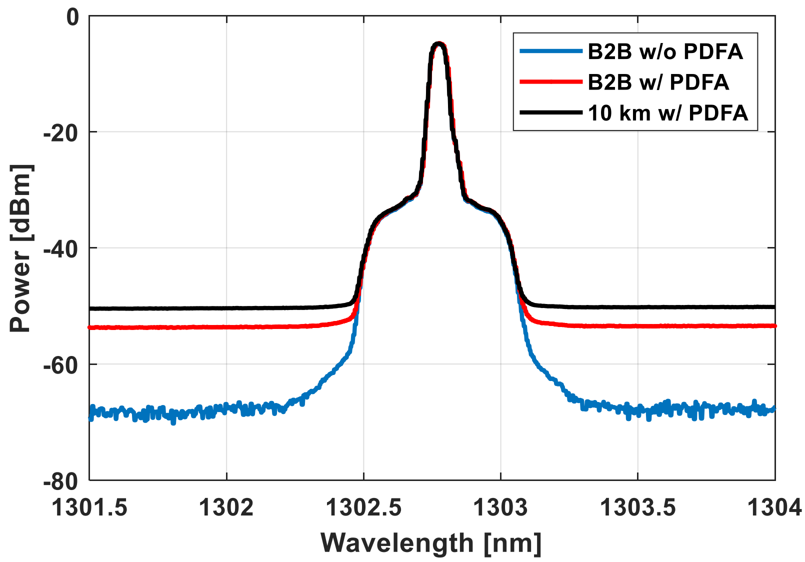

Fig. 3.13 Optical Spectrum w/ and w/o PDFA in B2B and after 10 km Tx

3.2.4.5 Experiment Results with shorter MZM

Next, we focus on the shorter MZM with a phase shifter length of 1.5 mm. This modulator has a 3 dB E-O bandwidth of over 50 GHz and a lower optical propagation loss, but this comes at the expense of a higher V_π. The optimized reverse bias voltage for this modulator is found to be 0.5 V. From Table 3.2 and Fig. 3.14, we find that despite the higher E-O bandwidth, the shorter MZM shows worse transmission performance compared to the longer one for all formats. Fig. 3.14 plots the NGMI versus interface rate with this MZM at B2B and after 2 km propagation with a VNLE. The shorter MZM achieves 270 Gbps PAM8 (net 225 Gbps) at the B2B scenario and after 2 km, the highest interface rate that is above the NGMI threshold is 264 Gbps, corresponding to a throughput of 220 Gbps. As the roll-off factor chosen for the 90 Gbaud signal is 0.1, the one-sided signal bandwidth is 49.5 GHz. Therefore, the higher E-O bandwidth of the shorter MZM does not improve the performance significantly, rather the higher V_π decreases the modulation depth of the transmitted signal and causes the overall results to degrade. Even at higher symbol rate operation, this modulator shows worse performance. But the total footprint of this modulator is 0.9 mm × 2.2 mm, as compared to the longer one with 0.9 mm × 3.2 mm footprint, which makes it good choice if space is an important factor.

Table 3.2 MZM BER Performance for short and long modulator

Modulation Format	Interface Rate (Gbps)	Short MZM	Long MZM
100 Gbaud PAM4	200	5e-3	3.4e-3
90 Gbaud PAM6	225	4e-3	3.2e-3

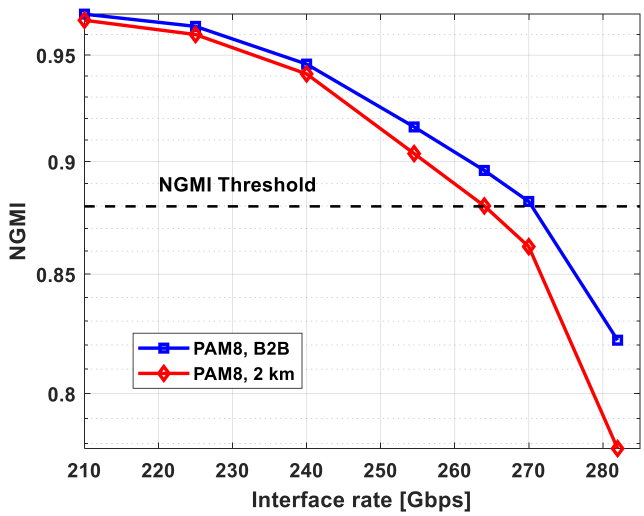

Fig. 3.14 NGMI vs. interface rate with PAM8 format for shorter MZM

3.2.5 C-band transmission experiment results

In this section, we present the transmission results using the C-band modulator. As shown is Table 3.1, the C-band modulator has a much higher V_π as compared to the O-band design. Based on the previous explanations, we choose the modulator with the longer phase shifter length (2.5 mm) for better phase shifter efficiency. In Fig. 3.15, we show the BER of PAM4 and PAM6 format and NGMI of PAM8 signaling at different interface rates. The B2B BER for 100 Gbaud signaling is found to be 8.5e-3, which is worse than the O-band designs because of its higher V_π. Net 200 Gbps below the HD-FEC threshold is still achievable using 86 Gbaud PAM6 at B2B. After 500 m the maximum throughput below the HD-FEC threshold is 195 Gbps at 84 Gbaud with PAM6 format. For PAM8 signaling, at B2B maximum 264 Gbps (net 220 Gbps) is achievable above the NGMI threshold and for a 500 m transmission, it is reduced to 258 Gbps (net 216 Gbps). For 2 km reach, the signal is heavily affected due to dispersion induced power fading which is clear from the received electrical spectrum of the 85 Gbaud signal shown in Fig. 3.16. 72 Gbaud PAM8, which is equivalent to a net 180 Gbps signal can be transmitted over 2 km of SMF using receiver VNLE at the SD-FEC threshold.

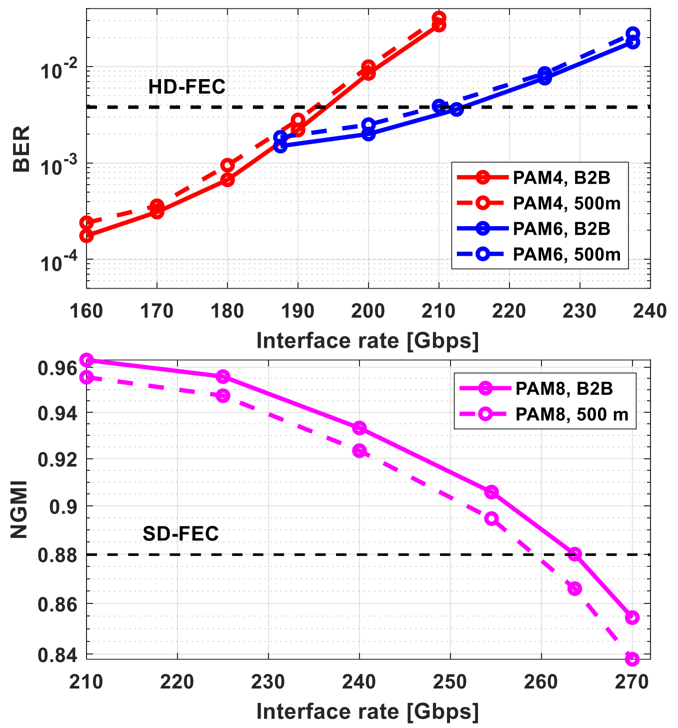

Fig. 3.15 BER (top) and NGMI (bottom) vs interface rate for C-band MZM

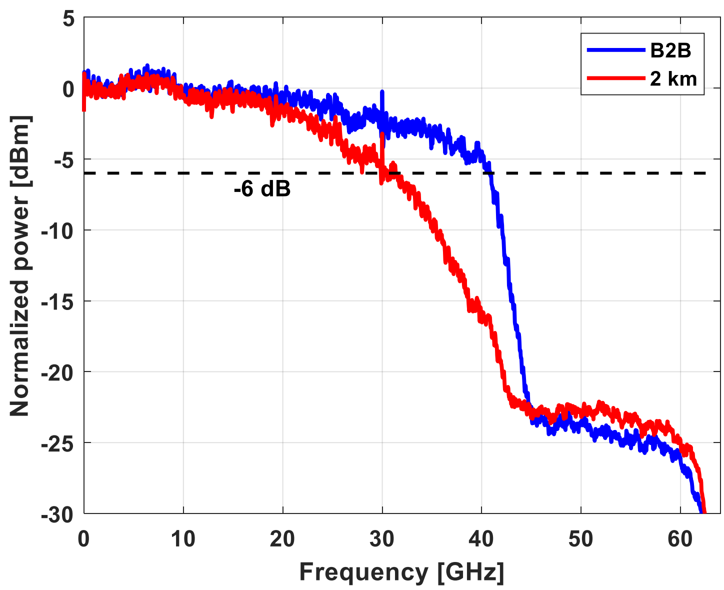

Fig. 3.16 Received Electrical spectrum at B2B and after 2 km for 85 Gbaud signal.

3.2.6 Summary

In the prior sections, we report the small-signal, and large-signal characterization of high bandwidth SiP MZM modulators. It is found that besides the importance of a high E-O bandwidth, the transmitter driving voltage and modulator V_π are also key factors which determines system performance. Since meeting the low power consumption constraint in data centers necessitates a low driving power, modulator designs with optimized phase shifting efficiency are preferable. In our case, the modulator with the longer phase shifter has lower V_π compared to the design with shorter phase shifter, and thus delivers better transmission performance despite a slightly lower E-O bandwidth of 47 GHz. This modulator design enables 100 Gbaud PAM4 signal transmission below the 7% HD-FEC threshold with only linear FFE. Since it is desirable to use high code rate HD-FEC for real-time short reach systems with a high throughput decoder, PAM6 seems to be an attractive signal format to attain net 200 Gbps and works as a compromise between PAM4 and PAM8 modulation formats in terms of the system bandwidth and SNR requirement. Our results also show that higher order formats such as PAM8 or PS-PAM8 allow higher throughput at the expense of higher overhead SD-FEC. Considering the power constraint of transceivers used within the data centers, nonlinear equalizers are not preferred and depending on the system non-linearity, reduced-complexity Volterra equalizers [93] or look-up-table (LUT) based nonlinear pre-distortion schemes [94] might be adopted, and short block length distribution matchers such as CMDM can be utilized to facilitate the high-speed parallel signal processing.

3.3 Net 300 Gbps/λ Transmission over 2 km of SMF with a Silicon Photonic MZM

3.3.1 Motivation

In Section 3.2, we demonstrated the transmission of net 225 Gbps PAM8 signaling over 2 km of SMF in the O-band. But this required a higher order PAM8 format and the adoption of more power-hungry SD-FEC. 200G at HD-FEC of KP4-FEC is a more practical solution for the 800G and 1.6T transceivers, which requires high operational bandwidth of each transceiver component. As mentioned at the start of the chapter, the limited bandwidth of DAC is a major challenge in achieving this objective. However, with the advancement of CMOS, better DAC and ADC are now available that can push the limit farther. In this section, we evaluate the transmission performance of the same O-band SPP MZM with 2.5 mm phase shifter length with a newer generation of Keysight AWG (M8199A). The AWG operates at a sampling rate of 128 GSa/s and by interleaving two channels, we can generate signals at 256 GSa/s. As compared to the AWG employed in section 3.2, this has a better BW of around 65 GHz and a better ENoB. This allows us to transmit 134 Gbaud PAM-4 (net 250 Gbps) below the 6.7% overhead (OH) HD-FEC BER threshold of 3.8×10^{-3} and 115 Gbaud PAM-8 (net 288 Gbps) above the 19.02% OH SD-FEC NGMI threshold of 0.8798 over 2 km of SMF in the O-band, with only a linear feed-forward equalizer (FFE) and a single 3 V peak-to-peak driving signal. With the aid of post-filter and maximum likelihood sequence detection (MLSD), we extend this transmission capacity to 140 Gbaud for PAM-4 signaling. To explore the capacity limit with this SiP MZM, we adopt probabilistic shaping (PS), and show net 310 Gbps operation. To the best of our knowledge, these are the highest reported net rates with a SiP modulator in an IM/DD system.

3.3.2 Experimental Setup

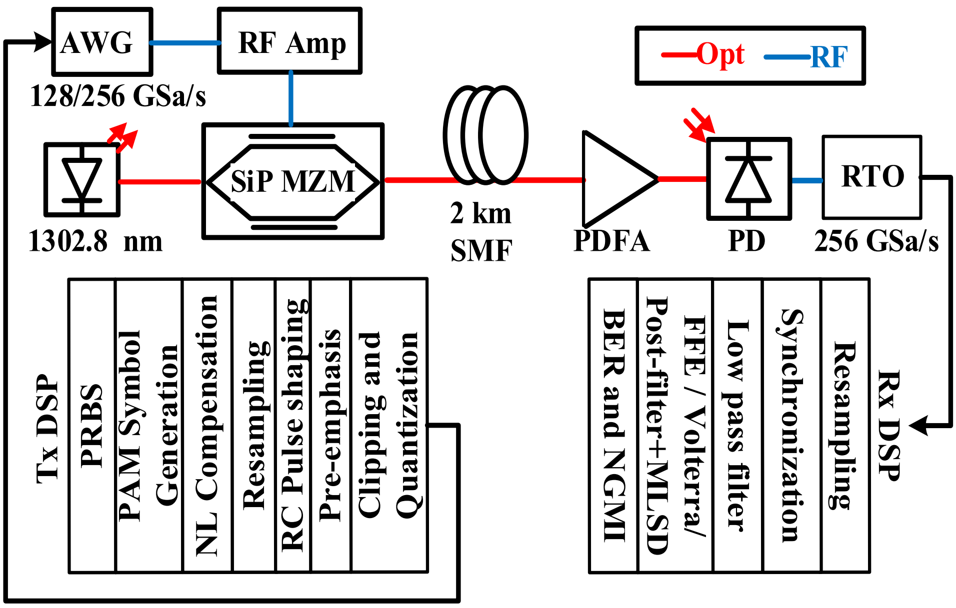

Fig. 3.17 Experimental Setup and offline DSP. (© 2021 IEEE)

Fig. 3.17 presents the experimental setup along with offline DSP blocks to test the system performance. The same O-band tunable laser is used as the CW light source. And the DSP section is almost identical except that we employ an additional non-linear compensation at the transmitter and more complex probabilistic shaping is utilized to improve the throughput. The 8-bit AWG can be operated at either 128 GSa/s or 256 GSa/s. The AWG output in both cases is amplified to about 3 V_{pp} voltage by an RF amplifier (SHF 807C) with 55 GHz 3-dB bandwidth and applied to the SiP MZM using 67 GHz RF probes. At the receiver, we replace our 50 GHz PD with a higher BW one (70 GHz). As before, this does not include a trans-impedance amplifier (TIA). Therefore, we still need to rely on PDFA to compensate for the modulator and coupling loss. The signal out of the PD is digitized using the same RTO, which operates at 256 GSa/s. The bandwidth of RTO is set to 65 GHz (75 GHz) when the AWG runs at 128 GSa/s (256 GSa/s) to filter the out of band noise. Finally, the signal is processed offline by the receiver DSP as shown in Fig. 3.17 and is discussed in more detail in the following sections.

3.3.3 Experimental Results with 128 GSa/s AWG

We first test the system performance of our MZM for PAM-4 and PAM-6 formats, which are the most promising options for the next generation DCI market. Fig. 3.18 (a) plots the BER vs. gross bit rate curves with linear and non-linear equalization after 2 km of SMF at 7.5 dBm received optical power (ROP). The figure shows that we can transmit 250 Gbps PAM4, the signal equivalent of net 234 Gbps below the 6.7% HD-FEC BER threshold. Though the PAM6 format requires 25% less bandwidth at the same bit rate, at this HD-FEC BER threshold, PAM6 shows worse BER with only linear equalization due to its higher SNR requirement and the non-linearity present in the system. With Volterra non-linear equalization (VNLE) PAM6 outperforms PAM4 at this BER threshold. We use third-order Volterra filter with memory lengths of 91, 3, and 5 for linear, second and third-order Volterra kernels, respectively and 91 filter taps for linear FFE for these results. It should be noted that for both PAM4 and PAM6, the improvement with VNLE diminishes at symbol rates close to 128 Gbaud. The signal swing out of the AWG becomes smaller due to stronger pre-emphasis and the system non-linearity is no longer dominant at high symbol rates. Therefore, considering the complexity of VNLE, the curves show that with a high BW SiP MZM, PAM4 is the suitable choice for 250 Gbps operation.

Next, we transmit PAM8 signals at different symbol rates and due to its high error floor compared to PAM4, we choose SD-FEC instead of HD-FEC. The NGMI curves in Fig. 3.18(b) and the histogram of the received symbols at 100 Gbaud PAM8 in Fig. 3.18 (c) reveal the presence of strong non-linearity in the system, which results in significant errors from the outermost levels. We use a peak-to-peak driving voltage of 3 V (55% of the DC V_π of the modulator) and bias the MZM at the quadrature point. This indicates that the non-linearity mostly comes from the RF amplifier, which shows a 1 dB output power compression (P_{01dB}) at 15 dBm (3.5 V_{pp}). Although lowering the input to the amplifier reduces the non-linear effect, the low modulator driving signal decreases the optical modulation amplitude and degrades overall system performance. To overcome this issue, we adopt a non-linearity compensation technique by means of a non-linear lookup table (NLLUT) with 3-symbol memory length [61] and compare its performance with VNLE. Both non-linear pre-distortion with FFE and third-order VNLE without any pre-compensation show similar performance and we can successfully transmit 336 Gbps PAM-8 (net 282 Gbps) over 2 km of SMF. Increasing the non-linear memory lengths of VNLE beyond the previously mentioned values do not improve the system performance significantly and is thus not adopted for these results. Unlike PAM4 and PAM6, due to higher number of inner levels and high peak-to-average power ratio (PAPR) of the transmitted signal, non-linear equalization or pre-distortion give better results for PAM8 for all the symbol rates of interest.

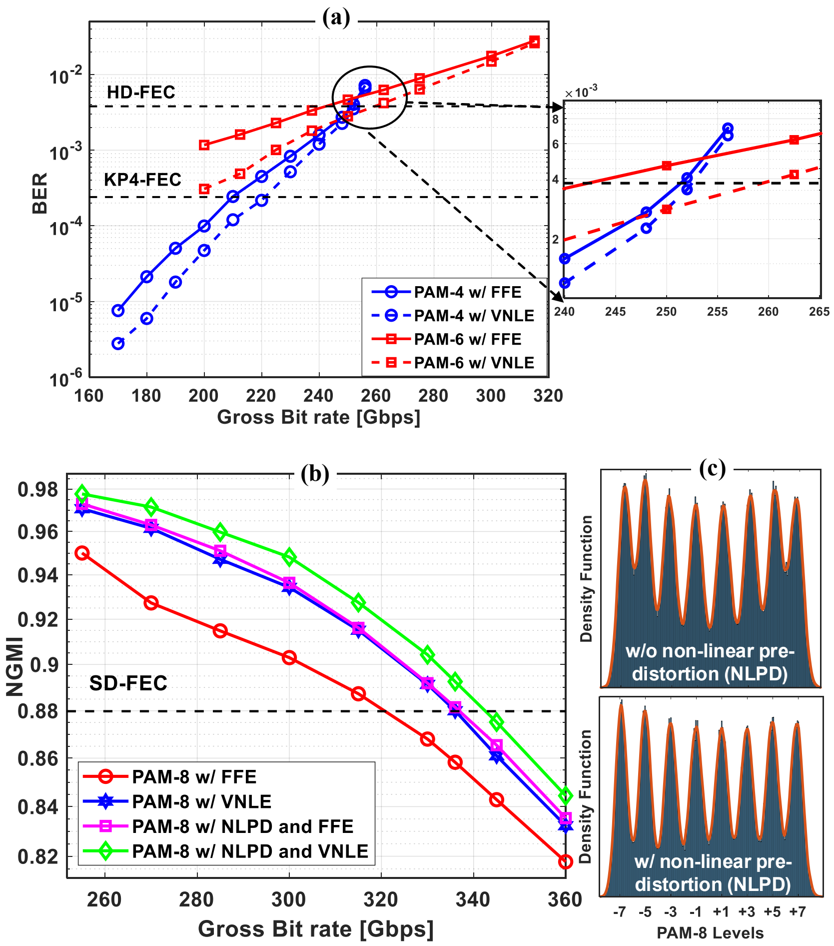

Fig. 3.18 (a) BER and (b) NGMI vs. gross bit rate for different PAM formats, (c) Histogram of the received PAM8 symbols at 100 Gbaud without and with NLPD. (© 2021 IEEE)

3.3.4 Extending Capacity limit with 256 GSa/s AWG

To test the attainable capacity of this SiP MZM, we time-interleave two AWG channels, that allows signal generation at 256 GSa/s sampling rate, and we can generate PAM signals at a symbol rate beyond 128 Gbaud. In Fig. 3.19, we plot the measured BER of 132 Gbaud and 134 Gbaud PAM-4 signals after 2 km transmission as we sweep the number of FFE taps. It can be observed that 51 (101) taps are required to reach the 3.8×10^{-3} BER threshold at 132 (134) Gbaud. As shown, the BER saturates beyond 101 taps, which is sufficient for the considered symbol rates.

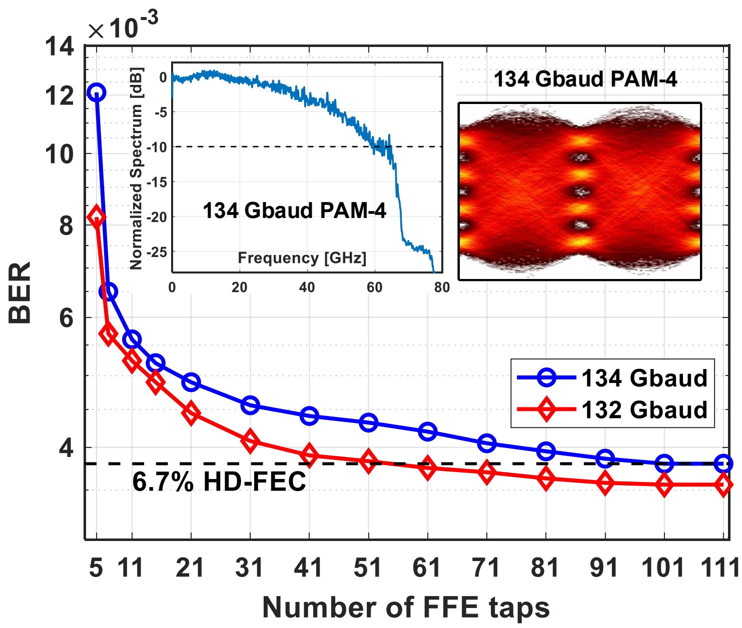

Fig. 3.19 132 Gbaud and 134 Gbaud PAM-4 BER performance vs. number of FFE taps after 2 km of SMF. Inset: Received electrical spectrum and PAM4 eye diagram at 134 Gbaud. (© 2021 IEEE)

In the inset of Fig. 3.19, we show the received electrical spectrum of 134 Gbaud PAM-4 signal and eye diagram after receiver linear FFE with 101 taps. As in the past section, VNLE or NLPD cannot improve the PAM4 BER performance much at these high symbol rates. The received spectrum shows 10 dB loss at 60 GHz, coming primarily from the modulator, which is then compensated by the FFE. However, this boosts the in-band noise at high frequencies, which cannot be compensated by only increasing the number of FFE taps. Therefore, to whiten the noise, we apply a two-tap post filter (Z-domain response: $1+\alpha z^{-1}$, where $\alpha\in[0, 1]$) and subsequently use MLSD to eliminate the post-filter induced ISI. The parameter α is optimized for each symbol rate and at 140 Gbaud, the optimum α is found to be 0.48. With this scheme, we can transmit up to 140 Gbaud PAM-4 signal below the HD-FEC threshold as shown in Fig. 3.20.

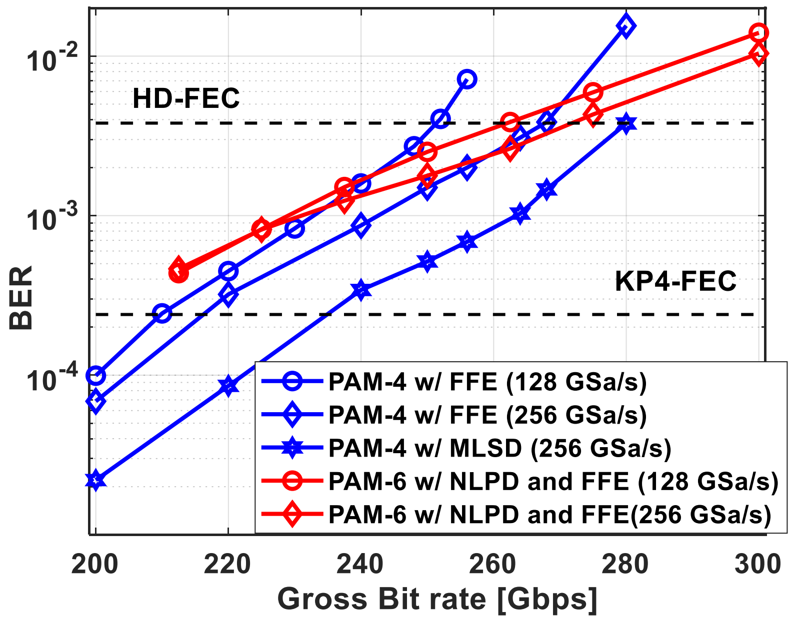

Fig. 3.20 BER vs. gross bit rate for PAM4 and PAM6 formats (128 GSa/s and 256 GSa/s AWG). (© 2021 IEEE)

At a higher AWG sampling rate, high symbol rate signals can be generated with a higher roll-off-factor, which lowers the PAPR of the transmitted signal. Along with the oversampling induced ENoB (Effective Number of Bits) improvement, this increases the signal-to-noise ratio (SNR) of the generated signal and results in better BER performance. Comparing the BER performances at the two different sampling rates, we can also see that the BER improvement increases at higher symbol rates for both PAM4 and PAM6 format when the AWG operates at 256 GSa/s AWG. Even with NLPD, PAM6 still does not show much throughput enhancement compared to PAM4 signaling. We also tested the shorter MZM with phase shifter length of 1.5 mm and >50 GHz 3-dB E-O BW, but the higher V_π results in worse B2B and 2 km transmission performance. Therefore, the inherent trade-off between phase-shifting efficiency and E-O BW must be considered in system design for optimum transmission performance.

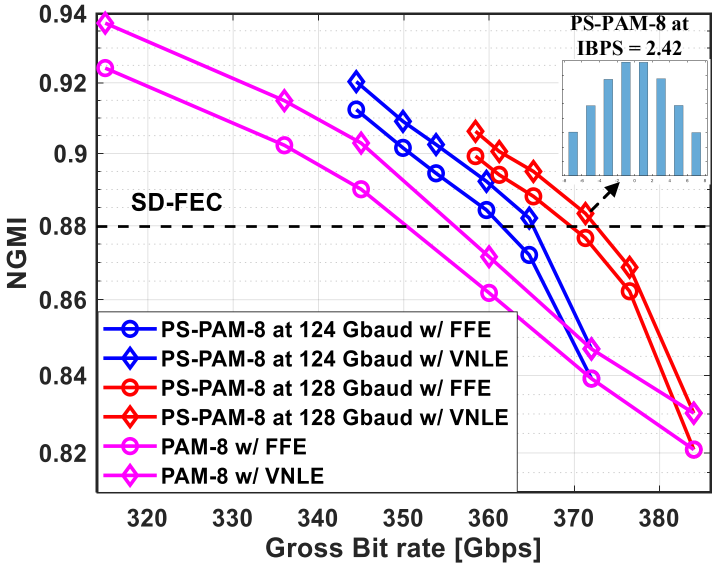

Fig. 3.21 NGMI vs. gross bit rate for PAM8 and PS-PAM8 signals (at 256 GSa/s with NLPD). Inset: Histogram of the transmitted and PS-PAM8 symbols at an IBPS of 2.42 bits/symbol. (© 2021 IEEE)

To maximize the system throughput, PAM-8 and PS-PAM-8 signal transmission with 256 GSa/s AWG is also studied. The results from Fig. 3.21 show that even with SD-FEC, it is not possible to achieve net 300 Gbps (gross bit rate of 358 Gbps) due to the higher SNR and linearity requirement of the PAM8 format. Probabilistic shaping can help in this regard as demonstrated in literature [95, 96]. Unlike previous section, in this section, we generate the PS-PAM symbols following Maxwell-Boltzmann (MB) distribution using constant composition distribution matcher (CCDM) within the probabilistic amplitude shaping (PAS) scheme. CCDM with long block length has negligible entropy loss and enables maximum capacity. Fig. 3.21 plots the NGMI curves at 124 and 128 Gbaud for different information bits per symbol (IBPS). The histogram of the transmitted symbols at an IBPS of 2.42 bits/symbol is also shown in the inset of Fig. 3.21. Compared to uniform PAM8, PS extends the system capacity beyond a net 300 Gbps at both these symbol rates. At 128 Gbaud, with an IBPS of 2.39 (2.42), we can transmit a net 305 (310) Gbps above the specified NGMI threshold of 0.8798 with FFE (VNLE). Increasing the symbol rate beyond 128 Gbaud with PS-PAM8 decreases the NGMI at the same bit rate due to severe ISI coming from the limited system bandwidth. Apart from the shaping gain, in PS scheme, more symbols are transmitted on the inner levels, and therefore become less impacted by the non-linear effect caused by the saturation of RF amplifier and modulator. As a result, going from an IBPS of 2.45 to 2.52 bits/symbol (corresponding to uniform PAM8) significantly reduces the NGMI. We should also note here that due to the use of PDFA, our system is average power limited and the benefit of PS is obvious. For short reach scenario without optical amplifier, PS with MB distribution might not be the optimum choice and the throughput improvement might be different [96].

3.3.5 Summary

The summary of the achieved throughputs with the 128 and 256 GSa/s AWG for different modulation formats is given in Table. 3.3. As is clear from the table, with the 256 GSa/s AWG, we can extend the capacity by 10 to 16 Gbps depending on the chosen modulation format, but it comes at the expense of one extra AWG channel and an interleaver. Therefore, considering the cost and power consumption of the application-specific integrated circuit (ASIC), a single AWG channel running at 128 GSa/s stands out as the suitable solution given the limited bandwidth of our SiP MZM. Compared to Section. 3.2, with PAM8 format, we could extend our capacity to 294 Gbps from 225 Gbps. This primarily comes from the better AWG, RF amplifier and partially from the better photodiode. Due to the SiP MZM being the main limiting factor for higher capacity, it is difficult to push the capacity even with a better AWG or RF amplifier.

Table 3.3 Summary of Net Bit Rate (with FFE and NLPD)

Modulation format	FEC OH	128 GSa/s AWG	256 GSa/s AWG
PAM4	6.7% HD	234	250
PAM6	6.7% HD	245	255
PAM8	19.02% SD	282	294
PS-PAM8	19.02% SD	290	305

Units: Gbps; OH: Overhead; HD: Hard-Decision; SD: Soft-Decision.

3.4 Net 350 Gbps/λ IM/DD Transmission Enabled by High Bandwidth Thin-Film Lithium Niobate MZM

3.4.1 Motivation

As discussed in the introduction of the thesis, simple pulse amplitude modulation (PAM) with moderate digital signal processing (DSP) is the preferred option for DCI applications. Since SiP modulators are limited in terms of BW and phase shifting efficiency, alternate solutions are being pursued actively. In recent years, intensity modulators with electro-optic (EO) bandwidths exceeding 100 GHz [97-99] and transmission rates beyond 300 Gbps have been demonstrated [10, 100-103]. In addition to a high bandwidth (BW), a low optical loss and low half-wave voltage (V_π) are also critical modulator parameters for DCI applications. Thin-film lithium niobate (TFLN) platform has recently emerged as one of the most promising candidates to deliver high-performance modulators fulfilling these three targets simultaneously [104, 105]. Ref. [106] showed 70 Gbaud PAM8 transmission at a BER of 1.5×10^{-2} with a 45 GHz TFLN Mach–Zehnder modulator (MZM) and also proposed a 100 GHz bandwidth design with shorter devices. 110 Gbaud PAM4 modulation was achieved with a 56 GHz BW and 2.6 V V_π TFLN modulator at the same BER threshold in Ref. [107]. These results were limited by the DAC bandwidth more than by the modulator itself. With the availability of 256 GSa/s DAC, 110 Gbaud PAM8 signal transmission over 500 m of standard single-mode fiber (SSMF) with a BER below the 25% SD-FEC threshold of 4×10^{-2} was demonstrated using a 110 GHz 3-dB BW and a high 4.74 V V_π TFLN MZM [108].

To minimize the module power consumption and system latency, the MZM V_π and the DSP complexity should both be minimized. Motivated by these requirements, in this section, we report 132 Gbaud PAM6 data transmission over 500 m of SSMF below the 6.7% OH HD-FEC BER threshold of 3.8×10^{-3} (net 308 Gbps), and 140 Gbaud PAM-8 transmission assuming a 19.02% OH SD-FEC (net 350 Gbps), both with a 1.4 V_{pp} single-ended drive signal. We also demonstrate 144 Gbaud PAM4 transmission with a 1 V_{pp} drive voltage. These results are enabled by a TFLN MZM with a low 1.5 V DC V_π and 95 GHz 6-dB EO BW, and by a 256 GSa/s DAC and ADC. We also characterize our system by comparing PAM-4/6/8 modulation with both linear and non-linear signal processing algorithms. The presented results demonstrate the feasibility of a 300G+ short-reach interconnect solution with TFLN modulators and low driving voltage.

3.4.2 Modulator Device Characteristics and Experimental Setup

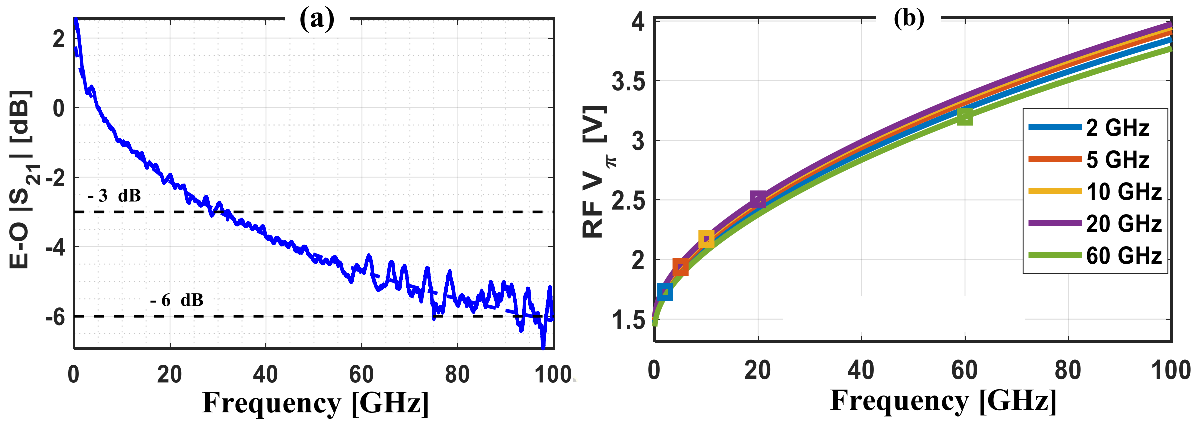

Fig. 3.22 (a) E-O S_{21} response (normalized to 5 GHz) of the TFLN MZM (b) RF V_π measured at different frequencies (with extrapolation). (© 2022 IEEE)

The TFLN traveling wave MZM adopts a typical coplanar waveguide (CPW) configuration and requires a single RF driving signal [106]. The CPW electrode has a length of 18 mm, with an on-chip termination close to 50 Ω. The E-O S_{21} and the RF V_π are plotted in Fig. 3.22. The E-O response shows 30 GHz 3-dB EO bandwidth (BW) and a slow frequency roll-off resulting in a 6-dB BW of 95 GHz (normalized to 5 GHz). The RF V_π is measured at 2, 5, 10, 20 and 60 GHz; and extrapolated in the DC - 100 GHz range for each data point using the E-O S_{21} response [109].

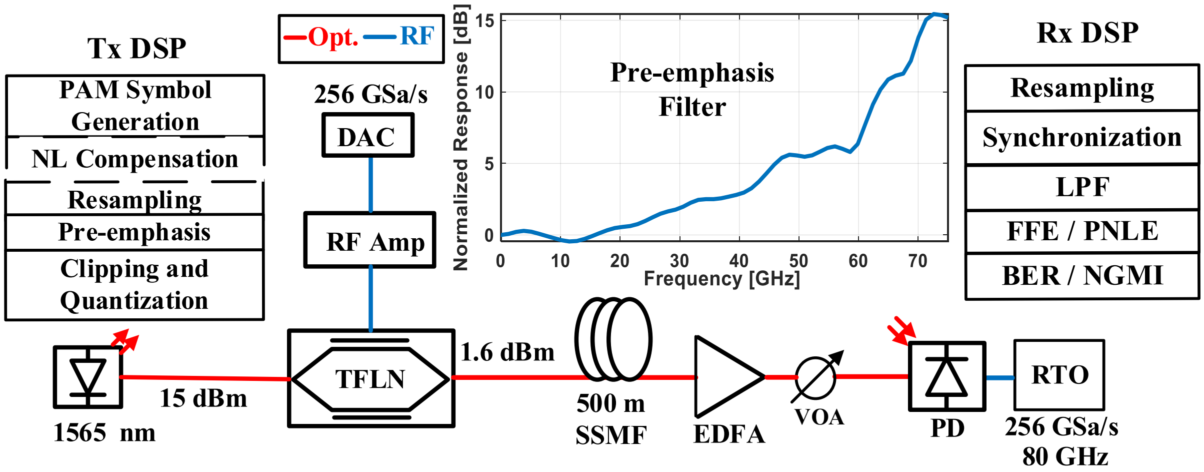

Fig. 3.23 Schematic of the experimental setup and the employed DSP. The inset shows the transmitter pre-emphasis filter frequency response. (© 2022 IEEE)

Fig. 3.23 presents the experimental setup and DSP applied in the transmission experiment. The setup and DSP algorithm are identical to the SiP MZM experiment presented in Section 3.2. Compared to Section 3.2, this is a C-band MZM, therefore we use EDFA and C-band tunable laser source. Like before we couple light into the TFLN MZM through vertical grating couplers with 10 dB back-to-back coupling loss. The operation point of the MZM is controlled by thermal phase shifters and the RF signal is applied through a 67 GHz GSG probe. The transmitter RF chain used in our experiment consists of a 256 GSa/s arbitrary waveform generator (AWG) and one 60 GHz RF amplifier (SHF 804b). PAM symbols with different modulation format are generated from a random sequence and up-sampled to 2 samples per symbol (sps) for raised cosine (RC) pulse shaping. For PAM-6 and PAM-8, non-linear pre-distortion (NLPD) is applied at the transmitter at symbol level using a lookup table (LUT). The 2 sps samples are then re-sampled to the DAC sampling rate and the low-pass response of the AWG, RF amplifier and RF cables is compensated up to 72 GHz by a pre-emphasis filter, as shown in the inset of Fig. 3.23. The samples are then clipped and quantized before being loaded into the DAC memory. The transmitted signal is limited to 144 Gbaud, mostly due to the sharp roll-off of DAC and RF amplifier response beyond 70 GHz. The optical spectra of the modulated signal for different symbol rates are shown in Fig. 3.24, which shows a 5 dB drop in the frequency response at 70 GHz (mostly from the probe and MZM). The signal is then launched into 500 m of SSMF and amplified by an EDFA before being detected with a 70 GHz photodetector (PD). The signal out of the PD is then captured by an RTO operating at 256 GSa/s with an 80 GHz brick-wall filter response. At the receiver, the signal is processed offline with a T/2 spaced linear feedforward equalizer (FFE) or polynomial nonlinear equalizer (PNLE). After equalization, the signal is down-sampled to 1 sps to measure the BER and calculate the NGMI, assuming Gray mapping.

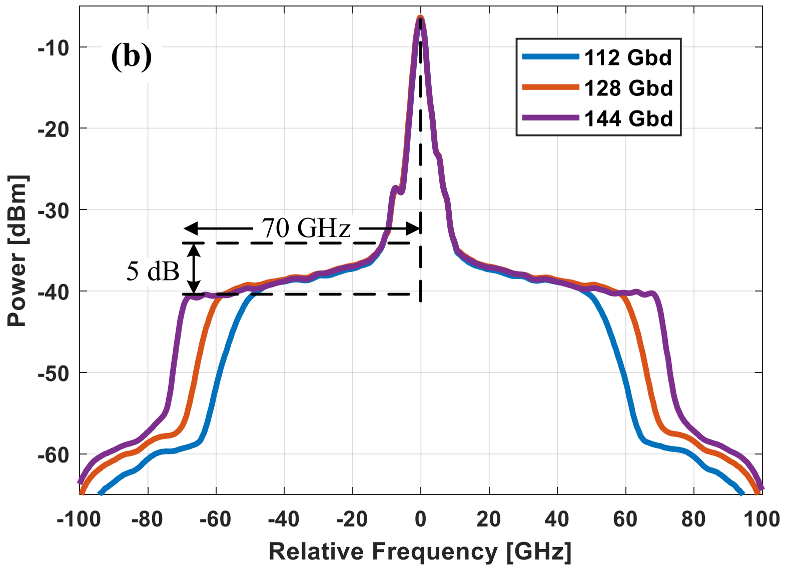

Fig. 3.24 Measured PAM-4 signals optical spectra (at 0.03 nm) at 1.4 V_{pp} drive voltage. (© 2022 IEEE)

3.4.3 Transmission Results

In a first experiment, we transmit PAM-4 signals with 1.0 V_{pp} and 1.4 V_{pp} drive voltages at 128 Gbaud and 144 Gbaud. Fig. 3.25 (a) plots the BER performance as a function of ROP with second order PNLE at the receiver. No non-linear compensation is applied at the transmitter for PAM4 format. At high ROP, the transmission performance is very similar for both driver swings, indicating that >1 V_{pp} is not necessary. Transmission performance only differs at lower ROP, where the ADC noise dominates due to very low received signal RMS level. At the KP4-FEC BER threshold of 2.4×10^{-4}, the 128 Gbaud B2B received signal with 1V_{pp} driving signal shows only a 0.5 dB ROP penalty compared to the 1.4 V_{pp} case. For the 144 Gbaud signal at the HD-FEC BER threshold of 3.8×10^{-3}, this increases to ~1.2 dB. We do not employ any optical dispersion compensation in our experiment. Therefore, 500 m transmission (~8-9 ps/nm dispersion) adds a 2.5 dB penalty due to the chromatic dispersion (CD) induced power fading, which is clear from the received RF spectrum shown in Fig. 3.25 (b). The fading causes ~6 dB drop in frequency response at 70 GHz, which requires adopting a higher number of filter taps. From the BER vs. number of linear taps sensitivity curves, plotted in the inset of Fig. 3.25 (b), 15 (43) taps are required to reach the HD-FEC BER threshold for the B2B (500 m) case, which corresponds to net 270 Gbps transmission assuming 6.7% OH HD-FEC. We also sweep the driver peak-to-peak voltage at 144 Gbaud PAM4 for a fixed ROP of 7 dBm. Fig. 3.26 (a) shows that a 1 V_{pp} drive signal (225 mV RMS) is enough to get to the BER floor, and further increasing it does not improve the result. This is observed with both linear and non-linear equalization. This demonstrates the promise of TFLN modulators to operate driver-free, which would reduce the module power consumption significantly.

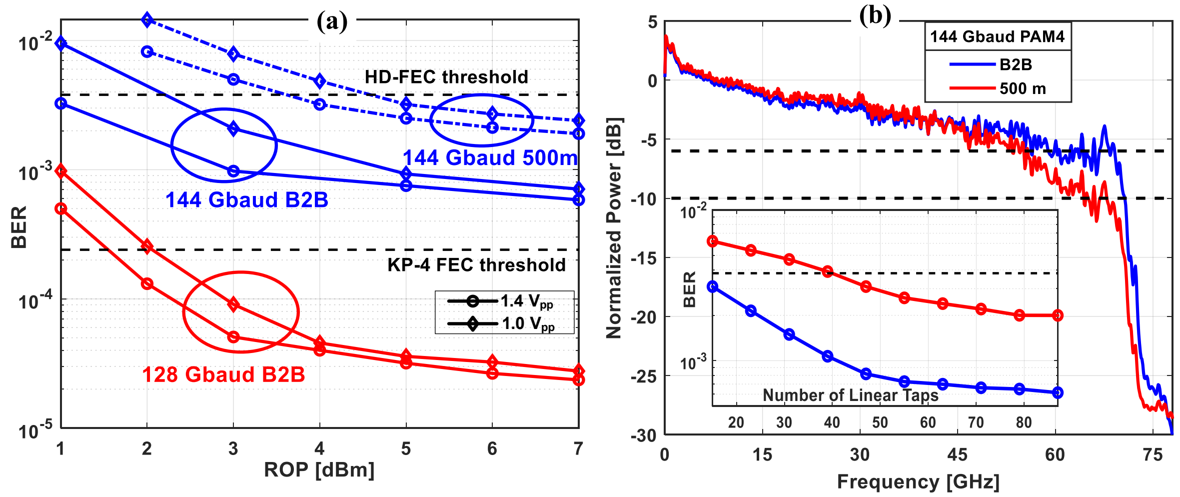

Fig. 3.25 (a) BER vs. ROP for 128 Gbaud and 144 Gbaud PAM-4 signal with 1.0 V_{pp} and 1.4 V_{pp} drive voltages at B2B and after 500 m transmission, (b) Received RF spectrum (144 Gbaud PAM-4) captured from RTO (ROP: 7 dBm). Inset: BER vs. number of FFE taps. (© 2022 IEEE)

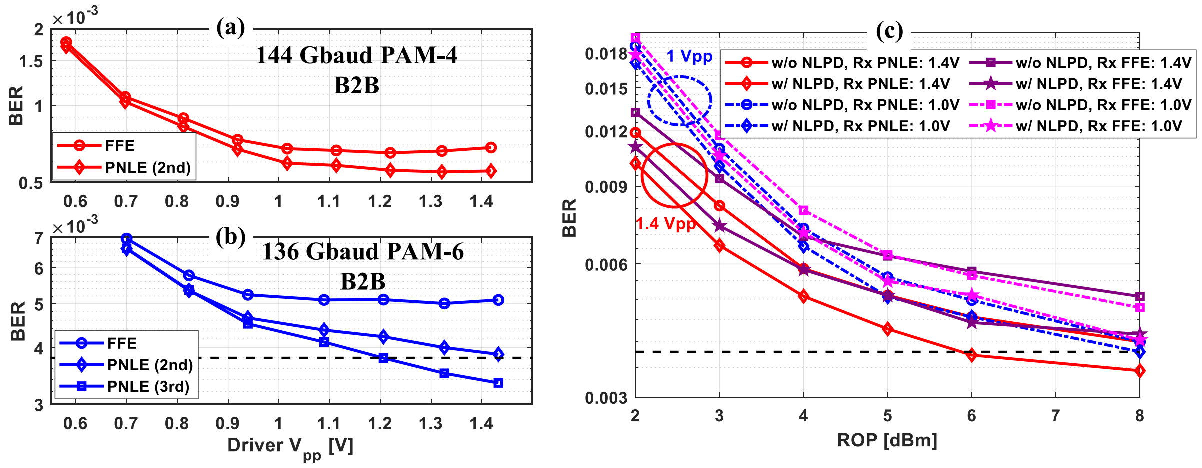

Fig. 3.26 (a)-(b) BER vs. driver voltages at B2B (ROP: 7 dBm). (c) BER vs. ROP for 132 Gbaud PAM-6 signal after 500 m transmission (with and without non-linear pre-distortion). (© 2022 IEEE)

Now, to increase the system capacity, we transmit PAM-6 signals, which increases the net rate by 25% at the same symbol rate. In Fig. 3.26 (b), we test the driver requirement for 136 Gbaud PAM-6 signal. In this case, at B2B, with only linear equalization, 1 V_{pp} driving signal gets us to the BER floor. But non-linear equalization keeps on improving the BER performance with higher drive voltages. This means that with only linear FFE, the performance improvement due to a higher driver swing and extinction ratio (ER) is offset by the system non-linearity, and higher order PNLE can bring down the BER floor. For all the three curves in Fig. 3.26 (b), 71 linear taps are used. For higher order PNLE, 11 second order and 3 third order beating terms are utilized. Considering the complexity of third order non-linear equalizer, we keep ourselves limited to 2nd order PNLE with a maximum of 11 beating terms for the reminder of the work.

As shown in Fig. 3.26 (b), with only 2nd order PNLE at the receiver, we can barely reach the HD-FEC threshold at B2B. This degrades further after transmission and BER below the HD-FEC threshold is not achievable. Therefore, we also employ non-linear pre-distortion (NLPD) based on a LUT at the transmitter side. In Fig. 3.26 (c), we test the different DSP schemes for 132 Gbaud PAM-6 after 500 m for the two driver voltages. Transmitter side NLPD and receiver PNLE with a 1.4 V_{pp} drive voltage shows the best performance, the HD-FEC BER threshold being reached at 6 dBm ROP. Interestingly, at a higher ROP (8 dBm), a 1 V_{pp} driving signal can also get us to the BER threshold. Akin to the PAM-4 case, at low ROP, higher driving signal helps but the BER differences become less pronounced at higher ROP. We can also find that the curves with NLPD and receiver FFE almost coincide with receiver PNLE curves with no pre-compensation. Given the complexity of PNLE (and VNLE in general), the former combination could be an attractive choice for the next generation high speed IM/DD transceivers. Next, to evaluate the BER penalty coming from the CD induced fading, we plot the BER vs. ROP for two different symbol rates in Fig. 3.27 (a). 132 Gbaud PAM-6 shows a 3.3 dB penalty at 500m vs. the B2B case. For 128 Gbaud this is found to be around 2.2 dB (not shown here). 144 Gbaud BER curves are well above the adopted HD-FEC threshold but reach a BER below 1.5×10^{-2} at a high ROP after 500 m transmission.

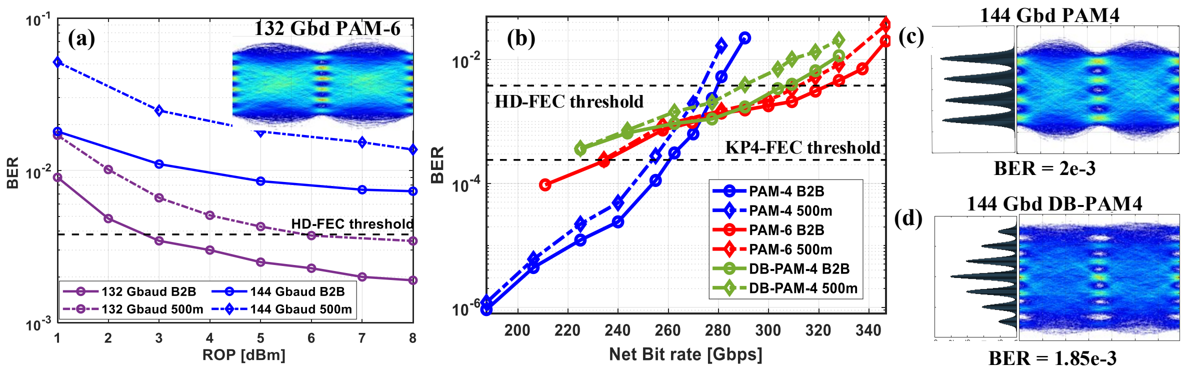

Fig. 3.27 (a) BER vs. ROP for 132 Gbaud and 144 Gbaud PAM-6 signal (with NLPD and PNLE). (b) BER vs. net bit rate assuming 6.7% OH HD-FEC BER threshold (ROP: 7 dBm with receiver PNLE). (c)-(d) Eye-diagram of processed eye along with symbol histogram at 144 Gbaud after 500m. (© 2022 IEEE)

Next, Fig. 3.27 (b) presents the BER vs. net bit rate assuming a 6.7% OH HD-FEC, for PAM4, DB-PAM4 and PAM6 format. An additional DB pre-coding and encoding is required for DB signaling. We use both NLPD and PNLE for DB-PAM4 and PAM-6 and only PNLE for PAM4 case (optimal performance). DB-PAM4 is attractive because of its lower BW requirement. However, the downside is that it creates 7-level signaling, which requires stronger SNR, and suffers from non-linearity (Fig. 3.27 (d)). Therefore, at B2B, where the transmitter is the main BW limiting factor, DB-PAM4 outperforms PAM4 format by a good margin but the difference decreases after transmission. We could transmit 162 (155) Gbaud DB-PAM4 as compared to

148 (144) Gbaud PAM4 at B2B (500 m transmission). Fig. 3.27 (b) shows that for our setup, beyond 265 Gbps, PAM6 outperforms PAM4 format, and we can transmit net 318 Gbps (136 Gbaud PAM6) at B2B and net 308 Gbps (132 Gbaud PAM6) over 500 m. At a lower overhead KP4-FEC BER threshold, PAM4 is the optimum format, and net 250 Gbps (132 Gbaud PAM-4) is also achievable. We can see that beyond 140 Gbaud (net 262 Gbps PAM4 and net 330 Gbps PAM6), the BER deteriorates rapidly, and this is due to the degradation of generated driving RF signal. The figure also demonstrates that with the current generation of DACs and drivers, PAM6 is the format to choose for net 300G IM/DD.

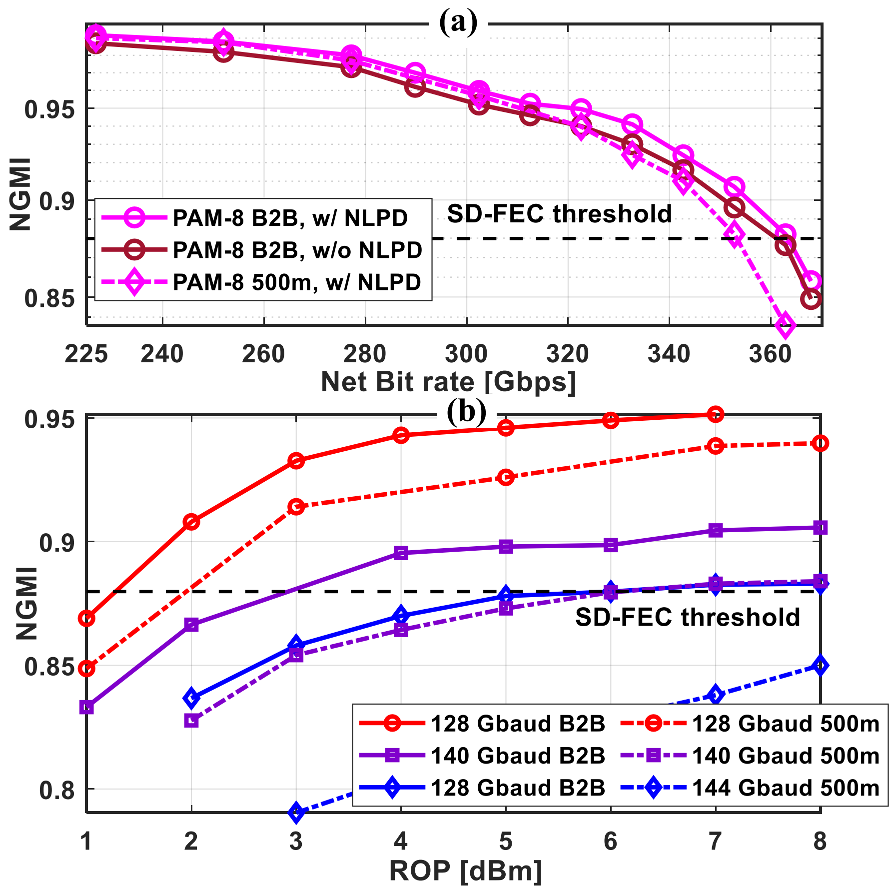

Fig. 3.28 (a) NGMI vs. net bit rate at B2B and after 500 m transmission assuming 19.02% OH SD-FEC (ROP: 7 dBm), (b) NGMI vs. ROP for 128 Gbaud, 140 Gbaud and 144 Gbaud PAM-8 format. (© 2022 IEEE)

Finally, to assess the maximum achievable throughput with our TFLN modulator, we test the MZM with PAM8 format at different symbol rates from 90 Gbaud to 146 Gbaud. Since better extinction ratio is required for PAM8 signal, we drive the MZM with 1.4 V_{pp} (~300 mV RMS) and use 2nd order PNLE at the receiver to compensate for the nonlinearity. Fig. 3.28 (a)-(b) show that we can transmit net 360 (350) Gbps at 144 (140) Gbaud at B2B (500 m) with our high bandwidth modulator. At lower symbol rates, the effect of power fading is small, and we achieve similar NGMI values at both B2B and after 500m. The NGMI gap increases with symbol rate as the power fading gets severe. Stronger DSP, like maximum likelihood sequence detection (MLSD) could further improve the overall performance but is not well suited in practice for short links given the stringent power constraints.

3.4.4 Summary

In this section, we presented transmission results with a 95 GHz 6-dB EO BW and 1.5 V V_π TFLN MZM in the C-band. With a 1.4 V_{pp} drive signal (275 mV RMS) we transmitted net 308 Gbps (132 Gbaud) PAM6 signal over 500 m of SSMF (~ 8-9 ps/nm dispersion) below the 6.7% HD-FEC BER threshold of 3.8×10^{-3}. 144 Gbaud PAM-4 was also achieved with a 1 V_{pp} drive signal (225 mV RMS) below this BER threshold. Adopting 19.02% OH SD-FEC, we could further extend the system capacity to net 350 Gbps (140 Gbaud) with PAM-8 signaling. These are the highest reported PAM transmission rates using a TFLN modulator. We expect similar BW and V_π performance with the O-band MZM design, which are preferred for short reach due to much lower dispersion values and longer transmission reach will be achievable. Our results demonstrate the suitability of the TFLN modulator platform for single lane 250, and 300+ Gbps intra-data center applications.

To conclude the chapter, in Table 3.4, we present a summary of recent high-speed demonstrations in IM/DD system with SiP, TFLN and other modulator materials highlighting the significance of the results presented in this chapter. Results of Ref [13] and Ref [18] are included in this chapter and Ref [112] is an extension of the TFLN work with a next generation DAC.

Table 3.4 State-of-the-art single-polarization single-wavelength demonstrations in IM/DD system

Year [Reference]	Transmitter	Symbol Rate (Gbaud)	Net rate (Gbps)	FEC OH	Driver and DSP
2021 [18]	SiP MZM	128	310	19.04%	Single drive (Linear FFE)
2023 [110]	SiP MRM	110	275	20%	Single drive (PNLE)
2023 [111]	SiP MZM	150	282	6.25%	Single drive (FFE+DFE)
2022 [13]	TFLN MZM	132 140	310 350	6.7% 19.04%	Single drive (PNLE)
2023 [112]	TFLN MZM	172 180	400 450	6.7% 20%	Single DAC driveless (PNLE)
2023 [113]	EML	160	376	6.25%	Single drive (FFE+DFE)
2021 [101]	EML	134	348	15.31%	Single drive (VNLE+DFE)
2022 [114]	$LiNbO_3$ MZM	100	300	27%	Single drive (PNLE)
2019 [103]	InP	162	420	27%	2Ch AMUX DAC (NLPD+FFE)
2022 [52]	Plasmonic MZM	143.7	36.4	19%	Single drive (VNLE+DFE)

Chapter 4 Reach Extension for C-band IM/DD Transmission enabled by Optical Filtering

4.1 Overview

In chapter 3, we demonstrated high-capacity transmission with SiP and TFLN modulators for DCI applications. But the transmission reach was limited in this case. For C-band, we limited ourselves to 500 m and for O-band it was 10 km. 4 channel parallel single mode (PSM) and CWDM transmission for 100 Gbps+ transmission mostly uses O-band due to lower dispersion. C-band operation is important for full duplex bidirectional transmission systems and WDM passive optical networks (PON). In order to allow link capacities of several Tbps, dense wavelength division multiplexing (DWDM) is necessary, which also requires the system to work in the 1550 nm transmission window [115]. But the operation at 1550 nm is challenged by strong chromatic dispersion (CD) as mentioned several times in the previous sections. In this chapter, we focus on optical domain solutions to extend the transmission reach in C-band.

To tackle the CD induced power fading in IM/DD system, either dispersion compensating fiber (DCF), or an optical dispersion compensation module (ODCM), or optical filter becomes necessary for high symbol rate transmission. In section 4.2, we report the characterization and transmission performance of a SiN optical dispersion compensator for 10 km transmission. The designed all-pass ring resonator-based dispersion compensator shows an FSR of 100 GHz (0.8 nm), which can be used in DWDM application. The ODC is utilized in an MZM based dual pole IM/DD system with Stokes Vector Receiver (SVR) to enable the transmission of 60 Gbaud PAM4 signal over 10 km of SSMF in the C-band.

In section 4.3 and 4.4, we focus on C-band DML transmission. DML is an attractive choice for next generation DCI application for its power efficiency and simple structure. However, the inherent chirp and non-linear behavior makes it difficult to predict the BER performance of DML/DD system over a range of propagation distance. In section 4.3, we present a detailed simulation of PAM4 BER performance with DML. We try to analyze the impact of transient and adiabatic chirp over positive and negative dispersion regime and determine their impact. We also characterize a commercial DML and show strong agreement between simulation and experimental results. Next, in section 4.3, we try to improve DML performance with the aid of an optical filter, which is most commonly known as chirp managed laser. We propose a semi-analytical approach to identify the optimal filter profile and its offset with respect to the DML signal spectrum. This can be applicable for any DMLs with different laser parameters, as well as various modulation formats to achieve a desired ER. We present a detailed simulation study of the proposed method for both OOK and PAM4 format, with a particular emphasis on PAM4 signaling for higher throughput. Finally, we test the impact of optical filtering and DSP algorithm in a 35 Gbaud PAM4 transmission system with a 17 GHz directly modulated DFB laser.

4.2 224 Gbps C-band Transmission over 10 km enabled by a SiN Optical Dispersion Compensator

4.2.1 Motivation

To achieve higher spectral efficiency, polarization multiplexed signaling is important and the Stokes vector receiver (SVR) can enable dual-polarization (DP) IM signal detection with simple digital signal processing (DSP). The DSP can recover the transmitted Stokes vector through linear multiple-input multiple-output (MIMO) equalization to invert the polarization [116, 117]. In this section, we present the use of an integrated optical dispersion compensator (ODC) in a high symbol rate polarization-division-multiplexed (PDM) direct detect system, that enables 224 Gbps net rate transmission over 10 km of SSMF in the C-band at a BER below the 6.7% overhead HD-FEC threshold of 3.8×10^{-3}.

4.2.2 Optical Dispersion Compensator based transmission setup

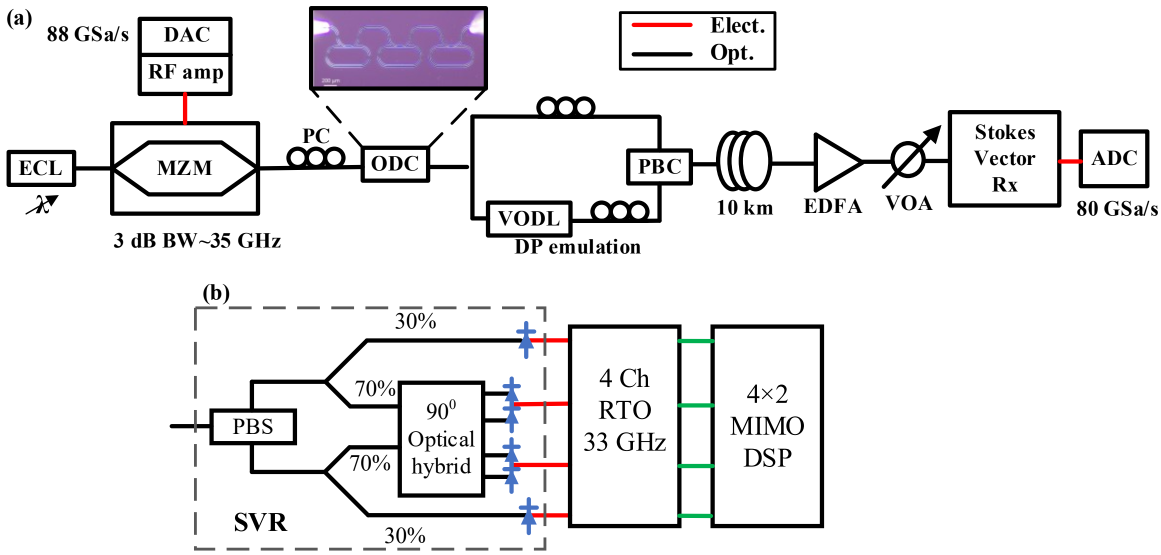

Fig. 4.1 (a) Experimental setup, (b) Structure of SVR (© Optica Publishing Group)

Figure 4.1 (a) shows the experimental setup. At the transmitter (Tx), a tunable laser operating at 1550 nm and a 35 GHz $LiNbO_3$ intensity modulator is used. The modulator is driven by an amplified RF signal. As in the previous chapter, the Tx side DSP includes PAM4 symbol generation, pulse shaping via a raised cosine (RC) filter, pre-emphasis of the RF chain, nonlinear pre-compensation of the modulator, clipping and resampling to the DAC sampling. Here we use an older generation of DAC, that runs at 88 GSa/s. After the modulator, the ODC is used for CD pre-compensation. The ODC is fabricated on a Silicon Nitride platform and is composed of three cascaded all-pass microring resonators to compensate for a total group delay of 68 ps [118, 119]. This value corresponds to the total group delay introduced by 10 km of SSMF (170 ps/nm CD) with a constant dispersion passband of 50 GHz (0.4 nm). The total footprint of the device is 2.2×0.56 mm^2. As the ODC is polarization sensitive, it is used before dual-polarization emulation.

The DP signal is then launched into 10 km of SMF and then amplified before entering the Stokes vector receiver (SVR). Figure. 4.1(b) depicts the SVR implementation as reported in multiple works [116]. It comprises a polarization beam splitter (PBS), two 70/30 power splitters and a 90° optical hybrid followed by two balanced and two single ended photodetectors. The output photocurrents are then digitized using a 4-channel 80 GSa/s RTO with 33 GHz bandwidth (BW) and fed to subsequent DSP that recovers the transmitted X-pol and Y-pol intensity through linear 4×2 MIMO filtering to invert the polarization rotation that occurred along the fiber. The principle of SVR and required DSP processing have been discussed in greater detail in section 2.4.

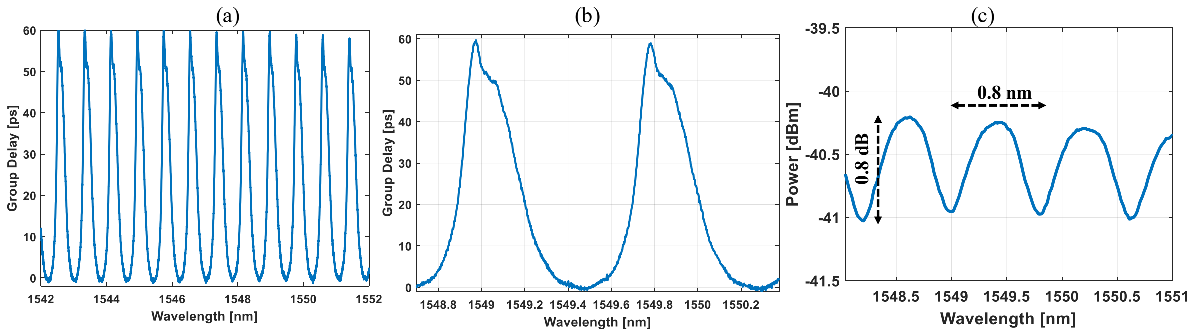

Fig. 4.2 (a) Group delay response (b) Group delay for only channels (c) Optical spectrum of the ODC.

4.2.3 Experimental Results

At first, we try to characterize the ODC. Fig. 4.2 (a) plots the group delay response of the fabricated ODC measured by an optical vector network analyzer (OVNA). From Fig. 4.2 (a) and Fig. 4.2(b), we can see that the ODC exhibits a maximum group delay (GD) of 62 ps and is very similar over the wavelength range. The group delay is slightly lower than the targeted GD of 68 ps. The ring resonators of the ODC were designed with a target free-spectral range (FSR) of 100 GHz (0.8 nm). Fig 4.2 (c) plots the optical frequency response of the ODC, which shows that the magnitude response is flat within 0.8 dB with an FSR of 0.8 nm.

Fig. 4.3 (a) shows the transmission results with the designed ODC. Here, single polarization (SP) PAM4 results are obtained by disconnecting one branch of the emulator. As can be seen from the blue (SP) and black (DP) curves, 65 Gbaud PAM4 signaling is achievable below HD-FEC threshold in B2B. This limit is mainly due to the low pass responses of the system components and the 33 GHz brick wall RTO BW. Due to power fading, this high symbol rate signal cannot be transmitted over 10 km without CD compensation. The red curve in Fig. 2(a) shows that the fabricated ODC enables 60 Gbaud (240 Gbit/s) and 50 Gbaud (200 Gbit/s) PDM

PAM4 signal transmission over 10 km at a BER below the HD-FEC threshold of 3.8×10^{-3} and KP4-FEC threshold of 2.4×10^{-4} respectively. These results are obtained when 39 MIMO filter taps are used to de-rotate the polarization and mitigate the residual ISI.

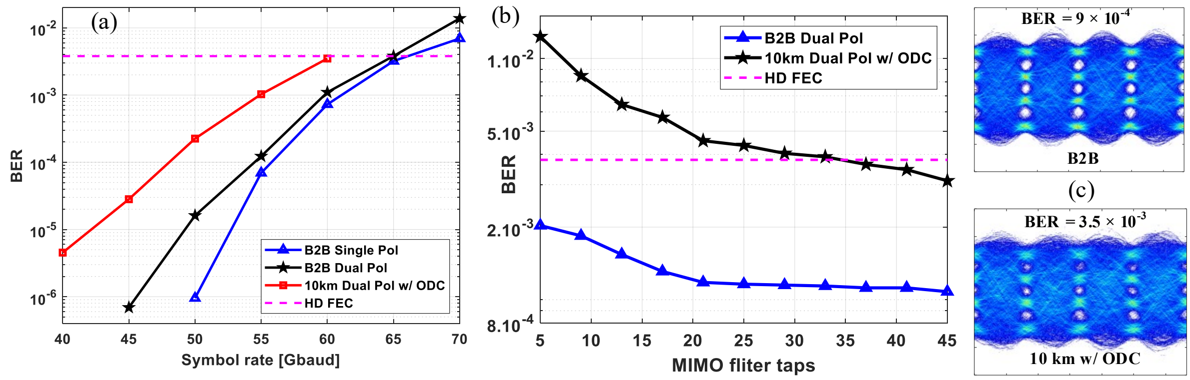

Fig. 4.3 (a) BER vs. symbol rate for PAM4 signal (b) BER vs. MIMO filter taps for 60 Gbaud PDM PAM4 signal (c) Eye diagrams at 60 Gbaud (only one polarization is shown) (© Optica Publishing Group).

Fig. 4.3 (b) shows the BER dependence as the number of taps of the receiver filter is varied for the 60 Gbaud signal. A minimum of 37 taps are required to get a BER below the HD-FEC threshold and the eye diagrams of the received signal are shown in Fig. 4.3 (c). It is seen that, despite using the ODC, after 10 km transmission, some residual dispersion exits, and this results in more errors between the top two levels degrading the BER.

4.2.4 Summary

Successful transmission of 60 Gbaud PDM PAM4 signaling (net 224-Gbps/λ) below the HD-FEC threshold of 3.8×10^{-3} over 10 km in the C-band is demonstrated in this work. An all pass microring resonator based ODC and a Stokes vector receiver (SVR) enabled this transmission reach. This reach can be farther extended by cascading multiple ODC blocks on the same photonic circuit.

4.3 DML based PAM4 Signal Transmission

4.3.1 Motivation

As mentioned previously, directly modulated lasers (DMLs) are a cost-effective, compact and low-power transceiver solution for the next generation high data rate optical access systems, including passive optical networks (PON), 5G wireless networks, and dense wavelength-division multiplexing (DWDM). Compared to externally modulated lasers, DMLs provide higher output power with lower power consumption for long-range transmission reach without the need for optical amplification. However, the limited electro-optic bandwidth of a DML restricts its capacity to achieve higher transmission speed using on-off keying (OOK). To improve the throughput, 4-level pulse amplitude modulation (PAM4) is employed [120]. Several recent reports demonstrate up to 100 Gbps PAM4 transmission in the O-band [121-125], and ongoing efforts are being made to improve DML bandwidths (BW) [125-127]. Despite these advances, the inherent frequency chirp of a DML is a significant limiting factor that restricts its transmission reach and speed in the presence of fiber dispersion (C-band) in DML/DD systems. The development of C-band DML/DD systems is necessary for the 1.3/1.55-µm full duplex bidirectional transmission systems and WDM passive optical networks (PON) [128]. Lower optical loss (0.18 dB/km) and mature device technology of C-band components also demand investigation of C-band DML transmission. Due to higher chromatic dispersion (CD) in the C-band, its speed is limited to lower rates [129-132] and digital signal processing (DSP) becomes necessary to compensate for waveform distortions [133-135], increasing the system complexity and power consumption.

Most of the research into directly modulated distributed feedback (DFB) lasers or vertical-cavity surface-emitting lasers (VCSELs) focuses on either improving the device response or developing better digital signal processing (DSP) algorithms capable of high-speed operation. Nevertheless, predicting the BER performance of these systems over long dispersion ranges is challenging due to the nonlinear response and complex interaction between laser chirp and fiber dispersion [136, 137]. In prior studies, the transmission performance of OOK and PAM4 signaling in the C-band for directly modulated DFB lasers and VCSELs [129, 131, 138-140] has been investigated. However, the mutual dependency of the chirp, overshoot, and laser bandwidth renders it difficult to obtain generalizable receiver sensitivity curves in cases where a specific DML is employed [129, 138] or where a nonlinear laser rate equation models the DML [139, 140]. In order to obtain such generalized results, it is important to de-couple the effects of chirp from overshoot and laser bandwidth.

To that end, this study utilizes the established frequency chirp equation and small signal system response to evaluate DML transmission performance over both anomalous and normal dispersion regimes. This is done while implementing the PAM4 format. Unlike a chirp-free transmitter, the BER of such a system does not increase monotonically with increasing fiber dispersion; rather, there is a noticeable BER improvement in particular chromatic dispersion (CD) ranges, which depends on DML's transient and adiabatic chirp parameters, output average power, and the considered symbol rate. Furthermore, we demonstrate a strong agreement between simulation and experimental results. Since, optical filtering has been shown to improve the performance of DML via proper chirp management [43, 128, 141-144], we also incorporate an optical filter in our transmission system and test its effect. Finally, we transmit a 16.5 Gbaud PAM4 signal over -10 km to +20 km of single-mode fiber (510 ps/nm dispersion range) without any DSP below the 3.8e-3 hard-decision (HD) forward-error-correction (FEC) BER threshold, using a Super Gaussian (SG) optical filter.

4.3.2 Simulation study of PAM4 signaling in a DML/DD system

4.3.2.1 Small signal frequency response and baseband simulation

The frequency response of the dispersive SMF fiber in an intensity modulation/direct detection (IM/DD) transmission system can be approximated as [41, 145, 146]:

$$H_{IM\leftrightarrow DD}(f,L) = \left|\cos\big(\theta(f,L)\big) - \sin\big(\theta(f,L)\big).H_{IM\leftrightarrow PM}(f,L)\right| \tag{4.1}$$

Here, $H_{IM\leftrightarrow PM}(f,L)$ is the complex small-signal transfer function between phase and intensity modulation in the light source characterizing its chirp; $\theta(f,L)$ is the phase variation induced by CD and is expressed as $\theta(f,L) = -2\pi^2\beta_2 f^2 L$; where β_2 is the dispersion parameter with a typical value of −21.66 ps^2/km at 1550 nm, and L is the fiber transmission reach. In the case of a DML based transmitter, the interaction between phase and intensity modulation in a laser is described using laser rate equations. Assuming the optical filed of the DML output $E_{DML}(t) = \sqrt{P_{DML}(t)}\, e^{i\varphi_{DML}(t)}$, the frequency chirp, $\delta f_{DML}(t)$ is shown to be [127]:

$$\delta f_{DML}(t) = \frac{1}{2\pi}\frac{d\varphi_{DML}(t)}{dt} = \frac{\alpha}{4\pi}\left(\frac{1}{P_{DML}(t)}\frac{dP_{DML}(t)}{dt} + \kappa P_{DML}(t)\right) \tag{4.2}$$

where α is the linewidth enhancement factor (LEF) and κ the adiabatic chirp coefficient and $P_{DML}(t)$ is the output optical power. And $H_{IM\leftrightarrow PM}(f,L)$ can be expressed as [41]:

$$H_{IM\leftrightarrow PM}(f,L) = \alpha\left(1 - \frac{j\kappa P_{avg}}{2\pi f}\right)$$

And the final frequency response can be simplified as:

$$H_{IM\leftrightarrow DD}(f,L) = \sqrt{1+\alpha^2}\cos(\theta + \tan^{-1}\alpha) + j\frac{\kappa P_{avg}}{2\pi f}\sin\theta \tag{4.3}$$

The theoretical small signal transfer function has been shown to closely match with the experimental frequency responses [129] and therefore we start by looking at this channel response for different amounts of dispersion assuming $\alpha = 4$, $\kappa = 5.25\, GHz/mW$ and $P_{avg} = 14\, mW$. These values fit the parameters of commercially available DML already available in our lab. Here, by negative values of L, we denote negative cumulative dispersion, which can be achieved by negative dispersion fiber (NDF) or dispersion compensating fiber (DCF) and is also important for O-band transmission.

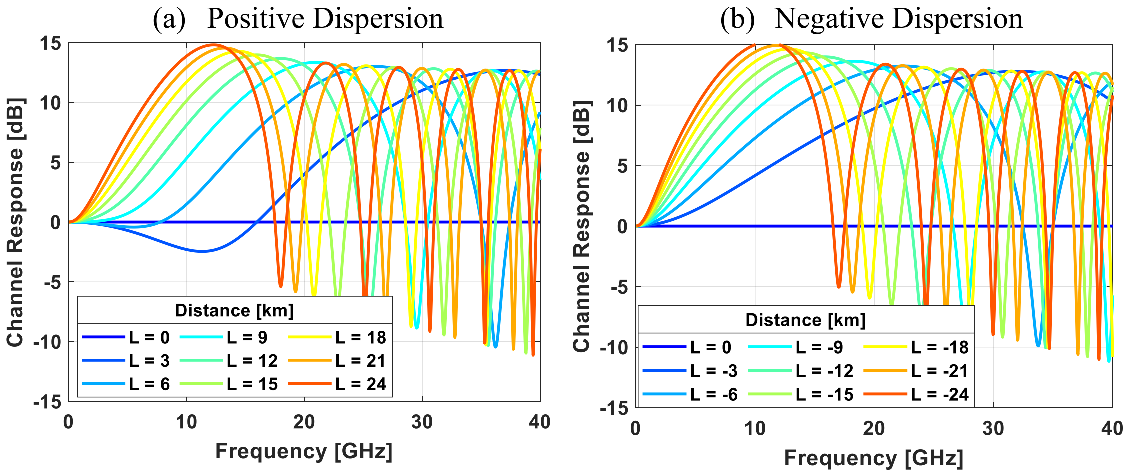

Fig. 4.4 Frequency responses of fiber channel (SMF) in a DML/DD system induced by adiabatic and transient chirp after (a) positive distance and (b) negative distance.

Fig. 4.4 illustrates the frequency response of the channel as a function of the transmission distance. The observed response is influenced by the interplay between the transient and adiabatic chirps and fiber dispersion. For the positive dispersion case, at short distances (say 3 km), in the low frequency region, the response mimics that of a low-pass filter (LPF). Then it shows a rising trend over a frequency range followed by multiple notches at higher frequencies. It is the transient chirp that acts as a LPF (cosine term) whereas the adiabatic chirp exhibits a high pass filtering (HPF) response (sine term) and as the transmission distance increases, due to the combined effect of both chirps, the frequency response shows band pass effects in the low frequency region and multiple notches at higher frequencies. However, in the negative dispersion region, the rising trend is present from the beginning due to positive α value, making the sign of the second term in Eq. 4.1 positive.

Next, assuming an ideal transmitter (i.e., no low pass response from signal generator), we investigate the impact of the dispersive channel due to chirp alone, resulting in some interesting observations. We generate a baseband PAM4 signal, and after adding white Gaussian noise, we analyze the BER and eye diagrams of the filtered signal. We simulate 2^{18} symbols with 16 samples per symbol period (sps) and BER bathtub curve is used to find the best sampling point. The small signal response in Fig. 4.4 is used to filter the signal, and we vary the LEF

(α), adiabatic chirp factor (κ) and P_{avg} while keeping the symbol rate fixed at 16.5 Gbaud, as shown in Fig. 4.5 (a-c). At the receiver, we employ a 4th order Bessel receiver with a 3-dB bandwidth of 75% of symbol rate (B) to filter the noise.

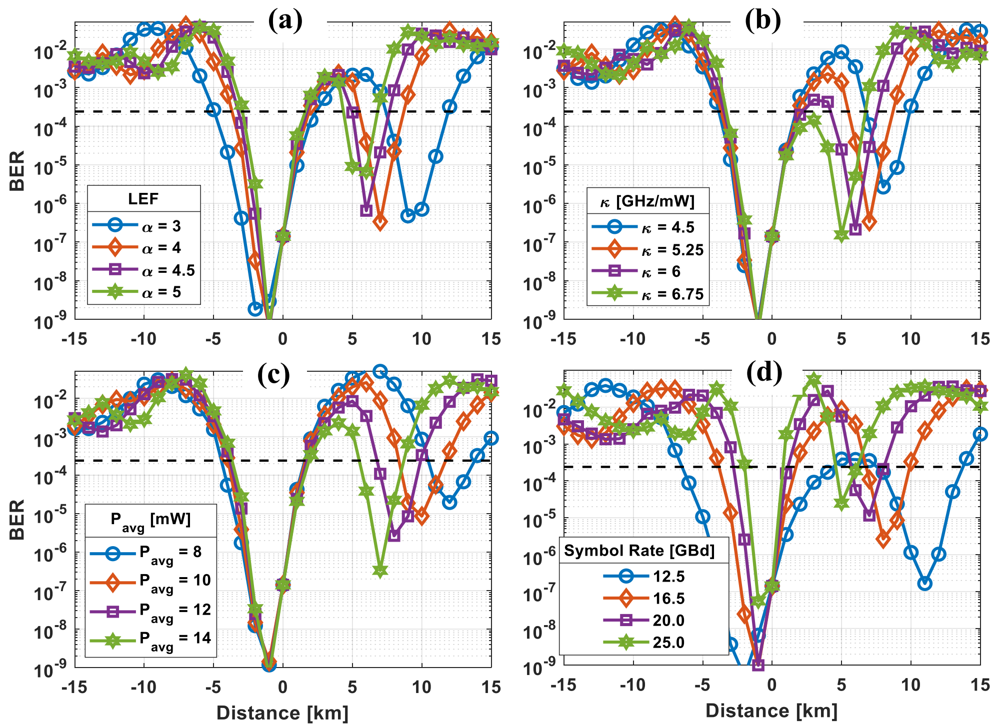

Fig. 4.5 Effect of chirp-CD interaction for different transmission distances (a) B = 16.5 Gbaud, κ = 5.25 GHz/mW, Pavg = 14 mW, and various α values (b) B = 16.5 Gbaud, $\alpha = 4$, Pavg = 14 mW and various κ values, (c) B = 16.5 Gbaud, $\alpha = 4$, $\kappa = 5.25\ GHz/mW$ and different average power, (d) $\alpha = 4$, $\kappa = 5.25\ GHz/mW$, Pavg = 14 mW for different symbol rates.

In the positive dispersion region, from Fig. 4.5, we can see that the BER degrades drastically as the total accumulated dispersion (CD) increases until a certain transmission distance and then suddenly starts improving and subsequently starts becoming worse again. The distance where it starts improving depends on the chirp parameter, symbol rate, average output power and is proportional to $\frac{T}{\alpha k P_{avg}}$, where T is the symbol duration. On the negative dispersion region, the BER improves initially and then keeps on degrading due to the high pass channel response. It also shows a slight trend of improvement for a short range but much less than the positive CD region.

To better understand this behavior, we observe the eye diagrams after several distances for $\alpha = 4,\ \kappa = 5.25\ GHz/mW$ and $P_{avg} = 14\ mW$. For B2B (0 km), the receiver LPF (4th order Bessel) introduces some inter-symbol-interference (ISI). After 4 km, the eyes are almost closed due to strong low pass filtering. Followed by that, the eye starts opening due to the HPF effect. This results in much clearer eyes after 8 km and after that the eyes start degrading again and show strong overshoots. Therefore, receiver LPF becomes helpful for longer distances. The minimum BER is achieved after -2 km propagation due to the slight high pass filtering, which counteracts the receiver LPF. Without receiver LPF, the BER is minimum at B2B and keeps on degrading as negative CD increases.

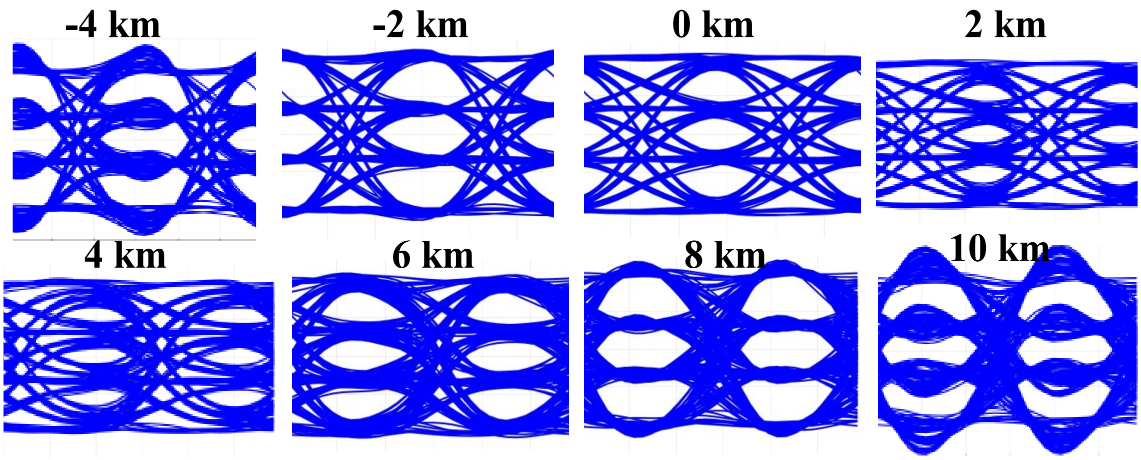

Fig. 4.6 Simulated PAM4 eye diagrams after different transmission distances for 16.5 Gbaud signal filtered with channel response as given by Eq. (2).

4.3.2.2 Complete transmission system simulation

Next, to verify this behavior, we conduct simulation for the same chirp parameters but taking the electrical to optical and optical to electrical conversion into consideration. The DML response can best be described by a set of nonlinear equations involving carrier and photon densities [127]. By extracting the rate equation parameters, it is possible to model the DML response quite accurately [136]. However, to simplify the simulation environment, instead of using the non-linear laser rate equations, we use specific values for α and κ parameters to predict the DML response. Complex optical waveform samples are generated based on Eq.

(4.2) for a certain average output optical power, P_{avg} and optical modulation amplitude (OMA), defined as $OMA = P_{high} - P_{low}$; where P_{high} and P_{low} represent the power of the top and bottom levels. By OMA, we mean the outer OMA in our simulation. Using Eq. (4.2) instead of the coupled rate equations allows us to independently look at the impact of chirp parameters, DML BW, DML average power and OMA. As in the previous section, we perform simulation at 16.5 Gbaud. Electrical waveforms are generated by filtering an ideal square pulse train with a Gaussian filter with a 3-dB BW of 25 GHz mimicking a pulse pattern generator (PPG) response. We use a Butterworth low-pass filter of 2nd order (3-dB BW equals to 18 GHz) for the DML, PIN photodiode (PD) with 4th order Bessel response and a transimpedance amplifier (TIA) with 2nd order Bessel response, transimpedance, Z_T = 4000 Ω, input referred noise current spectral density of 13.5 pA/√Hz, and a BW of 15 GHz. The fiber is assumed to be loss-less with a dispersion coefficient, D=17 ps/nm/km (or, β_2=−21.66 ps^2/km). The received optical power (*ROP*) onto the PD is fixed to -7 dBm. Higher *ROP* gives better BER performance with very similar trend. Higher OMA at B2B also results in improved BER due to higher extinction ratio (ER) and better receiver swing. However, after fiber transmission, higher OMA does not ensure better performance due to detrimental effects of broader spectrum, higher overshoot and stronger eye skewing. The eye skewing can be explained by the fact that due to adiabatic chirp, each of the four PAM4 intensity levels correspond to different frequency offsets and propagate at different speeds through the fiber causing amplitude-dependent skew [147]. In Fig. 4.7 (a) and 4.7 (b), we use an OMA of 4.8 mW and P_{avg} = 14 mW to demonstrate the impact of LEF and adiabatic chirp coefficient for a propagation range of -15 km to +15 km.

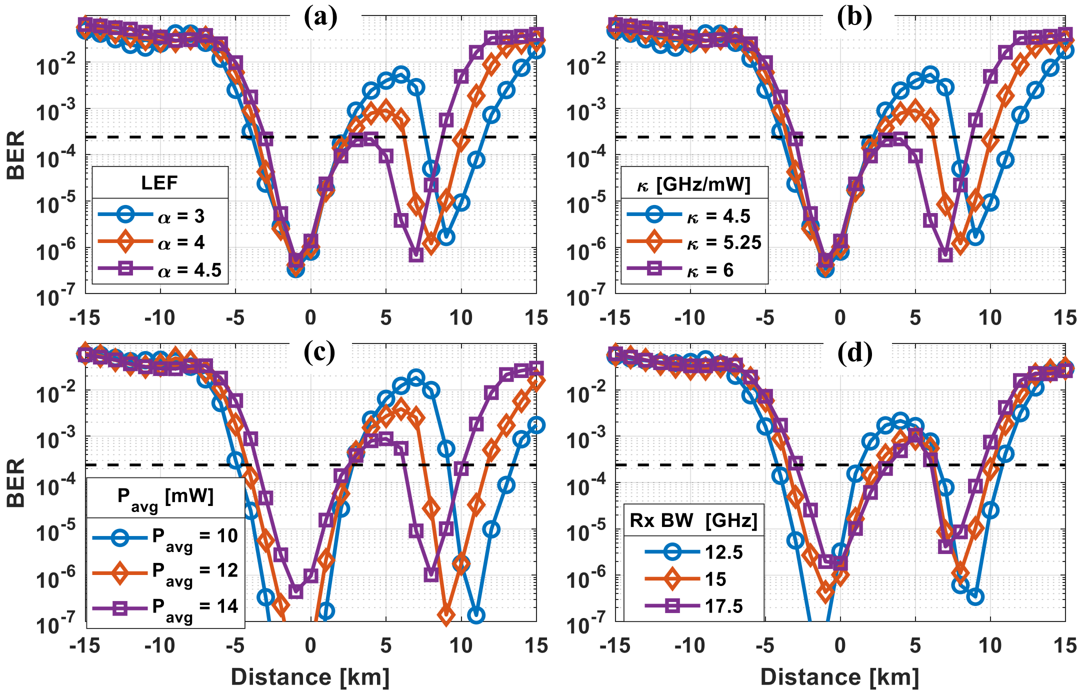

Fig. 4.7 16.5 Gbaud PAM4 BER performance after3 different transmission distances with 4.8 mW OMA (a) κ = 5.25 GHz/mW, P_{avg} = 14 mW, and various α values (b) $\alpha = 4$, P_{avg} = 14 mW and various κ values, (c) $\alpha = 4$, $\kappa = 5.25\ GHz/mW$ and different values of average power, (d) $\alpha = 4$, $\kappa = 5.25\ GHz/mW$, P_{avg} = 14 mW for different values of receiver BW.

The complete transmission system response shows similar trends compared to small signal simulation. However, the BER in this case depends on several additional factors like PPG, DML, PD and TIA BW response and noise performance. Additionally, the eye skewing effect and the sampling instance used also affect the BER performance significantly. Fig. 4.7 shows that as we increase the transmission distance on the positive dispersion region, the BER initially degrades for some distance and then improves for a range of CD values followed by continuous degradation. This has been observed in previous research works for DML and VCSEL transmission with both OOK [129, 138, 139] and PAM4 [131]. As for the negative transmission distance, the BER at first improves slightly (due to positive α) and then deteriorates fast followed by a slow degradation. The B2B BER and the BER after the optimum CD value are nearly the same. For example, for a LEF of 3 (4) and $\kappa = 5.25\ GHz/mW$, BER after 10 km (8 km) is close to the B2B BER. However, this depends strongly on the receiver

BW and sampling instances. In Fig. 4.7 (d) we plot the BER vs. Rx BW. The optical eye diagrams after different propagation distances are shown in Fig. 4.8. Receiver BW helps reduce the impact of overshoots after longer transmission reach significantly and needs to be chosen carefully [139, 148].

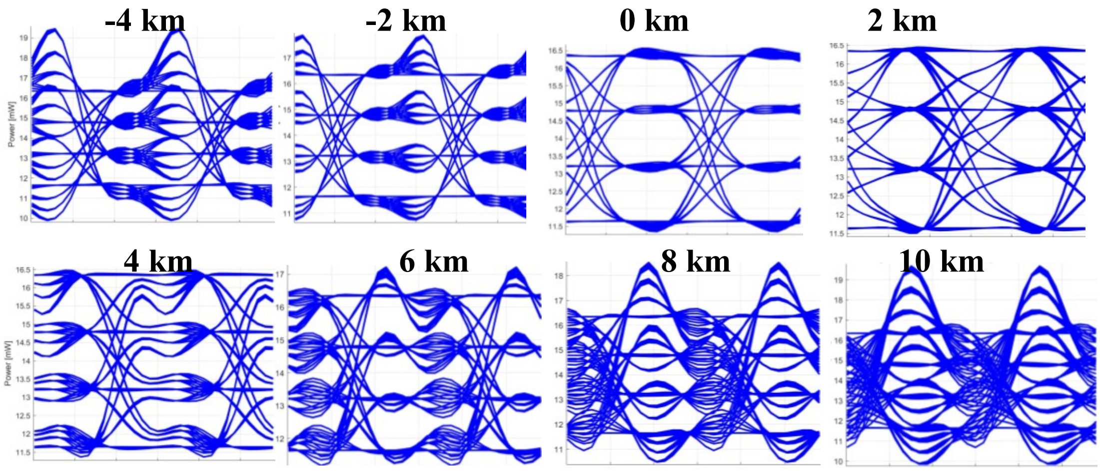

Fig. 4.8 Simulated PAM4 optical eye diagrams after different transmission distances for $\alpha = 4$, $\kappa = 5.25$ GHz/mW, $P_{avg} = 14$ mW, OMA = 4.8 mW.

In Fig. 4.5 (c) and Fig. 4.7 (c), we demonstrate the BER performance versus CD for different average DML output powers. Although Fig. 4.5 (c) shows little variation in BER using small-signal model, Fig. 4.7 (c) demonstrates a clear improvement in the BER when the average output power is reduced, especially at low dispersion values. For small signal model we kept the SNR of the RF signal generated at B2B identical in all cases and therefore found the BER to remain unchanged and this result is also independent of the OMA. However, this is no longer the case for the complete transmission system simulation. Reducing the average output power for the same OMA increases the extinction ratio (ER) of the signal, which in turn enhances the receiver sensitivity and improves the eye opening at the detector output. However, this improvement comes at the cost of increased transient chirp, which widens the optical spectral width and leads to high pulsation by the relaxation oscillation. Therefore, at B2B, lower average output power gives better performance. But after fiber propagation, this results in worse BER performance compared to the case of higher average power. To extend the propagation distance, one may enhance the ER without affecting the transient chirp, which could then mitigate the adverse effects of both transient and adiabatic chirps. However, this condition is not achievable solely through direct modulation and a post- optical processing step may be required after the DML, as elaborated in the following section.

4.3.2.3 Effect of optical filtering in a DML/DD system

From Fig. 4.4 to Fig. 4.8, we demonstrated that the BER of a DML/DD system is severely impaired by the chirp-dispersion interplay, and it is not possible to transmit signal to even 15 km. The impact of transient chirp can be suppressed by working at a higher bias current, and the adiabatic chirp can be utilized by proper optical spectral reshaping. For OOK, this concept is known as chirp-managed laser (CML), where an optical bandpass filter is carefully positioned to cut the zero frequency components increasing the ER (by FM-AM conversion) and the DML is driven with an optimum drive current that allows for phase-correlative modulation between adjacent bits [43]. The filter can be an arrayed-waveguide grating (AWG) filter [148], or a micro-ring resonator based filter [143, 144], or a Bessel filter [141], or a delay interferometer based notch filter [149]. More details regarding the optimum filtering are presented in section 4.4. The optimum OMA for CML condition depends on the symbol rate and chirp parameters and is given as [141]:

$$OMA_{CML} = \frac{2\pi}{\alpha k} B$$

For $\alpha = 4, \kappa = 5.25$ GHz/mW, at 16.5 Gbaud the required OMA is 4.93 mW for OOK signaling. For PAM4, due to the presence of four levels, the same argument does not hold. Nevertheless, an optical filter improves the system performance due to frequency modulation to amplitude modulation (FM-AM) conversion, AM-FM conversion, optical duobinary (ODB) effect, minimum shift keying format generation, the vestigial sideband (VSB) effect etc. [127]. Here, we employ a SG filter of 2nd order with a bandwidth of 50 GHz to show the impact of optical filtering. The center frequency is initially set to the maximum transmission of the DML spectrum, and then shifted to attenuate the low frequency contents. The frequency offset is defined as the center frequency of the optical filter and peak DML spectrum. We show the effect of filtering in Fig. 4.9 for two different OMA values for the same DML output power and ROP. We can see that filtering can significantly improve the transmission performance of DML/DD system. However, the curves still follow the same trend as achieved with only DML transmission. If the excess filtering loss is considered, the BERs at higher offset values become worse but still is found to better than "DML only" case (not shown here).

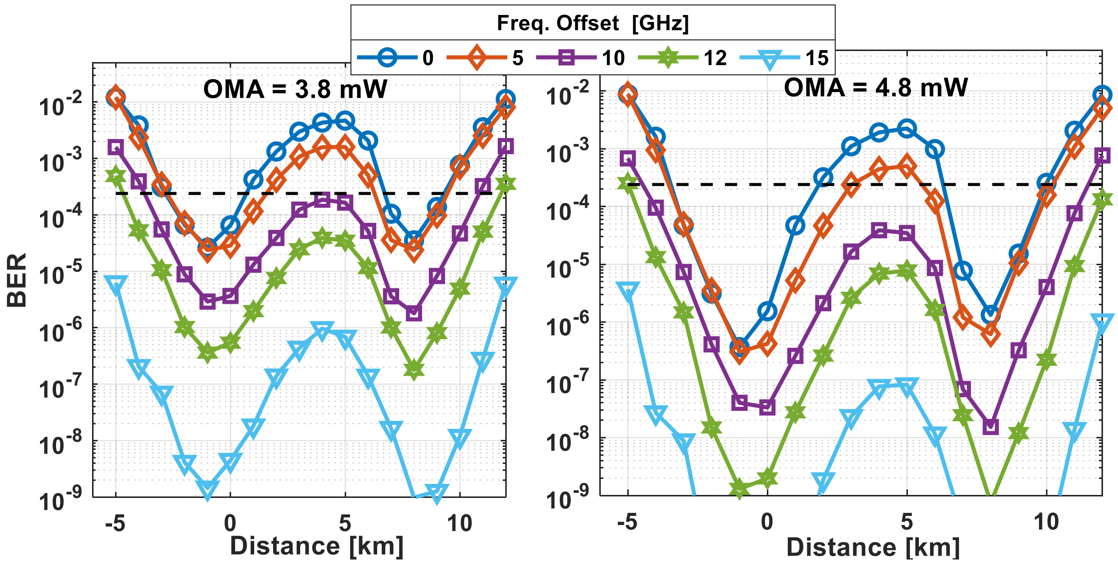

Fig. 4.9 Simulated PAM4 BER vs. transmission distance after a super gaussian (SG) optical filter with 50 GHz BW for different frequency offsets calculated from the peak of DML spectrum.

Fig. 4.10 (a) and 4.10 (b) demonstrate the optical eye diagram after 4 km and 20 km respectively. We use a 50 GHz Bessel filter for the optical eyes. We can clearly see that for longer propagation, stronger filtering is required. In Fig. 4.10 (c), we plot the electrical eyes after 15 GHz PD (4^{th} order Bessel filter) and a 15 GHz TIA. The LPF helps improve the eyes significantly. The eyes are almost completely open after 25 GHz SG filter. However, the temporal skew caused by the velocity mismatch is also visible after 20 km propagation, which ultimately degrades the BER. In anomalous region, the topmost level (highest frequency components) arrives earliest, and it causes a left tilt and in the normal region, it is simply the opposite. The maximum skew between the outermost levels can be estimated as:

$\Delta T_{skew} = (\delta\lambda_{pp})LD$, where $\delta\lambda_{pp} = (\delta\nu_{pp})\lambda_0^2/c$ and peak-to-peak chirp, $\delta\nu_{pp} = \frac{\alpha}{4\pi}\kappa\,(OMA)$; λ_0 being the wavelength of operation. Therefore, for a 20 km transmission with an $OMA = 4.8\,mW$, the estimated skew is 21.84 ps, which is ~36% of UI (unit interval). In our simulation it is slightly smaller due to the receiver LPF. However, as will be shown in next section, the DML output at B2B usually shows slight left tilt at higher OMA [121, 122]. This is because the DML turns on faster when driven with a higher modulation current (higher BW), causing the lower transition eye to lag the upper eyes in PAM4 waveforms. This aggravates the skew effect and makes the optimum sampling harder at the detector output. Due to this, after longer transmission, PAM4 BER degrades faster for higher OMA and sets an ultimate limit on the reach. This is even more destructive in a practical system, where there is timing jitter and determining optimum sampling point and the threshold values are difficult with level dependent noise and eye-skew. Linear signal processing cannot compensate for this timing skew and nonlinear pre or post compensation becomes necessary to tackle this as demonstrated in Ref. [150].

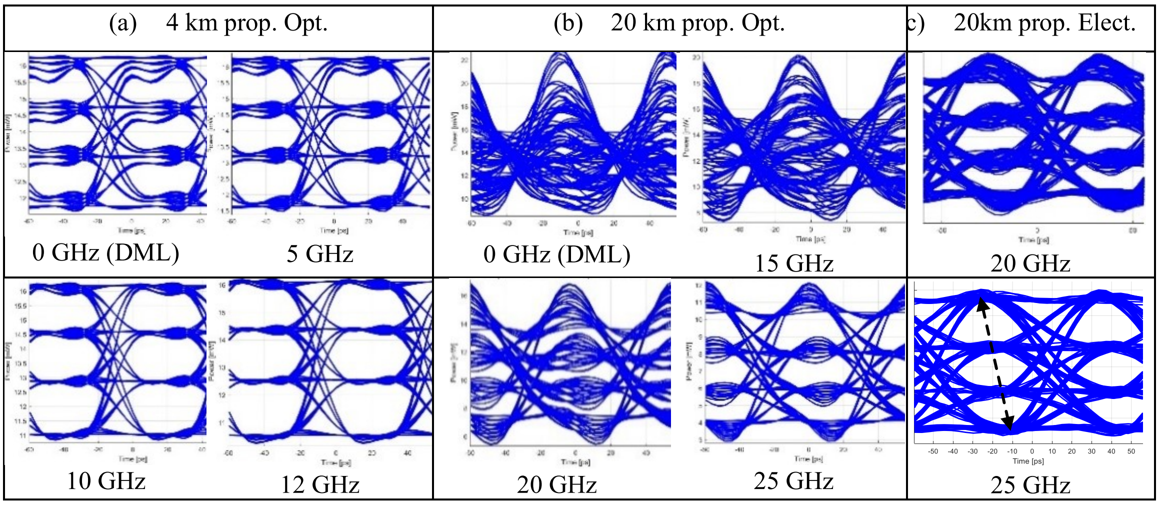

Fig. 4.10 Simulated PAM4 optical and electrical eye diagrams after a super gaussian (SG) optical filter with 50 GHz BW. $\alpha = 4$, $\kappa = 5.25$ GHz/mW, $P_{avg} = 14$ mW, OMA = 4.8 mW.

4.3.3 DML characterization

In this section, we show the characterization of the DML used in our experiment and verify the simulation model used in the previous sections.

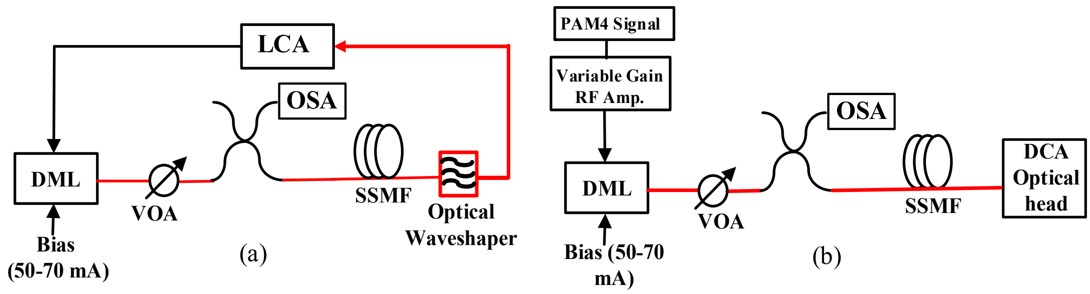

Fig. 4.11 (a) Experimental setup to measure channel response after SSMF and test the effect of optical filtering, (b) Experimental setup to test the effect of OMA, CD and receiver BW.

Since the parameters α and κ play a critical role in our simulation, we at first try to estimate them by doing a small signal measurement with Keysight lightwave communication analyzer (LCA) as depicted in the experimental setup (Fig. 4.11 (a)). We start with the measurement of the EO S21 response of the DML itself at various bias currents. The threshold current of the distributed-feedback laser diode (DFB-LD) was around 15 mA and at a bias current higher than 60 mA, the packaged module exhibited a 3-dB BW of 18 GHz. The average optical output power at 70 mA and 25^{0}C was found to be 14 mW, with the lasing wavelength at 1546 nm. Next, we propagate the modulated DML signal through standard single mode fiber (SSMF) of various lengths and measure the channel response. In Fig. 4.12 (a), we show the channel response at B2B and after 43 km fiber. To determine the true channel response, we normalized the frequency response using B2B data. We fit the 20 km, 43 km, and 63 km system responses using Eq. (4.3) and the parameters for the best fit were found to be $\alpha = 4$, $\kappa = 5.25\ GHz/mW$. The measured frequency responses shown in Fig. 4.12 (b) are in good agreement with the theoretically calculated curves. Although some deviation was observed in the low frequency regime, the notches are very well predicted by Eq. (4.3). To investigate the impact of bandpass optical filtering, we use a programmable optical filter (Finisar waveshaper) which allows us to study the impact of different filter profiles like Gaussian, SG, Butterworth and Bessel with different bandwidths and frequency offsets. In Fig. 4.12 (c), we plot the system response for different filters, when the filtering loss is uncompensated (these are not the optimum filters). This figure illustrates that attenuating the low frequency signal spectrum with an appropriate filter can flatten the system response, which helps to improve the overall BER performance.

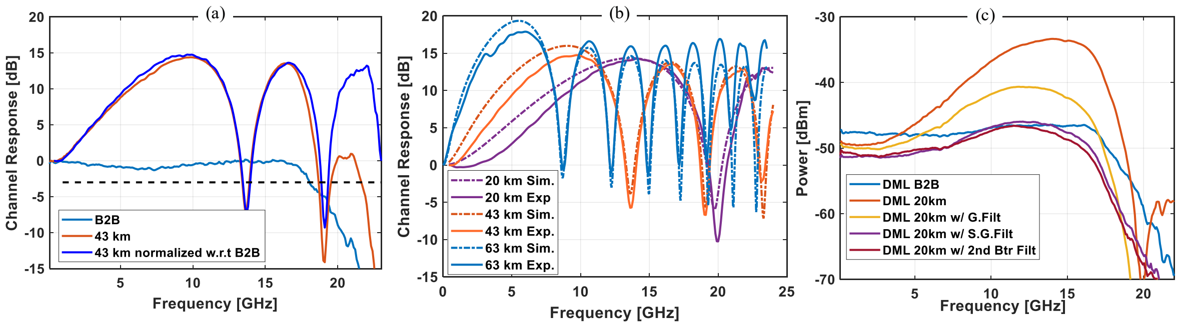

Fig. 4.12 (a) Measured channel response of the packaged DML at B2B after 43 km of SSMF, (b) Measured and simulated channel responses with $\alpha = 4$, κ = 5.25 GHz/mW, Pavg = 14 mW, (c) Effect of optical filtering in a DML/DD system as measured by LCA.

As a next step, we modulate the DML with a PPG and variable gain RF amplifier (VGA). The setup is shown in Fig. 4.11 (b). We then observe the optical eyes on the digital communication analyzer (DCA) with 12.8 GHz BW receiver filter (4^{th} order Bessel) and the spectrum with an optical spectrum analyzer (OSA) with 0.01 nm resolution. We start with OOK signaling at a lower symbol rate of 10 Gbaud and tune the gain of the VGA to get to different OMA values. At a lower OMA of 4 mW, the spectrums corresponding to 0 and 1 are not separated well enough for the OSA to differentiate. However, with a higher OMA of 7 mW, the frequency modulation of DML output spectrum is clearly visible. But for the PAM4 case, the spectrums corresponding to the 4 levels are close to each other and therefore even at 7 mW or 8 mW OMA they are not distinguishable. The simulated spectrum with 0.01 nm resolution matches well with the experimentally obtained spectrum. However, this requires fitting the DML EO S_{21} well with the simulation. The eyes after DML for OOK and PAM4 for different OMAs are also plotted in Fig. 4.13. The simulated and experimental eyes verify that the simulation model used in section 4.3.2 is accurate enough to predict the DML response except the small eye-skew resulting from the nonlinear dynamics of the DML which causes the rising edge of the output to be faster than the falling edge.

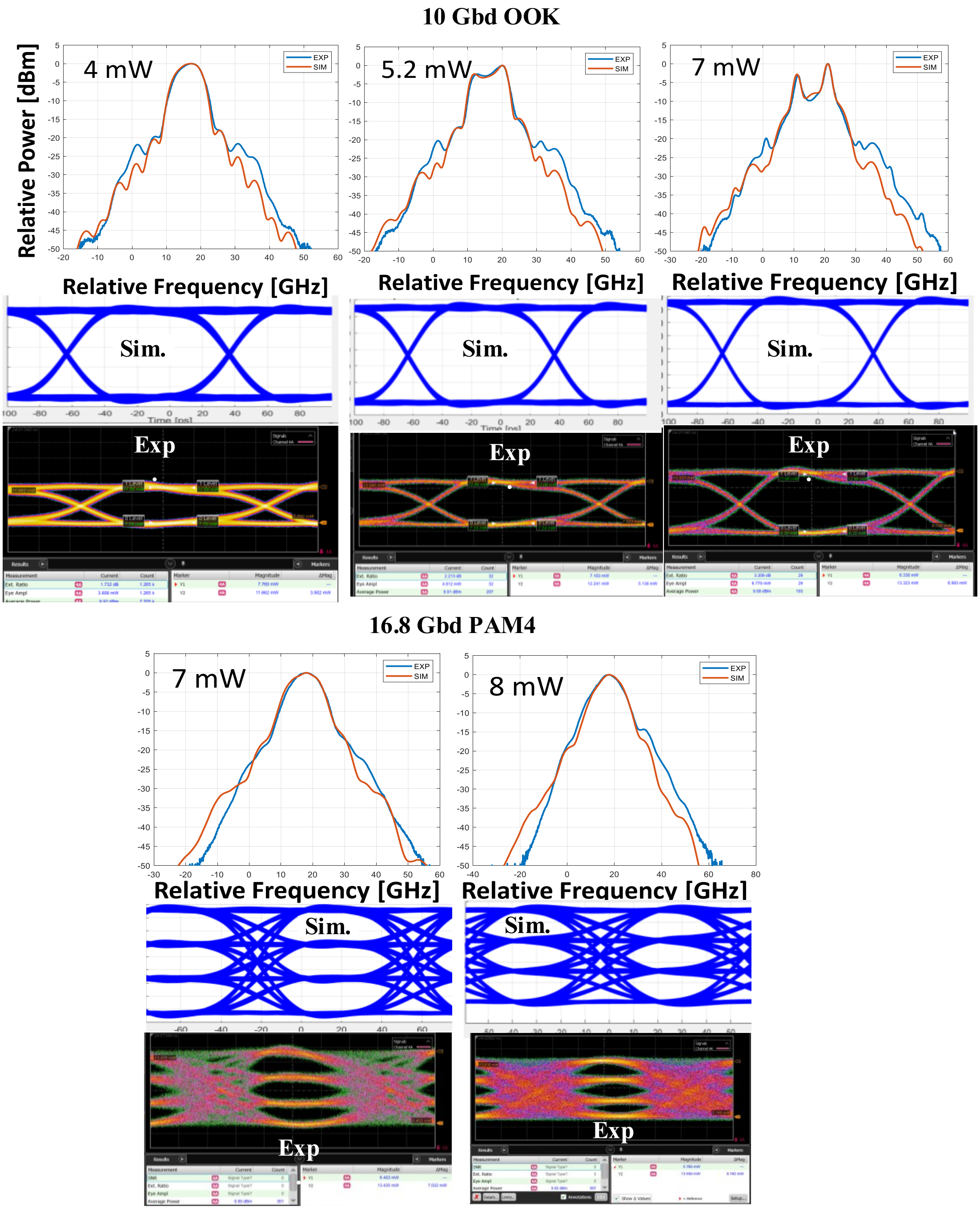

Fig. 4.13 Measured (Blue) and simulated (Orange) optical spectra and eye diagrams for 10 Gbaud OOK and 16.8 Gbaud PAM4 for different OMA (50 mA bias current).

4.3.4 PAM4 transmission experiment

In this section, we look at the effect of OMA, chromatic dispersion, and receiver BW on PAM4 eyes. Since higher bias currents ensure better EO BW, maximizes output power, and suppresses the transient chirp, we bias the DML at 70 mA for the subsequent transmission measurements. At lower bias currents more eye closure and skew were observed in the optical eyes due to lower BW and higher nonlinearity [147]. The same experimental setup as in Fig. 4.11 (b) is utilized for this target. The received optical power was kept constant to around 2 dBm for the different distances by controlling a variable optical attenuator (VOA). Given the limited BW of the DML, we limited our analysis below 20 Gbaud in this section. Fig. 4.14 shows the optical eye diagrams at three different OMAs and transmission distances for 12.8 Gbaud PAM4 signaling. At B2B, the eyes show better openings at a higher OMA. However, after propagation we observe stronger eye skew due to higher peak-to-peak adiabatic chirp and overshoot coming from both the adiabatic and transient chirps. Similar conclusion is drawn for 16.8 Gbaud and 20 Gbaud signaling as well.

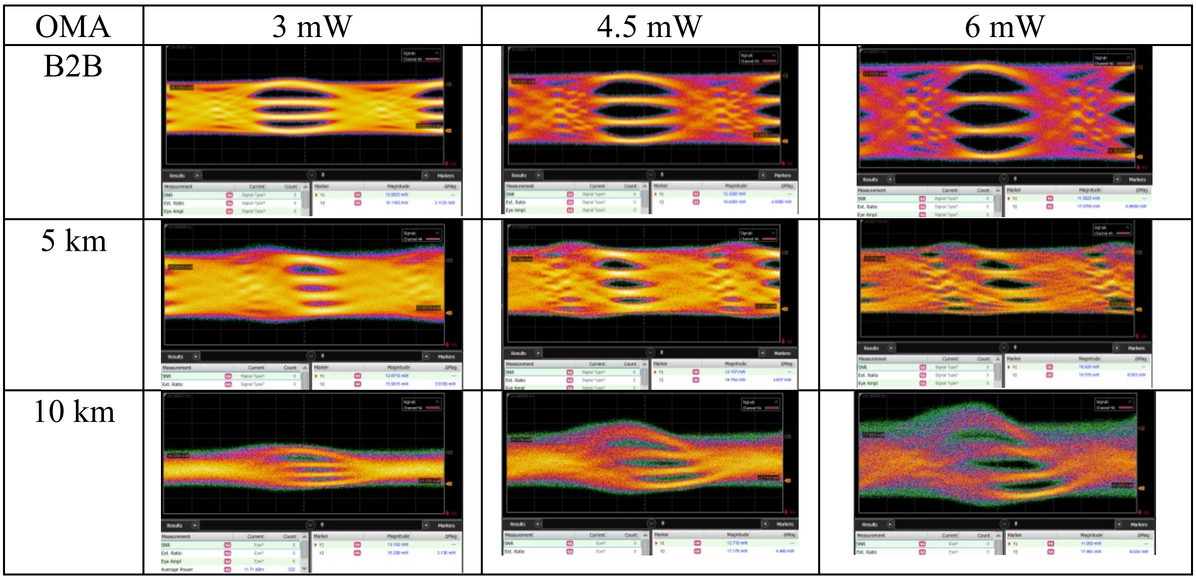

Fig. 4.14 12.8 Gbaud PAM4 optical eye diagrams for different OMAs at B2B and after fiber propagation.

The overshoots seen after propagation can be reduced by the receiver low pass filter. To verify this we use DCA’s signal processing toolbox to find the optimum receiver BW for 12.8

Gbaud and 16.8 Gbaud signaling after 12 km propagation. Fig. 4.15 demonstrates that 9-10 GHz BW is optimum at these symbol rates. Without proper receiver filtering the eyes are almost closed for 16.8 Gbaud and would not be recoverable. Therefore, the optimum receiver PD+TIA bandwidth should be chosen carefully based on the target reach and symbol rate.

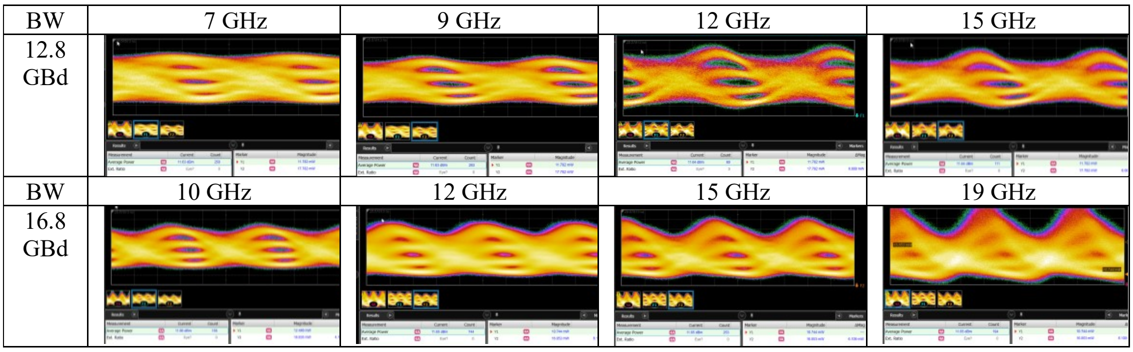

Fig. 4.15 Effect of receiver BW for PAM4 signaling after 12 km of SSMF for 12.8 and 16.8 Gbaud signal.

Next, we observe the eyes after different propagation distances to verify the CD dependency as discussed in detail in section 4.2. We propagate the modulated DML output over various lengths of SSMF and observe the eyes and Fig. 4.16 and Fig. 4.17 plot the eyes on the DCA at 16.8 Gbaud and 20 Gbaud. We can clearly see that the eyes are quite degraded after 5 km and then improve until 10 km and then start degrading again. Although lower BW receiver is shown to be helpful for longer reach, for the purpose of practicality, we kept it fixed at 12.8 GHz. A similar trend is found for a lower OMA of 3 mW and a higher OMA of 6 mW. In Fig. 4.14, where the symbol rate was 12.8 Gbaud, the BER did not degrade as fast as 16.8 Gbaud or 20 Gbaud signaling. This can be explained by the fact that the eyes start improving after a shorter distance for higher symbol rate signaling as seen in Fig. 4.5 (d). However, the effects of skew and nonlinearity are found to be stronger than the simulation after longer reach degrading the eyes.

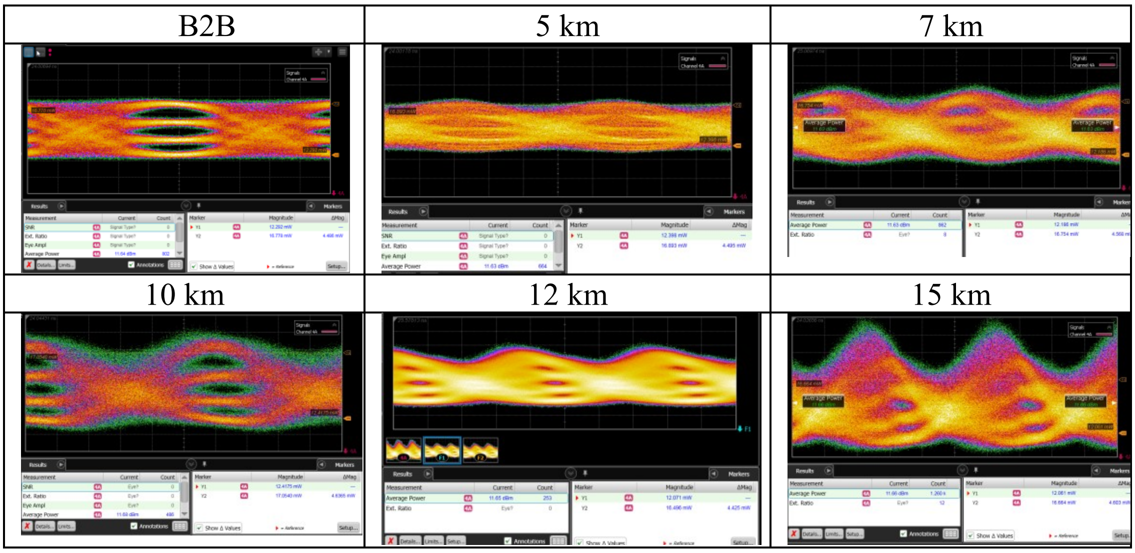

Fig. 4.16 16.8 Gbaud PAM4 optical eye diagrams for $OMA = 4.5\, mW$ after different transmission distances (Rx BW = 12.8 GHz).

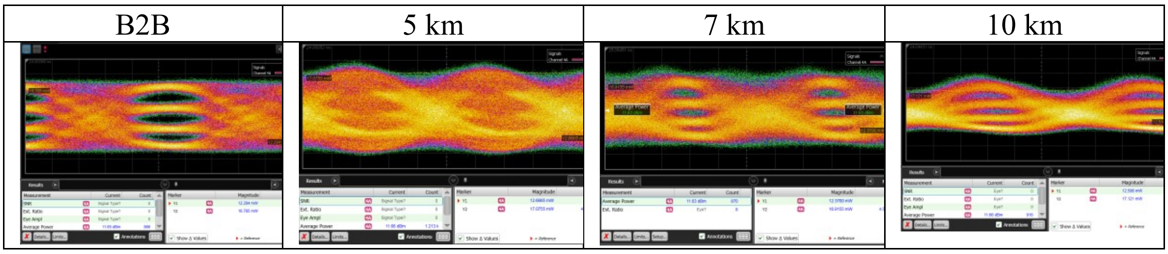

Fig. 4.17 20 Gbaud PAM4 optical eye diagrams for $OMA = 4.5\, mW$ after different transmission distances (Rx BW = 12.8 GHz).

Finally, we perform a BER analysis with the DML at 16.5 Gbaud. The experimental setup is shown in Fig. 4.18. A Keysight PAM4 BERT is used for data generation and detection. The single ended output from the remote head of the pattern generator was limited to 900 mV and directly drove the DML biased at 70 mA without any RF amplification. This results in an OMA of 3.8 mW, and an ER of 1.18 dB. The modulated optical spectrum with a 0.05 nm resolution OSA is shown in the inset of Fig. 4.18. Different lengths of SSMF and DCF are used to test the performance with positive and negative dispersion. The waveshaper filter is initially set to be centered at the maximum transmission frequency of DML spectrum so that the signal is not attenuated. After the fiber, the VOA was tuned to keep the power into the PD to be constant for various fiber lengths (except for ±20 km due to loss limitation). Due to the low ER of the signal, a high ROP of -2 dBm was chosen which gives a BER of 3e-5 at B2B for the DML only case. The PD+TIA showed a 22 GHz 3-dB bandwidth with small peaking. The differential outputs of the TIA were then fed to the error analyzer for BER measurement. An internal clock recovery module was used to recover the clock from the PAM4 patterns to clock the error analyzer.

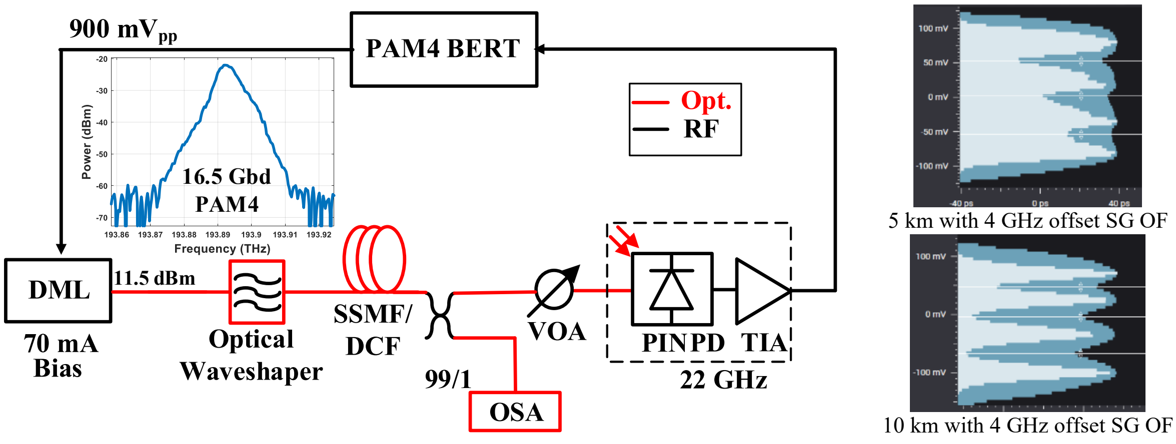

Fig. 4.18 (a) Schematic of the experimental setup with PAM4 BERT (inset: Optical spectrum at 0.05 nm resolution) (b) Histogram of the received PAM4 samples (from error analyzer)

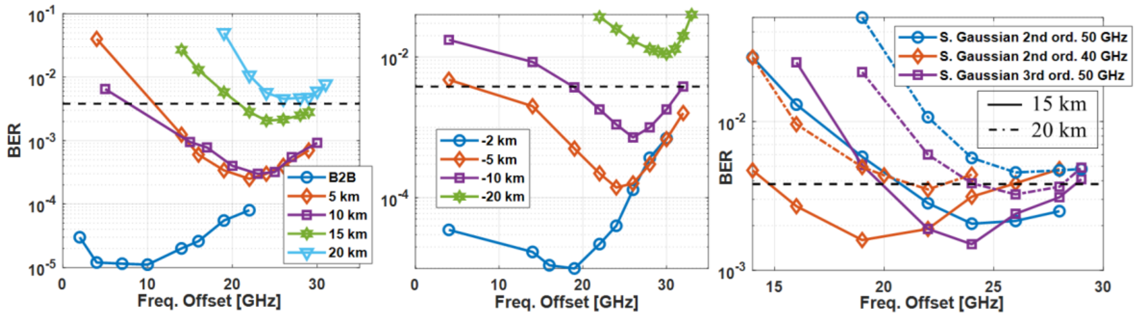

Fig. 4.19 BER vs. frequency offset after different lengths of (a) SSMF and (b) DCF with a 50 GHz SG OF and (c) with SG filter of different order and BW.

As shown previously, the eyes are quite degraded after fiber propagation and in most cases the error analyzer fails to recover the clock for BER measurements. As explained in section 4.3.2, filtering the low frequency contents can improve the eyes significantly. Even at B2B, filtering can improve BER due to ER enhancement [151]. However, cutting the signal partially also lowers the ROP and introduces non-linearity. In our experiment, we do not compensate for the excess filtering loss (insertion loss of the waveshaper is applicable for all cases).

Therefore, with higher offset values, BER starts degrading and the BER vs. frequency offset curves show a convex shape. In Fig. 4.19 (a) and 4.19 (b), we show the BER dependency with a 50 GHz SG filter for different offset values. At B2B, 5-10 GHz offset works best but the improvement is not too significant. Beyond 10 GHz offset, the gain coming from a better ER is countered by the ROP loss, increased ISI and added non-linearity. But for 5 km and beyond, the analyzer fails to even lock the received signal for BER measurement with the “DML only” case. Fig. 4.18 (b) shows the histogram of the received PAM4 samples at the optimum sampling point after a SG filter of 4 GHz offset. The histogram and the BER curves for 5 km and 10 km verify the better performance at longer distances for DML/DD system. An offset of 22-24 GHz gives the best BER for 5 and 10 km. It is important to point out that although the “DML only” BER was worse after 5 km, with strong optical filtering, similar BER values are achieved for 5 km and 10 km case. This might be due to the stronger skew after 10 km propagation. For 15-20 km of SSMF, an offset of 25-26 GHz gives optimum BER. At these offset values, the ROP was around 3 dB lower than the DML case. Still, the improved (flattened) system response as shown in Fig. 4.12 (c) helps to achieve a better BER. For Fig. 4.18 (b), we use DCFs that can compensate CD for different lengths of SSMF. The BER for the normal dispersion region keeps degrading for higher CD as expected from Fig. 4.5-4.7. We can see that for higher CD (both positive and negative) cutting more low frequency component becomes necessary. Lastly, we try 3rd order SG filter with 50 GHz BW and 2nd order SG filter with 40 GHz BW for 15 and 20 km distances in Fig. 4.18(c). A lower BW filter of the same order enables better performance. Too narrow BW will however introduce strong ISI (20 dB signal BW is ~25 GHz in our case) and therefore we did not choose low BW filters. We can also deduce that ~3dB attenuation of signal power (25 GHz offset for 50 GHz or 20 GHz offset for 40 GHz filter) is close to optimum for higher CD values and can be regarded as a good starting point for the best performance. The BER achieved here can be further improved with a lower BW receiver as demonstrated in Fig. 4.15. For a 20 Gbaud PAM4 signal, we could transmit over 15 km with proper filtering below the HD-FEC BER threshold, which shows the potential of DML based system for 50G applications without the need for complicated DSP.

4.3.5 Summary

In this section, we presented an investigation into the transmission of PAM4 signals using directly modulated lasers for different chirp parameters and fiber chromatic dispersion. Both baseband simulation and complete transmission system simulation were utilized to evaluate the BER performance over a wide dispersion range, and experimental verification was conducted for 16.5 Gbaud PAM4. We also incorporated an optical filter in our transmission system to evaluate its impact. Finally, with the aid of optical filter, we extended the transmission reach to 20 km of SSMF in the C-band without requiring digital to analog converter (DAC) or DSP. The results obtained from the simulations and experiments provide insights into the performance of the DML/DD system in a broad dispersion range and can be useful for future access networks.

4.4 Chirped managed laser for multilevel modulation formats: A semi-analytical approach for efficient filter design

4.4.1 Motivation

As mentioned in section 4.3.2.3, it is possible to enhance the chromatic dispersion (CD) tolerance of DML/DD system by properly controlling the adiabatic chirp. This approach is known as chirp-managed laser (CML), and extensive research on non-return-to-zero (NRZ) CMLs has been conducted over the past two decades [43, 127, 141, 142, 148, 152-155]. For CML, an optical spectral reshaper (OSR) needs to be carefully used with an optimum drive current that enables phase-correlative modulation between adjacent bits [156]. The passband profile of the optical filter (OF) used for the optical spectrum reshaping needs to be optimized to obtain a desired extinction ratio (ER). For example, Bessel shaped OF with a 3-dB BW of

7.11 GHz and order of 3 is used in the commercial Finisar DM-200-01 to attain an ER of approximately 11 dB for a DML with a linewidth enhancement factor, $\alpha \approx 3$ and adiabatic chirp coefficient, $\kappa \approx 11\,GHz/mW$ [157]. However, to the best of our knowledge, no intuitive filter design procedure has been identified in the literature that explains how CML-based filter designs are achieved, or how the frequency offset (FO) between the OF and the DML spectrum should be determined. Various types of optical filters have been reported in the literature, such as micro-ring resonator based filter [143, 144], Bessel filters [141], Gaussian filters [154], arrayed-waveguide grating (AWG) filter [148], and delay interferometer based notch filters [149]. Nonetheless, the criteria for choosing a particular filter over others remains unclear. The fabrication limitations of the filters, and their suitability in wavelength-division multiplexing (WDM) applications can influence the selection of filter configurations.

In recent times, several efforts have been made to expand the chirp-managed laser (CML) approach to pulse amplitude modulation with four levels (PAM4) signaling in order to achieve higher throughput [151, 158-160]. However, the same NRZ CML concept may not be directly applied for PAM signals due to the multi-level signaling, particularly at high symbol rates. At such high symbol rates, higher optical modulation amplitude (OMA) is necessary to satisfy the phase-correlative modulation condition, which may lead to significant eye-skew after transmission through the fiber. Nonetheless, optical filtering is still helpful to extend the reach since the filter not only improves the ER but also produces vestigial sideband (VSB) effect reducing the information bandwidth. However, the inter-symbol-interference (ISI) and nonlinearity stemming from the chirp-dispersion interaction is more severe for PAM4, prompting the adoption of both linear and non-linear DSP algorithms to mitigate these impairments [133, 140, 150, 161, 162].

In [151], the authors used commercial arrayed waveguide grating (AWG) and demonstrated 100 Gbps PAM4 transmission in the O-band over -70 ps/nm to +53 ps/nm dispersion range. In [160], with the aid of strong DSP (19-tap cascaded multi-modulus algorithm and 389-tap

Volterra filter) and tunable optical filter, 100 Gbps over 45 km of standard single mode fiber (SSMF) has been demonstrated. But the effect of excess loss due to the applied filter and the optimum filtering conditions have not been fully investigated in these previous works.

In this section, we propose a novel semi-analytical approach to identify the optimal filter profile and its offset with respect to the signal spectrum. This is applicable for any DMLs with different laser parameters (α, κ), and OMAs, as well as various modulation formats to achieve a desired ER. We present a detailed simulation study of the proposed method for both OOK and PAM4 format, with a particular emphasis on PAM4 signaling for higher throughput. Using a 17 GHz C-band distributed feedback (DFB) DML with an optical filter (OF), we successfully transmit a 35 Gbaud PAM4 over 20 km (340 ps/nm dispersion) of SSMF at a BER below the HD-FEC threshold of 3.8e-3. In this experiment, we utilize linear feed forward equalization (FFE) at the receiver and non-linear pre-distortion (NLPD) at the transmitter. In this optically unamplified system, we also study the effect of filtering loss and determine the proper filtering shape and position with respect to the DML spectrum.

4.4.2 CML optical filter design principle

4.4.2.1 Chirp Characteristics of DMLs

The optical field of a directly modulated laser (DML) can be expressed as $E_{DML}(t) = A_{DML}(t)\, e^{j\varphi_{DML}(t)}$, where $A_{DML}(t)$ is the amplitude and $\varphi_{DML}(t)$ is the phase of the optical field. The frequency chirp of the laser is given as [127]:

$$\delta f_{DML}(t) = \frac{1}{2\pi}\frac{d\varphi_{DML}(t)}{dt} = \frac{\alpha}{4\pi}\left(\frac{1}{P_{DML}(t)}\frac{dP_{DML}(t)}{dt} + \kappa P_{DML}(t)\right) \qquad (4.2)$$

where $P_{DML}(t) = |A_{DML}(t)|^2$ is the optical power, α is the linewidth enhancement factor (LEF) and κ is adiabatic chirp coefficient. This equation is useful for understanding the behavior of the DML's optical frequency and how it changes in response to variations in the output power. The frequency chirp can be expressed as a combination of transient and adiabatic contributions corresponding to the first and second term of Eq. 4.2. Transient chirp is a fast chirp that effectively occurs in the rising and falling slopes of the symbols. For a given α, the transient chirp is approximately determined by $\frac{dP_{DML}(t)}{dt} \approx \frac{OMA}{t_{rise/fall}}$ and the laser output power $\frac{1}{P_{DML}(t)}$. Therefore, for a given laser BW (the rise time/fall time), the optical modulation amplitude (OMA) and the average optical power, P_{avg} will determine the transient chirp. The OMA represents the power difference between the outermost levels and the ER is related to the OMA and P_{avg} as $ER = (P_{avg} + OMA/2)/(P_{avg} - OMA/2)$. For larger ER, the transient chirp will be larger, specifically during the fall time in which $P_{DML}(t)$ becomes even smaller which in turn causes a larger frequency excursion to the red frequency, as shown in Fig. 4.20(a) and 4.20(b) for $OMA \approx 4\,mW$, and $P_{avg} \approx 10\,dBm$ (Fig. 4.20(a) : ER $\approx$ 1.7 dB) and $P_{avg} \approx 7\,dBm$ (Fig. 4.20(b) : ER $\approx$ 3.6 dB). The spectra in the absence of transient chirp are also plotted here. The laser overshoot is pronounced for a larger ER (lower average power). Transient chirp can lead to broadening of the laser spectrum which can have negative effects on the transmission distance, for example by creating an erroneous 1 bit in a 0 bit duration by constructive interference of two neighboring 1 bits with a 0 bit in between (101). On the other hand, adiabatic chirp is a slow chirp that depends on the physical properties of the laser (α, κ) as well as the output power $(P_{DML}(t))$. This chirp causes the frequency modulation (FM) between the different levels of signal. For example, for NRZ, $\delta f_{adb} = \frac{\alpha\kappa}{4\pi}(P_1 - P_0) = \frac{\alpha\kappa}{4\pi}OMA$, which leads to an asymmetric laser spectrum making the 1 bits blue shifted relative to the 0 bits. Therefore, as the signal propagates over the fiber in the anomalous dispersion region (C-band transmission in standard single mode fiber), for example, 1 bits propagate faster than 0 bits causing overshoot over 1 bits by constructive interference of the 1 bits and 0 bits if the ER is not large, and also induces a temporal skew.

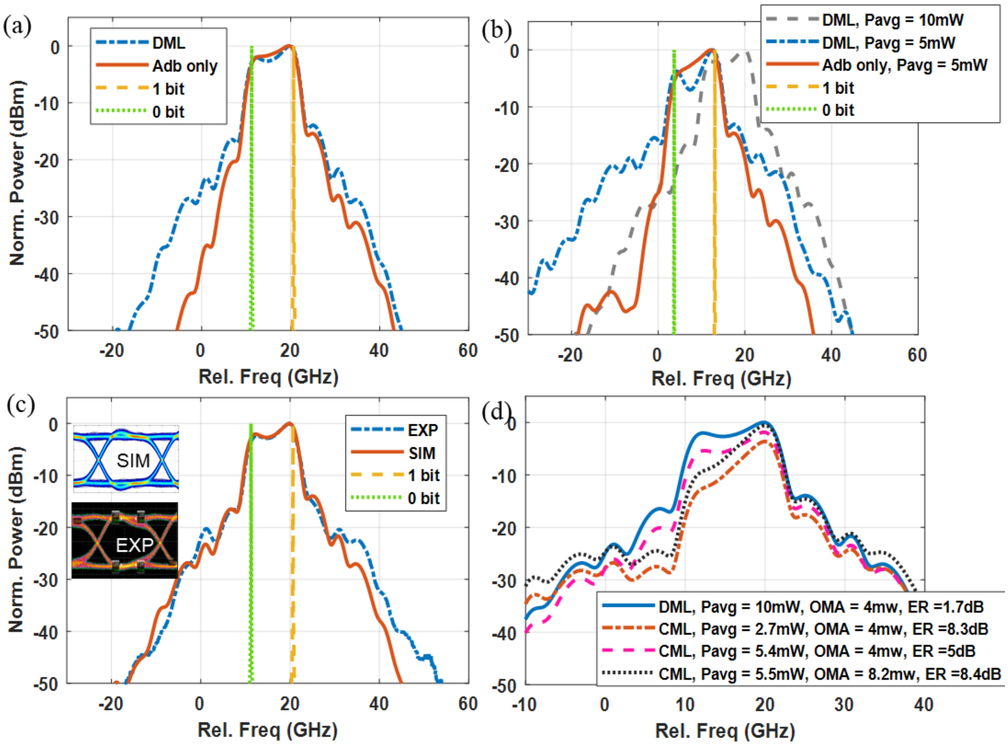

Fig. 4.20 (a)-(b) Simulated DML optical spectra of 10 Gbaud OOK for $\alpha = 4$, $\kappa = 5.25\ GHz/mW$, $OMA = 4\ mW$ for different ER, (c) Measured and simulated optical spectra and eye diagrams for $OMA = 5.2\ mW$, (d) Simulated DML and CML optical spectra.

One would require a low ER to reduce the negative impact of transient chirp. However, to extend the propagation distance, one needs to enhance the ER without affecting the transient chirp, which could then mitigate the adverse effects of both transient and adiabatic chirps. Therefore, with the DML alone, simultaneously satisfying these conditions would not be possible. Nevertheless, taking advantage of the frequency modulation (FM) property, one solution is to first drive the laser with a large bias current (larger output power, also giving a larger EO-BW) to minimize the transient chirp for a given OMA, and a small ER. In this case, the adiabatic chirp will be dominant. Then, an optical filter can be used to perform a frequency modulation (FM) to amplitude modulation (AM) conversion to enhance the ER by reducing the power of 0 bits. Indeed, this technique which is referred to as the chirped managed laser (CML) converts a partially FM signal into a substantially AM signal [43]. Appropriate OMA value ($\delta f_{adb} = B/2$, B is the symbol rate) will enhance the dispersion tolerance of the CML due to a phase-correlative modulation between adjacent bits [156].

4.4.2.2 Filter Design

In our approach, we leverage the conventional filter design method for linear and time-invariant (LTI) systems. The filter transfer function is identified by:

$$H(f) = E_{CML}(f)/E_{DML}(f)$$

where $E_{DML}(f) = FT\{E_{DML}(ft)\}$ is the Fourier transform (FT) of the DML signal and $E_{CML}(f) = FT\{E_{CML}(t)\}$ is the FT of the target signal or CML output signal, $E_{CML}(t) = A_{CML}(t)\ e^{j\varphi_{CML}(t)}$. By understanding the input signal and the desired output signal, we can easily derive the transfer function of the filter for FM-to-AM conversion. Several techniques have been developed in the past to accurately obtain the models of DMLs, either through rate-equation parameters extraction and using the rate equation [136] or in our case using Eq. 1 and extracting the laser parameters (α, κ) by matching the small signal response after fiber transmission [41] and optical spectra of a low and high baud rate signals with a large OMA, as shown in Fig. 4.20(c), which gives us the flexibility of independently setting and changing the chirp parameters.

The key part of this filter design is to properly define the target CML output signal $E_{CML}(t)$, which can be achieved by comprehending the input signal $E_{DML}(t)$. The goal of the CML technique is to increase the ER without causing transient chirp enhancement. In other words, we want to modify the input signal's P_{avg} and OMA, without modifying the frequency chirp or phase, as illustrated in Fig. 4.21(a). Thus, $E_{CML}(t)$ should have an $A_{CML}(t)$ which would be a modified version of $A_{DML}(t)$ for a desired ER, provided the energy conservation is not violated, but a similar frequency chirp or phase: $\varphi_{CML}(t) = \varphi_{DML}(t)$. Fig. 4.20(d) shows three examples of CML output spectra compared to that of the DML spectrum. The input NRZ DML signal, solid blue curve, has a $P_{avg,DML} = 10\ mW$ and $OMA_{DML} = 4\ mW$, resulting to an ER of 1.7 dB. We first fix the $OMA_{CML} = OMA_{DML}$ and reduce the average power to obtain two

ER values of 5 dB ($P_{avg,CML} = 5.4\,mW$), dashed magenta curve, and 8.3 dB ($P_{avg,CML} = 2.7\,mW$), brown curve. Next, we modify both OMA and average power to obtain an ER of ~8.3dB ($P_{avg,CML} = 5.5\,mW$ and $OMA_{CML} = 8.2\,mW$), dotted black curve. It can be inferred that the CML spectral shape is similar for the same ERs, though with a lower average power.

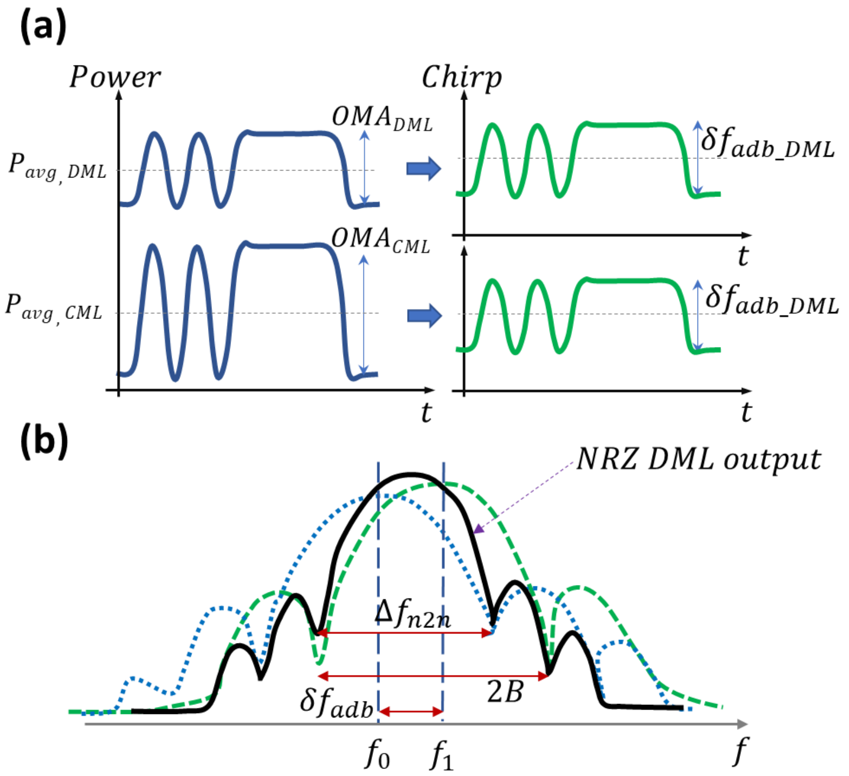

Fig. 4.21 (a) Power and chirp profile for DML and targeted CML output, (b) optical spectrum of DML output for NRZ signaling.

Next, we further explain the filter design procedure using an example as presented in [157] to also be able to compare the outcome. The 10 Gbps NRZ CML has $\alpha \approx 3, k \approx 11\ GHz/mW$, and $EO\ BW_{3dB} \approx 5.0GHz$ (this bandwidth would only keep one strong lobe on either side of the spectrum, as seen in Fig. 4.22(b)). The OMA is set to $OMA_{DML} = 1.9\,mW$ to satisfy $\delta f_{adb} = B/2$ condition. Using a Bessel filter of order 3 and $BW_{3dB} \approx 7.11\ GHz$, an ER of ~11dB is achieved.

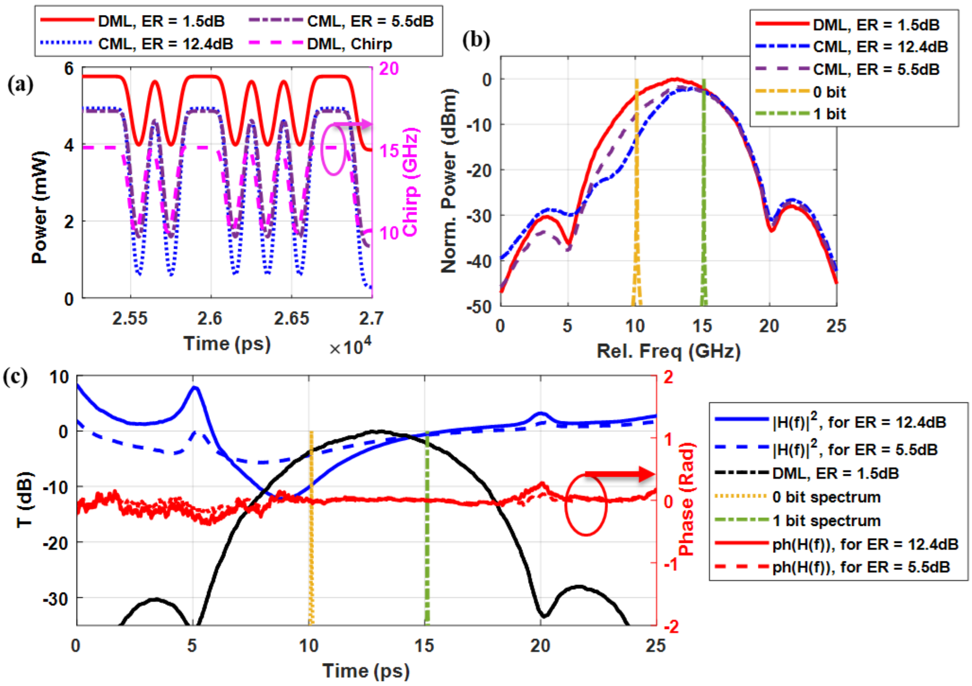

Fig. 4.22 DML and target CML (a) optical power and chirp profile, (b) optical spectra (c) required power and phase profile of required filter.

Fig. 4.22 shows the results of our analysis. Fig. 4.22 (a) shows the input DML (ER = 1.5 dB), and two target CML's (ER = 5.5 dB and ER = 12.4 dB) optical powers along with the frequency chirp. For this example, we used a Gaussian filter shaper for the DML. Fig. 4.22 (b) shows the respective power spectra $P_{DML}(f)$ and $P_{CML}(f)$. The spectrum of a DML signal can be comprehended as a combination of two sinc functions (Fourier Transform of a rectangular pulse with a width of bit-period and a linear phase whose slope corresponds to the bit power level) each centered around spectrum corresponding to 0 and 1 levels, as shown in Fig. 4.21(b). By enhancing the ER (reducing the power in zero bits spectrum), the spectrum matches more closely to a 1 level's spectrum with its peak slightly shifted towards the 1 level's spectrum (dashed green). Fig 4.22(c) shows the spectral amplitude and phase of the resultant $H(f)$. The effective region of the filter is indeed between the zero and one spectra, indicated by dashed yellow and green lines. In this region, and nearly over the main lobe of the signal, the filter phase is nearly flat. As expected, the filter's amplitude response is falling from the one spectrum towards the zero spectrum.

Fig. 4.23 (a) shows the next step in the filter design: finding a standard filter profile that matches best with the amplitude response of $H(f)$ between zero and one spectrum. We employed a numerical optimization function using the Nelder-Mead simplex algorithm (fminsearch) [163] to optimize our filter design. We report the minimum value of the objective function (fval) obtained by this function as a measure of the fitness of the resultant filter with respect to the target filter. A lower value of fval indicates a better fit between the obtained and target filters. As shown in Fig. 4.23 (a), we find that the filter found in [157] provides a good matching (fval~4.8). The optimization function identified a filter with the same Bessel order, but a slightly narrower bandwidth of approximately 6.8 GHz (fval ~4.1). However, this small difference did not produce a noticeable difference in the overall performance of the CML. Also, a Gaussian filter of 7.11 GHz BW (fval ~5.7) as well as a ring resonator filter with a Q factor of 7281 (fval ~5.3) show good match with the target filter. Nevertheless, as shown in Fig. 4.23 (b), Bessel filter has a group delay that is the opposite of SMF which may be beneficial for longer distances.

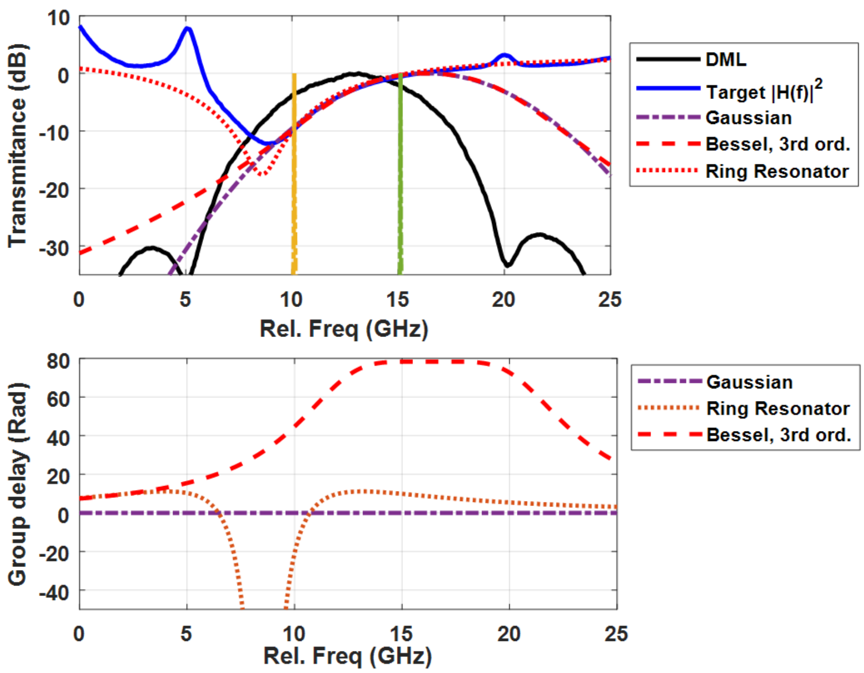

Fig. 4.23 Targeted and best-fit filters for ER = 12.4 dB. Transmittance profile (top) and group delay (bottom) of the optical filters.

4.4.2.3 NRZ Signal Transmission

Fig. 4.24 shows the eye diagram for B2B, 100 km, and 200 km for all three filters. All filters provide the target ERs. Fig. 4.24 (d) shows the eye diagrams for a target ER of 5.5 dB, for which the best filter fit is a Bessel filter with a BW of 11 GHz and order of 1. The objective of CML is indeed achieved by finding the required ER. As seen from Fig. 4.24, the best CML output is achieved when we use the MRR, as there is almost no ISI. However, for a longer propagation of the signal in the optical fiber, a filter may be chosen that also narrows the signal spectrum, as is the case with Gaussian and Bessel filters. Additionally, a Bessel filter may be chosen over Gaussian because of its group delay that compensates for some dispersion.

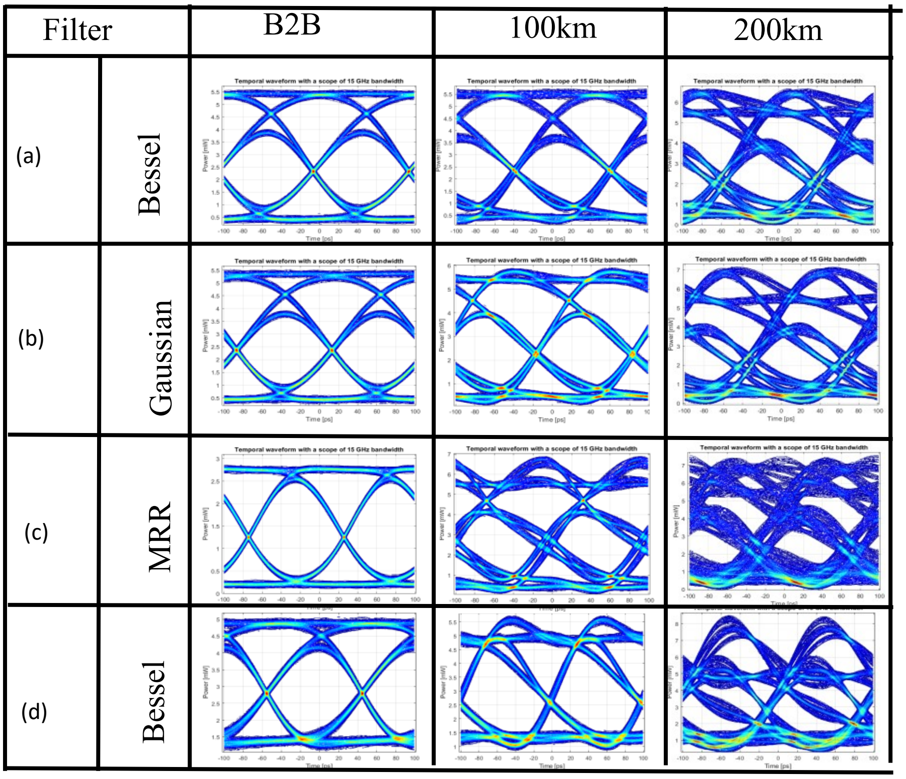

Fig. 4.24 Eye Diagrams at B2B, after 100 km, and after 200 km of fiber propagation. ((a)-(c) are for a targeted ER = 12.4 dB, (d) is for targeted ER = 5.5 dB)

4.4.2.4 PAM4 Signal Transmission

Next, we apply the same methodology to multi-level signals. We focus on PAM4 signaling and use the parameters of the DML available in our lab ($\alpha \approx 4, k \approx 5.25\ GHz/mW$). We use the same OMA value of 4 mW, where the OMA represents the power difference between the outermost levels. The EO response of the DML is modeled using a Gaussian filter of 6 GHz BW for 10 Gbaud signaling.

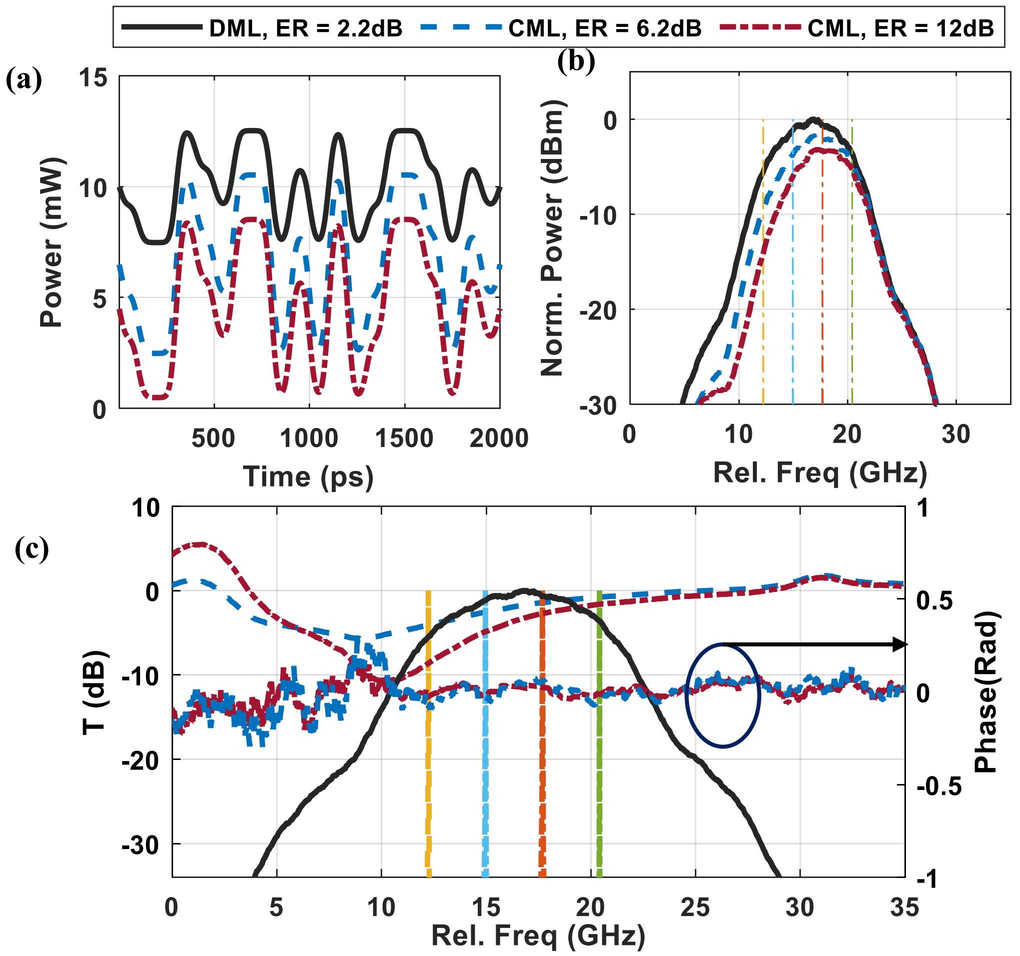

Fig. 4.25 DML and target CML (a) optical power, (b) optical spectra (c) required power and phase profile of required filter for PAM4..

Fig. 4.25 (a) shows the optical power of the input DML (ER = 2.2 dB), and two target CMLs (ER = 6.2 dB and ER = 12 dB) for PAM4 signaling. Fig. 4.25(b) shows the respective power spectra $P_{DML}(f)$ and $P_{CML}(f)$. Identical to the NRZ case, the spectrum of a PAM4 DML signal can be comprehended as a combination of four sinc functions each centered around each level CW power spectrum. By enhancing the ER, the spectrum appears to shift towards the highest power level (P3) spectrum. Fig. 4.25(c) shows the spectral amplitude and phase of the resultant filter $H(f)$. The effective region of the filter is indeed between the spectra corresponding to zero and three levels (P0 and P3), indicated by dashed yellow and green lines. Identical to NRZ signals, the spectral phase is nearly unchanged over the main lobe of the signal. Fig. 4.26 displays the filters that were identified to match the spectral amplitude of design $H(f)$ for frequency range between zero and three spectra. To achieve a target ER of 6.2 dB, a Bessel filter of 2nd order with a bandwidth of ~20 GHz and a Gaussian filter with a bandwidth of ~20 GHz exhibited the best match, as evidenced by fval values of 0.93 and 1.1, respectively (Fig. 4.26(a)). The results for the target ER of 12 dB are presented in Fig. 4.26(b), which shows that three filters matched well, that are a 4th order Bessel filter with a bandwidth of ~13.1 GHz, a SuperGaussian (SG) filter with a bandwidth of 27 GHz, and an MRR with a Q-factor of 7480. The corresponding fval values were 2.03, 2.13, and 1.7, respectively, which are higher compared to those obtained for ER=6.2 dB.

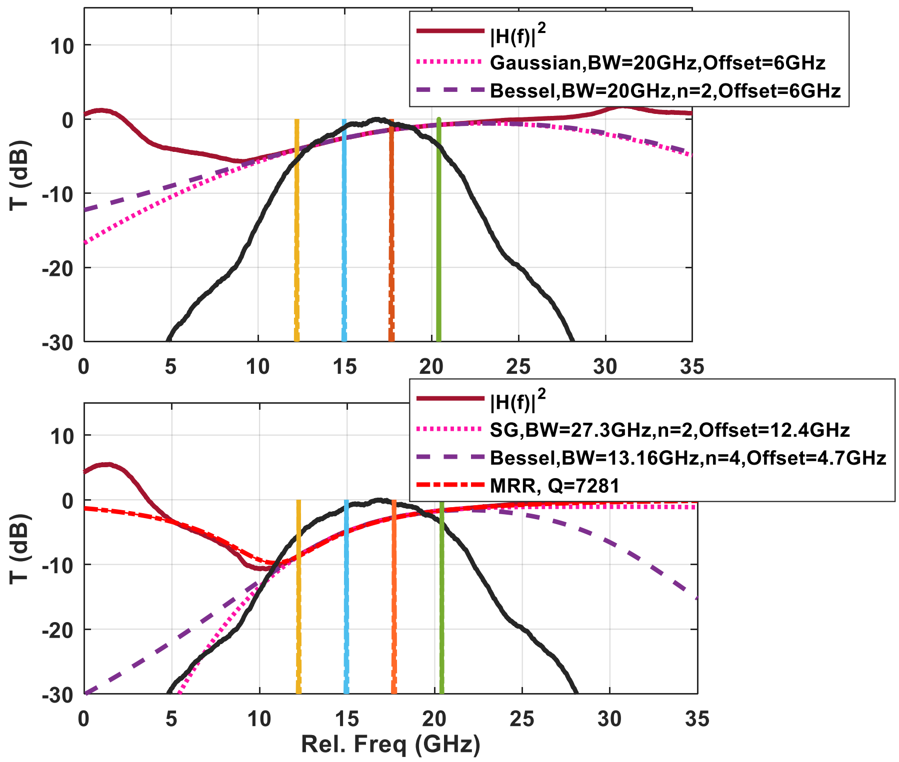

Fig. 4.26 Targeted and best-fit filters for ER = 6.2 dB (top) and ER = 12 dB (bottom)

Next, to achieve the FM-to-AM conversion, we pass the DML signal through the identified filters. The temporal power and frequency chirp of the DML output, target CML, and resultant CML are depicted in Fig. 8 (Bessel filter is chosen with ER of 6.2 dB and SG filter with ER of 12 dB in this figure). The target and resultant CMLs demonstrate good agreement, indicating the appropriate selection of the identified filters. However, the achieved ER value is slightly lower than the anticipated value for both cases, i.e., ~5.6 dB and 9.5 dB respectively.

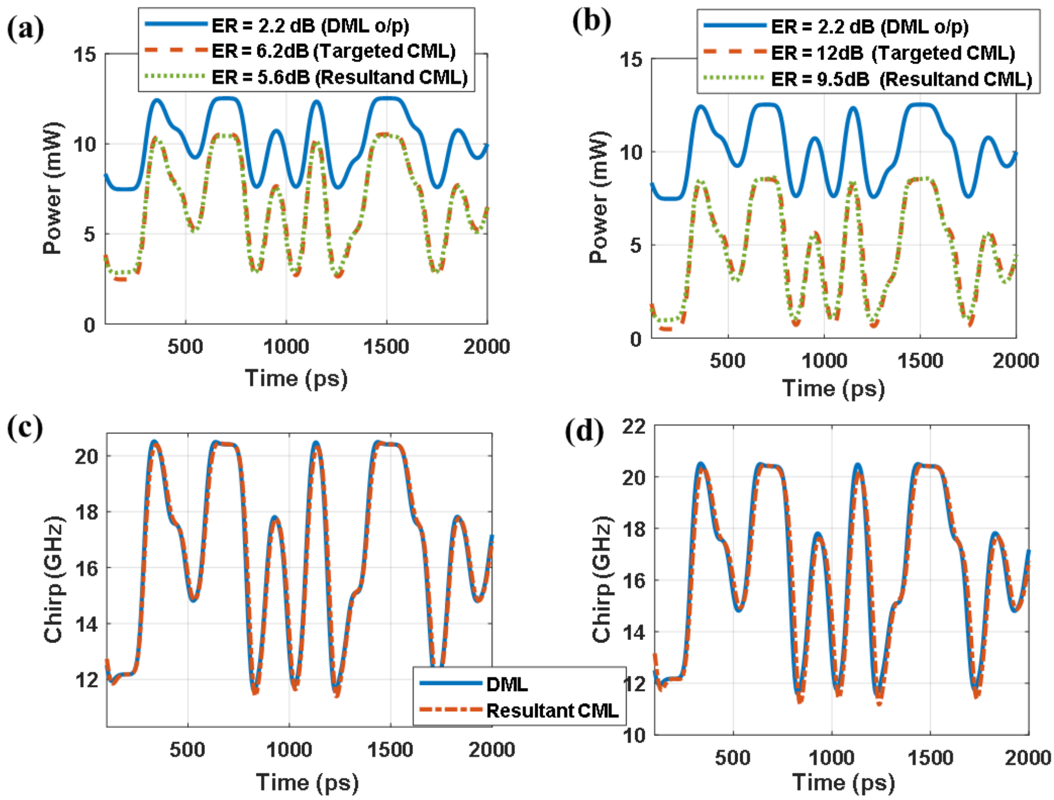

Fig. 4.27 (a)-(b) Temporal optical power and (c)-(d) frequency chirp of the DML output (ER = 2.2 dB, blue curve), target CML (ER = 6.2 dB and ER = 12 dB), and resultant CML (ER = 5.6 dB and ER = 9.5 dB)

Similar to NRZ CMLs, the selection of the most suitable filter from the identified options may be influenced by the propagation of the signal over optical fiber. Fig. 4.28 depicts the eye-diagrams and BER vs. distance for the filters specified in Fig. 4.26, with a received optical power (ROP) of -10 dBm. The BER curve for the DML follows the behavior explained in detail in section 4.3. The curves demonstrate that both identified filters for ER of 6.2 dB yield the same BER over fiber distance. For the ER of 12 dB, though MRR filter shows a better performance up to 8 km, the SG filter surpasses the others for fiber propagation up to 40km.

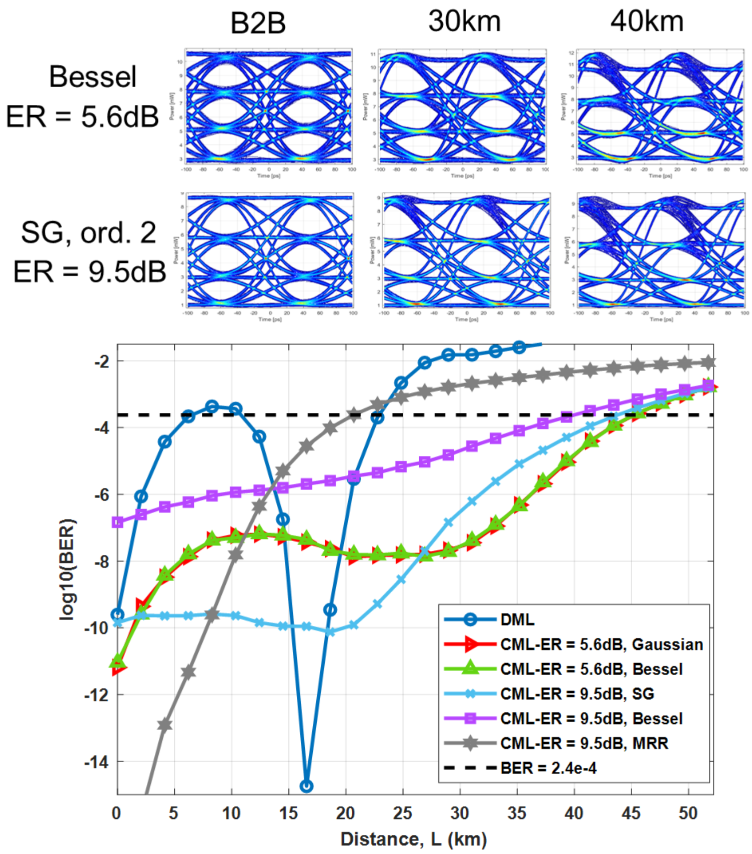

Fig. 4.28 Eye Diagrams and BER performance over various distances with designed filter

4.4.2.5 Eye Skew and ISI considerations for PAM4

It should be noted that as the ER value increases, such as with an ER of 12 dB, the CML output exhibits a tendency towards an asymmetric eye opening. To counteract this asymmetry, we may use some level dependent non-linearity compensation that would create a non-uniform eye from the RF transmitter to counteract the non-linearity introduced by the optical filter [164].

As can be inferred from the results of Fig. 4.28, the temporal skew between PAM eyes after propagation becomes the main challenge for multi-level CML signals. We can see that proper filtering enables us to get open eyes even after 40 km. However, the BER is degraded because of the skew. The maximum skew can be approximately estimated using the OMA of the DML signal and optical fiber dispersion and can be given as $\Delta T_{skew} = (\delta\lambda_{adb})LD$ and $\delta\lambda_{adb} =$

$(\delta f_{adb})\lambda_0^2/c$; λ_0 is the wavelength of operation, D is dispersion coefficient and L is fiber transmission distance. Therefore, the initial step in designing the filter might involve selecting an appropriate OMA. Assuming ±10% UI skew from the middle eye or 20% UI between top and bottom eyes (UI = unit interval = 1/B) to be the maximum tolerable skew, Fig. 4.29 shows an example of the required OMA vs. distance to respect the phase-correlative CML condition ($\delta f_{adb} = B/2$) shown in dashed line and the 20% UI skew constraint. For higher symbol rates, the phase correlative CML condition requires a higher OMA, while the skew would increase severely degrading the BER.

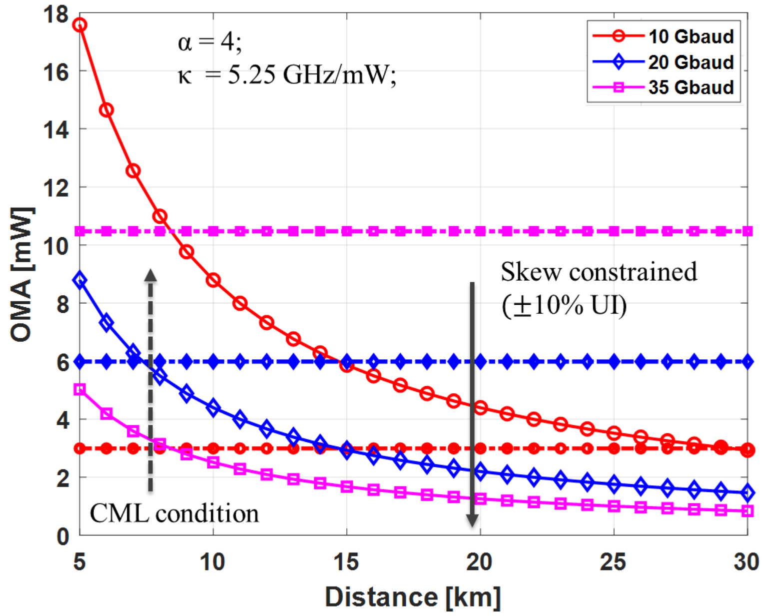

Fig. 4.29 Required OMA vs. fiber propagation distance for optimum CML condition (dashed lines) and a maximum of 20% UI skew condition.

Next, for the example in Fig. 4.28, we rerun the simulation for an ER of 6.2 and change the OMA from 2 mW to 7 mW, where OMA = 3 mW corresponds to the optimum condition, i.e., $\delta f_{adb} = B/2$. To enhance the maximum distance, the OMA can be reduced. However, lower OMA results in a lower ER and a lower received signal swing, degrading the signal-to-noise ratio (SNR). Therefore, for longer propagation distance and higher symbol rate, transmission with an optimum OMA needs to be determined.

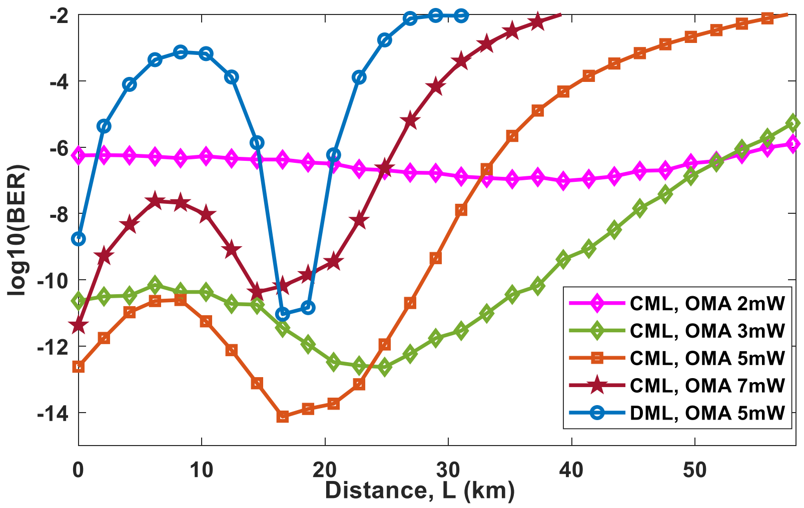

Fig. 4.30 BER vs. propagation distance for different initial OMA and a target ER of 6.2 dB

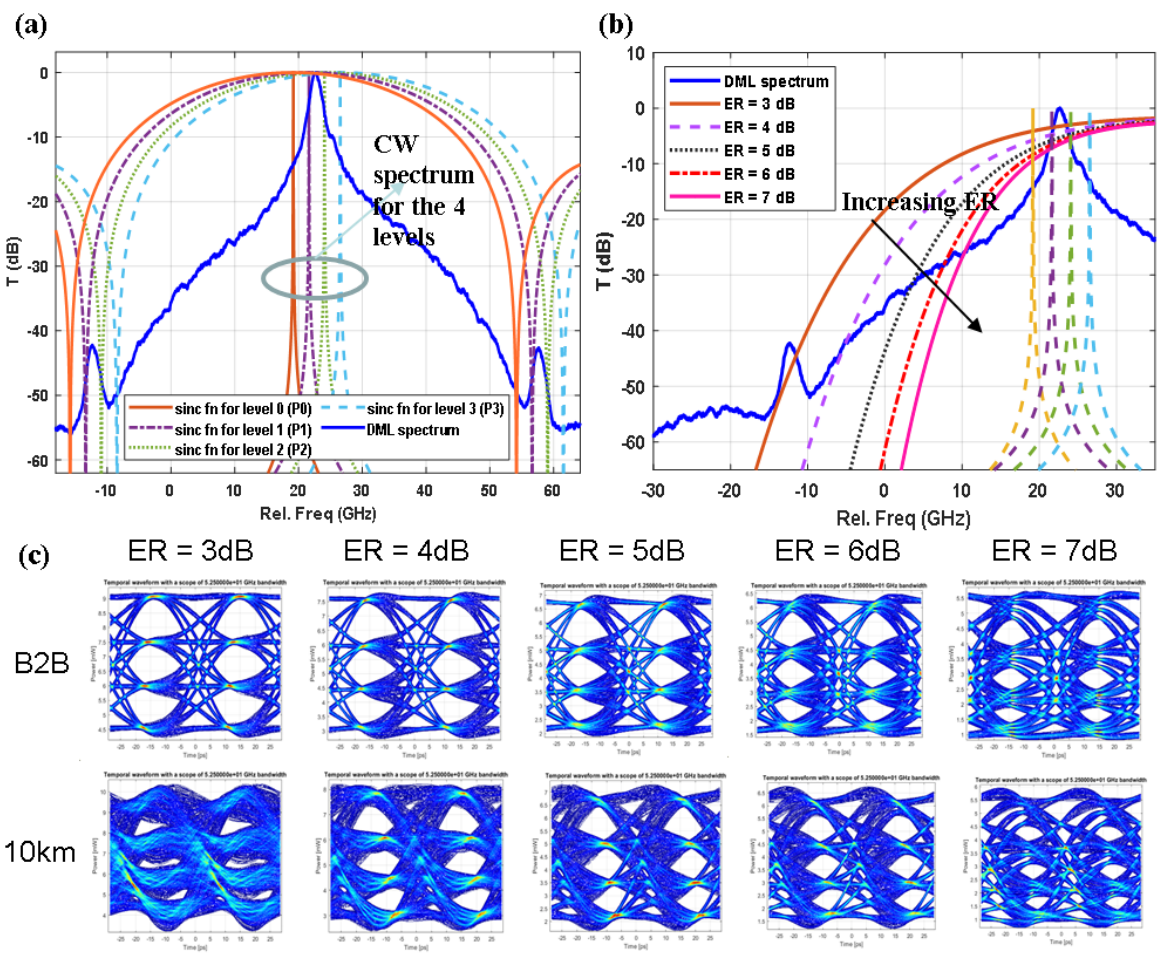

Fig. 4.31 (a) sinc and CW spectrum corresponding to the four levels of PAM4 signal, (b) DML spectrum and required 2nd order SG OF for different ERs (c) Eye diagram at B2B and after 10 km propagation for different targeted ER.

To illustrate this, we focus on a higher symbol rate of 35 Gbaud and assume that the DML is driven at a higher bias current leading to an ER of 1.4 dB. As the symbol rate increases, selecting the appropriate CML becomes more challenging due to both temporal skew and signal inter-symbol interference (ISI) limitations. As mentioned above, the spectrum of a PAM4 DML signal can be described as a combination of four sinc functions, each centered around a different level of CW power spectrum, as illustrated in Fig. 4.31(a). The filter required to achieve a specific ER can fulfill its purpose in shaping the spectrum, but it may lead to severe ISI at higher ERs. As a result, to minimize ISI, it may be necessary to limit the target ER. Fig. 4.31(c) provides an example of the CML output (B2B) and after 10 km fiber propagation for five different ER values. We adopt a 2nd order SG OF for this purpose. The 3-dB bandwidth and the offset requirement for the best fitting is given in Table 4.1. For this example, from the eye diagrams, the optimum eye after filtering occurs for the target ER of around 3-5 dB and considering a transmission over 10 km fiber, it is found to be 4-5 dB. With an ER of 3 dB, the filter's -20 dB point on the low-frequency side aligns with the -10 dB point of the sinc function for the P3 level, resulting in only a small ISI on the P3 level. As the ER increases, the filter's -20 dB point moves leftward, causing ISI to appear on the P3 for ER>3. Further increasing the ER attenuates more of the spectrum content, resulting in stronger ISI, degrading the eye. Therefore, for this example, it would be preferable to choose a filter design that, in addition to fulfilling the ER value, has a -20 dB point ($f_{CML,-20dB}$) around the -10 dB point ($f_{sinc,-10dB}$) of the sinc function for the P3 level on the lower frequency side to reduce ISI, i.e.,$f_{CML,-20dB} = f_{sinc,-10dB} - \Delta f$ where $-\delta f_{adb} \leq \Delta f \leq \delta f_{adb}$.

Table 4.1 Best fit SG OF parameters for 35 Gbaud PAM4 DML signal (ER= 1.4 dB)

ER (dB) / Parameter	**2**	**3**	**4**	**5**	**6**	**7**
BW (GHz)	148	97	66	49	40	35
Offset (GHz)	57	45	32	24	20	17
fval	0.6	2.54	2.5	5	8.2	11.7

In Fig. 4.32, we present the BER values for different target ERs. The BER vs. fiber propagation distance (L) indicates that an ER of 4-5 dB is best for propagation over 10-15 km. However, propagation beyond 15 km is not possible at the HD-FEC threshold due to ISI and strong eye skew. This indicates that for longer propagation distance, only optical filtering is not enough for high symbol rate PAM4 signals. Therefore, we employ symbol spaced (1 samples/symbol) linear FFE (9 taps) and look at the BER vs. L curves. With FFE, the propagation distance can be extended up to 18 km. The improvement with FFE is significant for "DML only" case, where receiver equalization extends the reach from 5 km to 14 km. With proper optical filtering, the improvement with linear equalization is found to be small. In Fig. 4.32(c), we plot the BER vs. ROP for 20 km propagation. The curves indicate that it is not possible to extend the reach to 20 km with only optical filtering and linear signal processing even at higher ROP. Non-linear compensation is therefore required for longer transmission reach as will be discussed in greater detail in the experimental section.

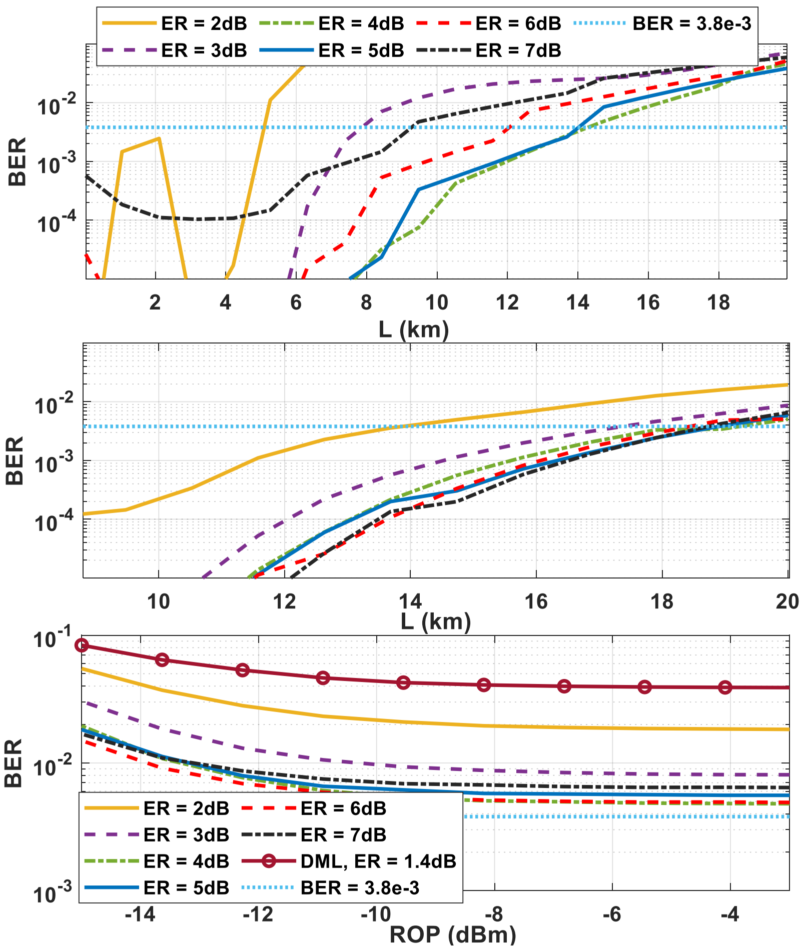

Fig. 4.32 (a) BER vs. propagation distance for different CML ERs w/o FFE. (b) BER vs. propagation distance, L for different CML ERs w/ FFE. (c) BER vs. ROP for different CML ERs w/ FFE after 20 km propagation with filters for different ERs.

4.4.3 Experimental results and discussions

4.4.3.1. Experimental Setup

Fig. 4.33 depicts the experimental setup along with the transmitter (Tx) and receiver (Rx) DSP employed to test the C-band DML transmission performance. We focus on 35 Gbaud PAM4, which is the maximum the DML can generate given its limited BW of 17 GHz. At first, we create random PAM4 symbols and then apply nonlinear compensation to partially compensate for the eye-skew and asymmetric eye-opening arising from optical filtering. We use a look-up-table (LUT) of 43 or 64 entries with length 3 (four PAM4 levels with 3 symbol memory) to distort the symbols and then resample to 2 samples per symbol (sps) for root-raised cosine pulse shaping. Therefore, we use a small roll-off factor of 0.12 to limit the bandwidth of the RF signal. The threshold current for this DML is 15 mA and biasing at a high current ensures maximum bandwidth and output power and it suppresses the transient chirp as well. Pre-emphasis is employed at the Tx DSP to compensate for the low-pass response of Tx RF chain (digital to analog converter, RF attenuators, RF amplifier and cables). The digital signal is then resampled and loaded to the digital to analog converter (DAC) memory running at 120 GSa/s. The analog signal at the DAC's output is first attenuated by 3 dB and then amplified by an RF amplifier (SHF 804b) with 22 dB of gain followed by another 6 dB RF attenuator before driving the DML. We keep our analysis limited to 20 km of SSMF transmission to test the impact of optical filtering and DSP. The fiber launch power is set below 6 dBm and after transmission, a 35 GHz PIN photodetector (PD) with transimpedance amplifier (TIA) is used at the Rx (AC transimpedance gain of 960 V/A). The output RF signal is then digitized by an 80 GSa/s real-time-oscilloscope (RTO) for offline signal processing. A 22 GHz brick-wall filter is used on the RTO to reduce the out-of-band noise and overshoot. The receiver DSPs are performed at 2 sps and 31 linear filter taps are used in all cases to equalize the distorted signal before BER calculation. We use the Finisar optical waveshaper as in past section to test the effect of different filter configurations and frequency offset (FO) tolerance.

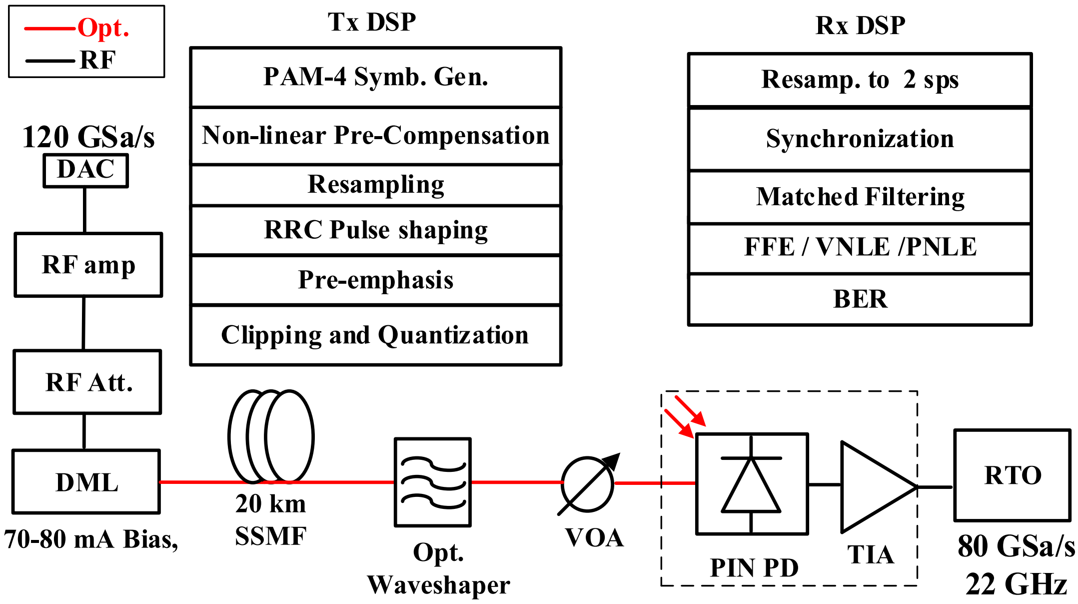

Fig. 4.33 Experimental setup with employed DSP at the transmitter and receiver.

4.4.3.2. DML transmission results with DSP

First, we check the B2B and 20 km DML transmission performance at 70 mA and 80 mA bias currents. We use a fixed driving signal of 1.2 V_{pp}. A higher driving signal causes stronger adiabatic chirp induced skew after propagation, which is detrimental for PAM4 signal, as described in the previous section. As for the biasing, at a lower bias current, the extinction ratio (ER) of the signal is higher for a fixed driving voltage and this results in a higher receiver swing at the fixed ROP. Therefore, at B2B, working at a lower biasing improves the SNR and BER. However, higher ER increases the impact of the transient chirp by the term $dlnP(t)/dt$, P being the DML output power, which broadens the spectrum. This results in worse BER after 20 km transmission for lower bias current as can be seen from Fig. 4.34(a). Here, we plot the BER vs. ROP for 70 mA and 80 mA biasing with linear FFE and 2nd order polynomial non-linear equalizer (PNLE) at the receiver. PNLE is the simplest form of Volterra non-linear equalizer (VNLE) where only the self-beating terms (i.e., polynomial terms composed of signals sampled at the same time) are utilized [67]. Due to the strong non-linearity caused by the chirp-CD interaction, PNLE improves the transmission results significantly. 80 mA biasing shows a better performance than 70 mA biasing after propagation due to lower overshoot and reduced spectrum width. Therefore, we fix our biassing to 80 mA for the rest of the work. As 2nd order PNLE gives clear improvement in BER performance, as a next step, we try stronger non-linear equalization schemes for 80 mA case with 3rd order PNLE and full Volterra filter of 2nd order. Fig. 4.34(a) plots the BER vs. ROP for these different equalization schemes and the memory lengths for different orders are given beside the schemes. It shows that the DML/DD system has high order of non-linearity and requires long memory lengths for best performance. However, taking the complexity of full VNLE and higher order non-linear equalizers into consideration, we keep ourselves limited to second order PNLE with 31 linear taps and 11 second order beating terms. For all the curves in Fig. 4.34, we can see that beyond -3 dBm of ROP, the BER degrades. This comes due to the saturation of TIA, which causes the outer eyes to close at high ROP.

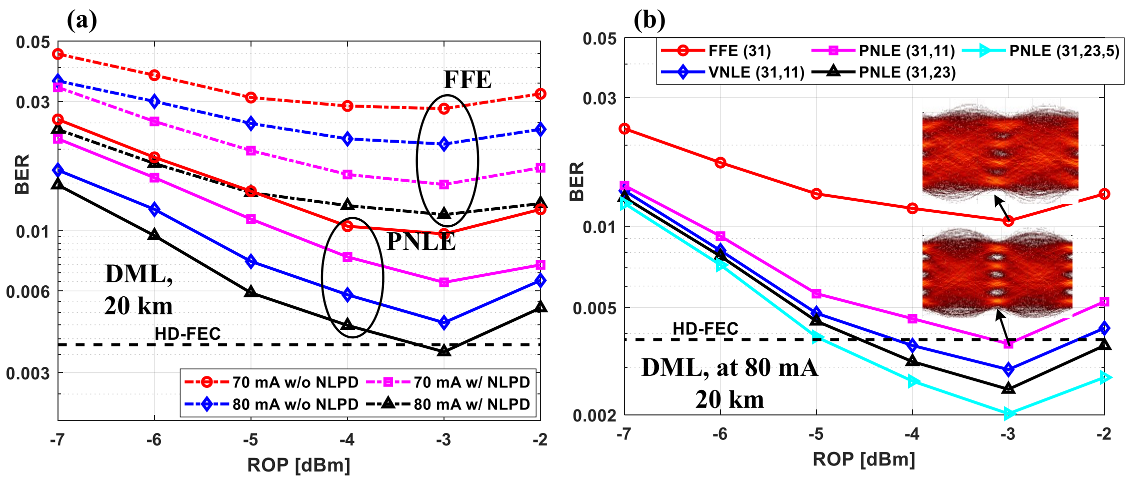

Fig. 4.34 (a) BER vs. ROP at two biasing points (70 mA and 80 mA) after 20 km transmission with (solid line) and without NLPD (dash-dot line) at the transmitter (b) BER vs. ROP with NLPD at 80 mA biasing with different equalization schemes. Eye diagrams after DSP are shown in the inset for –3 dBm ROP.

4.4.3.3. CML transmission results

Next, we employ a Super Gaussian (SG) optical filter (OF) with 50 GHz 3-dB BW (order 2) and check the filtering impact at B2B. As explained in the previous section, an SG filter can be a well-fit optical filter to improve the transmission results. Another reason for choosing SG is that it acts only as an amplitude filter and its response is close to a flat-top MUX/DEMUX filter already available commercially (Huber+Suhner CWDM filter). Filtering causes FM-AM conversion and increases the outer ER of the modulated signal, which in turn increases the receiver swing and ultimately the SNR of the signal. For Fig. 4.35 (b), we keep the ROP fixed at -3 dBm. For this case, the receiver swing keeps increasing with the increase in ER and BER keeps improving as well. At a high offset value, BER starts degrading due to the added nonlinearity and ISI in the system. However, if we apply NLPD, we can generate eye with unequal opening from the transmitter side, and this helps improve the BER even at high offsets. For each offset value, the LUT needs to be created independently since the added nonlinearity is different in each case. In Fig. 4.35 (c), we show the BER dependency on ROP when the offset is set to 25 GHz with and without NLPD. Similar to previous section BER improves until the signal saturates the TIA.

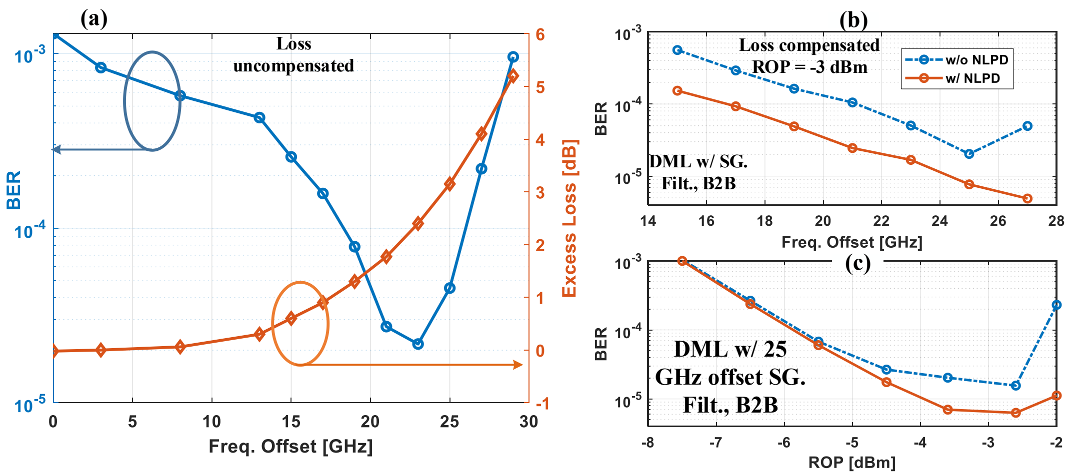

Fig. 4.35 (a) (a) BER vs. Frequency offset at a fixed ROP of -3 dBm and (b) BER vs. ROP at B2B with 2nd order SG filter at B2B with FFE.

The optical filtering becomes necessary after fiber transmission. To better understand this, in Fig. 4.36, we plot the optical and electrical spectra for different frequency offsets. From Fig. 4.36 (b), we see that for 20 km transmission, the DML/DD system acts as a high pass filter with around 17 dB attenuation of low frequency components. As the OF cuts more and more low frequency contents and increases the ER, the spectra tend to be flat indicating much improved transmission performance. As explained in the previous section, this is a result of various effects such as FM-AM conversion, AM-FM conversion, dispersion supported transmission effect, optical duobinary (ODB) effect, minimum shift keying format generation, the vestigial sideband (VSB) effect [127].

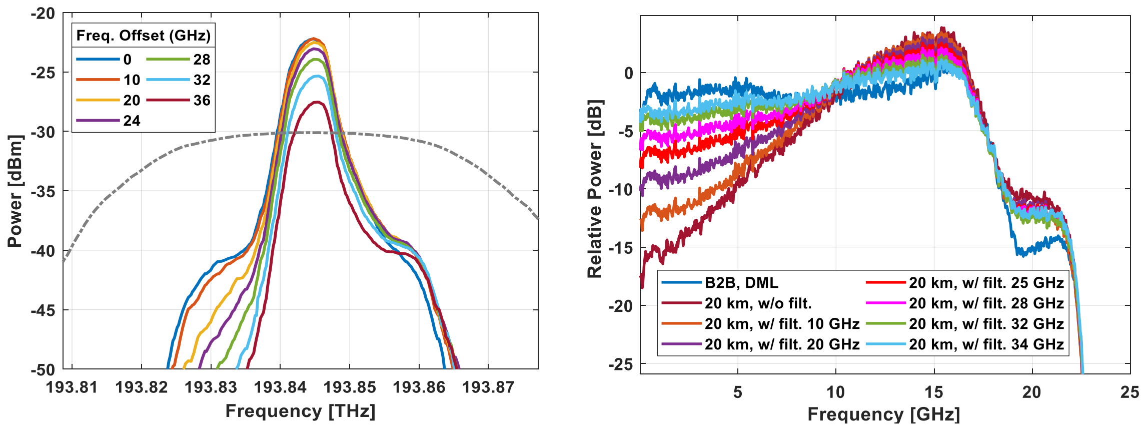

(a) Optical Spectra (b) RF Spectra

Fig. 4.36 (a) Optical spectra for different frequency offsets (FO) after 50 GHz SG OF (order 2). The filter shape for zero-offset case is shown in gray dash-dot line (b) RF spectra for different frequency offsets showing the impact of filtering.

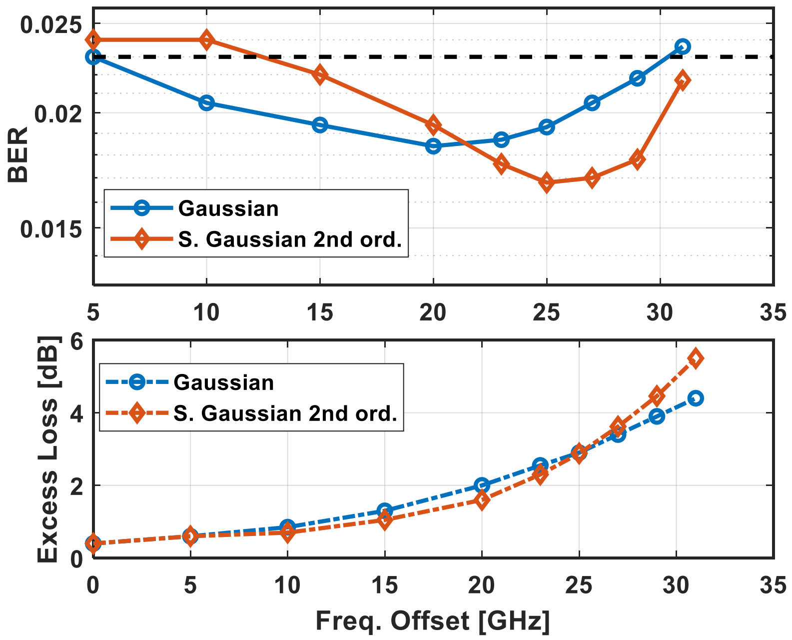

Fig. 4.37 (a) BER vs. FO w/ FFE after 20 km with 50 GHz 3-dB OF when the excess filtering loss is not compensated (black dashed line shows the BER for DML only case for -4 dBm of ROP) (b) Excess filter loss vs. FO for Gaussian and SG filter

However, the OF attenuates the modulated signal power, which has been neglected in many prior works. Since optical amplification is not preferred in IM/DD systems, the excess filtering loss needs to be considered. Keeping that in mind, in Fig. 4.37 (a), we plot the BER vs. FO with linear FFE for different orders of gaussian filters when the ROP with zero frequency offset is set to -4 dBm. The filter insertion loss is not considered here, since optical MUX/DEMUX filter can be utilized instead of the programmable filter used in this experiment. We also plot the excess loss due to the intentional attenuation of part of the signal spectrum in Fig. 4.37 (b). Since the loss is uncompensated in this case, due to the lower ROP, the received signal swing tends to decrease. But due to FM-AM conversion, ER increases and the swing at the receiver remains close to a constant except for very high offset values. Therefore, the BER improvement occurs primarily due to the flattened system response.

Both Gaussian and SG filters improve performance even when filtering loss is considered. Flat-top Mux/Demux filter can also be used as a filtering, but the offset needs to be chosen very carefully. As seen here, a 20 GHz offset works best with Gaussian response, but a higher offset is best with a sharper SG filter. An offset of 25 GHz gives optimum performance, which is very close to the simulation parameters presented in Table 4.1. Finally, we plot the BER vs. ROP curves for Gaussian and 2nd order SG filter with NLPD applied at the transmitter. We choose 25 GHz offset for these curves, although it adds 3 dB of signal attenuation. The filter enables 20 km transmission below the HD-FEC BER threshold with only linear FFE at the receiver. With PNLE, we could even lower the BER below 1e-3.

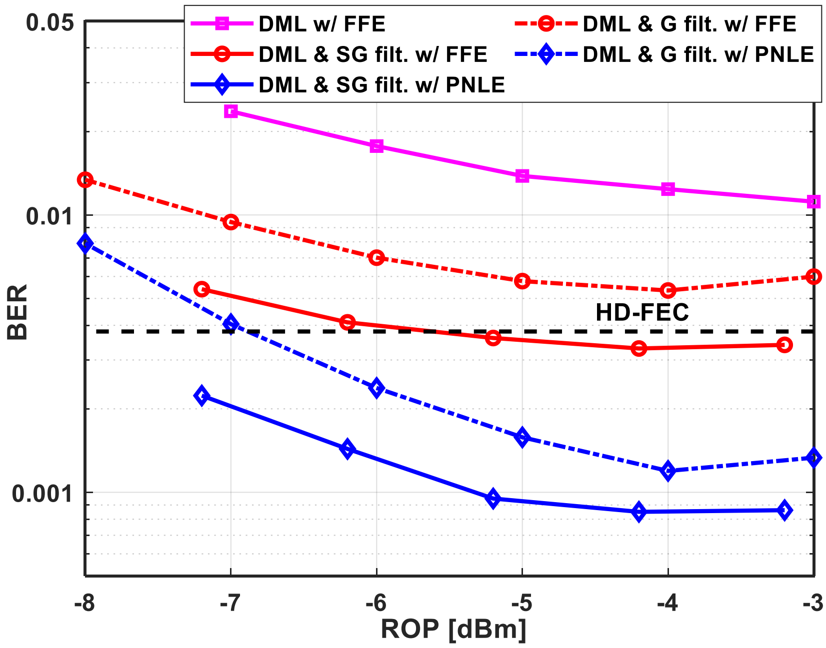

Fig. 4.38 BER vs. ROP with Gaussian and SG filter (2nd order) optical filter (with NLPD at the transmitter) for 25 GHz offset.

4.4.4 Summary

To conclude, we have presented the design methodology of optimum filter design for proper chirp management with different laser parameters (α and κ) and OMAs with NRZ and PAM4 format. This allows one to identify the best filter profile based on the DML output spectrum to enable transmission over longer fiber propagation distances. We demonstrated that only optical filter is insufficient for PAM4 signaling at higher symbol rates and DSP is necessary. Finally, we verified the impact of CML optical filtering in a C-band DML/DD system. It is shown that simple polynomial nonlinear equalization with the optimized CML filter can significantly improve the transmission performance and enables 70 Gbps PAM4 transmission over 20 km of SSMF without the need for any chromatic dispersion compensation.

Chapter 5 Self-coherent single-sideband systems for 40 km C-band Transmission

5.1 Overview

In the previous chapter, we demonstrated MZM and DML based IMDD transmission over 10 to 20 km, with the aid of optical filters: an all-pass phase filter as ODC and an amplitude filter for CML. However, if we want to further increase the transmission distance, simple filtering might not be enough. For DML, going above 100 Gbps is difficult due to BW limitation. Therefore, we need to rely on EML or MZM for 200G throughput. Here, in this chapter, we focus on transmitting high data rate signals (200 Gbps) over 40 km transmission reach in a C-band direct detect system using dual drive Mach-Zehnder modulator (DDMZM). As described in Chapter 2 and 3, for an MZM based system after fiber transmission, there is significant amount of power fading, which limits the transmission speed and reach. Self-coherent (SC) single-sideband (SSB) transmission is immune to this fading and enables a longer transmission reach, making it a promising choice for longer transmission distances. But generating high quality SSB signal is challenging. Chapter 2 describes some common ways of generating SSB signal. Since the real and imaginary part of an optical SSB signal needs be a Hilbert transform pair, compared with the transmitters primarily used in a conventional IM/DD system, optical SSB transmitters are more complicated. It requires either optical filtering or optical synthesizing. The first approach utilizes an optical filter to reject a sideband of a double sideband (DSB) signal, which creates a vestigial sideband (VSB) signal due to the limited edge roll-off of optical filters [165, 166]. However, the filter needs to ultra-sharp to properly create an SSB signal. The alternative way is to drive an IQM or DDMZM with two driving signals that acts as a Hilbert transform pair. Although an IQM can create high quality SSB signal, this comes at the price of an added DAC channel, which ultimately increases the cost and complexity of the system. The carrier in this case can be generated virtually [167] or by off-biasing the IQM [168] or by a separate laser source [169], making it even more complex.

Another approach for SSB signal is to use a 90^0 RF quadrature hybrid and drive the DDMZM with the Hilbert transform pairs [35, 170]. This scheme requires a high quality and wide bandwidth RF quadrature hybrid, making it difficult for high data rate transmission. In [35], we demonstrated 100 Gbps SSB signal transmission over 60 km using a commercial quadrature hybrid. This RF scheme, however, requires only one DAC channel, making it attractive for low-cost IMDD applications. In [171, 172], authors proposed a vestigial sideband (VSB) signal generation method using a time skew and dual drive Mach-Zehnder modulator (DDMZM) and demonstrated the transmission of 38 Gbaud PAM-4 signal over 80 km of SSMF. However, this scheme has a high DSP complexity and leads to a stronger image band when the system operates at higher symbol rates. Therefore, we utilize the time skew approach with practical optical filtering to transmit high data rate signals. First, we present detailed numerical simulations in section 5.2 for 106 Gbaud PAM4 signaling where only optical filter or optical filter along with optimized RF skew are utilized for SSB generation. Followed by that we verify the idea experimentally in section 5.3, where we transmit 92 Gbaud PAM signals over 40 km of standard single mode fiber (SSMF) without any optical or electrical dispersion compensation.

5.2 Operation principle of RF delay assisted SSB transmitter

As shown in [171, 172], the Fourier transform of the output optical field $E_o(t)$ of a DDMZM when there is a time skew τ between the differential driving signals is given as:

$$FT\{E_o(t)\} = C - 2e^{-j\pi f\tau}\, sin(\varphi + \pi f\tau) S(f),$$

where C is the CW-tone, φ is the phase shift in each MZM arm due to a voltage bias, and $S(f)$ is the Fourier transform of the driving signal, $s(t)$. Therefore, we can see that the time skew acts as a shaping filter, $G(f) = \sin(\varphi + \pi f\tau)$, where φ is usually fixed to $\pi/4$ or $3\pi/4$ for linear modulation at quadrature bias point. The RF skew (τ) determines the bandwidth of the passband. Fig. 5.1 shows the architecture of the SSB transmitter.

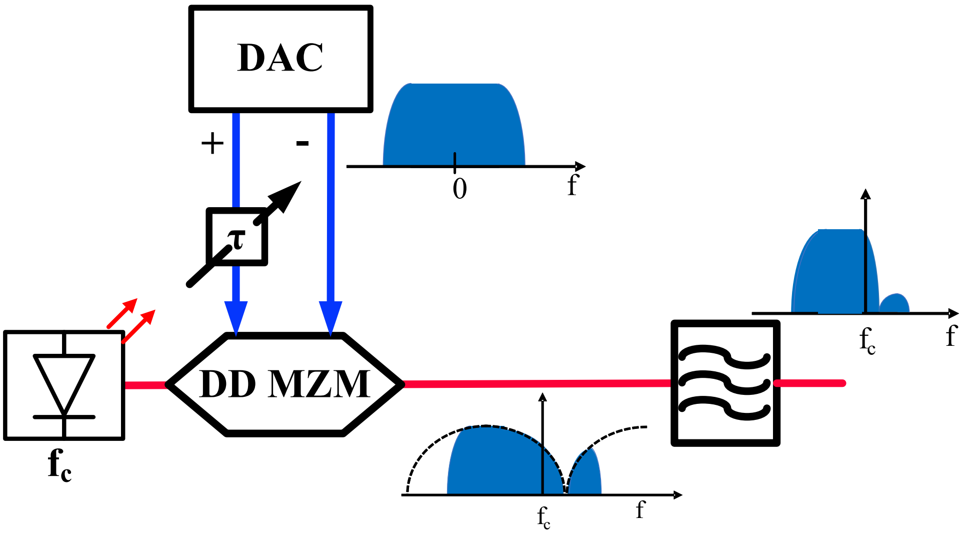

Fig. 5.1 Schematic diagram of the SSB transmitter.

As depicted in Fig. 5.1, by properly tuning the delay, we can introduce a notch close to the carrier and that creates a VSB signal. However, for high BW signal, there will be significant amounts of power in the high-frequency region of the image band. We use a moderate roll-off optical filter to attenuate this part of the spectrum. Flat-top wavelength-division multiplexing (WDM) Mux-Demux filters can also be used instead, which are employed for multi-wavelength operation, like ER4 or LR4 applications.

Now, let us look at the optical spectra immediately after the DDMZM when we drive it with a 53 Gbaud and 106 Gbaud PAM4 signals, which corresponds to net 100 Gbps and 200 Gbps, respectively. We use a roll-off-factor of 0.1 for these results. We assume no bandwidth limitation from the RF transmitter. The spectra plotted in Fig. 5.2 shows that as the time-skew (RF delay) is increases, we can bring the notch close to the carrier creating a VSB signal. If no additional optical filtering is employed, then the power in the high frequency region of the image band will be significant and degrade the transmission performance. To visualize the impact of the skew on the BW of the shaping filter, we plot the optical spectra over a wider frequency range in Fig. 5.3 for 106 Gbaud PAM4 signal. We can also see the shaping filter also acts as a high pass filter within the signal BW (if set appropriately) and can compensate for the low-pass response of DAC, RF drivers, delay lines, MZM and PD to some extent. This is useful since this will reduce the amount the pre-emphasis required for the signal transmission.

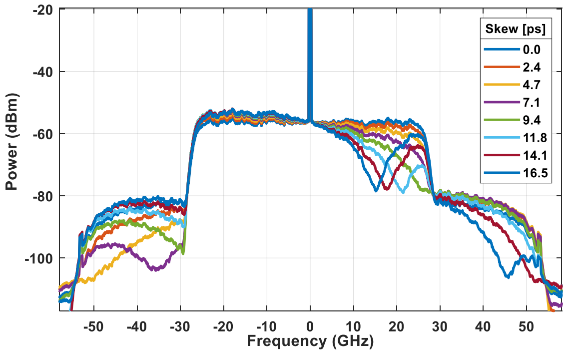

53 Gbaud

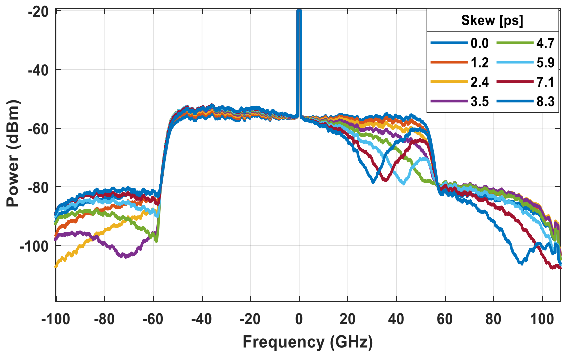

106 Gbaud

Fig. 5.2 Optical spectra after the DDMZM for different amounts of skew. Frequency axis is plotted relative to the carrier frequency.

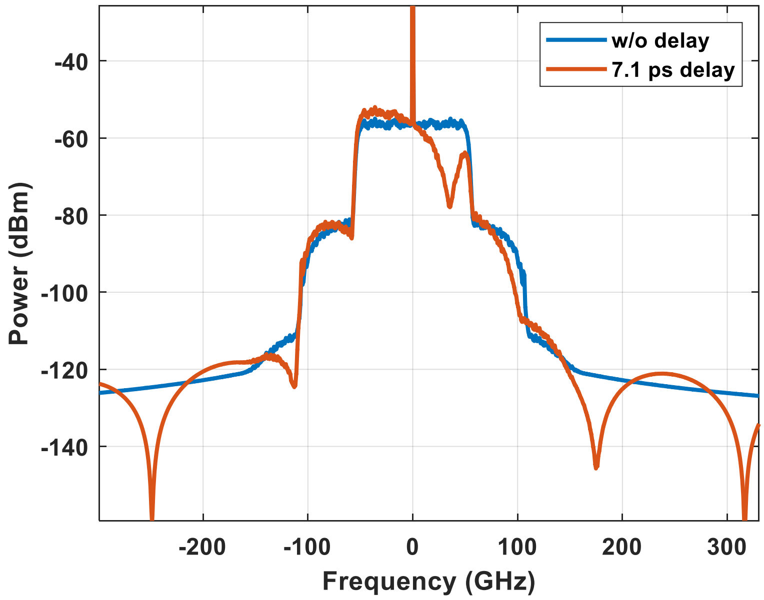

Fig. 5.3 Optical spectra after the DDMZM with and without delay for 106 Gbaud PAM4 signal.

In Fig. 5.4, we plot the eye diagrams after the driver and DDMZM. The eyes after the DDMZM shows open eye. However, when we introduce skew, as it attenuates part of the optical spectra, it creates an ISI. With strong skew (8.3 ps), it almost creates a 7-level duobinary signal. And due to the power in the image band, it will still cause power fading after PD squaring.

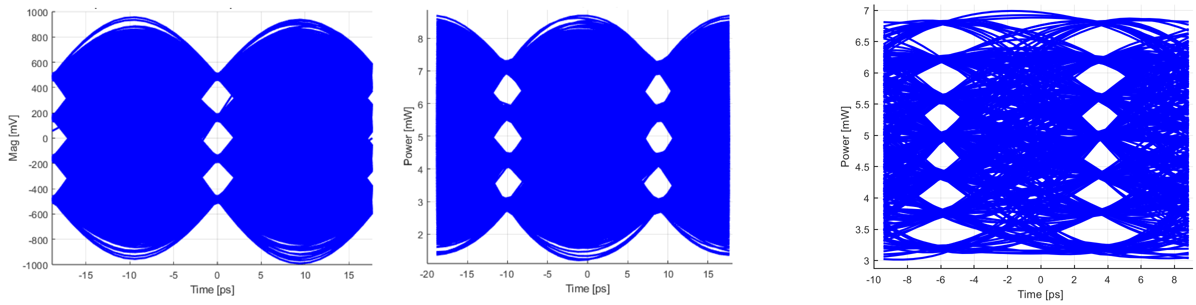

(a) Electrical Eye after driver (b) Optical eye after DDMZM (no skew) (c) Optical eye after DDMZM (8.3 ps skew)

Fig. 5.4 Eye diagrams after driver and DDMZM

As a next step, we look at the effect of optical filtering on the signal, when no time skew is employed. We choose an optical filter of 125 GHz 3-dB BW with Super Gaussian (SG) shape. The center frequency is set such that it attenuates 3-dB of carrier power, i.e., for all cases the optical signal power after the filter remains the same. It should be noted that this is not the optimized position of the filter for best transmission performance since the carrier-to-signal power ratio (CSPR) needs to be optimized for optimum performance [173]. Now if we look at the system response after 40 km of SSMF transmission, we can see that a sharp optical filter is required to reduce the power fading. With a SG filter of 2nd order, there are strong notches in the system spectrum, which are difficult to compensate at the receiver. However, if we shift the filter center frequency to attenuate more signal power in image band, it will attenuate the carrier power as well. This will lower both the average optical power and the CSPR of the signal. Since it is undesirable to employ optical amplifier in IM/DD system, we cannot attenuate the signal power unconditionally, and therefore the filter position needs to be chosen carefully.

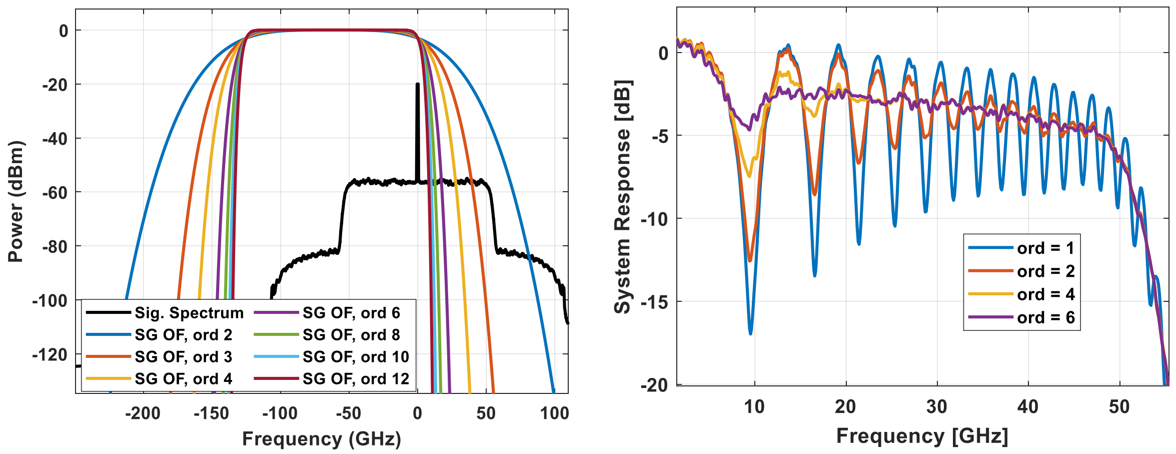

Fig. 5.5 Signal spectrum and optical filter spectra for different orders (left). The system response after 40 km of SSMF transmission (right)

Since our target is to use the RF skew in conjunction with optical filter, we check the system response for different amounts of skew along when we employ an additional optical filter to suppress the power in the image band. In Fig. 5.6, we plot the system response after 40 km of SSMF transmission for different RF skew with Gaussian and SG filter of order 2. We can clearly see that a SG filter of order 2 with 7-8 ps of RF skew can reduce the depth of notches significantly. Due to the presence of signal power in the low frequency region of the image band, the first two-three notches are still present and cannot be avoided.

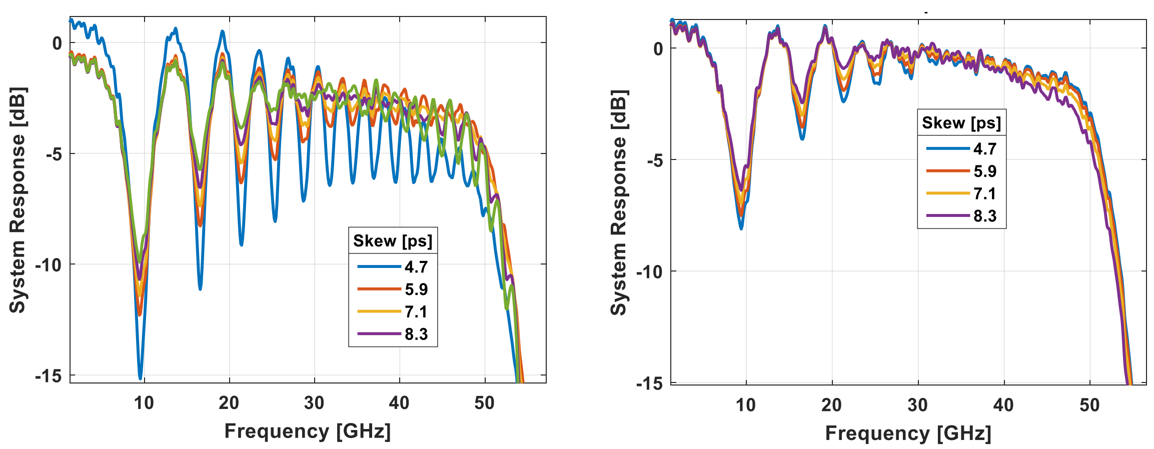

Fig. 5.6 System response after 40 km of SSMF transmission for different RF skew with Gaussian filter (left) and SG filter of order 2 (right)

Lastly, we did BER analysis to test the filter sharpness requirement along with the skew. In Fig. 5.7 (a), we show the BER curves with different optical order of filters and RF skew. We use polynomial non-linear equalizer with 101 linear taps, and 11 second order taps for the results. No signal-signal beat interference (SSBI) cancelation or Kramers-Kronig (KK) scheme were employed in this simulation. Since the transmission distance is limited to 40 km, no CD compensation is done at the receiver. This is why many linear taps are required to equalize the received signal. The blue curve with circle marker shows the results for filter only case. The BER improves sharply as the order increases from 1st order to 4th order and then improves slowly. While with RF skew, even Gaussian filter can bring the BER below the HD-FEC threshold of 3.8e-3. Increasing beyond the 2nd order improves the results marginally. In Fig. 5.7 (b) we plot the equalizer filter taps for this optical filter. It is understood that a large number of taps are required in both cases to compensate for the impairment.

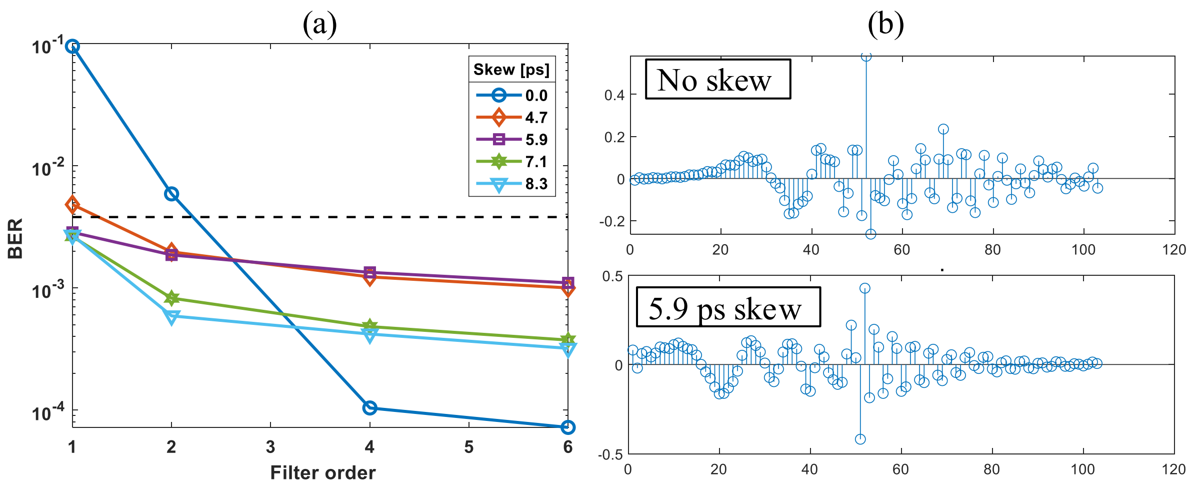

Fig. 5.7 (a) BER vs SG Filter order for different time-skew, (b) Linear filter taps with 2nd order SG filter

5.3 Experimental setup and DSP deck

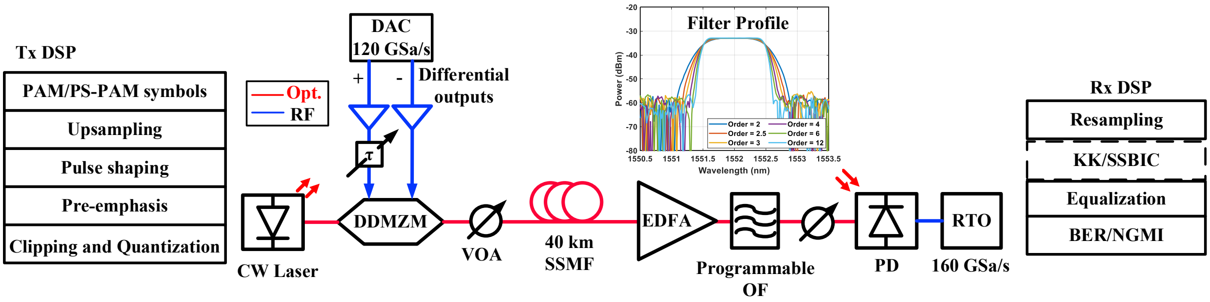

Fig. 5.8 Experimental set up and DSP deck. DD-MZM: Dual drive Mach-Zehnder modulator. The inset shows filter response of OF as captured by an OSA (resolution: 0.05 nm)

In this section, we demonstrate the RF-skew assisted SSB signal transmission scheme for a single channel case. Fig. 5.8 depicts the experimental setup to evaluate the performance. The transmitter (Tx) incorporates a tunable laser operating at 1550 nm and a 32 GHz (3-dB BW) $LiNbO_3$ DDMZM. The modulator is biased at the quadrature point and is driven by a pair of RF amplifiers connected with the differential DAC outputs. Two phase adapters (67 GHz) are utilized in the RF paths that can generate a time delay of up to 25 ps between the RF signals. The Tx side DSP includes symbol generation, raised cosine pulse shaping, pre-emphasis of the RF chain, clipping, and resampling to the DAC sampling rate of 120 GSa/s. After modulation, the signal is transmitted over 40 km of SSMF, amplified by an EDFA, and filtered by a programmable waveshaper. The EDFA is required in our system to compensate for the insertion loss of the waveshaper and the absence of TIA. The system incorporates one variable optical attenuator (VOA) to optimize the launch power (LOP), and another VOA before the photodetector (PD) to adjust the received optical power (ROP). The inset of Fig. 5.8 shows filter profiles of different orders of Super Gaussian (SG) optical filter (OF). The 3-dB bandwidth of the filters is fixed at 125 GHz, and the central wavelength is adjusted to create a SSB signal. Finally, the output of the 50 GHz PD is digitized using a 62 GHz RTO and processed offline for equalization with linear feed forward equalizer (FFE) and BER/NGMI calculation. We employed KK and SSBIC in the receiver DSP, however no CD compensation is performed.

5.4 Results and discussions

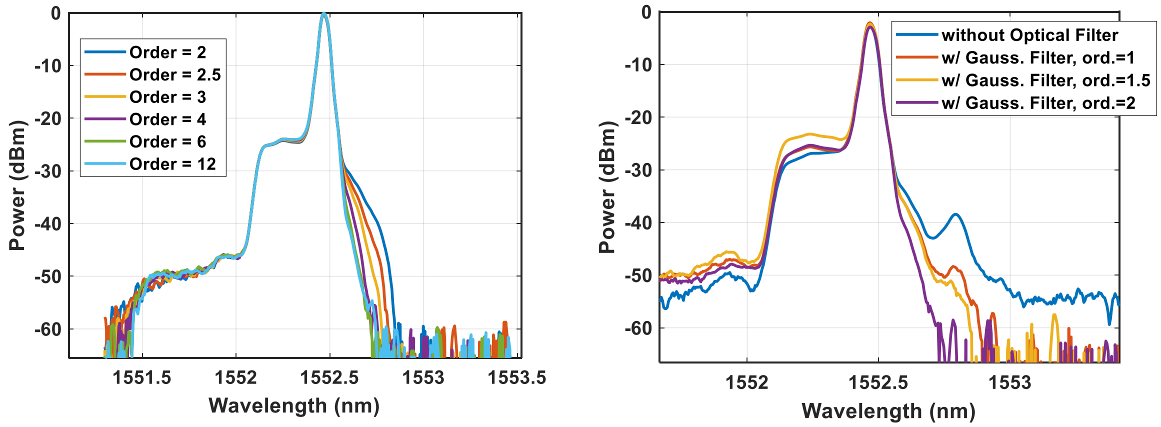

Fig. 5.9 (a) Optical Spectra after Gaussian filtering (no delay), (b) Optical Spectra with optimized delay and w/wo optical filter

Since the DAC and DDMZM have severe bandwidth limitations, we cannot generate high quality 106 Gbaud PAM4 signaling. The transmitter limits the symbol rate below 100 Gbaud. Fig. 5.9(a) presents the optical spectra with a resolution of 0.05 nm obtained by filtering an 89 Gbaud PAM4 DSB signal with different orders of SG OF. We tune the delay lines to create a notch in the spectrum near the carrier, as shown in Fig. 5.9 (b). The blue curve shows that although the sideband is suppressed by the sine envelope near the carrier, significant power remains in the high-frequency region of the image band, which will ultimately degrade the system response. To demonstrate the impact of the optical filtering, we plot the received signal spectrum after 40 km transmission in Fig. 5.10 with and without time skew. The spectrum without any RF delay and a high 12^{th} order SG filter is also plotted, where the notches in the spectrum are barely noticeable.

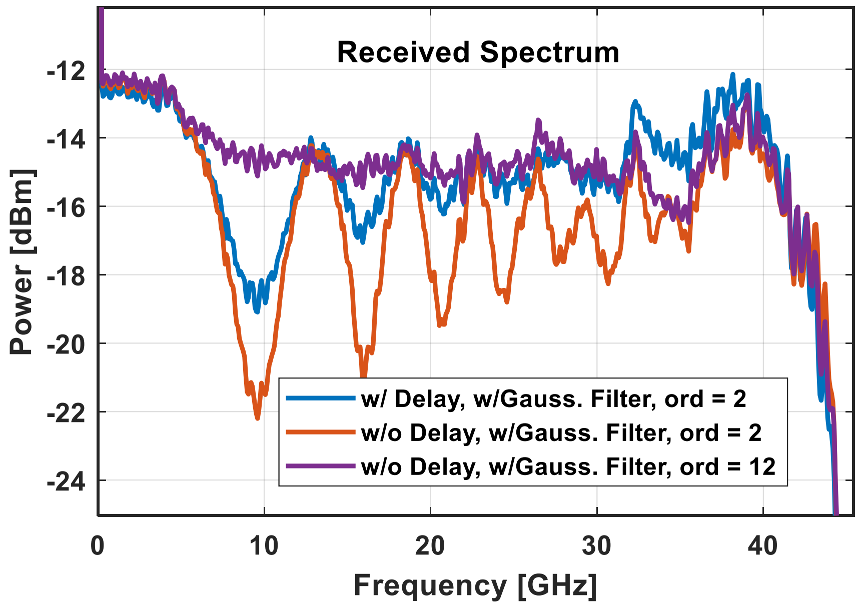

Fig. 5.10 Signal spectrum (FFT of received waveform) after 40 km transmission.

Fig. 5.11 (a) and 5.11 (b) plot the measured BER and NGMI vs. ROP for an 89 Gbaud PAM4 and PS-PAM8 signal, respectively with and without a delay and OF. The PS-PAM8 signal is selected because the limited BW of the transmitter cannot generate a net 200G signal even at B2B with PAM4. However, PS-PAM8 requires a higher SNR and hence SD-FEC is adopted to achieve net 200 Gbps transmission. An IBPS of 2.35 bits/symbol is chosen for this figure. Since SSBIC is utilized, we limit ourselves to linear equalization with 81 linear taps. A launched optical power of 5.5 dBm and a CSPR of 14.5 dB are used for the transmission results. Higher LOP should improve the performance further. However, the loss of the DDMZM limited the LOP to 5.5 dBm. With a 2^{nd} order SG filter, we could transmit 89 Gbaud PAM4 and PS-PAM8 (IBPS = 2.35 bits/symbol) signal at the HD-FEC BER and SD-FEC NGMI threshold, respectively. We test the maximum IBPS that we can transmit at 89 Gbaud in Fig. 5.12. An IBPS of 2.43 bits/symbol is achievable at the 0.8798 NGMI threshold with a 2^{nd} order SG filter, which corresponds to a net rate of 216 Gbps.

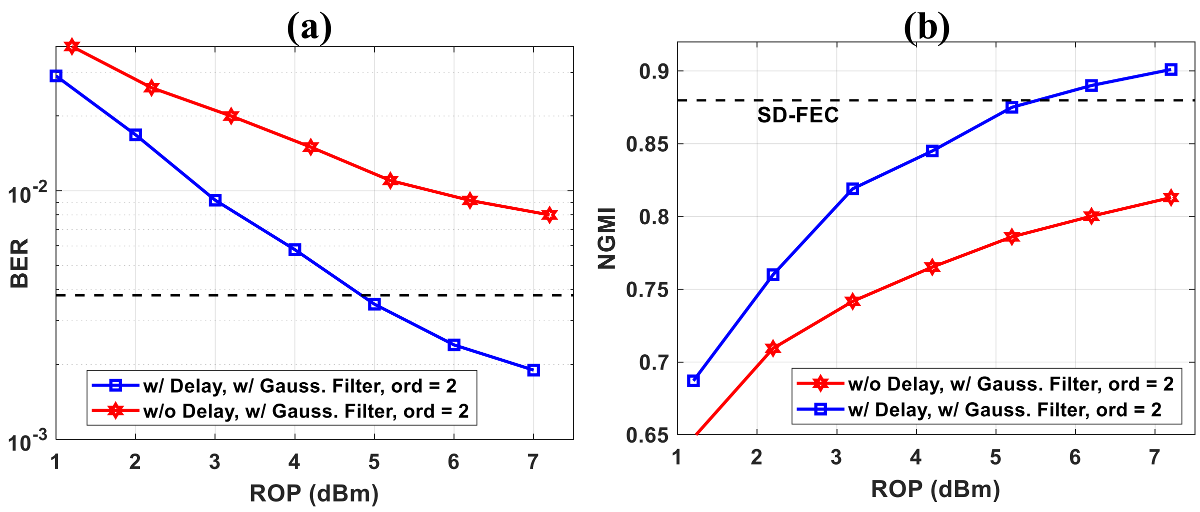

Fig. 5.11 (a) BER versus ROP for PAM4, (b) NGMI versus ROP for PS-PAM8 (IBPS = 2.35 bits/symbol) at 89 Gbaud

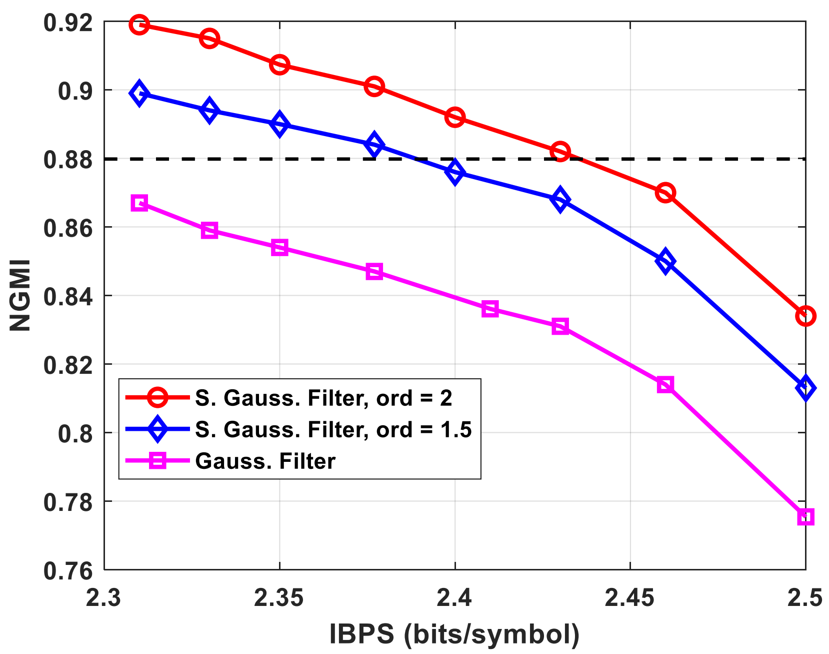

Fig. 5.12 NGMI versus IBPS for PS-PAM8 signal with different optical filters.

Although the optimal skew depends on symbol rate, we fixed the delay for Fig. 5.13 and vary the symbol rates of PAM4 and PS-PAM8 signaling. 92 Gbaud PAM4 (net 172 Gbps) and PS-PAM8 (net 216 Gbps) can be successfully transmitted over 40 km of SSMF at HD (SD) FEC threshold. Therefore, 92 (89) Gbaud PS-PAM8 with an IBPS of 2.35 (2.43) bits/symbol can be chosen for maximum throughput for our system.

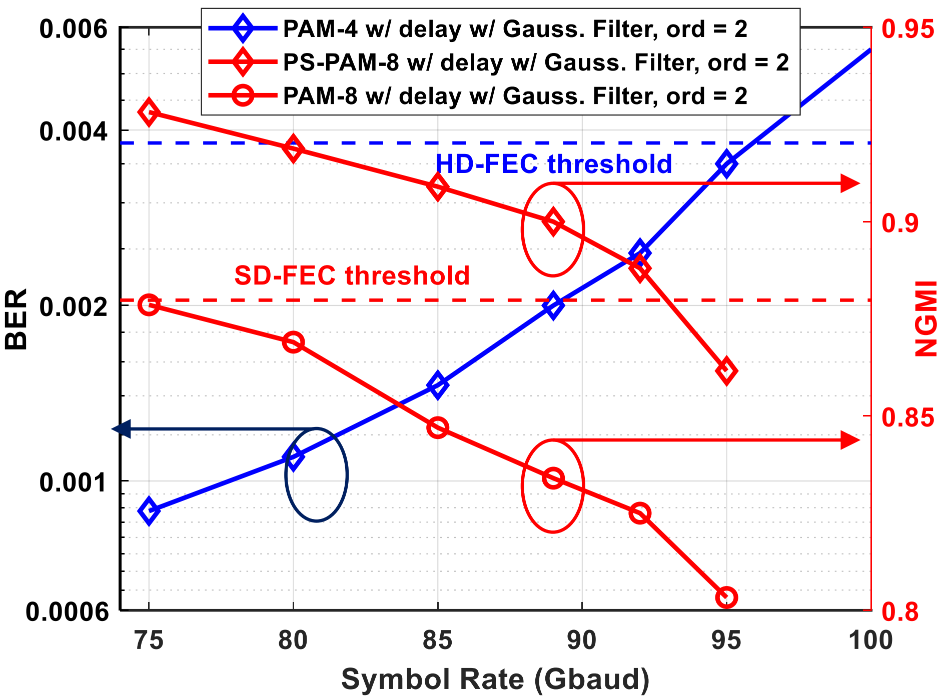

Fig. 5.13 BER/NGMI vs symbol rate for PAM-4, and PS-PAM8 (IBPS = 2.35 bits/symbol) signal

As previously mentioned, the choice of SG optical filter is motivated by the commercially available four channel Huber+Suhner DWDM Mux-Demux pair with a channel spacing of 200 GHz. The filter response of the DWDM Mux is plotted in Fig. 5.14 (a). The 4×1 DWDM Mux has a flattop response with the passband center wavelengths ranging from 192.98 THz to 193.58 THz. The 3-dB BW of the Mux filter is around 150 GHz. The shape of the Mux filter closely resembles an SG filter of order 2.5 as shown in Fig. 5.14 (b). Since, in a DWDM system, two of these filters will be used, the passband BW will be reduced. The BW of a cascade of two 2^{nd} order SG filters each with 150 GHz 3-dB BW is another SG filter with $\frac{150}{\sqrt[4]{(2)}} = 126$ GHz 3-dB BW. Therefore, we chose a 3-dB BW of 125 GHz in our single channel experiment.

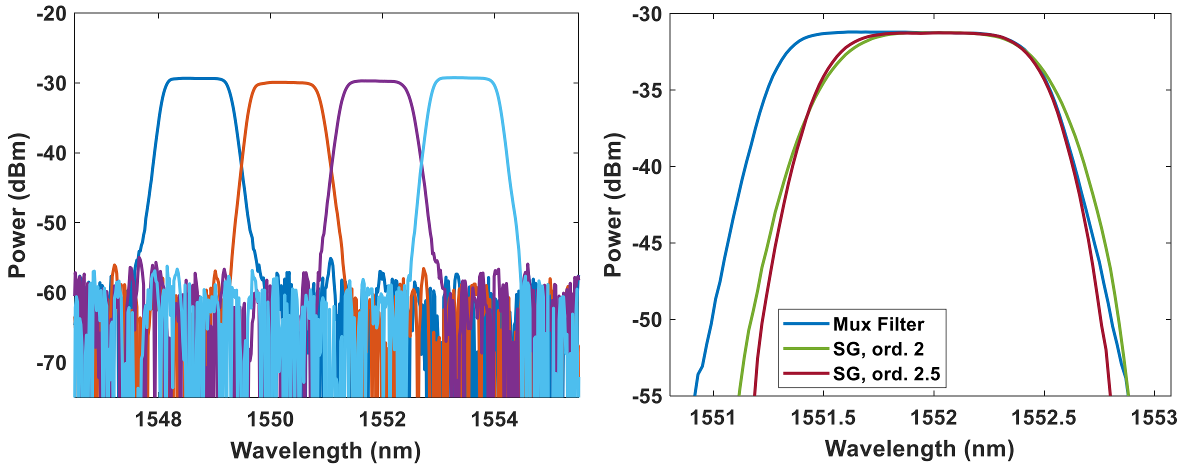

(a) DWDM Mux/Demux Filter shape (b) One channel of DWDM filter and 125 GHz SG filter

Fig. 5.14 Filter Response of optical filters

We also conducted a 4 channel DWDM experiment with the proposed method. Here, four tunable ECLs generate 4 optical carriers, whose wavelengths are shifted to the passband edge of the DWDM filter to suppress the signal image band. We bulk modulate three channels with another $LiNbO_3$ MZM of similar BW with no RF delay. The optical spectrum of the WDM SSB signal, where the channel under test (CUT) is in the WDM channel centered at 193.32 THz or 1550.8 nm is shown in Fig. 5.15. Due to RF skew, the CUT shows a much better sideband suppression as compared to the remaining three channels. The 40 km transmission results of the four channels at 92 Gbaud are given in Table 5.1.

Table 5.1 IBPS and Throughput of each WDM channel

	Ch 1	Ch 2	Ch 3	Ch 4
NGMI	0.881	0.882	0.88	0.88
IBPS (bits/symbol)	2.33	2.33	2.31	2.37
Throughput (Gbps)	214	214	212.22	217.64

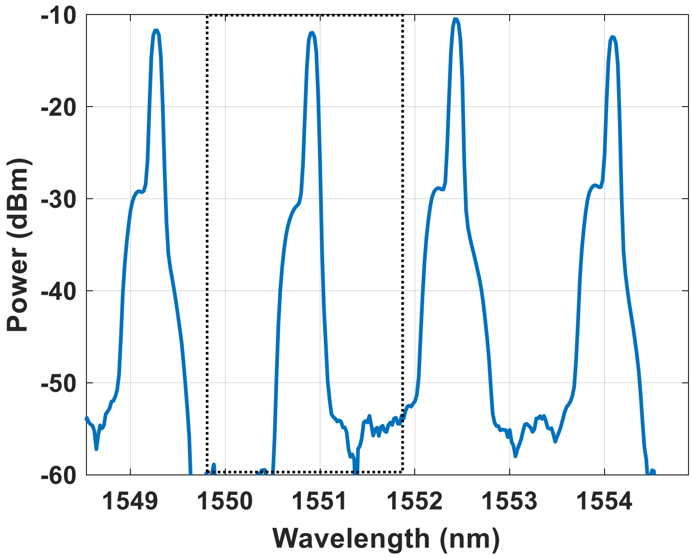

Fig. 5.15 Optical spectrum of the 4 channel WDM signal (CUT is the 2nd channel from left)

5.5 Summary

We propose to employ an RF skew in conjunction with an optical filter to create a single side band (SSB) signal, which can be propagated over 40 km of SSMF in the C-band. For single channel experiment, with a 2nd order SG filter, we transmitted 92 Gbaud PAM4 below the HD-FEC BER threshold. Adopting a higher order PAM8 signal and probabilistic shaping, we could achieve a throughput of 216 Gbps at the SD-FEC NGMI threshold. As a next step, we used a WDM mux filter and conducted a 4-channel experiment. Each of the channels could transmit a net 212 Gbps PS-PAM8 signal and an aggregate of 858 Gbps over 40 km of SSMF using SSBIC and a linear equalizer.

Chapter 6 Conclusion

6.1 Summary

In this thesis, we worked on three important targets in optical communication: higher throughput, lower cost, and longer reach. It is next to impossible to achieve all these three in a single system. The three main chapters of the thesis target each one of these research directions. But since meeting the data traffic demand is the main driving force of the next generation optical communication, we focus on higher order modulation format (mostly PAM4) and DSP in all our work. In Fig. 6.1, we try to illustrate this research endeavors with a block diagram. There are four points that we note for each chapter: Operation wavelength (O-band or C-band), throughput and cost, transmission reach, and modulation mechanism. We elaborate on these contents in the successive paragraphs.

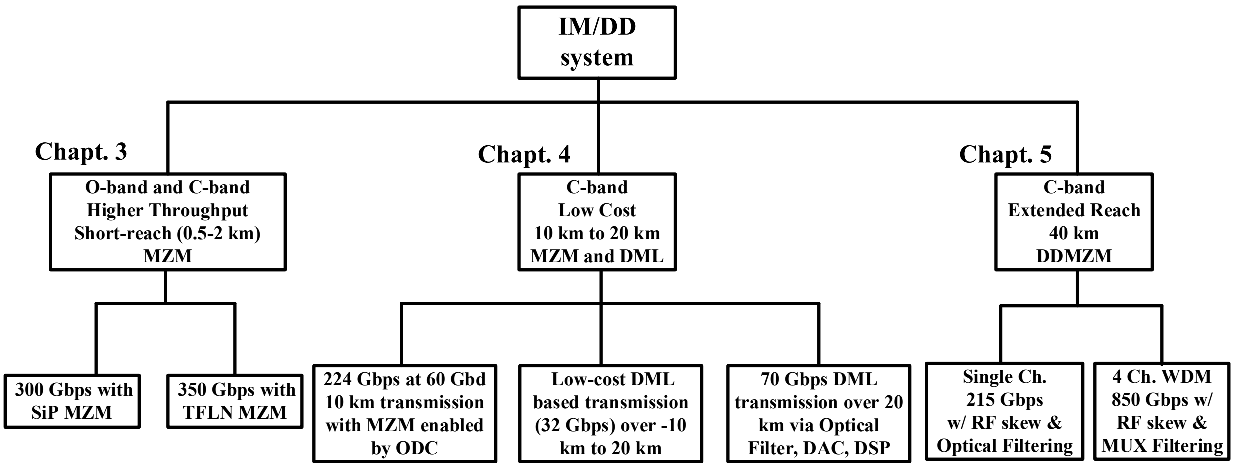

Fig. 6.1 Summary of the original contributions of the thesis.

In **Chapter 3**, we targeted the highest throughput that one can achieve in a typical IM/DD system. We focused on experimental demonstrations in this chapter and utilized advanced DSP and latest generation of DAC and ADC. We worked with two different material platforms: SiP and TFLN, where both utilized a single drive MZM. We presented the first net 300 Gbps transmission using a SiP MZM in an IM/DD link. We also transmitted net 300 Gbps with TFLN MZM. To achieve this, the SiP MZM required 3 V_{pp} driving voltage and a more aggressive SD-

FEC coding scheme. On the other hand, TFLN required 1.2 V_{pp} driving voltage at HD-FEC threshold. With TFLN, we could push the capacity to net 350 Gbps. Unlike SiP modulator, the results with TFLN modulator were limited by the RF transmitter itself. This chapter demonstrated that although SiP offers low-cost fabrication, it is much less power efficient and limited in terms of BW than TFLN modulators. With cost and footprint reduction, TFLN modulators will be a promising choice for future DCI applications.

In **Chapter 4**, we worked on C-band fiber transmission enabled by optical filtering (OF) targeting a cost-effective transceiver solution. In section 4.1, we used a $LiNbO_3$ MZM, and utilized a SiN ODC to compensate for the CD. The ODC can be integrated with an MZM and allows DWDM transmission to increase the aggregate throughput. The ODC is based on all-pass micro-ring resonator that provided 62 ps of group delay to allow 10 km SSMF transmission. In section 4.2 and section 4.3, we relied on low-cost DML to transmit PAM4 signal over different distances, which is also attractive for its power efficiency. At first, we comprehensively analyzed the DML chirp-CD interaction numerically. Next, we characterized a commercial DML and demonstrated 32 Gbps PAM4 transmission enabled by optical filter without resorting to any DAC or DSP. As a next step, we worked on optimizing the passband profile of the optical filter to obtain a desired extinction ratio (ER), that helps extend the transmission reach. Since DML/DD system has significant nonlinearity and BW limitation, we demonstrated that optimized optical filter and efficient DSP can push the transmission speed to 70 Gbps with a 17 GHz commercial DML.

Finally, in **Chapter 5**, we adopted SSB/VSB self-coherent scheme to extend the reach of an IM/DD system. Ideal SSB is immune to CD induced power fading, however, is hard to achieve. We proposed a joint RF and optical domain solution to tackle this issue. At first, we studied the impact of RF skew with a DD-MZM based system for net 200G PAM4 transmission. We demonstrated that only RF skew is not sufficient to create high quality SSB signal and moderate optical filtering is necessary. Following this, we presented RF-delay assisted single channel and multi-channel signal transmission over 40 km of SSMF. We showed that WDM Mux/DeMux filter can act as the required optical filter to enable net 215 Gbps/λ signal transmission.

6.2 Future work

Despite all the results presented in this thesis, there are still opportunities for future projects that can be built upon the completed work. We briefly introduce some of the prospective research avenues based on this thesis.

The work of Chapter 3 focused on high speed MZM based transmission over short reach (0.5 km to 2 km) distances. Here we presented results with two SiP O-band modulators, the longer 2.5 mm one showing the best performance. The obvious next target is to improve the BW and V_π of the MZM. One way to achieve this is to optimize the doping density, phase shifter length and on-chip termination. In our experiment, we needed to employ PDFA due to the absence of high BW PD-TIA. With proper peaking from the driver and TIA, and edge coupled MZM, the throughput could be further improved. The next step would be to design a DP-IQM with the optimized child MZM. Since coherent transmission ideally requires higher swing, the target would be to lower the V_π, even if it requires sacrificing some EO bandwidth. With 300 Gbps per degree of freedom (DOF), the DP-IQM should enable 1.2 Tbps/λ transmission, which has great potential in future DCI for 10 km O-band transmission. As for our TFLN experiment, the main limitation was the DAC and driver itself. With a smaller V_π TFLN MZM, we have already demonstrated 400 Gbps transmission in IM/DD link [174]. With the next generation of DAC and driver, we believe this can be further extended. This indicates the possibility of achieving net 1.6 Tbps (4×400 Gbit/s) in O-band, in both PSM and CWDM configurations. Since this requires operation beyond 200 Gbaud, CD induced penalty will come into play for CWDM links. Advanced DSP, for example DFE-FFE, nonlinear MLSE, Tomlinson-Harashima Precoding (THP) etc. need to be utilized to achieve net 1.6 Tbps IM/DD transmission over 2 km to 10 km reach.

In Chapter 4, we mostly dealt with optical filtering (phase or amplitude) for longer transmission. One future work involves integrating a SiP MZM with ODC on a single chip and making the ODC tunable by proper heater control. The passband of the ODC needs to be increased to handle higher BW signal (112 Gbaud). This can be applicable for O-band edge channels as well, which limits 200 Gbps signaling to 2 km. In section 4.2 and 4.3, we worked with low bandwidth C-band DML, which limited its performance to 35 Gbaud. 53 Gbaud PAM4 (net 100 Gbps) has already been demonstrated in O-band as mentioned previously. Therefore, an attractive short-term project is to test the BER vs. CD in the O-band at a higher symbol rate for the edge channels and compare its trend with C-band results. Another important research direction is to derive an analytical equation to predict the range of CD values, where the BER after positive dispersion improves. In section 4.3, we presented the filtering requirement considering C-band transmission. Similar analysis needs to be carried out in the O-band for 100G DML since it shows a higher potential in DCI market.

Finally, in Chapter 5, we combined RF and optical solution that can cost-effectively generate SSB/VSB signal. This delay can also be created via passive optical delay line, as demonstrated in our recent OFC work [175]. A promising next step is to combine the optical delay line and an optical filtering with DD-MZM on the same chip to create high quality SSB signal. The optical filter can be ring-resonator based notch filter that can selectively kill the unwanted signal power in the image band. An alternate way to generate SSB/VSB signal would be to use an RF hybrid along with an optical filter. This principle achieved 30 dB unwanted sideband suppression in a wide 2-40 GHz frequency range [176]. It would be interesting to test this principle in large signal transmission at high operating speeds. The impact of amplitude and phase imbalance between the RF hybrid coupler output ports needs to be analyzed as well to understand the practicality of this scheme.

Reference

[1] K. Zhong, X. Zhou, J. Huo, C. Yu, C. Lu, and A. P. T. Lau, "Digital signal processing for short-reach optical communications: A review of current technologies and future trends," *Journal of Lightwave Technology,* vol. 36, no. 2, pp. 377-400, 2018.

[2] "IEEE Standard for Ethernet - Amendment 11: Physical Layers and Management Parameters for 100 Gb/s and 400 Gb/s Operation over Single-Mode Fiber at 100 Gb/s per Wavelength," *IEEE Std 802.3cu-2021 (Amendment to IEEE Std 802.3-2018 and its approved amendments),* pp. 1-87, 2021, doi: 10.1109/IEEESTD.2021.9381783.

[3] X. Pang *et al.*, "200 Gbps/Lane IM/DD technologies for short reach optical interconnects," *Journal of Lightwave Technology,* vol. 38, no. 2, pp. 492-503, 2020.

[4] E. Forestieri, M. Secondini, L. Potì, and F. Cavaliere, "High-Speed Optical Communications Systems for Future WDM Centralized Radio Access Networks," *Journal of Lightwave Technology,* vol. 40, no. 2, pp. 368-378, 2021.

[5] M. Filer, S. Searcy, Y. Fu, R. Nagarajan, and S. Tibuleac, "Demonstration and performance analysis of 4 Tb/s DWDM metro-DCI system with 100G PAM4 QSFP28 modules," in *2017 Optical Fiber Communications Conference and Exhibition (OFC)*, 2017: IEEE, pp. 1-3.

[6] R. Rath, D. Clausen, S. Ohlendorf, S. Pachnicke, and W. Rosenkranz, "Tomlinson–Harashima precoding for dispersion uncompensated PAM-4 transmission with direct-detection," *Journal of Lightwave Technology,* vol. 35, no. 18, pp. 3909-3917, 2017.

[7] X. Tang, Y. Qiao, Y.-W. Chen, Y. Lu, and G.-K. Chang, "Digital Pre-and Post-equalization for C-band 112-Gb/s PAM4 Short-reach Transport Systems," *Journal of Lightwave Technology,* vol. 38, no.17, pp. 4683-4690. 2020.

[8] C. Antonelli, A. Mecozzi, M. Shtaif, X. Chen, S. Chandrasekhar, and P. J. Winzer, "Polarization multiplexing with the Kramers-Kronig receiver," *Journal of Lightwave Technology,* vol. 35, no. 24, pp. 5418-5424, 2017.

[9] K. Liu, C. R. Ye, S. Khan, and V. J. Sorger, "Review and perspective on ultrafast wavelength-size electro-optic modulators," *Laser & Photonics Reviews,* vol. 9, no. 2, pp. 172-194, 2015.

[10] M. S. Alam, X. Li, M. Jacques, E. Berikaa, P.-C. Koh, and D. V. Plant, "Net 300 Gbps/λ transmission over 2 km of SMF with a silicon photonic Mach-Zehnder modulator," *IEEE Photonics Technology Letters,* vol. 33, no. 24, pp. 1391-1394, 2021.

[11] M. S. Alam *et al.*, "Net 220 Gbps/λ IM/DD transmssion in O-Band and C-Band with silicon photonic traveling-wave MZM," *Journal of Lightwave Technology,* vol. 39, no. 13, pp. 4270-4278, 2021.

[12] M. S. Alam, E. Berikaa, and D. V. Plant, “High Bandwidth Thin-Film Lithium Niobate MZM for Net 300 Gbps/λ IM/DD Transmission,” in *2022 IEEE Photonics Conference (IPC)*, 13-17 Nov. 2022 2022, pp. 1-2, doi: 10.1109/IPC53466.2022.9975680.

[13] M. S. Alam, E. Berikaa, and D. V. Plant, “Net 350 Gbps/λ IMDD Transmission Enabled by High Bandwidth Thin-Film Lithium Niobate MZM,” *IEEE Photonics Technology Letters,* vol. 34, no. 19, pp. 1003-1006, 2022, doi: 10.1109/LPT.2022.3198322.

[14] M. S. Alam *et al.*, “224 Gb/s Transmission over 10 km of SMF at 1550 nm Enabled by a SiN Optical Dispersion Compensator and Stokes Vector Direct Detect Receiver,” in *OSA Advanced Photonics Congress (AP) 2020* Washington, DC, 2020: Optica Publishing Group, p. SpM4I.5, doi: 10.1364/SPPCOM.2020.SpM4I.5.

[15] M. S. Alam, R. Maram, K. A. Shahriar, P. Ricciardi, and D. V. Plant, “Chirped managed laser for multilevel modulation formats: A semi-analytical approach for efficient filter design,” *Journal of Lightwave Technology,* 2023 (submitted, under review).

[16] M. S. Alam, K. A. Shahriar, R. Maram, P. Ricciardi, and D. V. Plant, “PAM4 Signal Transmission using Directly Modulated Lasers: A Comprehensive Analysis of Chirp Parameters, Fiber Dispersion and Optical Filtering,” *IEEE Photonics Journal,* 2023 (submitted, under review).

[17] M. S. Alam, X. Li, Z. Xing, M. E. Mousa-Pasandi, M. O’Sullivan, and D. V. Plant, “C-band 4×200 Gbit/s transmission over 40 km of SSMF with an RF delay-assisted WDM-SSB transmitter,” in *Optical Fiber Communication Conference (OFC) 2021*, Washington, DC, 2021: Optica Publishing Group, p. W6A.50.

[18] M. S. Alam, X. Li, M. Jacques, E. Berikaa, P. C. Koh, and D. V. Plant, “Net 300 Gbps/λ Transmission Over 2 km of SMF With a Silicon Photonic Mach-Zehnder Modulator,” *IEEE Photonics Technology Letters,* vol. 33, no. 24, pp. 1391-1394, 2021, doi: 10.1109/LPT.2021.3124196.

[19] T. Kawanishi, *Electro-optic Modulation for Photonic Networks*. Springer, 2022.

[20] M. Xu and X. Cai, “Advances in integrated ultra-wideband electro-optic modulators,” *Optics Express,* vol. 30, no. 5, pp. 7253-7274, 2022.

[21] J. C. Campbell, “Recent advances in avalanche photodiodes,” *Journal of Lightwave Technology,* vol. 34, no. 2, pp. 278-285, 2016.

[22] J. Liu, S. Cristoloveanu, and J. Wan, “A Review on the Recent Progress of Silicon-on-Insulator-Based Photodetectors,” *Physica Status Solidi (a),* vol. 218, no. 14, p. 2000751, 2021.

[23] K. Zhong *et al.*, “Experimental study of PAM-4, CAP-16, and DMT for 100 Gb/s short reach optical transmission systems,” *Optics Express,* vol. 23, no. 2, pp. 1176-1189, 2015.

[24] E. Ip, A. P. T. Lau, D. J. F. Barros, and J. M. Kahn, “Coherent detection in optical fiber

systems," *Optics Express,* vol. 16, no. 2, pp. 753-791, 2008/01/21 2008, doi: 10.1364/OE.16.000753.

[25] S. J. Savory, "Digital filters for coherent optical receivers," *Optics Express,* vol. 16, no. 2, pp. 804-817, 2008.

[26] K. Kikuchi, "Digital coherent optical communication systems: Fundamentals and future prospects," *IEICE Electronics Express,* vol. 8, no. 20, pp. 1642-1662, 2011.

[27] J. Zhao, Y. Liu, and T. Xu, "Advanced DSP for coherent optical fiber communication," *Applied Sciences,* vol. 9, no. 19, p. 4192, 2019.

[28] D. Tauber *et al.*, "Role of Coherent Systems in the Next DCI Generation," *Journal of Lightwave Technology,* vol. 41, no. 4, pp. 1139-1151, 2023.

[29] M. Chagnon and D. Plant, "Advanced modulation formats for direct detection single carrier fiber optic short-reach systems," in *2016 Photonics North (PN)*, 24-26 May 2016 2016, pp. 1-1, doi: 10.1109/PN.2016.7537893.

[30] M. Morsy-Osman, M. Chagnon, and D. V. Plant, "Multi-Dimensional Modulation and Self Beating Direct Detection for Next Generation High Speed Short-Reach Optical Interconnects," in *Advanced Photonics 2016 (IPR, NOMA, Sensors, Networks, SPPCom, SOF)*, Vancouver, 2016: Optical Society of America, p. SpM4E.4.

[31] D. Che, A. Li, X. Chen, Q. Hu, Y. Wang, and W. Shieh, "Stokes vector direct detection for short-reach optical communication," *Optics Letters,* vol. 39, no. 11, pp. 3110-3113, 2014.

[32] M. Chagnon, M. Morsy-Osman, D. Patel, V. Veerasubramanian, A. Samani, and D. V. Plant, "Digital signal processing for dual-polarization intensity and interpolarization phase modulation formats using stokes detection," *Journal of Lightwave Technology,* vol. 34, no. 1, pp. 188-195, 2016.

[33] M. Zhu *et al.*, "Optical single side-band Nyquist PAM-4 transmission using dual-drive MZM modulation and direct detection," *Optics Express,* vol. 26, no. 6, pp. 6629-6638, 2018.

[34] J. Lee, N. Kaneda, and Y.-K. Chen, "112-Gbit/s intensity-modulated direct-detect vestigial-sideband PAM4 transmission over an 80-km SSMF link," in *ECOC 2016; 42nd European Conference on Optical Communication*, 2016: VDE, pp. 1-3.

[35] X. Li, Z. Xing, M. S. Alam, M. E. Mousa-Pasandi, M. O'Sullivan, and D. V. Plant, "Demonstration of C-Band Amplifier-Free 100 Gb/s/λ Direct-Detection Links Beyond 40-km SMF Using a High-Power SSB Transmitter," *Journal of Lightwave Technology,* vol. 38, no. 22, pp. 6170-6177, 2020.

[36] T. Bo, H. Kim, Z. Tan, and Y. Dong, "Optical Single-Sideband Transmitters," *Journal of Lightwave Technology,* vol. 41, no. 4, pp. 1163-1174, 2023.

[37] A. Mecozzi, C. Antonelli, and M. Shtaif, “Kramers–kronig receivers,” *Advances in Optics and Photonics,* vol. 11, no. 3, pp. 480-517, 2019.

[38] Z. Xing, *Direct Detection and Self-coherent Detection Short-reach Optical Communication Systems for Data Center Networking*. McGill University (Canada), 2021.

[39] X. Chen, C. Antonelli, A. Mecozzi, D. Che, and W. Shieh, “High-capacity direct-detection systems,” in *Optical Fiber Telecommunications VII*: Elsevier, 2020, pp. 419-441.

[40] G. P. Agrawal, “Nonlinear fiber optics,” in *Nonlinear Science at the Dawn of the 21st Century*: Springer, 2000, pp. 195-211.

[41] L. A. Neto *et al.*, “Simple estimation of fiber dispersion and laser chirp parameters using the downhill simplex fitting algorithm,” *Journal of Lightwave Technology,* vol. 31, no. 2, pp. 334-342, 2012.

[42] K. Zhang, Q. Zhuge, H. Xin, W. Hu, and D. V. Plant, “Performance comparison of DML, EML and MZM in dispersion-unmanaged short reach transmissions with digital signal processing,” *Optics Express,* vol. 26, no. 26, pp. 34288-34304, 2018.

[43] D. Mahgerefteh, Y. Matsui, X. Zheng, and K. McCallion, “Chirp managed laser and applications,” *IEEE Journal of Selected Topics in Quantum Electronics,* vol. 16, no. 5, pp. 1126-1139, 2010.

[44] C. M. Miller, “Intensity modulation and noise characterization of high-speed semiconductor lasers,” *IEEE LTS,* vol. 2, no. 2, pp. 44-50, 1991.

[45] L. A. Coldren, S. W. Corzine, and M. L. Mashanovitch, *Diode lasers and photonic integrated circuits*. John Wiley & Sons, 2012.

[46] C. Laperle and M. O’Sullivan, “Advances in high-speed DACs, ADCs, and DSP for optical coherent transceivers,” *Journal of lightwave technology,* vol. 32, no. 4, pp. 629-643, 2014.

[47] M. Jacques *et al.*, “Modulator material impact on chirp, DSP, and performance in coherent digital links: comparison of the lithium niobate, indium phosphide, and silicon platforms,” *Optics Express,* vol. 26, no. 17, pp. 22471-22490, 2018/08/20 2018, doi: 10.1364/OE.26.022471.

[48] B. P. Smith and F. R. Kschischang, “Future prospects for FEC in fiber-optic communications,” *IEEE Journal of Selected Topics in Quantum Electronics,* vol. 16, no. 5, pp. 1245-1257, 2010.

[49] E. Agrell and M. Secondini, “Information-theoretic tools for optical communications engineers,” in *2018 IEEE Photonics Conference (IPC)*, 2018: IEEE, pp. 1-5.

[50] A. Alvarado, E. Agrell, D. Lavery, R. Maher, and P. Bayvel, “Replacing the soft-

decision FEC limit paradigm in the design of optical communication systems," *Journal of Lightwave Technology,* vol. 33, no. 20, pp. 4338-4352, 2015.

[51] J. Cho and L. Schmalen, "Construction of protographs for large-girth structured LDPC convolutional codes," in *2015 IEEE International Conference on Communications (ICC)*, 2015: IEEE, pp. 4412-4417.

[52] Q. Hu *et al.*, "Ultrahigh-net-bitrate 363 Gbit/s PAM-8 and 279 Gbit/s polybinary optical transmission using plasmonic Mach-Zehnder modulator," *Journal of Lightwave Technology,* vol. 40, no. 10, pp. 3338-3346, 2022.

[53] P. Kabal and S. Pasupathy, "Partial-response signaling," *IEEE Transactions on Communications,* vol. 23, no. 9, pp. 921-934, 1975.

[54] Q. Wu, Y. Zhu, L. Yin, and W. Hu, "50GBaud PAM-4 IM-DD Transmission with 24% Bandwidth Compression Based on Polybinary Spectral Shaping," in *2021 European Conference on Optical Communication (ECOC)*, 2021: IEEE, pp. 1-4.

[55] Q. Zhang, N. Stojanovic, C. Prodaniuc, C. Xie, M. Koenigsmann, and P. Laskowski, "Single-lane 180 Gbit/s PAM-4 signal transmission over 2 km SSMF for short-reach applications," *Optics letters,* vol. 41, no. 19, pp. 4449-4452, 2016.

[56] N. Stojanovic, C. Prodaniuc, L. Zhang, and J. Wei, "210/225 Gbit/s PAM-6 Transmission with BER Below KP4-FEC/EFEC and at Least 14 dB Link Budget," in *2018 European Conference on Optical Communication (ECOC)*, 23-27 Sept. 2018 2018, pp. 1-3, doi: 10.1109/ECOC.2018.8535246.

[57] G. Böcherer, P. Schulte, and F. Steiner, "Probabilistic Shaping and Forward Error Correction for Fiber-Optic Communication Systems," *Journal of Lightwave Technology,* vol. 37, no. 2, pp. 230-244, 2019, doi: 10.1109/JLT.2019.2895770.

[58] P. Schulte and G. Böcherer, "Constant Composition Distribution Matching," *IEEE Transactions on Information Theory,* vol. 62, no. 1, pp. 430-434, 2016, doi: 10.1109/TIT.2015.2499181.

[59] F. Steiner *et al.*, "Experimental verification of rate flexibility and probabilistic shaping by 4D signaling," in *Optical Fiber Communication Conference*, 2018: Optica Publishing Group, p. M4E. 3.

[60] X. Li, Z. Xing, M. S. Alam, M. Jacques, P.-C. Koh, and D. V. Plant, "Cost-minimizing distribution matching supporting net 800 Gbit/s PS-PAM transmission over 2 km using a 4-λ EML TOSA," *Optics Letters,* vol. 45, no. 17, pp. 4718-4721, 2020.

[61] T. Rahman, S. Calabrò, N. Stojanovic, L. Zhang, J. Wei, and C. Xie, "LUT-assisted pre-compensation for 225 Gb/s/λ O-band transmission," in *45th European Conference on Optical Communication (ECOC 2019)*, 2019: IET, pp. 1-4.

[62] J. G. Proakis and M. Salehi, *Digital communications*. McGraw-hill New York, 2001.

[63] A. Napoli *et al.*, “Novel DAC digital pre-emphasis algorithm for next-generation flexible optical transponders,” in *Optical Fiber Communication Conference*, 2015: Optica Publishing Group, p. Th3G. 6.

[64] A. Napoli *et al.*, “Digital compensation of bandwidth limitations for high-speed DACs and ADCs,” *Journal of Lightwave Technology,* vol. 34, no. 13, pp. 3053-3064, 2016.

[65] D. Rafique, A. Napoli, S. Calabro, and B. Spinnler, “Digital preemphasis in optical communication systems: On the DAC requirements for terabit transmission applications,” *Journal of Lightwave Technology,* vol. 32, no. 19, pp. 3247-3256, 2014.

[66] N. Stojanovic, F. Karinou, Z. Qiang, and C. Prodaniuc, “Volterra and Wiener equalizers for short-reach 100G PAM-4 applications,” *Journal of Lightwave Technology,* vol. 35, no. 21, pp. 4583-4594, 2017.

[67] T. Wettlin, S. Pachnicke, T. Rahman, J. Wei, S. Calabro, and N. Stojanovic, “Complexity reduction of volterra nonlinear equalization for optical short-reach IM/DD systems,” in *Photonic Networks; 21th ITG-Symposium*, 2020: VDE, pp. 1-6.

[68] C.-Y. Chuang *et al.*, “Sparse volterra nonlinear equalizer by employing pruning algorithm for high-speed PAM-4 850-nm VCSEL optical interconnect,” in *Optical Fiber Communication Conference*, 2019: Optical Society of America, p. M1F. 2.

[69] M. Chagnon *et al.*, “Experimental study of 112 Gb/s short reach transmission employing PAM formats and SiP intensity modulator at 1.3 μm,” *Optics express,* vol. 22, no. 17, pp. 21018-21036, 2014.

[70] “PAM4 Signaling in High Speed Serial Technology: Test, Analysis, and Debug.” (accessed 31st August, 2023).

[71] C. V. Networking, “Cisco global cloud index: Forecast and methodology, 2017-2022. white paper,” *Cisco Public, San Jose,* p. 2016, 2017.

[72] P. L. IEEE802.3bs-2017 – IEEE Standard for Ethernet Amendment 10: Media Access Control Parameters, and Management Parameters for 200 Gbps and 400 Gbps Operation.

[73] S. Kanazawa *et al.*, “Transmission of 214-Gbit/s 4-PAM signal using an ultra-broadband lumped-electrode EADFB laser module,” in *Optical Fiber Communication Conference PDP*, Anaheim, California, 2016: Optica Publishing Group, p. Th5B.3.

[74] C. Kieninger *et al.*, “Ultra-high electro-optic activity demonstrated in a silicon-organic hybrid modulator,” *Optica,* vol. 5, no. 6, pp. 739-748, 2018.

[75] S. Lange *et al.*, “100 GBd intensity modulation and direct detection with an InP-based monolithic DFB laser Mach–Zehnder modulator,” *Journal of Lightwave Technology,* vol. 36, no. 1, pp. 97-102, 2018.

[76] O. Ozolins *et al.*, “100 GHz externally modulated laser for optical interconnects,”

Journal of Lightwave Technology, vol. 35, no. 6, pp. 1174-1179, 2017.

[77] P. O. Weigel *et al.*, "Bonded thin film lithium niobate modulator on a silicon photonics platform exceeding 100 GHz 3-dB electrical modulation bandwidth," *Optics express,* vol. 26, no. 18, pp. 23728-23739, 2018.

[78] T. Wettlin, T. Rahman, J. Wei, S. Calabrò, N. Stojanovic, and S. Pachnicke, "Comparison of PAM formats for 200 Gb/s short reach transmission systems," in *Optical Fiber Communication Conference*, 2020: Optica Publishing Group, p. Th2A. 37.

[79] H. Zhang *et al.*, "800 Gbit/s transmission over 1 km single-mode fiber using a four-channel silicon photonic transmitter," *Photonics Research,* vol. 8, no. 11, pp. 1776-1782, 2020.

[80] A. Samani *et al.*, "Silicon photonic Mach–Zehnder modulator architectures for on chip PAM-4 signal generation," *Journal of Lightwave Technology,* vol. 37, no. 13, pp. 2989-2999, 2019.

[81] J. Zhou, J. Wang, L. Zhu, and Q. Zhang, "High baud rate all-silicon photonics carrier depletion modulators," *Journal of Lightwave Technology,* vol. 38, no. 2, pp. 272-281, 2019.

[82] Y. Zhu *et al.*, "Toward single lane 200G optical interconnects with silicon photonic modulator," *Journal of Lightwave Technology,* vol. 38, no. 1, pp. 67-74, 2019.

[83] M. Li, L. Wang, X. Li, X. Xiao, and S. Yu, "Silicon intensity Mach–Zehnder modulator for single lane 100 Gb/s applications," *Photonics Research,* vol. 6, no. 2, pp. 109-116, 2018.

[84] A. Samani *et al.*, "A low-voltage 35-GHz silicon photonic modulator-enabled 112-Gb/s transmission system," *IEEE Photonics Journal,* vol. 7, no. 3, pp. 1-13, 2015.

[85] W. Shi, Y. Xu, H. Sepehrian, S. LaRochelle, and L. A. Rusch, "Silicon photonic modulators for PAM transmissions," *Journal of Optics,* vol. 20, no. 8, p. 083002, 2018.

[86] Y. Zhang *et al.*, "200 Gbit/s optical PAM4 modulation based on silicon microring modulator," in *2020 European Conference on Optical Communications (ECOC)*, 2020: IEEE, pp. 1-4.

[87] M. Jacques *et al.*, "240 Gbit/s silicon photonic Mach-Zehnder modulator enabled by two 2.3-Vpp drivers," *Journal of Lightwave Technology,* vol. 38, no. 11, pp. 2877-2885, 2020.

[88] M. Jacques *et al.*, "Net 212.5 Gbit/s Transmission in O-Band with a SiP MZM, One Driver and Linear Equalization," in *2020 Optical Fiber Communications Conference and Exhibition (OFC)*, 8-12 March 2020 2020, pp. 1-3.

[89] D. Patel *et al.*, "Design, analysis, and transmission system performance of a 41 GHz

silicon photonic modulator," *Optics Express,* vol. 23, no. 11, pp. 14263-14287, 2015.

[90] H. Yu and W. Bogaerts, "An equivalent circuit model of the traveling wave electrode for carrier-depletion-based silicon optical modulators," *Journal of Lightwave Technology,* vol. 30, no. 11, pp. 1602-1609, 2012.

[91] D. Petousi *et al.*, "Analysis of optical and electrical tradeoffs of traveling-wave depletion-type Si Mach–Zehnder modulators for high-speed operation," *IEEE Journal of Selected Topics in Quantum Electronics,* vol. 21, no. 4, pp. 199-206, 2014.

[92] L. Zhang *et al.*, "Kernel affine projection for nonlinearity tolerant optical short reach systems," *IEEE Transactions on Communications,* vol. 68, no. 10, pp. 6403-6412, 2020.

[93] N.-P. Diamantopoulos, H. Nishi, W. Kobayashi, K. Takeda, T. Kakitsuka, and S. Matsuo, "On the complexity reduction of the second-order Volterra nonlinear equalizer for IM/DD systems," *Journal of Lightwave Technology,* vol. 37, no. 4, pp. 1214-1224, 2018.

[94] J. Zhang *et al.*, "PAM-8 IM/DD transmission based on modified lookup table nonlinear predistortion," *IEEE Photonics Journal,* vol. 10, no. 3, pp. 1-9, 2018.

[95] J. Zhang *et al.*, "280 Gb/s IM/DD PS-PAM-8 transmission over 10 km SSMF at O-band for optical interconnects," in *2020 Optical Fiber Communications Conference and Exhibition (OFC)*, 2020: IEEE, pp. 1-3.

[96] D. Che, J. Cho, and X. Chen, "Does probabilistic constellation shaping benefit IM-DD systems without optical amplifiers?," *Journal of Lightwave Technology,* vol. 39, no. 15, pp. 4997-5007, 2021.

[97] M. Burla *et al.*, "500 GHz plasmonic Mach-Zehnder modulator enabling sub-THz microwave photonics," *APL Photonics,* vol. 4, no. 5, p. 056106, 2019.

[98] C. Han, M. Jin, Y. Tao, B. Shen, H. Shu, and X. Wang, "Ultra-compact silicon modulator with 110 GHz bandwidth," in *Optical Fiber Communication Conference*, 2022: Optica Publishing Group, p. Th4C. 5.

[99] N.-P. Diamantopoulos *et al.*, ">100-GHz bandwidth directly-modulated lasers and adaptive entropy loading for energy-efficient> 300-Gbps/λ IM/DD systems," *Journal of Lightwave Technology,* vol. 39, no. 3, pp. 771-778, 2021.

[100] R. Borkowski *et al.*, "Experimental evaluation of PAM and polybinary modulation for intra-DCI optical lanes with up to 300 Gbit/s net bitrates," in *Optical Fiber Communication Conference*, 2022: Optica Publishing Group, p. M4H. 6.

[101] M. S. B. Hossain *et al.*, "402 Gb/s PAM-8 IM/DD O-Band EML Transmission," in *2021 European Conference on Optical Communication (ECOC)*, 2021: IEEE, pp. 1-4.

[102] X. Chen, S. Chandrasekhar, J. Cho, and P. Winzer, "Single-wavelength and single-photodiode entropy-loaded 554-Gb/s transmission over 22-km SMF," in *Optical Fiber Communication Conference*, 2019: Optica Publishing Group, p. Th4B. 5.

[103] H. Yamazaki *et al.*, "Net-400-Gbps PS-PAM transmission using integrated AMUX-MZM," *Optics Express,* vol. 27, no. 18, pp. 25544-25550, 2019.

[104] M. Zhang, C. Wang, P. Kharel, D. Zhu, and M. Lončar, "Integrated lithium niobate electro-optic modulators: when performance meets scalability," *Optica,* vol. 8, no. 5, pp. 652-667, 2021.

[105] D. Zhu *et al.*, "Integrated photonics on thin-film lithium niobate," *Advances in Optics and Photonics,* vol. 13, no. 2, pp. 242-352, 2021.

[106] C. Wang *et al.*, "Integrated lithium niobate electro-optic modulators operating at CMOS-compatible voltages," *Nature,* vol. 562, no. 7725, pp. 101-104, 2018.

[107] Y. Zhang *et al.*, "220 Gbit/s optical PAM4 modulation based on lithium niobate on insulator modulator," in *45th European Conference on Optical Communication (ECOC 2019)*, 2019: IET, pp. 1-4.

[108] F. Yang, X. Fang, X. Chen, Y. Li, and F. Zhang, "Up to 360 Gb/s optical interconnects with ultra-high bandwidth thin film lithium niobate modulator," in *2022 Optical Fiber Communications Conference and Exhibition (OFC)*, 2022: IEEE, pp. 1-3.

[109] M. M. Howerton and W. K. Burns, *Broadband traveling wave modulators in $LiNbO_3$.* Cambridge Univ. Press, 2002.

[110] D. W. Chan, X. Wu, A. P. T. Lau, C. Lu, and H. K. Tsang, "Single Lane 330 Gb/s Silicon Photonic Microring Modulator with sub 2 V pp Driving Voltage," in *2023 Optical Fiber Communications Conference and Exhibition (OFC)*, 2023: IEEE, pp. 1-3.

[111] A. Ostrovskis *et al.*, "240/160 Gbaud OOK Silicon Photonics MZM/RRM Transmitters for Short-Reach Applications," in *2023 IEEE Silicon Photonics Conference (SiPhotonics)*, 2023: IEEE, pp. 1-2.

[112] E. Berikaa *et al.*, "TFLN MZMs and Next-Gen DACs: Enabling Beyond 400 Gbps IMDD O-band and C-band Transmission," *IEEE Photonics Technology Letters,* 2023.

[113] O. Ozolins *et al.*, "Optical Amplification-Free 310/256 Gbaud OOK, 197/145 Gbaud PAM4, and 160/116 Gbaud PAM6 EML/DML-based Data Center Links," in *Optical Fiber Communication Conference*, 2023: Optica Publishing Group, p. Th4B. 2.

[114] J. Zhang *et al.*, "Nonlinearity-aware PS-PAM-16 transmission for C-band net-300-Gbit/s/λ short-reach optical interconnects with a single DAC," *Optics Letters,* vol. 47, no. 12, pp. 3035-3038, 2022.

[115] M. Filer, S. Searcy, Y. Fu, R. Nagarajan, and S. Tibuleac, "Demonstration and performance analysis of 4 Tb/s DWDM metro-DCI system with 100G PAM4 QSFP28 modules," in *Optical Fiber Communication Conference*, 2017: Optica Publishing Group, p. W4D. 4.

[116] M. Morsy-Osman, M. Chagnon, M. Poulin, S. Lessard, and D. V. Plant, "224-Gb/s 10-

km transmission of PDM PAM-4 at 1.3 μm using a single intensity-modulated laser and a direct-detection MIMO DSP-based receiver," *Journal of Lightwave Technology,* vol. 33, no. 7, pp. 1417-1424, 2015.

[117] D. Che and W. Shieh, "Polarization demultiplexing for Stokes vector direct detection," *Journal of Lightwave Technology,* vol. 34, no. 2, pp. 754-760, 2016.

[118] C. K. Madsen, G. Lenz, A. J. Bruce, M. Cappuzzo, L. Gomez, and R. Scotti, "Integrated all-pass filters for tunable dispersion and dispersion slope compensation," *IEEE Photonics Technology Letters,* vol. 11, no. 12, pp. 1623-1625, 1999.

[119] V. Sorianello *et al.*, "100Gb/s PolMux-NRZ Transmission at 1550nm over 30km Single Mode Fiber Enabled by a Silicon Photonics Optical Dispersion Compensator," in *Optical Fiber Communication Conference*, 2018: Optical Society of America, p. W2A. 31.

[120] T. Sudo *et al.*, "Challenges and opportunities of directly modulated lasers in future data center and 5G networks," in *Optical Fiber Communication Conference*, 2021: Optical Society of America, p. Tu1B. 3.

[121] N. Sasada *et al.*, "Wide-temperature-range (25–80° C) 53-Gbaud PAM4 (106-Gb/s) operation of 1.3-μm directly modulated DFB lasers for 10-km transmission," *Journal of Lightwave Technology,* vol. 37, no. 7, pp. 1686-1689, 2019.

[122] T. Nakajima *et al.*, "106-Gb/s PAM4 Operation of Directly Modulated DFB Lasers from 25 to 70° C for Transmission Over 2-km SMF in the CWDM Range," *Journal of Lightwave Technology,* vol. 40, no. 6, pp. 1815-1820, 2022.

[123] K. Nakahara *et al.*, "Superior Lowest TDECQ (3.3 dB at 106 Gb/s, 4.4 dB at 112 Gb/s) under PAM-4 Operation at up to 85° C with High Extinction Ratio (4 dB) in 1.3-μm Uncooled Directly modulated InGaAlAs MQW-BH Lasers," in *2022 European Conference on Optical Communication (ECOC)*, 2022: IEEE, pp. 1-4.

[124] M. O. Shuhei Ohno, Takayuki Nakajima, Akira Nakanishi, Noriko Sasada, Shinichi Tanaka, Ryosuke Nakajima, Kazuhiko Naoe, "10-km Transmission of 106-Gb/s PAM4 With Directly Modulated DFB Lasers in the CWDM Range " in *2023 Optical Fiber Communications Conference and Exhibition (OFC)* 2023: IEEE, pp. 1-3.

[125] R. M. Kosuke Shinohara, Yosuke Suzuki, Ryoko Suzuki, Go Sakaino, Masaaki Shimada, Keisuke Matsumoto, "106-Gbps PAM4 Operation at an Extinction Ratio Above 3.5 dB Using a Conventional Buried-Heterostructure Directly Modulated Laser," in *2023 Optical Fiber Communications Conference and Exhibition (OFC)*, 2023: IEEE, pp. 1-3.

[126] N. H. Zhu *et al.*, "Directly modulated semiconductor lasers," *IEEE Journal of Selected Topics in Quantum Electronics,* vol. 24, no. 1, pp. 1-19, 2017.

[127] Y. Matsui, “Directly Modulation Laser Technology: Past, Present and Future,” in *Datacenter Connectivity Technologies*, 1st ed.: River Publishers, 2018, ch. 3, pp. 87-211.

[128] Z. Zhou, M. Bi, S. Xiao, Y. Zhang, and W. Hu, “Experimental demonstration of symmetric 100-Gb/s DML-based TWDM-PON system,” *IEEE Photonics Technology Letters,* vol. 27, no. 5, pp. 470-473, 2014.

[129] S. H. Bae, H. Kim, and Y.-C. Chung, “Transmission of 51.56-Gb/s OOK signal using 1.55-µm directly modulated laser and duobinary electrical equalizer,” *Optics express,* vol. 24, no. 20, pp. 22555-22562, 2016.

[130] M. Kim, S. Bae, H. Kim, and Y. C. Chung, “Transmission of 56-Gb/s PAM-4 signal over 20 km of SSMF using a 1.55-µm directly-modulated laser,” in *2017 Optical Fiber Communications Conference and Exhibition (OFC)*, 2017: IEEE, pp. 1-3.

[131] C. Sun, S. H. Bae, and H. Kim, “Transmission of 28-Gb/s duobinary and PAM-4 signals using DML for optical access network,” *IEEE Photonics Technology Letters,* vol. 29, no. 1, pp. 130-133, 2016.

[132] M. T. Costas *et al.*, “30 Gbit/s PAM4 transmission using an 8-GHz directly modulated multi-section laser,” *Optics Express,* vol. 30, no. 12, pp. 20194-20202, 2022.

[133] Y. Yu, M. R. Choi, T. Bo, Z. He, Y. Che, and H. Kim, “Low-complexity second-order Volterra equalizer for DML-based IM/DD transmission system,” *Journal of Lightwave Technology,* vol. 38, no. 7, pp. 1735-1746, 2019.

[134] Y. Fu *et al.*, “Piecewise linear equalizer for DML based PAM-4 signal transmission over a dispersion uncompensated link,” *Journal of Lightwave Technology,* vol. 38, no. 3, pp. 654-660, 2019.

[135] Y. Gao, J. C. Cartledge, S. S. Yam, A. Rezania, and Y. Matsui, “112 Gb/s PAM-4 Using a Directly Modulated Laser with Linear Pre-Compensation and Nonlinear Post-Compensation,” in *ECOC 2016;* 18-22 Sept. 2016, pp. 1-3.

[136] J. C. Cartledge and R. Srinivasan, “Extraction of DFB laser rate equation parameters for system simulation purposes,” *Journal of Lightwave Technology,* vol. 15, no. 5, pp. 852-860, 1997.

[137] I. Tomkos, I. Roudas, R. Hesse, N. Antoniades, A. Boskovic, and R. Vodhanel, “Extraction of laser rate equations parameters for representative simulations of metropolitan-area transmission systems and networks,” *Optics Communications,* vol. 194, no. 1-3, pp. 109-129, 2001.

[138] J. Zhou, C. Yu, and H. Kim, “Transmission performance of OOK and 4-PAM signals using directly modulated 1.5-µm VCSEL for optical access network,” *Journal of Lightwave Technology,* vol. 33, no. 15, pp. 3243-3249, 2015.

[139] S. Mohrdiek *et al.*, “10-Gb/s standard fiber transmission using directly modulated 1.55-μm quantum-well DFB lasers,” *IEEE Photonics Technology Letters,* vol. 7, no. 11, pp. 1357-1359, 1995.

[140] A. S. Karar, J. C. Cartledge, J. Harley, and K. Roberts, “Electronic pre-compensation for a 10.7-Gb/s system employing a directly modulated laser,” *Journal of Lightwave Technology,* vol. 29, no. 13, pp. 2069-2076, 2011.

[141] Y. Matsui *et al.*, “Chirp-managed directly modulated laser (CML),” *IEEE Photonics Technology Letters,* vol. 18, no. 2, pp. 385-387, 2006.

[142] Z. Jia, J. Yu, and G.-K. Chang, “Chirp-managed directly-modulated DFB laser,” *Recent Patents on Engineering,* vol. 1, no. 1, pp. 43-47, 2007.

[143] Y. An, A. L. Riesgo, J. Seoane, Y. Ding, H. Ou, and C. Peucheret, “Modulation speed enhancement of directly modulated lasers using a micro-ring resonator,” in *2012 Optical Interconnects Conference*, 2012: IEEE, pp. 32-33.

[144] V. Cristofori *et al.*, “Directly modulated and ER enhanced hybrid III-V/SOI DFB laser operating up to 20 Gb/s for extended reach applications in PONs,” in *Optical Fiber Communication Conference*, 2017: Optica Publishing Group, p. Tu3G. 7.

[145] L. Bjerkan, A. Royset, L. Hafskjaer, and D. Myhre, “Measurement of laser parameters for simulation of high-speed fiberoptic systems,” *Journal of Lightwave Technology,* vol. 14, no. 5, pp. 839-850, 1996.

[146] J. Wang and K. Petermann, “Small signal analysis for dispersive optical fiber communication systems,” *Journal of Lightwave Technology,* vol. 10, no. 1, pp. 96-100, 1992.

[147] R. Motaghiannezam *et al.*, “52 Gbps PAM4 receiver sensitivity study for 400GBase-LR8 system using directly modulated laser,” *Optics Express,* vol. 24, no. 7, pp. 7374-7380, 2016.

[148] Y. Matsui *et al.*, “Transceiver for NG-PON2: Wavelength tunablity for burst mode TWDM and point-to-point WDM,” in *Optical Fiber Communication Conference*, 2016: Optical Society of America, p. Tu2C. 1.

[149] Z. Li, L. Yi, X. Wang, and W. Hu, “28 Gb/s duobinary signal transmission over 40 km based on 10 GHz DML and PIN for 100 Gb/s PON,” *Optics Express,* vol. 23, no. 16, pp. 20249-20256, 2015.

[150] N. Kikuchi, R. Hirai, and T. Fukui, “Non-linearity compensation of high-speed PAM4 signals from directly-modulated laser at high extinction ratio,” in *ECOC 2016; 42nd European Conference on Optical Communication*, 2016: VDE, pp. 1-3.

[151] S. T. Le, Y. Matsui, G. Raybon, A. Venna, M. Kwakernaak, and T. Sudo, “Reach Extension for 100 Gb/s PAM-4 IM/DD Transmission by Chirp Managed Laser,” in

2022 Optical Fiber Communications Conference and Exhibition (OFC), 2022: IEEE, pp. 1-3.

[152] P. N. Ji *et al.*, “Chirp-managed 42.8 Gbit/s transmission over 20 km standard SMF without DCF using directly modulated laser,” in *33rd European Conference and Exhibition of Optical Communication*, 2007: VDE, pp. 1-2.

[153] D. Mahgerefteh *et al.*, “Tunable chirp managed laser,” *IEEE Photonics Technology Letters,* vol. 20, no. 2, pp. 108-110, 2008.

[154] J. Yu *et al.*, “Applications of 40-Gb/s chirp-managed laser in access and metro networks,” *Journal of Lightwave Technology,* vol. 27, no. 3, pp. 253-265, 2009.

[155] M. Dalla Santa, C. Antony, G. Talli, and P. D. Townsend, “Chirp control in directly modulated 25G PAM4 transmitters for optical access networks,” in *CLEO: Science and Innovations*, 2017: Optical Society of America, p. SF1L. 3.

[156] A. Lender, “Correlative digital communication techniques,” *IEEE Transactions on Communication Technology,* vol. 12, no. 4, pp. 128-135, 1964.

[157] A. S. Karar, *Digital signal processing for directly modulated lasers in optical fiber communications*. Queen's University (Canada), 2013.

[158] C. Yang *et al.*, “IM/DD-based 112-Gb/s/lambda PAM-4 transmission using 18-Gbps DML,” *IEEE Photonics Journal,* vol. 8, no. 3, pp. 1-7, 2016.

[159] M. Dalla Santa, C. Antony, G. Talli, and P. D. Townsend, “Chirp control in directly modulated 25G PAM4 transmitters for optical access networks,” in *2017 Conference on Lasers and Electro-Optics (CLEO)*, 2017: IEEE, pp. 1-2.

[160] J. Zhang *et al.*, “Demonstration of 100-Gb/s/λ PAM-4 transmission over 45-km SSMF using one 10G-class DML in the C-band,” in *Optical Fiber Communication Conference*, 2019: Optical Society of America, p. Tu2F. 1.

[161] Y. Yu, T. Bo, Y. Che, D. Kim, and H. Kim, “Low-complexity nonlinear equalizer based on absolute operation for C-band IM/DD systems,” *Optics Express,* vol. 28, no. 13, pp. 19617-19628, 2020.

[162] K. Zhang *et al.*, “Intensity directed equalizer for the mitigation of DML chirp induced distortion in dispersion-unmanaged C-band PAM transmission,” *Optics Express,* vol. 25, no. 23, pp. 28123-28135, 2017.

[163] J. C. Lagarias, J. A. Reeds, M. H. Wright, and P. E. Wright, “Convergence properties of the Nelder--Mead simplex method in low dimensions,” *SIAM Journal on optimization,* vol. 9, no. 1, pp. 112-147, 1998.

[164] H. Li *et al.*, “A 3-D-integrated silicon photonic microring-based 112-Gb/s PAM-4 transmitter with nonlinear equalization and thermal control,” *IEEE Journal of Solid-State Circuits,* vol. 56, no. 1, pp. 19-29, 2020.

[165] H.-Y. Chen, N. Kaneda, J. Lee, J. Chen, and Y.-K. Chen, "Optical filter requirements in an EML-based single-sideband PAM4 intensity-modulation and direct-detection transmission system," *Optics Express,* vol. 25, no. 6, pp. 5852-5860, 2017.

[166] Z. Xing *et al.*, "100Gb/s 16-QAM Transmission over 80 km SSMF using a silicon photonic modulator enabled VSB-IM/DD system," in *2018 Optical Fiber Communications Conference and Exposition (OFC)*, 2018: IEEE, pp. 1-3.

[167] S. T. Le *et al.*, "1.72-Tb/s virtual-carrier-assisted direct-detection transmission over 200 km," *Journal of Lightwave Technology,* vol. 36, no. 6, pp. 1347-1353, 2018.

[168] Z. Li *et al.*, "Spectrally efficient 168 Gb/s/λ WDM 64-QAM single-sideband nyquist-subcarrier modulation with Kramers–Kronig direct-detection receivers," *Journal of Lightwave Technology,* vol. 36, no. 6, pp. 1340-1346, 2018.

[169] Y. Zhu, K. Zou, Z. Chen, and F. Zhang, "224 Gb/s optical carrier-assisted Nyquist 16-QAM half-cycle single-sideband direct detection transmission over 160 km SSMF," *Journal of Lightwave Technology,* vol. 35, no. 9, pp. 1557-1565, 2017.

[170] G. H. Smith, D. Novak, and Z. Ahmed, "Overcoming chromatic-dispersion effects in fiber-wireless systems incorporating external modulators," *IEEE Transactions on Microwave Theory and Techniques,* vol. 45, no. 8, pp. 1410-1415, 1997.

[171] Y. Zhu, L. Li, X. Miao, and W. Hu, "Time skew enabled vestigial sideband modulation for dispersion-tolerant direct–detection transmission," *Optics Letters,* vol. 45, no. 22, pp. 6138-6141, 2020/11/15 2020, doi: 10.1364/OL.406146.

[172] Y. Zhu, L. Li, X. Miao, and W. Hu, "Time skew-based filter-free VSB Nyquist PAM-4/6 generation and 80km SSMF transmission with direct detection," in *2020 European Conference on Optical Communications (ECOC)*, 2020: IEEE, pp. 1-5.

[173] D. Lu *et al.*, "Theoretical CSPR analysis and performance comparison for four single-sideband modulation schemes with Kramers-Kronig receiver," *IEEE Access,* vol. 7, pp. 166257-166267, 2019.

[174] E. Berikaa, M. S. Alam, and D. V. Plant, "Net 400-Gbps/λ IMDD transmission using a single-DAC DSP-free transmitter and a thin-film lithium niobate MZM," *Optics Letters,* vol. 47, no. 23, pp. 6273-6276, 2022/12/01 2022, doi: 10.1364/OL.476399.

[175] E. Berikaa, M. S. Alam, Y. Hu, W. Li, and D. V. Plant, "C-Band 100 Gb/s Transmission Over 40 km SSMF Using a Silicon Photonic Vestigial Sideband Transmitter Based on Dual-Drive MZM and Passive Optical Delay Line," in *2023 Optical Fiber Communication Conference (OFC)*, California, USA, p. Th3E.7, 2023.

[176] J. Zhang, Y. Cao, X. Wang, X. Feng, B.-O. Guan, and E. H. W. Chan, "Ultra-Broadband optical single sideband modulation with large sideband suppression ratio," in *2017 International Topical Meeting on Microwave Photonics (MWP)*, 2017: IEEE, pp. 1-4.